Fakultät für Maschinenwesen
Lehrstuhl für Angewandte Mechanik

Modular sound & vibration engineering by substructuring

Listening to machines during virtual design

Michael Häußler

Vollständiger Abdruck der von der Fakultät für Maschinenwesen der Technischen Universität München zur Erlangung des akademischen Grades eines

Doktor-Ingenieurs (Dr.-Ing.)

genehmigten Dissertation.

Vorsitzender: Prof. Dr. Markus Zimmermann

Prüfer der Dissertation:

1. Prof. dr.ir. Daniel J. Rixen

2. Prof. Dr.-Ing. Bernhard Seeber

Die Dissertation wurde am 25. Juni 2020 bei der Technischen Universität München eingereicht und durch die Fakultät für Maschinenwesen am 24. Februar 2021 angenommen.

Acknowledgement

> Everyone has a plan, until they get punched in the mouth.
>
> *Mike Tyson,*
> *interview before a fight*

There is no need to be worried: I did not receive a single "punch in the mouth" during this research project. However, the Mike Tyson quote not only made me laugh, but also made me think about my $4^{1/2}$ years in academics. Certainly not all went as initially planned, but in retrospect, I think this is what made the whole journey interesting. Ingenuity comes when it is not clear from the beginning what you should do. Then you are back to basic physical relations and mathematical equalities.

I want to thank you, Daniel Rixen, for inspiring students that this is possible. You fascinate young engineers by showing how to have "Newton on your side". I also want to thank all members of the Chair for Applied Mechanics, for having an inspiring work environment while keeping the chair well organized. It was a pleasure to be in this team!

During my time at the chair, I was lucky enough to meet an extraordinary set of people, all desiring to get an understanding of physical reality and making something better with it. Stefan Sendlbeck, Ron Reichart, Kui Yen-Chen, Dawid Kobus, Felix Benner, Francesco Trainotti, and Tom Müller: You are all great engineers and colleagues! Your contributions to this work make the whole picture complete [14, 15, 25, 89, 126, 144, 161, 176]. It was (and is) an enjoyable time working with you!

I want to thank all the people at BMW who helped me out, be it big or small favors. Explaining years long experience, helping me plan experiments, or just telling me where the tools are. It is crucial for future success, that experts in industry see the potential of new ideas, and are courageous enough to provide the resources to make it work. I want to thank Dr. Michael Spickenreuther, Dr. Peter Genender and Matthias Fenzl for making this whole journey possible. BMW was and is an engineers playground.

Additionally, I want to thank the team of VIBES.technology for having open discussions and sharing knowledge with me, despite building a tech company on the side. I remember countless discussions which helped me to point my attention at the key issues. Lets make the world a more quiet and pleasant place!

It might sound worn out to thank ones wife for being patient, and waiting outside of what is considered "regular office hours". But Finni you truly have and I deeply want to thank you for consistently encouraging me. I want to thank you for listening to me when spraying with enthusiasm and technical ideas, that might not even make sense to you at first. You are a person that lights up the whole room when coming in! Being on your side with Janna and Elisa is a blessing.

Munich, June 21, 2020

Michael Häußler

Abstract

This thesis is the result of a 4-year collaboration between the Technical University of Munich and the BMW Group. The goal was to apply substructuring methods to the Noise Vibration Harshness (NVH) engineering needed for integrating electric climate compressors in upcoming vehicles. The compressor is one of the major contributors to the cabin noise in battery electric vehicles (BEVs). An accurate yet practical development process for its vehicle integration is crucial for industry. Specifically, the aim was to simulate the compressor noise in the cabin for different, virtual design variants of the isolation concept. Therefore, the methods from two broader fields were applied: First, the excitation of the compressor was modeled with component transfer path analysis (TPA) methods. Second, the full transfer path from the compressor to the driver's ear is assembled from multiple subcomponent models, via dynamic substructuring (DS).

For accomplishing the above mentioned goals, different gaps in the current technology have been identified, which will be addressed in this thesis. With frequency based substructuring (FBS), a subclass of DS, it is possible to couple experimental and numerical substructure models in a virtual assembly. For the compressor, it was found that including rigid body models in the transfer path is a valuable addition. The proper formulation and integration of rigid body models in the framework of FBS will be presented. Another bottleneck at the onset of this project, was the proper modeling of rubber bushings in the transfer path. A novel method for experimentally identifying accurate substructure models of rubber isolators was developed. The rotating components in the compressor introduce gyroscopic effects that influence its dynamics. A novel substructuring method for virtually coupling gyroscopic terms to a component could prove that these effects are not relevant for the compressor case. The compressors excitation is described by blocked forces. Applying the blocked forces to the substructured transfer path of the assembly allows to simulate the sound in a virtual prototype. One goal was to make the simulated results audible to non-acoustic experts, which required the creation of sound files. This allowed for a subjective comparison of different designs at an early development stage. Since the noise predictions with TPA are typically in the frequency domain, some signal processing is required to create sound files in the time domain. Different methods for auralization will be compared, which could not be found in the existing TPA literature. Due to the inverse process for identifying the blocked forces, measurement noise can be amplified to unacceptably high levels, which are audible in the sound predictions. Regularization methods have the potential to significantly suppress the noise amplification, which is explained and exemplified for blocked force TPA. Additionally, it was found that only the structure-borne sound transmission was not sufficient to describe the compressor noise in the cabin. The compressor is also directly radiating air-borne sound from its housing, which will be included in the NVH model by means of equivalent monopoles. The application examples at the thesis' end are extending the current state-of-the-art, by showing how the modular vehicle models can be used for early phase, parametric design optimizations on a complex NVH problem.

Zusammenfassung

Die vorliegende Arbeit entstand während eines 4-jährigen Kooperationsprojekts zwischen der TU München und der BMW Group. Das Ziel war die akustische Integration von elektrischen Klimakompressoren, in einer frühen Entwicklungsphase, durch virtuelle akustische Prototypen. Dies wurde durch Substrukturierungsmethoden erreicht. Der Klimakompressor ist eine der dominantesten Geräuschquellen in batterie elektrischen Fahrzeugen. Daher ist es essenziell für Automobil-Hersteller die akustische Integration in einem genauen und praktisch umsetzbaren Entwicklungsprozess zu beherrschen. Das konkrete Vorhaben war das Kompressor-Geräusch im Innenraum virtuell für verschiedene Isolationskonzepte vorherzusagen und somit Optimierungen am virtuellen Prototyp durchzuführen. Dies wurde durch Anwendung von Methoden aus zwei Forschungsfeldern erreicht: Zuerst wird die Anregung des Kompressors mit Methoden der Komponenten-basierten Transfer Pfad Analyse (TPA) modelliert. Anschließend wird der komplette Übertragungspfad vom Kompressor bis zum Fahrerohr aus mehreren Einzelkomponenten, durch dynamische Substrukturierung (DS), virtuell zusammengebaut.

Um die oben genannten Ziele zu erreichen, wurden einige Beiträge zum aktuellen Stand der Technik geleistet, welche in dieser Arbeit beschrieben werden. Durch frequenz-basierte Substrukturierung (FBS) ist es möglich experimentelle und numerische Substruktur-Modelle virtuell miteinander zu koppeln. Für den Kompressor stellte sich heraus, dass es von großem Vorteil ist auch Starrkörper-Modelle in den Übertragungspfad zu koppeln. Die Herleitung einer Formulierung zur akkuraten Integration von Starrkörpermodellen in den Übertragungspfad ist Teil dieser Arbeit. Zu Beginn der Arbeit war nicht klar wie Gummilager mit ausreichender Genauigkeit für eine Substrukturierung modelliert werden können. Eine neue Methode zur experimentellen Identifikation von Gummilagermodellen wurde entwickelt, um diese Anforderung zu erfüllen. Die rotierenden Teile im Kompressor erzeugen Kreiseleffekte, welche die Dynamik des Systems beeinflussen. Eine neue FBS basierte Methode wurde entwickelt um die Kreiseleffekte virtuell an ein System zu koppeln, wobei nachgewiesen werden konnte, dass diese für den Fall der Klimakompressor-Akustik nicht relevant sind. Die Anregung des Kompressors wird durch sog. „blocked forces" beschrieben. Werden diese auf die substrukturierte Übertragungsfunktion des Gesamtfahrzeugs angewendet, kann der Schall im Innenraum vorhergesagt werden. Ein Ziel der Arbeit war es diese Ergebnisse auch Nicht-Akustikern zugänglich zu machen. Dies geschieht durch das Erstellen von Sound-Dateien mittels derer die Ergebnisse für unterschiedliche virtuelle Konzepte subjektiv verglichen werden können. Da die TPA Ergebnisse üblicherweise im Frequenzbereich vorliegen, ist es notwendig Signalverarbeitungs-Methoden anzuwenden um die Sound-Dateien im Zeitbereich zu erstellen. Verschiedene Methoden zum Erstellen der Zeitsignale werden in dieser Arbeit erklärt und verglichen, was oft in der TPA Literatur nicht beschrieben wird. Bei der Ermittlung der „blocked forces" wird eine Matrix invertiert, was das Messrauschen in den aufgenommenen Signalen hörbar und inakzeptabel stark verstärken kann. Regularisierungs-Methoden können dieses Problem signifikant reduzieren, was an einigen konkreten Beispielen erklärt und demonstriert wird. Für den Kompressor ist der über die Struktur übertragene Schall nicht ausreichend, um den Schalldruck im Innenraum vollständig zu beschreiben. Der direkt vom Kompressor-Gehäuse abgestrahlte Schall wird zusätzlich über äquivalente Monopole in das akustische Modell eingebaut. Die Beispiele am Ende der Arbeit zeigen wie die entwickelten, modularen Akustik-Modelle schon in frühen Entwicklungsphasen für eine parametrische Optimierung des Systems eingesetzt werden können.

Contents

Nomenclature

Matrices will be denoted with bold upper case characters, e.g. $\mathbf{Y}$. Vectors will be dispayed as bold lower case characters, e.g. $\mathbf{q}$. Scalars are denoted by plain letters, e.g. Ψ. Throughout the document, the convention is used that differentiation of a scalar with respect to a vector, yields a row vector, e.g.:

$$\frac{\partial \Psi}{\partial \mathbf{q}} = \begin{bmatrix} \frac{\partial \Psi}{\partial q_1} & \frac{\partial \Psi}{\partial q_2} & \cdots & \frac{\partial \Psi}{\partial q_n} \end{bmatrix}$$

Differentiation of a vector, e.g. $\mathbf{u}$, by another vector, e.g. $\mathbf{f}$, yields a matrix corespondingly

$$\frac{\partial \mathbf{u}}{\partial \mathbf{f}} = \begin{bmatrix} \frac{\partial u_1}{\partial f_1} & \frac{\partial u_1}{\partial f_2} & \cdots & \frac{\partial u_1}{\partial f_n} \\ \vdots & & \ddots & \\ \frac{\partial u_m}{\partial f_1} & & & \frac{\partial u_m}{\partial f_n} \end{bmatrix}$$

The substructures that are being coupled to each other can be modeled with different approaches. They are indicated by the following symbols:

   Substructure modeled analytically as rigid body
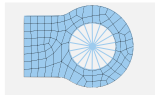
   Substructure modeled numerically with the finite element method

   Substructure modeled experimentally

In the following Nomenclature, the symbol $(\star)$ is a place holder for any type of variable. It is used for explaining sub- or superscripts.

Mathematical Symbols

$(\mathbf{Y})^+$ Pseudo inverse of matrix $\mathbf{Y}$

$(\mathbf{Y})^{-1}$ Standard inverse of matrix $\mathbf{Y}$

$(\mathbf{Y})^{\#}$ Regularized inverse of matrix $\mathbf{Y}$

$(\star)^*$ Complex conjugate of scalar, or conjugate transpose of vectors and matrices (aka. Hermitean)

Δ Laplace operator $\Delta = \left(\frac{\partial^2}{\partial x^2} + \frac{\partial^2}{\partial y^2} + \frac{\partial^2}{\partial z^2} \right)$

$\delta(t)$ Dirac impulse

η_r Modal coordinate for eigenmode r of the system

$\forall$ for all

γ^2 Coherence function with $\gamma^2 \in [0, 1]$

$\hat{\star}$ Noise free signal

$\mathbb{C}$ Set of complex numbers

$\mathbb{R}$ Set of real numbers

$\mathbb{R}_+$ Set of positive real numbers

$\boldsymbol{\Theta}_Q$ Rotational inertia tensor of a body around point Q

$\mathbf{r}_{QX}$ Position vector from point Q to point X

∇ Nabla operator $\nabla = [\frac{\partial}{\partial x} \; \frac{\partial}{\partial y} \; \frac{\partial}{\partial z}]^T$

Ω Discrete increment in frequency domain (aka. frequency resolution)

Ψ Objective/Cost function which is to be minimized by coresponding variable choice

ρ Density

$\tilde{\star}$ Slightly perturbed quantity

$\mathbf{B}$ Signed Boolean matrix (i.e. containing only $-1, 0, 1$)

$\mathbf{e}_f, \mathbf{e}_u$ Random error on e.g. the force or acceleration channels

$\mathbf{F}$ Filter matrix

$\mathbf{f}$ Force

$\mathbf{p}$ Sound pressure

$\mathbf{R}$ IDM matrix

$\mathbf{T}$ Transformation matrix

$\mathbf{u}, \dot{\mathbf{u}}, \ddot{\mathbf{u}}$ Displacement, velocity or acceleration

$\mathbf{x}$ Vector of design variables

$\mathbf{x}_r$ Vibration eigenmode r of the system

$\mathbf{Y}_{21}^A$ Admittance matrix structure A, relating input in DoFs 1 to output in DoFs 2

$\mathbf{Z}_{21}^A$ Dynamic stiffness matrix strucutre A, relating input in DoFs 1 to output in DoFs 2

$\boldsymbol{\theta}$ Vector containing the small rotations of a rigid body around the coordinate axis (Cardan angles)

$a := b$ "a is by definition equal to b"

$z, \dot{z}, \ddot{z}$ Volume displacement, velocity or acceleration

Abbreviations

APS	Auto-power spectrum
ATF	Airborne transfer function [Pa s^2 / m^3]
BEV	Battery electric vehicle
CMS	Component mode synthesis
CPS	Cross-power spectrum
DFT	Discrete Fourier transform
DoF	Degree of freedom
DS	Dynamic substructuring
EMA	Experimental modal analysis
EMPC	Equivalent multiple point connection
FBS	Frequency based substructuring
FEM	Finite element method
FFT	Fast Fourier transform
FIR	Finite impulse response
FRF	Frequency response function
GA	Genetric algorithm
ICC	Interface completeness criterion
IDM	Interface displacement mode
IS	Inverse substructuring
ISD	Inverse substructuring diagonal
KKT	Karush Kuhn Tucker conditions
LS	Least squares
NTF	Noise transfer function [Pa/N]
ODS	Operational deflection shapes
OSI	Operational system identification
RDoF	Rotational degree of freedom
SEMM	System equivalent model mixing
SEREP	System equivalent reduction and expansion
SH	Shore hardness
SNR	Signal to noise ratio

SQP   Sequential quadratic programming

SVD   Singular value decomposition

TPA   Transfer path analysis

TSVD   Truncated singular value decomposition

VP   Virtual point

VPT   Virtual point transformation

Chapter 1

Introduction

Contents:

All too often people shy away from innovation due to fear of failure or short-sighted arguments, like losing jobs in case of a successful try. The latter seems almost ironical, considering the fact that we face a demographic problem in the western world and in Germany in particular. Once the "baby boomer" generation starts to retire, we will see a shrinking workforce paralleled by a significantly increasing pensioner number. There are two genuinely unattractive options if we stick to the status quo: higher workload for the young, or lower pensions for the elder. Most likely it would be a balance of both, and finding that balance is going to be a generational fight which we should ultimately try to avoid. No wishful thinking or printing of money is going to solve the underlying problem. So the only way around it is to innovate, and thereby sustain or hopefully improve our living standard with the decreased workforce. Advances in the way we design and produce products has proven to be a viable way of achieving this goal. With this thesis, the author hopes to contribute a tiny piece to solve the puzzle, by giving a perspective on how to design quiet and pleasant products in a more effective manner.

Talking of the future, there is no doubt that we are currently seeing a strong push towards battery electric vehicles (BEVs) within the automotive industry. BEVs offer a better energy efficiency than combustion engine vehicles, especially when driving in urban areas. At the same time, most people are enthusiastic about BEV's after getting acquainted with their "fun-to-drive" vehicle dynamics, due to the instant torque and low center of gravity. Currently the lower range for long distance trips is a concern for many potential customers (rightfully or not). So next to increasing battery capacities, engineers are trying to push the envelope in terms of their efficiency even further. Typical approaches include better aerodynamcis, more intelligent recuperation strategies but also higher thermal efficiency. The electric climate compressor, originally only used for cooling the interior, can additionally be used as a heat pump for warming the driver's cabin. This results in significantly improved energy efficiency in colder weather [95]. Many automotive companies are offering this option for their vehicles, like the BMW i3, the Hyundai Kona or the VW e-Golf just to name a few. Also Tesla recently introduced a heat pump in the Model Y. A leaked document claimed that the VW ID.3's optional heat pump results in a range increase by 60km at a temperature below $5°C$, which would corespond to almost 20% range increase [117]. In long range BEVs, the compressor is also responsible for cooling the battery pack during fast charging, or heating it to optimal operating temperature in colder weather. As a result of these additional tasks, the climate compressor is going to be running in almost all operational conditions of the vehicle.

What the mode of transport is going to be in the far future is not known for sure. What we do know for sure now, is that no one will want a climate compressor that is blaring at him while driving or spending time at the charging station. The methods explained in this thesis are generally applicable, but will be exemplified on the engineering example of the climate compressor's noise and vibration performance.

1.1   The art of NVH engineering: designing comfort with minimal resources

Noise vibration harshness (NVH) is a field of engineering which designs the vibro-acoustic properties of different machines for maximum comfort and reliability. NVH engineers work on a great variety of products, ranging from house hold appliances like fridges to different means of transport like airplanes, trains and passenger cars. Most often the result of an NVH engineer's effort cannot not be noticed directly, since in the majority of cases the goal is to make the product as silent as possible. But NVH engineering is unmistakably noticed by the user when comparing a well-designed product to a bad one. A well-designed machine with good NVH characteristics simply offers a relaxed experience and high quality perception. My wife and me just had a train trip from Munich to Hamburg in an intercity express (ICE) of the currently newest generation, the ICE4. We perceived the train as considerably more silent than its predecessors, which resulted in a very comfortable ride and us arriving relaxed after six hours of traveling. This is the intrinsic goal of NVH engineering: creating pleasant and appealing products.

However, it is not the *only* goal of an NVH engineer to make a machine as silent as possible. In fact, it is quite easy to get any noisy and vibrating machine silent, by simply introducing heavier counter masses or more insulation material. Just recently, our neighbor bought a new washing machine of a brand which is renowned for high quality and low operational noise and vibration (and high prices). After helping him carry the machine, the author had a pretty good idea why the machine is so silent: it had a weight of 95kg compared to typical weights of other machines in the range of 70kg. For passenger cars, weight is definitely an important design criterion, so simply adding mass for vibration isolation is not a successful strategy. Next to that, the automotive business is all about volume production. For example, the E90 generation of BMW's 3 series was sold 3.1 million times in the years 2007-2012 [162]. One can imagine that introducing an acoustic counter measure which costs say 30 euro per unit, will result in serious discussions about its necessity during the design process. Alternatively, if one can prove that there is a clever design that can achieve the same NVH performance with no extra cost, one can gain a lot of new friends within the company. An intelligent design could utilize the mass of existing components for vibration isolation, e.g. the 12V battery. Or one could attach the vibration source to parts of the vehicle that are already very stiff, e.g. for crash reasons. One could also utilize the masking effects that other noise sources produce (e.g. only start the compressor after the fan already started blowing). So this is really the art of NVH engineering: designing comfort with minimal resources.

One often hears that cost savings, even if they are significant, are a not a societal relevant challenge. However, this is not true in an overall picture. The author likes to think about money as an abstract time-store of human effort. What happens if a company can figure out a clever design, so that a certain isolation mass is not needed? Well, the superficial answer is a saving in terms of money. But the underlying origin of that saving is the human effort which is spared by not having to mine the needed raw materials, producing the excess

part and not requiring the operators on the assembly line to lift and mount a heavy part. Over time, the lighter car has reduced energy consumption and if the NVH engineering is done right, the reduced vibrations result in a longer product live. Considering the matter from this perspective, it becomes apparent that an NVH engineer does indeed have some key responsibilities: in terms of resource efficiency, solving our demographic "lack-of-labor" problem, and providing mental well-being to the product user. Modernizing the way we do NVH engineering therefore seems like a meaningful endeavor.

1.2 Modular NVH design methods

In order to fully exploit the potential of better designs, it is essential to have flexible and accurate NVH development tools, which help to make reasonable design choices early in the development stage. If the engineer is free to play with different designs, without actually having to build them (prototpyes are expensive and take forever!), this will provide the required freedom for discovering the best solution. Therefore, the NVH model needs to be precise, so one can clearly distinguish a good from a bad design early in the development. The NVH model also needs to be accurate: if the models noise predictions reach the design goals (with some safety margin), also the physically built up prototype needs to be within the target range.
Unfortunately, NVH problems are in practice often encountered late in the development process. Most of the design is already fixed at this point, and the introduced counter measures are often a result of trouble-shooting efforts. The time to fix the problem is very limited at this point, since the one thing that is almost certainly more costly than a bad design, is a delay in the start-of-production date. Not only is this trouble-shooting phase stressful to everyone involved, but the resulting solutions are often exactly the ones we want to avoid for the reasons stated above: excess isolation material, additional masses and dynamic absorbers. New techniques, which do not default to overly simplified models, are needed for early phase NVH development.

The above stated difficulties in early phase NVH design are, in the authors opinion, a result of multiple reasons which can be grouped into two general categories:

1. **Complex transfer paths:** The vibration behavior of the full assembly is hard to simulate, since it depends on all components in the transfer path from the source to receiver, and there are multiple unknown parameters. These include materials which are hard to model, unknown friction in joints or high modal density of subcomponents, just to name a few. Even if these parameters were known, it would be a lengthy and tedious task to create a trustfull numerical model with it, especially if manufacturing tolerances shall be considered as well.

2. **Complex excitation mechanisms:** The internal forces of a machine are often hard to model accurately, or simply not known since the noise source is a supplier part. For the electric climate compressor, the internal forces are due to unbalance in the rotor, periodic excitations of the motor pole-pairs passing each other, compression shocks in the refrigerant fluid, high frequency excitations from the power electronics, etc.

In this thesis, the above stated problems are treated with strategies coming from two fields of research:

1. **Dynamic Substructuring:** A typical way to solve a large problem, like the assembly of a full vehicle, is to break it into smaller pieces and solve them individually. Dy-

namic Substructuring (DS) is the analogue to this "divide and conquer" strategy in the field of vibration analysis [5, 31]. In fact, the underlying idea of solving a large and difficult problem by finding the solution to several easier sub-problems has evolved over a long time. Its conceptual start is often seen as Schwartz' [154] solution of a Poisson problem on a complex domain. He solved the problem on two easier overlapping subdomains that constitute the whole domain, and could prove the method would eventually converge to the true solution. This was already in the late 19th century. It was followed by the Rayleigh-Ritz method [47, 143, 146] where the vibration solution is approximated with only a few admissible functions (at the beginning of the 20th century). A further development of the idea (by mathematicians like Courant [28]) led to the finite element concept which constrained the admissible functions to smaller, *finite* element domains (around the 1940s). Literally subdividing a structure into smaller substructures was introduced in the 1960s to solve systems, which would have otherwise not been computable with the limited computer memory at that time [29]. In the 1980s and 1990s, these techniques were further developed so that problems with billions of degrees of freedom could be efficiently solved on multi-processor computer architectures [5]. With the availability of increasingly accurate measurement equipment at the beginning of the 21st century, the field of DS has seen a push towards experimentally modeled substructures which can be coupled to each other [85, 109, 157].

Let us consider the brief evolution of DS (which can be read in much more detail in [31]), in the light of above stated problem 1: complex noise transfer paths in vehicles. It seems natural to build the whole vehicle transfer path from individual subcomponent models. Components with a large complexity can be abstracted by experimental models, while components that are easy to describe with a computer model are included as such. This is precisely how the first challenge, i.e. the complex transfer paths, will be approached in this thesis.

2. **Component TPA:** No matter how complex the excitation mechanisms in the source component, they ultimately have to enter the receiver structure over the connection points. The field of transfer path analysis (TPA) describes a set of different methods [159] which are, in some way, abstracting away the complex source excitation mechanism. The underlying ideas can be traced back to electrical network theory [171]. This abstraction is often achieved by focusing on the vibrations that are transferred over the connection points.

Some of the first TPA applications to machine sound were focused on understanding and reducing the vibration transfer from a military ship's engine to the hull, to make it stealthy. See e.g. Verheijs PhD thesis [184]. Nowadays, classical TPA methods are widely adopted in the automotive industry [139] where they help understanding the cause of vibration problems by finding the critical vibration transfer paths. Classic TPA is mostly used as trouble-shooting tool, applicable when the prototype already exists. A current trend is to move to component TPA methods for early phase development [85, 109, 157, 199]. Within the family of component TPA methods, the source excitation is often described with blocked forces [119, 120]. With this equivalent force quantity, it becomes possible to simulate the NVH properties of a given source in an assembly which does not yet exist.

The blocked force concept will be utilized in this thesis to abstractly describe the source excitation of the compressor.

Combining the concept of Dynamic Substructuring and Component TPA allows to build virtual acoustic prototypes. This combination is an up-and-coming set of methods [85, 109, 157, 198], with the vision to make accurate, early phase NVH design a reality.

1.3 In a nutshell: creating virtual acoustic prototypes

At this point it is important to paint a clearer picture of the proposed NVH development process. Simulating the acoustical responses on machines which do not yet exist is called virtual acoustic prototyping [122]. The proposed workflow is explained with the brief overview given in figure 1.1.
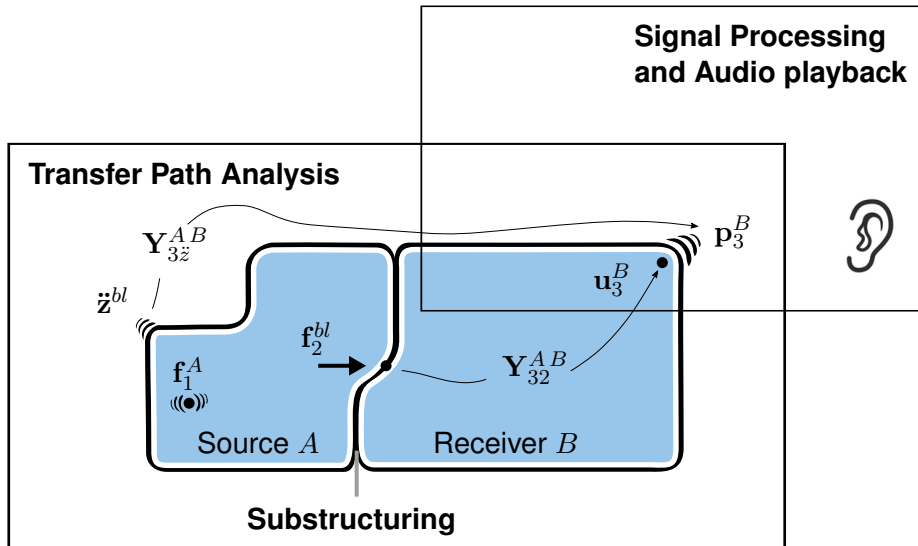
Figure 1.1: Overview of air- and structure- borne transmission of source vibrations.

A source component A is integrated in an assembly with a receiver structure B. Within the source, some internal forces $\mathbf{f}_1^A$ are acting. These are the internal excitation mechanisms of the source. The subscript $(\star)_1$ indicates that these internal forces are acting at a subset of DoF, denoted as 1. The superscript $(\star)^A$ indicates that they are acting within the source component A. The resulting responses on the receiver can equivalently be simulated with the virtual quantity of blocked forces $\mathbf{f}_2^{bl}$, which would be acting on the set of interface DoF 2. The resulting vibrations and sound pressures on the receiver are denoted by $\mathbf{u}_3^B$ and $\mathbf{p}_3^B$ at the receiver DoF 3. These responses on the receiver can be predicted by knowing the blocked forces $\mathbf{f}_2^{bl}$ and the transfer function $\mathbf{Y}_{32}^{AB}$ from the interface to the receiver points (subscript $(\star)_{32}$). The superscript $(\star)^{AB}$ denotes that the transfer function is a property of the assembly (source A with receiver B). The assemblies transfer function $\mathbf{Y}_{32}^{AB}$ can be obtained by dynamic substructuring. The source A and the receiver B can be coupled to each other by having an accurate model of their dynamics at the interface and enforcing the coupling conditions between them. In fact, the receiver can itself be an assembly of multiple substructures which can virtually be modified or exchanged. Thereby, the responses to a given source component in different receiver designs can be simulated. A virtual acoustic prototype.

For making the responses $\mathbf{u}_3^B$ and $\mathbf{p}_3^B$ audible, some signal processing is needed, to get the results from the frequency domain to audio files in the time domain.

For having a complete description of the receiver response, it was found necessary to also include the airborne source contribution of the compressor. The airborne contribution is due to the directly radiated sound pressure from the compressor housing. Said differently, the airborne contribution is what you would hear if the compressor was only held in place, without any structural connections to the vehicle. This contribution is described by modeling the airborne excitation with equivalent monopoles. The volume accelerations of these virtual monopoles is denoted as $\ddot{\mathbf{z}}^{bl}$. They will be called "blocked volume accelerations", in analogy

to the blocked forces, since the underlying ideas are common. With the airborne transfer function $\mathbf{Y}_{3\ddot{z}}^{AB}$ and the blocked volume accelerations $\ddot{\mathbf{z}}^{bl}$, the resulting contribution of the airborne path can be simulated.

The proposed workflow yields a modular assembly of the full machine, and makes it possible to virtually predict the acoustical performance of different designs. This can be done, by modifying the structure-borne transfer path $\mathbf{Y}_{32}^{AB}$ with a virtual exchange of parts in the assembly. Often, this is a modification of rubber bushing stiffnesses or modifications on the FEM models of suspension structures. This could also be done by determining the blocked volume accelerations $\ddot{\mathbf{z}}^{bl}$ for different sound insulation materials on the source's surface. The success of these virtual design changes can be evaluated without needing to build a new prototype, since the complex parts of the transfer path have been modeled experimentally and remain unchanged.

This provides the requested flexibility in the early design stage, so that the best design can be found (from a performance and cost perspective). It also provides a clear way of collaboration for products which are designed by multiple engineering teams including suppliers. The teams can individually work on their subcomponents, suppliers can provide the blocked forces for their source component, and the full vehicle acoustics team can assemble the full system, simulate the receiver responses, and raise a red flag if the current design is missing the acoustic targets.

This way of working also makes the development less costly. Consider a company that has 5 variants of a given source component, say an electric motor, that goes into 20 different vehicle variants. If all combinations of source and receiver need to be tested, this would require 100 different vehicle tests. In case one of the variants turns out to miss the acoustic targets, one would not fully understand the system yet and need to go into trouble-shooting mode. Now turn the situation around: The excitation of the 5 e-motor variants is known via their blocked forces, and the 20 vehicle variant's transfer functions are known, by substructuring each e-motor into an experimental vehicle model. In total, this would require only 25 measurements (5 for the blocked forces and 20 for the experimental vehicle models). Additionally, a faulty design can be detected earlier in the design process and dealt with, by virtually introducing counter measures to the vehicle. The growing library of substructures and source descriptions would over the years also provide a plentiful database for investigating completely new design concepts by means of a few mouse clicks.

The contents of this thesis summarize a few techniques that were found necessary to implement such a procedure for the electric climate compressor.

1.4   Outline of the thesis

Part I describes the necessary tools for assembling full structural vibration paths from individual component models. The assembled system is versatile in the sense that each component can be modeled with the most suitable approach, which can be a finite element, a multi-body[1], or an experimental model. In the end, it doesn't matter how the relationship between applied forces and the resulting vibrations was obtained. The assembly is modular in the sense that individual component models can be reused in other projects or easily replaced by other components to simulate the effect of design modifications. For coupling subcomponents it is necessary to have an accurate description of their linearized dynamics on the connection interfaces. Once that is established, the coupling merely comes down

---

[1]In this thesis, a multi-body model means a lumped element model consisting of multiple simple elements, like rigid bodies and analytical joint elements.

to enforcing that the structures have the same vibration on the interface (by computing the necessary coupling forces). Therefore, Part I is split into four chapters:

- **Chapter 2: Structural Dynamics**
  This chapter is not a replacement for a good course or book on structural dynamics [29, 47]. But if the reader has some training, most of the equations should look familiar. The chapter starts with structural dynamics in the well known format of mass, damping and stiffness matrices. From that, a modal, frequency and impulse based representation of the system is derived. The aim is, aside from introducing the notation, to show that all mathematical representations of structural dynamics are equivalent, provided the modeling is done right. This will serve as a reference for the upcoming chapters, when the models of individual components are explained. Hence, the equations are formulated such that they are easily usable in the substructuring framework. A special emphasis is put on the acquisition of high quality experimental models (data quality is key!). Additionally, the proper formulation of rigid body models for use in substructuring is explained.

- **Chapter 3: Substructuring**
  The dynamic models of individual components can be coupled by enforcing the same vibration on the interface. Since experimental substructure models naturally come in the form of frequency response functions (FRFs), the coupling is formulated in the frequency domain. Finite element and multi-body models can easily be transformed to the frequency domain. The coupling process will be called frequency based substructuring (FBS) and some details regarding implementation and interpretation will be discussed. The chapter also explains the virtual point transformation (VPT), which allows to project experimentally measured FRFs on a common set of interface degrees of freedom (DoF). The same set of interface DoF can be obtained from all modeling approaches, also rigid bodies and finite element models, and thus the structures can be coupled. Again, a focus is on the physical properties that a high quality experimental substructure model should possess.

- **Chapter 4: Experimental rubber element models**
  One of the key pieces in a structural vibration path (which frequently causes headaches to the engineer modeling it) are rubber mounts. This chapter presents a comparatively easy approach to obtain high quality experimental substructure models of available rubber mounts. These yield good results up to high frequencies (ca. 3kHz), which is validated by comparison to stiffnesses obtained from a hydraulic test machine and a validation where the rubber isolator models are used for substructuring. One aspect that currently receives high attention, are the dynamic stiffening effects, which start occurring at high frequencies (typically around 500Hz - 1kHz). This is an important aspect when designing the noise isolation for high frequency noise sources, like electric motors.

- **Chapter 5: Gyroscopic effects,**
  These effects are well known to every structural dynamics student from the experiments with a revolving bicycle wheel on an axis. And yes, the compressor running at full speed shows the same, tangible, behavior. Whether this effect is important for correctly modeling the vibrations of the system was unclear at the beginning of the project, and left the author restless. Long story short: it is not a relevant effect for e-compressor NVH. But the chapter lays out the modeling that lead the author to this conclusion. It might provide a helpful tool to others trying to find out if the gyroscopic term is important for their system (e.g. fast revolving e-motors).

Part II contains the necessary tools for understanding an equivalent source description with blocked forces, and determining them with high accuracy. The source's excitation, combined with modular transmission paths, allows for prediction of sound and vibration levels on virtual prototypes.

- **Chapter 6: Transfer path analysis**
  The chapter contains a brief explanation of the difference between classical TPA and component TPA. The thought concept underlying blocked forces is explained, so that the reader understands why blocked forces can describe a source independently of a specific receiver structure. This enables sound predictions after virtual design changes. An experimental example is used to explain some practicalities.

- **Chapter 7: Auralization of TPA results**
  The TPA and substructuring results are typically in the frequency domain. For communicating simulation results to non-acoustic experts, it is useful to provide audio files, i.e. signals in the time domain. This chapter compares different methods for creating these sound files. A non-cyclic convolution with finite impulse responses was found to yield the best results.

- **Chapter 8: Regularization methods for component TPA**
  The blocked forces are often obtained with a matrix inverse applied to recorded vibration signals. All inverse methods that deal with measurement data are concerned with the topic of noise amplification due to bad conditioning of the matrix. This chapter explains the effects that lead to this noise amplification. This is exemplified with the virtual noise prediction on the e-compressor example from chapter 6. Different regularization methods are explained and compared, where some did provide effective remedies to the noise amplification for the e-compressor. The audible improvement in the sound predictions is demonstrated with sound files.

Part III introduces the field of direct airborne sound radiation. This is the last missing link for predicting the sound pressure in the drivers cabin. Eventually all vibrations caused by the source are radiated from structural surfaces, creating small air pressure fluctuations that the ear can perceive.

- **Chapter 9: Vibro-acoustics**
  The chapter starts with the derivation of the Helmholtz equation, which governs the sound pressure in air. It was chosen to show the derivation, instead of referencing it, since this is important for the following explanation of airborne transfer function (ATF) measurements. Next to that, it can be explained from the derivation, and shown with the example of a measured ATF, that the volume accelerations are a frequency unbiased proxy for the sound pressure. This was important for the cost function in the design optimization shown in chapter 12. The topic of reciprocal noise transfer function (NTF) measurements is also briefly explained.

- **Chapter 10: Airborne TPA**
  The e-compressor sound that is introduced via its structural connections to the car body can be predicted with the methods shown in the previous chapters. This contribution is called the *structure borne sound*. The compressor is also directly radiating sound from its housing, which is called the *airborne sound*. This transfer path is important to consider for a complete description of the e-compressor acoustics. For describing the airborne path, the compressor is abstracted with a number of equivalent monopoles. This chapter describes the chosen approach.

Part IV applies the introduced methods to relevant engineering examples.

- **Chapter 11: Automotive application example**
  In this chapter the methods explained in Part I - III are applied to the NVH design of the e-compressor isolation in a prototype of a long range battery electric vehicle (BEV). The structure borne transfer path is obtained by coupling an analytical rigid model of the compressor, experimental rubber isolator models, a FEM model of a carrier and an experimental model of the vehicle via FBS. The FBS model was validated by FRF measurements on the fully assembled system, where a very good agreement with the reference measurement was found. Additionally, it was found that the FBS model allows to predict noise transfer functions from the compressor into the drivers cabin which would otherwise not be measurable on the full assembly (due to too low input energy of excitation equipment or space restrictions in the final assembly). Substructuring allowed to measure/model each subcomponent individually, with a good signal to noise ratio, and virtually couple them. The structure and airborne path contributions could be separated, which allowed for a deeper insight in the important paths at different operating speeds. The effect of virtual design modifications to the structure borne path are simulated by exchanging subcomponents in the transfer path. Changes to the airborne transfer path are simulated by applying blocked volume accelerations of a compressor with and without an airborne insulation capsule. Sound files are provided to give a better impression of the results.

- **Chapter 12: Parametric design optimization on virtual acoustic prototypes**
  The combination of a modular FBS model and component TPA lends itself naturally to parametric NVH design optimizations. The transfer path model is parametrized by design variables. For example, on FEM modeled subcomponents or a parametrized change of rubber bushings. Applying the blocked forces allows to predict sound and vibration on the modified receiver. A suitable objective function decides if one design is better than the other. An optimization algorithm then explores the design space to find the best design. Thereby, NVH issues can be solved earlier in the development cycle and the manual design iterations can be sped up. This chapter explains the proper choice of an objective function and what kind of optimization algorithm is applicable on a minimal example. The optimization is then applied to a compressor NVH isolation concept that was investigated on a testrig. Three of the designs found by the algorithm are physically build up and used for comparing reference measurements to the simulation results. It is found that the opitmization can predict the NVH performance within a margin of ± 4 dBA (considering the whole compressor run-up), and it was confirmed that the optimal design found by the algorithm is indeed performing better than the other designs.

Part V concludes the thesis with a summary and a few further research directions that the authors deems promising.

1.5   How to read this thesis

> Understanding is, after all, what science
> is all about — and science is a great
> deal more than mindless computation.
>
> *Roger Penrose*

Time is precious, we all know that. This thesis is longer than the author initially aimed
for, but this was found necessary for a full explanation of the methods described above.
However, as an experienced engineer or executive, the thesis summary given in the previous
sections should already suffice to understand most of the results shown in chapters 11 and
12. This would provide a quick overview of the current capabilities of the methods and give
a picture on the concrete application to industry relevant challenges. If the ideas underlying
substructuring and component TPA are of general interest, maybe read chapters 3 and 6
first.
However, if the implementation details are of interest, e.g. to a researcher, then there is no
way around reading the chapters consecutively, since the theory introduced in each chapter
builds on the previous ones.

1.6   Thesis contributions

This thesis summarizes a 4 year research project at the Chair for Applied Mechanics which
took place in collaboration with the BMW group. Research is an iterative process, where
one needs to come up with solutions, test them, acknowledge when they fail and try to un-
derstand the reasons, so one can come up with another solution. Some of the intermediate
results have already been published [54–60, 177]. Some, but not all, of these publication's
findings are embodied in this thesis. The developments should also be seen in a longer line
with previous research in the field, a few recent examples being [85, 109, 157, 198].
The following work performed in this thesis extends the current state of technology:

- Rigid body models are an easy way of describing a structures dynamics, and often
  valid for compact structures up to an upper frequency limit. In section 2.7 the neces-
  sary equations for including rigid body models in an FBS assembly are derived.

- This thesis has a clear focus on so called hybrid substructuring, where the engineer
  can freely chose the modeling approach for individual substructures: rigid body, finite
  element or experimental models. The contents of chapter 2 focus on the translation
  of each modeling approach to the frequency domain, so these can be coupled via
  FBS. The applications shown in chapters 11 and 12 are examples for the successful
  realization of this hybrid approach.

- Chapters 2 and 3 devote a fair share of their pages to experimental modeling quality.
  There are various checks one can perform during the measurement of an experimental
  substructure model, which the author could not find in this composition anywhere else
  (though [5, 157, 158] contain a number of these checks already).

- Chapter 4 explains a novel, experimental method for obtaining rubber element mod-
  els. They comprise six degrees of freedom on either connection point and yield good
  results in an FBS assembly up to the kilohertz range.

- Chapter 5 lays out a novel method for analytically checking if the presence of gyroscopic effects, due to revolving machinery, is important to consider for a certain structure.

- Chapter 7 compares and formulates different methods for an auralization of TPA results. The author could not find a similar compilation of auralization methods, especially in the field of TPA, where the implementation details of auralization is often not mentioned.

- Chapter 8 is a first investigation of regularization methods applied to the inverse problem for computing the blocked forces. Inverse methods are unfortunately tending to amplify the measurement noise of experimental equipment. To make things even more challenging, the transfer of blocked forces to a different, virtual design can amplify the measurement noise even more. These issues are addressed in this chapter, and a first application and comparison of regularization to blocked force TPA is shown.

- Chapters 11 and 12 contain an application of FBS and component TPA to a complex vehicle design, where the virtual design changes and the parametric optimization of the assembly can be considered new applications.

Part I

Substructuring: Modular assembly of structural vibration paths

Chapter 2

Structural dynamics

Contents:

> Basically, I believe in nothing but "*force equals mass times acceleration*". The rest follows from that.
>
> *Prof. Daniel Rixen,*
> *first lecture of the semester*

The purpose of this chapter is certainly *not* to give a textbook overview of classical Newtonian mechanics. It shall rather recap the findings which are relevant for creating the composite models of vibro-acoustic transfer paths treated in this thesis. In sound and vibration engineering, and classical mechanics generally, one tries to compute the change of some variables $\mathbf{u}$, that describe the motion of a given system of particles, due to some applied forces $\mathbf{f}$. This is a fascinating field with an immense wealth of insight and implication for engineering and science. It is astonishing that basically all followed from Newtons three simple axioms. Very good textbooks on fundamental findings in classical mechanics are [47, 91]. Special application to the theory and computation of vibrations can be found in [29, 47]. Multibody dynamics are treated in [136, 163].

In the following, some approaches for mathematically modeling the vibration of structures are presented. These descriptions are often called different *domains* and in theory they are all equivalent representations of the same physical relationships. This will be emphasized with small examples, which will be needed for modeling the transfer paths later in this thesis anyway. The choice of which domain to use depends upon; *i)* the availability of experimental

or computational resources, *ii)* the degree to which one is able to model the relevant physical phenomena, *iii)* the required type of analysis, and *iv)* perhaps also personal preference. Models in one domain can also be transferred to the other domains. The frequency domain is arguably the most important one in this thesis, since most of the coupling and sound prediction operations will be performed here. Therefore, special attention will be given to the transformation of models from other domains into the frequency domain. This chapter also serves to introduce the notation that is used throughout the thesis.

2.1 Physical domain

In the physical domain, the motion of a structural system is described with time t dependent degrees of freedom $\mathbf{u}(t)$, that result from applied forces $\mathbf{f}(t)$. If the system undergoes only small oscillations around a stable equilibrium position, a linearization of the, generally non-linear, equations of motion is admissible. This is typically a valid assumption in the analysis of sound and vibration. Linearizing the equations of multi-body systems, or using finite element modeling (FEM), yields the well known system of equations:

$$\mathbf{M}\ddot{\mathbf{u}}(t) + \mathbf{C}\dot{\mathbf{u}}(t) + \mathbf{K}\mathbf{u}(t) = \mathbf{f}(t) \qquad \text{with} \quad \mathbf{u}(t), \mathbf{f}(t) \in \mathbb{R}^n, \tag{2.1}$$

where $\dot{\mathbf{u}}$ and $\ddot{\mathbf{u}}$ denote the first and second time derivatives of the degrees of freedom $\mathbf{u}$. The physical domain has its name, since the matrices involved relate to physically intuitive and meaningful quantities, like the mass matrix $\mathbf{M}$, the damping matrix $\mathbf{C}$ and the stiffness matrix $\mathbf{K}$. It is important to note that the mass matrix is a symmetric positive definite matrix, i.e.:

$$\dot{\mathbf{u}}^T \mathbf{M} \dot{\mathbf{u}} > 0, \qquad \forall \dot{\mathbf{u}} \neq \mathbf{0}, \tag{2.2}$$

which is easily understood from the fact that the above quantity is the kinetic energy (multiplied by two), which can never be negative by definition. The symmetry of the matrix is a result of its derivation from the linearized Lagrange equations (the kinetic energy is derived with respect to the same vector of variables twice see [47, section 2.1]), or by the derivation from the discretized weak form in the FEM (see e.g. [202, chapter 2 & 16]). Additionally, the stiffness matrix of a stable system is also a symmetric positive (semi-) definite matrix:

$$\mathbf{u}^T \mathbf{K} \mathbf{u} \geq 0, \qquad \forall \mathbf{u} \neq \mathbf{0}, \tag{2.3}$$

where the existence of vectors $\mathbf{u}$ for which the term in equation (2.3) is equal to zero, indicates the existence of rigid body motions. After all, the above quantity is (twice) the elastic energy stored in the body, which is always greater than zero, unless the body is able to move without deformation. A *rigid* body mode. The damping matrix $\mathbf{C}$ is generally also symmetric and positive (semi-) definite, for a passive system (i. e. no internal energy sources). Additionally, the system is assumed to not undergo any transport motion, i. e. it is at rest for $\dot{\mathbf{u}} = \ddot{\mathbf{u}} = \mathbf{0}$. This is true for most systems. As an exception, one could consider a rotor that revolves at a given rotational speed, even if all variables $\mathbf{u}(t)$, chosen for modeling its motion, are zero. Thereby, gyroscopic effects would be introduced, which are treated in chapter 5 for the case of the climate compressor.

2.2 Modal domain

The set of equations in (2.1) tends to be very large for modern FEM simulations. Even modestly sized problems often have a number of equations in the order of $n > 10^6$. However, the response of a system in the audible frequency range, can often be represented by much fewer variables in the modal domain. The eigenmodes of the undamped system are the harmonic solutions to:

$$\underbrace{\mathbf{M}\ddot{\mathbf{u}}(t)}_{\text{inertia forces}} + \underbrace{\mathbf{K}\mathbf{u}(t)}_{\text{elastic forces}} = \mathbf{0}, \tag{2.4}$$

which can be understood as a free motion (i. e. no external forces $\mathbf{f}(t)$) of the undamped system (no damping matrix $\mathbf{C}$), where the inertia forces are in balance with the elastic forces for all time. Assume that one can represent the solution as a harmonic motion:

$$\mathbf{u}(t) = \mathbf{x}\,e^{-i\omega t} \tag{2.5}$$

where $\mathbf{x}$ is a vector containing the vibration amplitudes in the degrees of freedom. We can solve equation (2.4) by the eigenvalue problem:

$$\left(-\omega^2 \mathbf{M} + \mathbf{K}\right)\mathbf{x} = \mathbf{0}. \tag{2.6}$$

There is much to say about computationally efficient algorithms to solve this problem, where the Lanczos eigensolver [90] is probably one of the most efficient methods (see e.g. [47, chapter 6] and [29, chapter 15]). There are in total n solutions to equation (2.6), which are called the eigenmodes $\mathbf{x}_r$ and eigenfrequencies ω_r. The eigenmodes have the important property of orthogonality, which can be shown by inserting one solution r out of the n solutions, i. e. the eigenvector $\mathbf{x}_r$ and its corresponding eigenfrequency ω_r, in equation (2.6). Subsequent premultiplication with the eigenvector $\mathbf{x}_s$ of *another* eigenfrequency $\omega_s \neq \omega_r$, gives:

$$\mathbf{x}_s^T \mathbf{K}\mathbf{x}_r = \omega_r^2 \mathbf{x}_s^T \mathbf{M}\mathbf{x}_r. \tag{2.7}$$

Equally, inserting the solution $\mathbf{x}_s$ and ω_s in equation (2.6) and premultiplying with $\mathbf{x}_r$ yields

$$\mathbf{x}_r^T \mathbf{K}\mathbf{x}_s = \omega_s^2\, \mathbf{x}_r^T \mathbf{M}\mathbf{x}_s \tag{2.8}$$

Subtracting equation (2.8) from equation (2.7) gives:

$$0 = \underbrace{(\omega_r^2 - \omega_s^2)}_{\neq 0}\, \mathbf{x}_s^T \mathbf{M}\mathbf{x}_r, \tag{2.9}$$

where the symmetry of the stiffness and mass matrix, $\mathbf{K}$ and $\mathbf{M}$, as well as the fact that $\omega_s \neq \omega_r$ has been used. Therefore one can deduce that,

$$\mathbf{x}_s^T \mathbf{M}\mathbf{x}_r = 0, \qquad \forall s \neq r \quad \text{with} \quad \omega_s \neq \omega_r. \tag{2.10}$$

Inserting the result in (2.10) in equation (2.7) also means that:

$$\mathbf{x}_s^T \mathbf{K}\mathbf{x}_r = 0, \qquad \forall s \neq r \quad \text{with} \quad \omega_s \neq \omega_r. \tag{2.11}$$

These properties show that the eigenmodes of the problem are orthogonal to the mass and stiffness matrix[1]. For the damping matrix $\mathbf{C}$, one is often assuming a similar orthogonality property, since this makes the solution of the equations much simpler.

$$\mathbf{x}_s^T \mathbf{C} \mathbf{x}_r = 0, \qquad \forall s \neq r \quad \text{with} \quad \omega_s \neq \omega_r. \tag{2.12}$$

This assumption is often called *modal damping*. Additionally, one defines the scalar modal parameters,

$$\mathbf{x}_r^T \mathbf{M} \mathbf{x}_r = \mu_r, \qquad \mathbf{x}_r^T \mathbf{C} \mathbf{x}_r = \beta_r, \qquad \mathbf{x}_r^T \mathbf{K} \mathbf{x}_r = \gamma_r, \tag{2.13}$$

where μ_r, β_r and γ_r are called the modal mass, damping and stiffness respectively. Often the eigenmodes $\mathbf{x}_r$ are normed by requiring that:

$$\mathbf{x}_r^T \mathbf{M} \mathbf{x}_r = \mu_r \overset{!}{=} 1. \tag{2.14}$$

These orthogonality relations are a fundamental finding which help decoupling the n coupled equations in (2.1) and therefore greatly simplify their solution. The eigenmodes $\mathbf{x}_r$ can be used as a basis to represent any solution $\mathbf{u}(t)$, so that

$$\mathbf{u}(t) = \sum_{r=1}^n \mathbf{x}_r \, \eta_r(t) \tag{2.15}$$

where $\eta_r(t)$ are the time dependent coordinates in modal space. This is a powerful representation, since inserting (2.15) in equation (2.1) and premultiplying with $\mathbf{x}_s$ yields

$$\mathbf{x}_s^T \left(\mathbf{M} \sum_{r=1}^n \mathbf{x}_r \, \ddot{\eta}_r(t) + \mathbf{C} \sum_{r=1}^n \mathbf{x}_r \, \dot{\eta}_r(t) + \mathbf{K} \sum_{r=1}^n \mathbf{x}_r \, \eta_r(t) \right) = \mathbf{x}_s^T \mathbf{f}(t), \tag{2.16}$$

$$\mu_s \ddot{\eta}_s(t) + \beta_s \dot{\eta}_s(t) + \gamma_s \eta_s(t) = \mathbf{x}_s^T \mathbf{f}(t), \qquad \text{for} \ \ s = 1, ..., n. \tag{2.17}$$

This means that by knowing the eigenmodes and eigenfrequencies of the system, one can solve a set of decoupled scalar equations in the modal domain, equation (2.17), instead of a set of n coupled equations in the physical domain, equation (2.1).

2.3 Frequency domain

As already mentioned, the predominantly used domain for modeling structural dynamics in this thesis is the frequency domain. The Fourier transformation can represent any, infinitely long, time-signal as a superposition of infinitely many sinusoidals. This representation is called the frequency domain[2].

For the Fourier series, it is assumed that the signal in the time-domain, e.g. the external forces $\mathbf{f}(t)$ in our case, are periodically repeating after a certain time period T. Again, they can be represented by superposition of harmonically oscillating sinusoidals with different

---

[1]If the structure has some form of symmetry, then there might be modes with the same eigenfrequency $\omega_s = \omega_r$ with different mode shapes $\mathbf{x}_s \neq \mathbf{x}_r$. Also for these cases the mode shapes can be chosen as to satisfy the orthogonality in (2.10) and (2.11), see the degeneracy theorem [47, section 2.3].

[2]As widely accepted as the Fourier transform is today, when Joseph Fourier presented it for the first time, there was a big dispute about the validity of his claim, that you could represent *any* time-signal with a superposition of sinusoidals. In fact even his former teachers, Joseph-Louis Lagrange and Pierre-Simon Laplace argued that it is impossible to represent functions with corners (e.g. a rectangular window) with a superposition of smooth sinusoidals [185].

amplitudes, e. g. $\mathbf{f}(\omega)$ for the forces. This is a good assumption for e. g. the rotational orders of an electric motor and the sound resulting from it. These frequency dependent amplitudes of the Fourier series can be found from the real time-signal with:

$$\mathbf{f}(\omega) = \frac{1}{T} \int_\tau^{\tau+T} \mathbf{f}(t) \, e^{-i\omega t} \, dt, \qquad \text{with } \omega = n\frac{2\pi}{T} =: n\Omega, \qquad \text{and } n \in \mathbb{Z}, \qquad (2.18)$$

and for the inverse transformation,

$$\mathbf{f}(t) = \sum_{n=-\infty}^{\infty} \mathbf{f}(\omega) \, e^{i\omega t}, \qquad \text{with } t \in [\tau, \tau + T], \qquad (2.19)$$

The frequency dependent force amplitudes are denoted as $\mathbf{f}(\omega)$ and τ is some starting time. The frequency resolution is denoted as Ω, which is the lowest frequency for a sinusoidal that would still have one full period in the time length T. The amplitudes in $\mathbf{f}(\omega)$ are generally complex numbers. They describe the amplitude and phase of a spectral component in $\mathbf{f}(t)$. Remember Euler's great formula[3]:

$$e^{i\omega t} = cos(\omega t) + i \, sin(\omega t). \qquad (2.20)$$

From it, it also follows that the amplitudes in $\mathbf{f}(\omega)$ are the complex conjugates of $\mathbf{f}(-\omega)$. This can be seen directly from equation (2.18) and the fact that $e^{i\omega t}$ is the complex conjugate of $e^{-i\omega t}$. With this in mind it also becomes clear that the result of the inverse Fourier transform in (2.19) yields a real number again, namely:

$$\mathbf{f}(\omega)e^{i\omega t} + \mathbf{f}(-\omega)e^{-i\omega t} = 2Re[\mathbf{f}(\omega)] \, cos(\omega t) - 2Im[\mathbf{f}(\omega)] \, sin(\omega t), \qquad (2.21)$$

where $Re[\star]$ and $Im[\star]$ denote the real and imaginary part of a complex number.

2.3.1 Impedance and admittance notation

The fundamental advantage of the frequency domain is that the second order differential equation in time (2.1) is transformed to an algebraic equation. Since we can represent the force time signal $\mathbf{f}(t)$ as a sum of sinusoidals (see equation (2.19)), and the differential equation (2.1) is linear, one can solve the equations for each of the force sinusoidals $\mathbf{f}(\omega)e^{i\omega t}$ separately, and then add each of these solutions to end up with the full solution[4]. Assume that the displacement solution to this spectral component also has the form $\mathbf{u}(\omega)e^{i\omega t}$. Inserting that in equation (2.1), yields:

$$\underbrace{\left(-\omega^2 \mathbf{M} + i\omega \mathbf{C} + \mathbf{K}\right)}_{=\mathbf{Z}(\omega)} \mathbf{u}(\omega) = \mathbf{f}(\omega), \qquad (2.22)$$

where $\mathbf{Z}(\omega)$ is typically called the *dynamic stiffness*. If instead of displacement amplitudes $\mathbf{u}(\omega)$, the amplitudes of velocity $\dot{\mathbf{u}}(\omega)$ or acceleration $\ddot{\mathbf{u}}(\omega)$ are sought, the transformation is done easily:

---

[3]A good explanation for this identity is provided by Strang on the MIT open course ware [166].

[4]Fourier's series were initially introduced for this reason, in a paper where he was solving the heat equation with a superposition of sinusoidals (The earths temperature with the day and night cycles combined with the summer and winter cycle). Fourier is also believed to be the first one who found that there must be some form of greenhouse effect, since during his research he found that the earth would be much colder if it was only warmed by the heat radiation coming from the sun.

Dyn. Stiffness	Z	conversion	Admittance	Y	conversion
dynamic stiffness	f/u	1	receptance, compliance	u/f	1
impedance	$f/\dot{u}$	$1/i\omega$	mobility	$\dot{u}/f$	$i\omega$
apparent mass	$f/\ddot{u}$	$1/-\omega^2$	accelerance	$\ddot{u}/f$	$-\omega^2$

Table 2.1: Terminology for different frequency response functions often used in the description of structural dynamics.

$$\dot{\mathbf{u}}(t) = \frac{\partial}{\partial t} \sum_{n=-\infty}^{\infty} \mathbf{u}(\omega)\, e^{i\omega t} = \sum_{n=-\infty}^{\infty} \overbrace{i\omega\mathbf{u}(\omega)}^{\dot{\mathbf{u}}(\omega)}\, e^{i\omega t}, \tag{2.23}$$

$$\ddot{\mathbf{u}}(t) = \frac{\partial^2}{\partial t^2} \sum_{n=-\infty}^{\infty} \mathbf{u}(\omega)\, e^{i\omega t} = \sum_{n=-\infty}^{\infty} \overbrace{-\omega^2\mathbf{u}(\omega)}^{\ddot{\mathbf{u}}(\omega)}\, e^{i\omega t}. \tag{2.24}$$

Different names for the dynamic stiffness have found their way into the technical vocabulary, depending on the time derivative of the displacement quantity. This can be confusing at first. In table 2.1 an overview of the most commonly encountered terms is given. In case of velocity outputs, $\mathbf{Z}(\omega)$ is called the *mechanical impedance*, following the naming conventions in electrical network analysis (the product of current and voltage yields power, just like the product of velocity and force). In practice, one is often interested in the inverse of the dynamic stiffness, which is termed the *mechanical admittance*:

$$\mathbf{Z}^{-1}(\omega)\mathbf{f}(\omega) = \mathbf{Y}(\omega)\mathbf{f}(\omega) = \mathbf{u}(\omega), \tag{2.25}$$

where $\mathbf{Y}(\omega)$ is the mechanical admittance. In table 2.1 the most common admittance names are listed. Both, $\mathbf{Z}(\omega)$ and $\mathbf{Y}(\omega)$, can be called *frequency response functions* (FRF), since they both represent a relation of an input in the frequency domain to an output in the frequency domain. The mechanical admittance is often advantageous, since it directly allows to predict the vibration levels due to an applied force. More importantly, it is often also the only quantity that may be acquired experimentally (see section 2.4). Therefore, all the coupling operations between single substrucutres will be performed with their admittance matrices $\mathbf{Y}(\omega)$, as will be explained in chapter 3. Also the term FRF most often refers to a mechnical admittance in the rest of this thesis.

2.3.2 Admittance matrices from mode synthesis

If the admittance $\mathbf{Y}(\omega)$ shall be obtained from a finite element model, the full matrix inversion as denoted in equation (2.25) is not efficient, since it would require inverting a matrix with a large number of degrees of freedom n for each frequency ω. As was shown in equation (2.15), the solution $\mathbf{u}(t)$ can also be written in terms of the single decoupled modal contributions $\eta_s(t)$. When applying the Fourier transformation to the decoupled modal equations (2.17) one gets:

$$\left(-\omega^2\mu_s + i\omega\beta_s + \gamma_s\right)\eta_s(\omega) = \mathbf{x}_s^T\mathbf{f}(\omega), \qquad \text{for} \;\; s = 1,...,n, \tag{2.26}$$

and hence the solution for a single modal coordinate $\eta_s(\omega)$ in the frequency domain is:

$$\eta_s(\omega) = \frac{\mathbf{x}_s^T\mathbf{f}(\omega)}{-\omega^2\mu_s + i\omega\beta_s + \gamma_s}. \tag{2.27}$$

When representing the physical displacements $\mathbf{u}(\omega)$ as a superposition of the modal solutions $\eta_s(\omega)$, as in equation (2.15), this yields:

$$\mathbf{u}(\omega) = \underbrace{\sum_{s=1}^{n} \frac{\mathbf{x}_s \mathbf{x}_s^T}{-\omega^2 \mu_s + i\omega\beta_s + \gamma_s}}_{=\mathbf{Y}(\omega)} \mathbf{f}(\omega). \tag{2.28}$$

With the above expression one can represent the admittance matrix $\mathbf{Y}(\omega)$. Note that for doing this in an efficient way, only a small number of the most important modes $m \ll n$ can be used. With the convention that all modes $\mathbf{x}_s$ are scaled such that $\mu_s = 1$, it follows that $\gamma_s = \omega_s^2$. Hence, one can approximate equation (2.28) with just m modes as:

$$\mathbf{u}(\omega) \approx \underbrace{\sum_{s=1}^{m} \frac{\mathbf{x}_s \mathbf{x}_s^T}{(\omega_s^2 - \omega^2) + 2i\omega\omega_s\varepsilon_s}}_{\approx \mathbf{Y}(\omega)} \mathbf{f}(\omega), \qquad \text{with } m \leq n, \tag{2.29}$$

where ε_s is called the modal damping ratio and relates to β_s as: $\varepsilon_s = \beta_s/2\omega_s$. As a rule of thumb, it is sufficient to include only modes with eigenfrequencies up to twice the maximum frequency of interest in the analysis. Eigenfrequencies ω_s that are much higher have a low contribution to the admittance matrix, since the denominator in equation (2.29) grows very large due to the term $(\omega_s^2 - \omega^2)$. The modal damping ratio is in fact just a handy approximation to the complex phenomena leading to damping in the material. It is a dimensionless quantity, usually given in percent, since for $\varepsilon \geq 100\%$ the aperiodic case of vibration is reached (i.e. a non-zero initial displacement will directly go back to the equilibrium position, instead of first crossing the equilibrium position and perform some decaying oscilattions around it, as would be the case for $\varepsilon < 100\%$). For typical structures encountered in engineering, values for the modal damping ratio range from $0.1\% < \varepsilon_s < 10\%$ [29, chapter 10.3]. They can either be found from literature suggestions or from experiments ([29, chapter 18], [40]). From the authors personal experience, a modal damping ratio of $\varepsilon = 0.1\%$ is a good first guess for plain structural components made from e.g. aluminium or steel. For more complex structures (e.g. including bolted joints, different materials, interfaces or discrete damping elements), correctly modeling the damping is harder. This is usually circumvented in this thesis by using experimental models of these structures right away. If they need to be modeled numerically, a modal damping ratio of $\varepsilon = 3\%$ is usually a good first guess from the authors experience. If only a small subset of inputs j and outputs i is needed in the FRF matrix (as is most often the case), then one can evaluate only the needed entries of the admittance matrix Y_{ij} as,

$$Y_{ij}(\omega) = \sum_{s=1}^{m} \frac{x_{s,i} x_{s,j}}{(\omega_s^2 - \omega^2) + 2i\omega\omega_s\varepsilon_s}. \tag{2.30}$$

In combination with efficient numerical algorithms to solve the eigenvalue problem (2.6) (e.g. the Lanczos algorithm), this is an efficient way to compute the admittance matrices of large FEM systems, especially if one is interested in a large frequency range. All FEM models in this thesis will be transformed to admittance FRFs with (2.30).

2.4 Experimental acquisition of frequency response functions

For many mechanical systems, creating a trustworthy numerical model is either very cumbersome, or just not possible in the relevant frequency range (an example for a full vehicle will be shown in chapter 3). Therefore, it is often desirable to obtain the frequency dependent
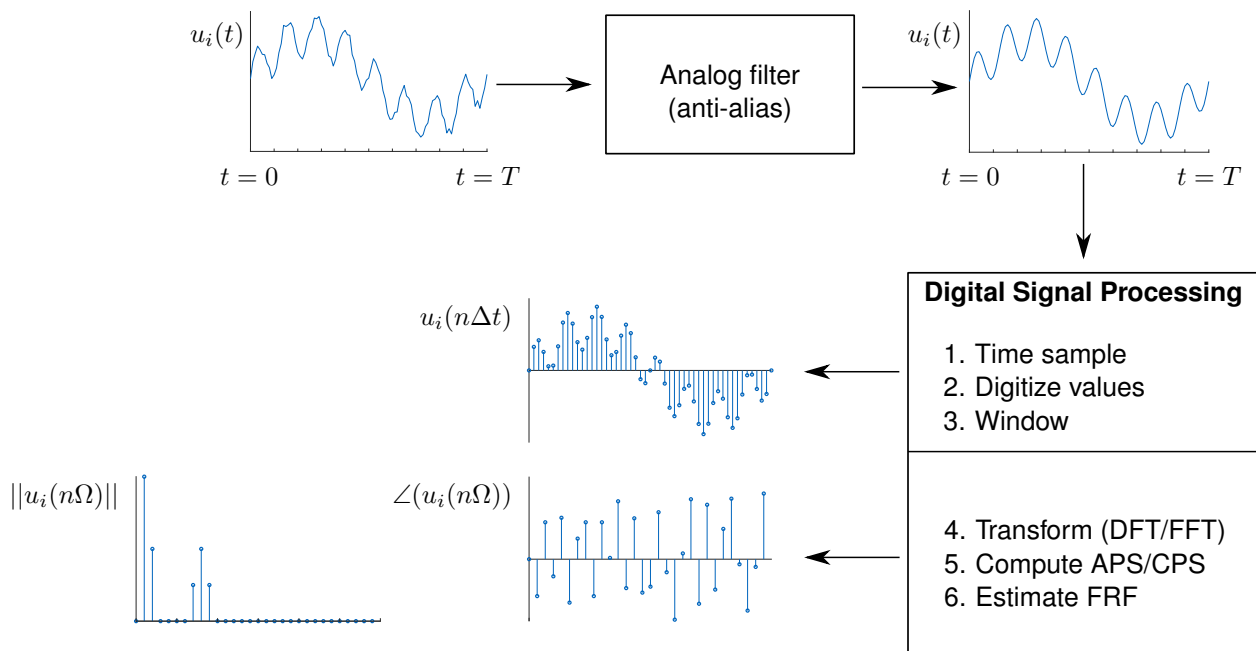
Figure 2.1: Schematic overview of signal processing for FRF estimation. Analog filtering of time domain signals is performed to prevent aliasing. The continuous signal is then sampled and digitized. The digital time signal is eventually windowed to prevent leakage. Subsequently it is transformed to the frequency domain (DFT or FFT algorithm). Form there on, all APS/CPS spectra for estimating the transfer functions can be computed.

admittance experimentally. One column j of the mechanical admittance matrix $\mathbf{Y}(\omega)$ can be identified by applying a force signal $f_j(t)$ and recording the response $\ddot{\mathbf{u}}(t)$ with multiple acceleration sensors[5]. The time signals of the force and acceleration sensors are sampled, digitized and transformed to the frequency domain. The general procedure of the involved data processing is shown in figure 2.1.

This section will not go into detail on all the signal processing applied to the continuous time signals of the outputs $\ddot{\mathbf{u}}(t)$ and the input $f_j(t)$. For well written books explaining the theory, see [99] for digital signal processing and [21] for the application to vibration analysis. Other books that describe practical issues and tips on how to perform clean measurements are e.g. [10, 40]. An enjoyable side-read are the "Modal space" articles by P. Avitabile [9].

For brevity, we assume for the rest of this section that the signals of the force input f and one sensor channel output u were already transformed to the frequency domain. Therefore, the explicit dependence on frequency ω is omitted. It will also not be distinguished between displacement, velocity and acceleration anymore, since those can be easily transferred into each other (equations (2.23) and (2.24)). This section will shortly discuss the determination of a single admittance matrix entry, which will be called "the FRF Y". All entries in the whole FRF matrix can then be obtained from the same procedure.

Measurements are always subject to small errors (external measurement noise or inaccuracies due to the manual conduction of the experiments). Therefore, the admittance is estimated from multiple measurements. The two most common FRF estimators, namely the H1 and H2 estimator, and the so called coherence function will be introduced.

---

[5]This is part of the reason why it is almost impossible to directly measure a mechanical impedance matrix $\mathbf{Z}(\omega)$ in practice. For measuring a column of the impedance, one would need to apply a motion $u_j(t)$ at one point while locking the motion at all other points ($u_{i \neq j}(t) = 0$) and measuring the resulting reaction forces $f_i(t)$. This is practically infeasible. On the other hand, applying a force at one point with no applied force at other points, i.e. measuring one column of the admittance matrix $\mathbf{Y}(\omega)$, is much easier.

2.4.1 Plain averaging

The simplest approach would use only one force and displacement spectrum u_k and f_k, where k stands for the experiment number, and take their ratio as FRF estimate: $Y = u_k/f_k$. If the structure was perfectly linear and there was no external noise and measurement inaccuracy, the FRF resulting from multiple tests n_{avg} would always be the same:

$$Y = \frac{u_k}{f_k}, \qquad \forall k \in [1, ..., n_{avg}], \tag{2.31}$$

and therefore one would get the same FRF from averaging:

$$Y = \frac{1}{n_{avg}} \sum_{k=1}^{n_{avg}} \frac{u_k}{f_k}. \tag{2.32}$$

Equivalently one could write:

$$Y = \frac{\sum_{k=1}^{n_{avg}} u_k}{\sum_{k=1}^{n_{avg}} f_k}. \tag{2.33}$$

The statement in (2.33) is the basis for the H1 and H2 FRF estimators. It is true, since the ratio of output u_k and force f_k is constant for all k. So, all u_k and f_k can be represented as the product of e.g. the first u_1 and f_1 with a scalar constant c_k, so that:

$$u_k = c_k u_1, \qquad\qquad f_k = c_k f_1, \qquad\qquad \text{with } c_k \in \mathbb{C}, \tag{2.34}$$

and therefore,

$$\frac{1}{n_{avg}} \sum_{k=1}^{n_{avg}} \frac{u_k}{f_k} = \frac{u_1}{f_1} \underbrace{\frac{1}{n_{avg}} \sum_{k=1}^{n_{avg}} \frac{c_k}{c_k}}_{=1}, \tag{2.35}$$

which is equivalent to:

$$\frac{\sum_{k=1}^{n_{avg}} u_k}{\sum_{k=1}^{n_{avg}} f_k} = \frac{u_1}{f_1} \underbrace{\frac{\sum_{k=1}^{n_{avg}} c_k}{\sum_{k=1}^{n_{avg}} c_k}}_{=1}. \tag{2.36}$$

2.4.2 FRF estimators and coherence

Plain averaging for determining the FRF, like in equation (2.33), is not used in experimental practice, since usually there is some noise included in the signals of input and output channels:

$$f_k = \hat{f}_k + e_{f,k}, \qquad\qquad u_k = \hat{u}_k + e_{u,k}, \tag{2.37}$$

where $e_{f,k}$ and $e_{u,k}$ denote random measurement errors in the input and output channels and $\hat{f}_k$ and $\hat{u}_k$ denote the "noise-free" signals, which are unfortunately not measurable. These errors can cause significant problems in the computation of the FRF. Therefore, one estimates the FRFs with dedicated averaging schemes. When multiple measurements n_{avg}

are performed on the structure, one can define the so called auto-power spectra G_{uu} and G_{ff}, and the cross-power spectra G_{uf} and G_{fu}:

$$G_{uu} = \frac{1}{n_{avg}} \sum_{k=1}^{n_{avg}} u_k \, u_k^*, \qquad\qquad G_{ff} = \frac{1}{n_{avg}} \sum_{k=1}^{n_{avg}} f_k \, f_k^*, \qquad (2.38)$$

$$G_{uf} = \frac{1}{n_{avg}} \sum_{k=1}^{n_{avg}} u_k \, f_k^*, \qquad\qquad G_{fu} = \frac{1}{n_{avg}} \sum_{k=1}^{n_{avg}} f_k \, u_k^*, \qquad (2.39)$$

where $(\star)^*$ denotes the complex conjugate. The estimation of the FRF is using the auto- and cross-power spectra, since they average out the uncorrelated, random measurement noise. If the errors are randomly distributed around a zero mean value, this means:

$$\frac{1}{n_{avg}} \sum_{k=1}^{n_{avg}} e_{u,k} = 0, \qquad \frac{1}{n_{avg}} \sum_{k=1}^{n_{avg}} e_{f,k} = 0, \qquad \text{for } n_{avg} \to \infty. \qquad (2.40)$$

In the terminology of uncertainty quantification, this is merely saying that the expected value, or mean value of the measurement noise is zero. If they are also uncorrelated to each other and the noise-free signals, this also means:

$$\frac{1}{n_{avg}} \sum_{k=1}^{n_{avg}} e_{u,k} \, e_{f,k} = 0, \qquad\qquad \text{for } n_{avg} \to \infty, \qquad (2.41)$$

$$\frac{1}{n_{avg}} \sum_{k=1}^{n_{avg}} \hat{u}_k e_{f,k} = 0, \qquad\qquad \text{for } n_{avg} \to \infty, \quad \text{etc.} \qquad (2.42)$$

Now one could rightfully ask the question: If the measurement errors average out in equation (2.40), why not just use equation (2.33) as an estimator in the determination of the FRF? The problem with equation (2.33) is that also the mean value of $\hat{u}_k$ and $\hat{f}_k$ goes to zero. As an example, say the FRF shall be determined by a shaker test with a random signal. The resulting $\hat{u}_k$ and $\hat{f}_k$ in each experiment, or time block, k would have a random phase. Therefore, the averages of $\hat{u}_k$ and $\hat{f}_k$ individually would go to zero, and equation (2.33) is not a meaningful way to estimate the FRF. However, the phase reference and amplitude ratio between $\hat{u}_k$ and $\hat{f}_k$ is constant in each experiment (it is the sought FRF Y). The estimation of the FRF with the auto- and cross-power spectra is taking advantage of this fact, as will be seen next.

One can deduct that for a sufficient amount of averages n_{avg} the auto and cross power spectra in equation (2.38) and (2.39) will average out the uncorrelated terms, i.e.:

$$G_{uf} \approx \frac{1}{n_{avg}} \sum_{k=1}^{n_{avg}} \hat{u}_k \, \hat{f}_k^* \qquad\qquad = G_{\hat{u}\hat{f}}, \qquad (2.43)$$

$$G_{fu} \approx \frac{1}{n_{avg}} \sum_{k=1}^{n_{avg}} \hat{f}_k \, \hat{u}_k^* \qquad\qquad = G_{\hat{f}\hat{u}}, \qquad (2.44)$$

$$G_{uu} \approx \frac{1}{n_{avg}} \sum_{k=1}^{n_{avg}} ||\hat{u}_k||^2 + ||e_{u,k}||^2 \qquad\qquad = G_{\hat{u}\hat{u}} + G_{e_u e_u}, \qquad (2.45)$$

$$G_{ff} \approx \frac{1}{n_{avg}} \sum_{k=1}^{n_{avg}} ||\hat{f}_k||^2 + ||e_{f,k}||^2 \qquad\qquad = G_{\hat{f}\hat{f}} + G_{e_f e_f}. \qquad (2.46)$$

So the random errors in the force and acceleration channels will eventually average out in the cross power spectra G_{uf} and G_{fu}, see equation (2.43) and (2.44). Provided the signal to noise ratio is good, the errors will at least be small in the auto power spectra due to the squaring, see equation (2.45) and (2.46). In experimental dynamics it is common to work with the so called $H1$ and $H2$ estimators of the FRFs, which are defined as:

$$\text{H1 estimator:} \quad H1 = \frac{G_{uf}}{G_{ff}} \quad \approx \quad \frac{G_{\hat{u}\hat{f}}}{G_{\hat{f}\hat{f}}} \left(\frac{1}{1 + \frac{G_{e_f e_f}}{G_{\hat{f}\hat{f}}}} \right) = Y \left(\frac{1}{1 + \frac{G_{e_f e_f}}{G_{\hat{f}\hat{f}}}} \right) \quad \leq Y, \quad (2.47)$$

$$\text{H2 estimator:} \quad H2 = \frac{G_{uu}}{G_{fu}} \quad \approx \quad \frac{G_{\hat{u}\hat{u}}}{G_{\hat{f}\hat{u}}} \left(1 + \frac{G_{e_u e_u}}{G_{\hat{u}\hat{u}}} \right) = Y \left(1 + \frac{G_{e_u e_u}}{G_{\hat{u}\hat{u}}} \right) \quad \geq Y. \quad (2.48)$$

Note, that the terms $G_{\hat{u}\hat{f}}/G_{\hat{f}\hat{f}}$ and $G_{\hat{u}\hat{u}}/G_{\hat{f}\hat{u}}$ correspond to the 'true' FRF Y. They contain the noise free signals $\hat{f}$ and $\hat{u}$, and are basically the same as the averaging formula given in equation (2.33) with some post multiplied constant c_k. Unfortunately, one can only measure the signals with the noise. Hence the $H1$ and $H2$ estimators are helpful for averaging out random measurement noise and provide an upper and lower bound to the 'true' value of Y. The coherence γ^2 is defined as a quality indicator for the measured FRF:

$$\gamma^2 = \frac{H1}{H2} \qquad \text{with: } \gamma^2 \in [0, 1]. \qquad (2.49)$$

Especially for hammer impact testing, one uses the $H1$ estimator for the FRF, since there the signal to noise ratio in the force channel is very good. Thus the term $G_{e_f e_f}/G_{\hat{f}\hat{f}}$ in equation (2.47) is small and it gets closest to the true FRF.

For shaker tests, a long time series of (often random) force signals is applied to the structure. The n_{avg} single spectra for averaging in equation (2.38) and (2.39) are obtained from cropping many, possibly overlapping, time blocks out of the long recorded signal and transform them to the frequency domain individually. This process is called the Welch method for obtaining the cross- and auto- power spectra [191]. This method will also be used for measuring airborne transfer functions with volume sources, as explained in chapters 9 and 10.

Remark 2.1: It was shown that the H1 estimator can average out random measurement noise on the output channels, as the number of averages n_{avg} increases. This is a very valuable tool when measuring e.g. noise transfer functions (NTFs) on a vehicle, i.e. performing impacts on the vehicle body and recording the resulting sound pressures in the driver's cabin. Often the signal to noise ratio on the microphones is poor. People then often tend to choose only a few similar impacts, in order to have a higher coherence on these measurements. However, in these cases it is not useful to chose the impacts that go into the averaging based on coherence. Basically one is then choosing the impacts where the stochastic noise on the microphones was by chance similar. In these cases, the author found that it is most useful to include as many impacts as possible in the estimation of the FRF, i.e. have a high number n_{avg}. While including more and more impacts into the H1 estimator one can usually observe how a previously very "peaky" or "noisy" looking NTF becomes smoother and more physical. So keep in mind that trying to get a maximum coherence is not always the goal, even though it is a good indicator for finding and excluding extreme outliers

during structural FRF testing.

2.5 Time domain

The term "time domain" for this section is somewhat sloppy. One could argue the variables in the physical domain $\mathbf{u}(t)$ (section 2.1) or in the modal domain $\eta_s(t)$ (section 2.2) are also time dependent variables, and therefore would fit some definition of being in the "time domain". In the context of this thesis, having a model in the time domain is rather related to the use of impulse response functions (IRFs) $\mathbf{Y}(t)$ which are closely related to the frequency response functions $\mathbf{Y}(\omega)$ as the notation already indicates.

2.5.1 Impulse response functions

An impulse response describes the vibration response of a system to a unit force impulse $f_{imp}(t)$ applied at a certain position.

$$f_{imp}(t) = \delta(t), \qquad \text{with: } \int_{-T}^{T} \delta(t) = 1, \qquad \text{and } \delta(t) = \begin{cases} \infty & \text{if } t = 0, \\ 0 & \text{otherwise.} \end{cases} \tag{2.50}$$

As already mentioned in section 2.3, all signals in time can be represented by a superposition of sinusoidals. The superposition of sinsoidals for the unit impulse, i.e. its Fourier transform is:

$$f_{imp}(\omega) = \frac{1}{T} \int_{0}^{T} f_{imp}(t)\, e^{-i\omega t}\, dt = \frac{1}{T} \int_{0}^{T} \delta(t)\, e^{-i\omega t}\, dt = \frac{1}{T}. \tag{2.51}$$

The delta function $\delta(t - \tau)$ (also called Dirac impulse) in an integral is basically 'sampling' the integrand at time τ. In equation (2.51) it samples $e^{-i\omega t}$ at $t = 0$, which is just 1. This also means that the response to a unit impulse in the frequency domain is:

$$u_{imp}(\omega) = Y(\omega)\, f_{imp}(\omega) = \frac{1}{T}\, Y(\omega), \tag{2.52}$$

and thus the time response to a unit impulse is the inverse Fourier transform, given as:

$$\underbrace{u_{imp}(t) = \frac{1}{T} \sum_{n=-\infty}^{\infty} Y(\omega)\, e^{i\omega t}}_{=Y(t)} \qquad \text{with } \omega = n\frac{2\pi}{T} = n\Omega, \qquad \text{and } n = 0, \pm 1, \pm 2, \ldots \tag{2.53}$$

2.5.2 Convolution with input forces

Impulse response functions (IRFs) are generally useful when the conditions for a treatment with the Fourier series in the frequency domain are not given. This is the case if the input force is not repeating after a time period T (e.g. transient signals, like rattling noises or engine runups), or the effect of initial conditions has not yet dampened out.
Any given time signal of an input force $f(t)$ can also be represented as a sequence of small impulses, see figure 2.2. The response of the system $u(t)$ can then be represented as a
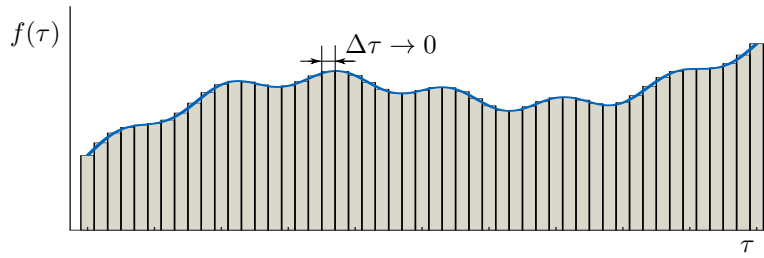
Figure 2.2: Representation of any input force signal as a series of force impulses.

sum of the responses to all these small force impulses. Eventually, the impulse at time τ becomes the small differential $f(\tau)d\tau$. At time $t > \tau$, this differential impulse happened $t - \tau$ seconds ago, and thus the response to this small impulse at time t is $Y(t - \tau)f(\tau)d\tau$. Summing, or more precisely integrating, over all small impulses that happened some time ago, gives for the response $u(t)$:

$$u(t) = \int_0^t Y(t - \tau)f(\tau)d\tau \tag{2.54}$$

This can be generalized to the case of multiple input forces and output signals to the matrix representation:

$$\mathbf{u}(t) = \int_0^t \mathbf{Y}(t - \tau)\mathbf{f}(\tau)d\tau \tag{2.55}$$

This computation of a vibration response $\mathbf{u}(t)$ resulting from a force input $\mathbf{f}(t)$ will be important for the auralization of sounds in chapter 7.

2.6 Application example

The purpose of this section is twofold. First, some of the modeling concepts discussed so far are exemplified on one structure. It is shown that experimental and finite element models can be used interchangeably for simple structures. Second, some important features of FRFs that are useful for checking the physical validity of experimental models are explained. The example is the aluminum plate shown in figure 2.3a.

2.6.1 Experimental and FEM model description

During the experimental tests, the plate was equipped with 14 triaxial acceleration sensors (PCB Model TLD356A32), and the impacts were performed with an impact hammer (PCB Model 086C03). The signals were recorded with a Mueller-BBM MKII data acquisition system, which includes a hammer measurement module for applying appropriate window functions and computing the $H1$ estimator and coherence. This equipment was used for all structural dynamics measurements in this thesis. It is important to choose the total recording time T long enough, so that all the system vibration has died out till the end of the time window ($T = 8s$ in this case, which is quite long but necessary due to the low damping of the structure). At least $n_{avg} = 3$ impacts were used for the estimation of each FRF (for simple structures with a good signal to noise ratio this is typically enough). The $H1$ FRF estimates and coherences were exported to a Matlab toolbox, developed for performing all
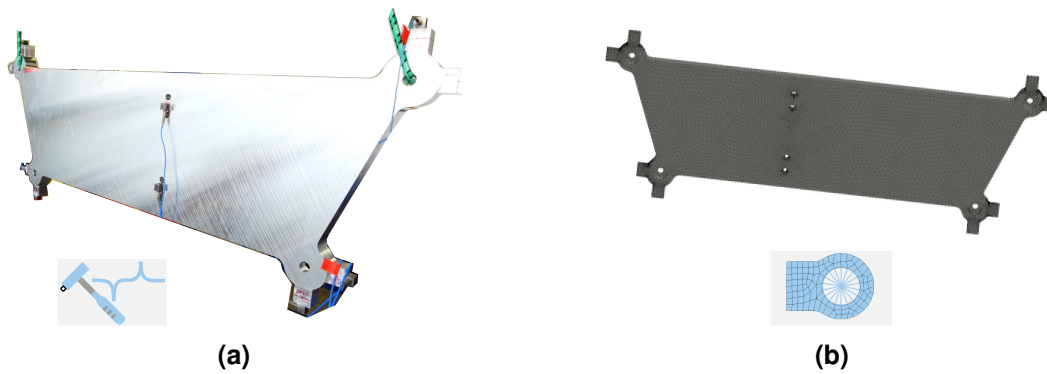
Figure 2.3: Application example of a plate. (a) During experimental FRF testing. (b) Modeled with finite elements (Viewer in Matlab toolbox, FE nodes on the surface are indicated as black dots). The symbols below indicate experimental and numerical models. These symbols will be used throughout this thesis to indicate the modeling approach which was used to obtain a specific substructure model.

operations described in this thesis. This includes the important checks on physical validity of the experimental models.

The plate was also modeled with the FEM in ANSYS. The obtained mass and stiffness matrices and the accompanying node, element and position information were exported to the Matlab toolbox (using the Harwell Boeing exchange format). The FEM model had 177.375 degrees of freedom (DoF) and standard material properties for aluminum. The FRFs were synthesized from the first 250 modes[6] with a modal damping ratio of $\epsilon_s = 0.1\%$ for all modes. The total mass of the plate was 18.7kg. The mass of one sensor with cable-connector was measured on a fine scale to 7.51g, so their total added mass to the plate was 105.14g. This contribution to the total mass might seem small. However, it often turned out that considering the added mass of the sensors helps refining the numerical or analytical models to a significantly better level of accuracy (which is also recommended by [9]). The mass of the sensors was considered by adding a lumped mass contribution to the three DoF of the geometrically nearest node in the mass matrix of the FEM model.

The comparison of a synthesized FRF from FEM, with and without considering the sensor mass, and the experimental reference is shown in figure 2.4. The shown FRF is a so-called a "driving-point" FRF, which simply means that the input and output DoF are the same (this would correspond to Y_{ii} in equation (2.30)). It is the driving-point FRF for the out-of-plane direction at the upper right plate corner in figure 2.3a. Here the benefits of including the sensor mass becomes apparent, since the experiment fits the FEM synthesized FRF better. Especially for the higher frequency modes the prediction is significantly better if the sensor masses are included (the mass effects contribution to the dynamic stiffness is proporional ω^2, see equation (2.22)). As explained in section 2.5, the impulse responses can be obtained from the FRFs in a straight forward manner. The positive effect of considering the sensor masses in the model can also be seen in the IRFs, see figure 2.5. It can thus be argued that, provided the modeling is done right, numerical and experimental models can be used interchangably for describing the same structural system.

---

[6]$\omega_{250} = 29.3kHz$, so one could have used less modes.

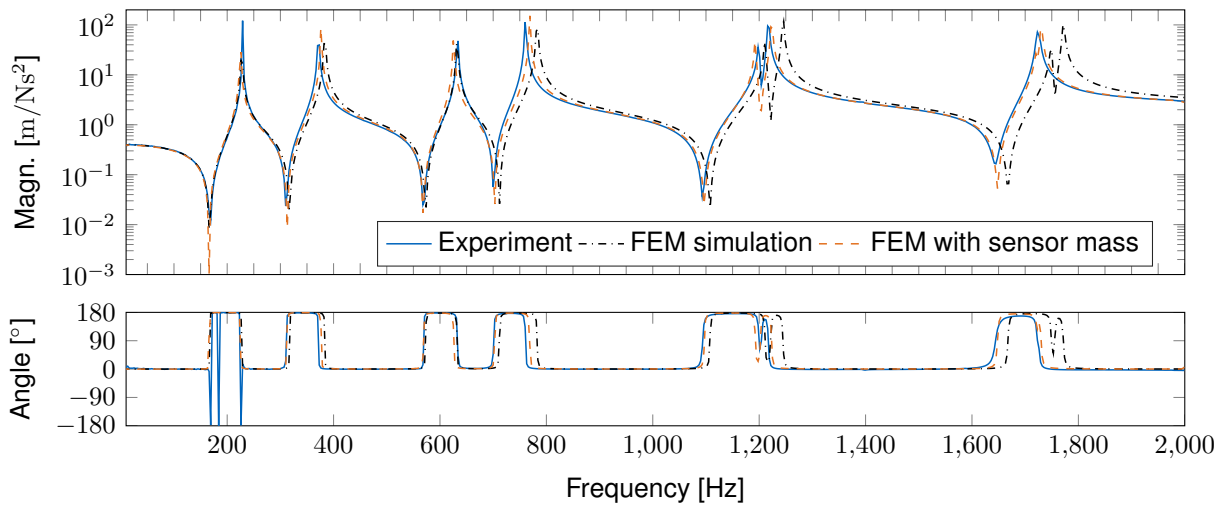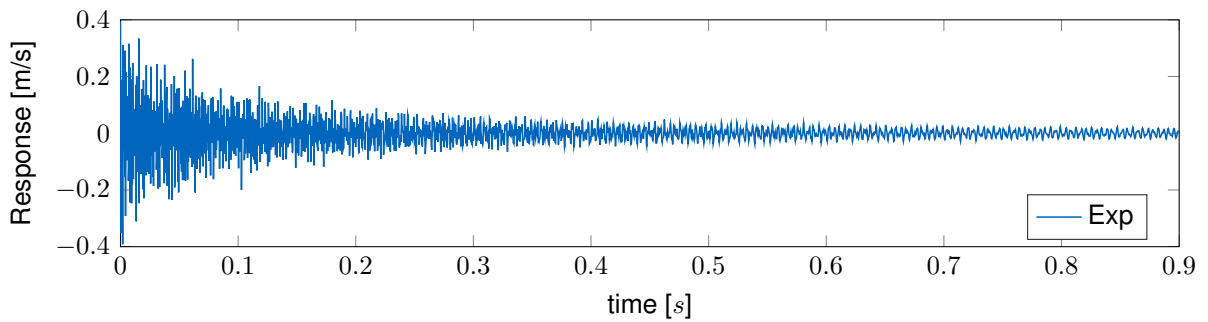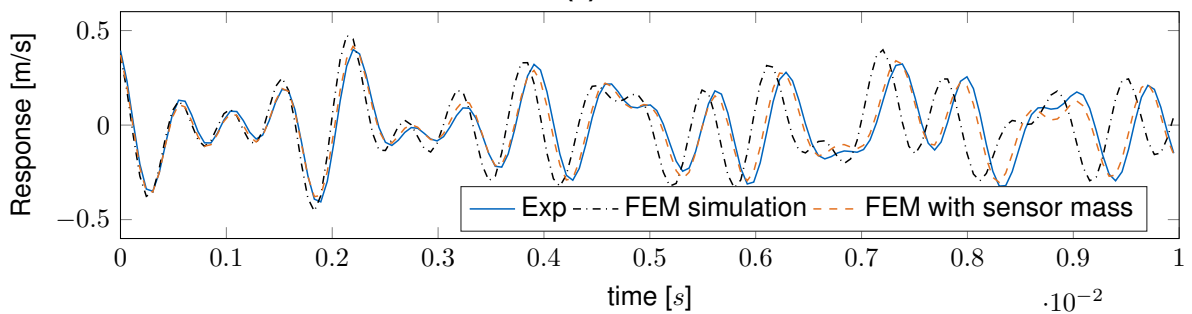**Figure 2.4:** Comparison of experimentally obtained FRF and an admittance synthesis of FEM modes.

(a)

(b)

Figure 2.5: Comparison of impulse responses from experimental and numerical models. (a) Impulse response of only the experimental measurements, to see that it takes much longer than 1 second until all the vibration response has damped out. (b) Short term response of experimental and numerical models.

2.6.2   Error checks for accurate FRF models

A driving point FRF Y_{ii} has some properties which can, and should, be used to check the physical correctness of FRF models, especially experimental ones. The following have been found to be valuable during this project, but more in depth understanding of correct FRF measurements can be found in [9, 40].

- **Driving point passivity:** In the mode synthesis of a driving point FRF Y_{ii} (equation (2.30)), one can see that the enumerator has to be positive ($x_{s,i}^2$). The damping term $i\omega\omega_s\varepsilon_s$ is always a positive imaginary number (frequencies are positive and the modal damping has to be positive). Therefore, one can say that the compliance (displacements u) FRF at a driving point must always have a negative imaginary part (positive real number divided by an imaginary number with positive imaginary part). In terms of the phase, this means that it should always be between $0°$ and $-180°$. For mobility ($\dot{u}$) and acceleration ($\ddot{u}$) FRFs, one can deduce similar bounds on the phase of driving point FRFs:

$$\angle Y_{ii}(\omega) \begin{cases} \in [-180°, 0°] & \text{for an admittance/receptance FRF} \\ \in [-90°, 90°] & \text{for a mobility FRF} \\ \in [0°, 180°] & \text{for an acceleration FRF} \end{cases} \qquad \forall i. \qquad (2.56)$$

  In figure 2.4, which shows an acclerance FRF, one can see that this condition is fulfilled perfectly for the FEM model and only violated slightly for the experimental FRF at around $200Hz$. This is an important check that one should carry out, for validity checks on either model. While impact testing a structure, it is also valuable to monitor the FRF to the sensor channel which is closest to the impact hammer and points roughly in the same direction (which can be considered a driving point). This phase criterion should usually be fulfilled for these FRFs. This comes with the advantage that most of the sensor channels are checked for validity during the measurement campaign, and provides some entertainment during a repetetive task.

- **(Anti-) Resonance Pattern:** At a resonance frequency $\omega = \omega_r$ the most significant contributor to the FRF, in the sum over the modes (2.30), is the resonant mode r. The real part of the numerator vanishes, and the imaginary part (damping) of the numerator is comparatively small. When the excitation frequency ω passes the resonance frequency ω_r the real part of enumerator changes from a small positive number to a small negative number. Hence one sees sudden phase changes of approximately $180°$ at all resonances. After ω passed the resonant frequency ω_r, the negative real part of mode r in the sum (2.30), will eventually be canceled out by the growing positive real part of the next mode ω_{r+1}. At this frequency an anti-resonance, i.e. a sharp drop in the FRF magnitude occurs. Also the phase changes by approximately $180°$ (for small damping) at the anti-resonance. This pattern, of each resonance being followed by an anti-resonance can be seen on all driving point FRFs (cf. figure 2.4). For non-driving point FRFs, this is not necessarily the case, since there the enumerator $x_{r,i}x_{r,j}$ can have a different sign for each mode r.

- **Free-Free Structures:** Driving point FRFs Y_{ii} on structures with rigid body modes should always start with a constant acceleration FRF at $\omega = 0$ (like the freely hung up plate in figure 2.4). This constant acceleration FRF should always be followed by first an anti-resonance and then the first resonance. It should be remarked, that in practice it is not possible to measure on a freely floating structure, so most often it is suspended with very soft rubber bands. So what one typically sees is some low frequent rigid body modes, followed by the constant line described above.

- **Supported Structures:** Structures without rigid body modes, e.g. on a clamped testrig, should always start with a zero acceleration at $\omega = 0$. After the zero magnitude at $\omega = 0$, the magnitude should increase a with a slope of ω^2. This can be checked most easily in a magnitude plot with logarithmic frequency and magnitude axes.

Before even conducting the full suite of experimental FRF measurements, there are some pre-checks that turned out to be valuable habit:

- **Sensor Isolation:** Check if the housing of all ICP sensors is isolated from the test structure (this can either be done with a multi-meter, or be detected from a higher noise floor on these sensors). The twisted coax cables which would usually suppress induction from electro-magnetic noise fields do not work if the sensor housing is grounded via the test structure.

- **Sensor Noise Floor:** Check the noise floor in all channels before the measurement. When the structure is at rest, the live FFT results in all sensor channels should be checked. When using the same sensors, all the noise floor levels should be in the same order of magnitude. Channels with higher noise floors can indicate broken measurement channels, or non-sufficient isolation of the sensor housing from the test structure.

- **Sensor Orientation:** Look at the so called operational deflection shapes (ODS) of the acquired FRFs. The ODS for a lower frequency should show a pure rigid body motion for a freely suspended part. Often it is easy to find wrong sensor orientations and interchanged cables quickly and intuitively by looking at the ODS. Software that provides this feature greatly improves the error avoidance when performing large tests with many measurement channels.

2.7 Rigid body models

During the course of this research project, it turned out that it is of great practical advantage to have analytical rigid body models for some substructures in the "toolbox". Substructures modeled as rigid bodies will be denoted with the symbol shown in figure 2.6b throughout the document. This is probably the easiest way to model a substructure, but it requires that the assumption of rigidity is valid in the frequency range of interest. The specific form of the following derivation could not be found in the standard literature, though the developments in [163, section 3.8] are similar. Therefore, the proper formulation of the mass matrix for a rigid body, with special attention to the practical needs for substructure coupling, shall get some attention here. This means the linearization of the Newton-Euler equations to get the mass matrix of the rigid body. For substructuring, the rigid body often needs to be coupled to another substructure at a point Q, which is not its center of gravity. Therefore, the rotational inertia tensor around point Q has to be derived from the rotational inertia around the rigid body's center of gravity C' (e.g. from a CAD model). Then additional point masses m_s have to be included, to account for the mass of acceleration sensors (see figure 2.6a).

2.7.1 Analytical mass matrix of rigid bodies

For describing the motion of a rigid body, we define a reference point Q, see figure 2.6a. The whole motion of the body can be described by the translation of the reference point $\mathbf{u}_Q$
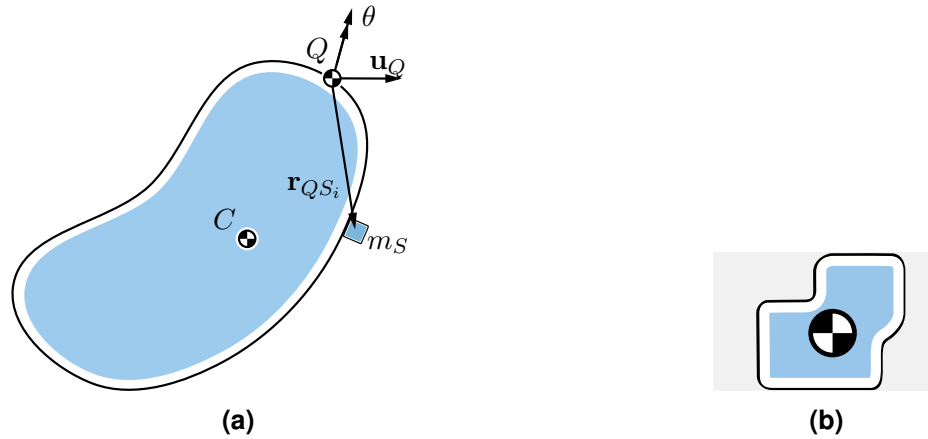
Figure 2.6: (a) Schematic overview of quantities and points on rigid body. Center of gravity without applied sensors is C' and with the attached sensor mass m_S it is C. The reference point Q and its small translation $\mathbf{u}_Q$ as well as the rotations θ define the vibration motion of the whole body. (b) Symbol which will be used to denote substructures that are modeled as rigid body (will be used throughout the document).

and a rotation vector θ around that point. Normally, the angles contained in the vector θ would have to be accompanied by a specific parametrization of the rotation (e.g. Euler or Cardan angles). However, in NVH typically only small vibrations are considered. Therefore, θ will be seen as *small* rotation angles of the body around the x, y and z axis (this can be seen as a linearized version of the Cardan angle parametrization). The inertial frame of reference and the body fixed frame of reference are approximately equal for small $\mathbf{u}_Q$ and θ. The displacement of each point X on the body can be written as:

$$\mathbf{u}_X = \mathbf{u}_Q + \theta \times \mathbf{r}_{QX}, \tag{2.57}$$

where $\mathbf{r}_{QX}$ is the vector from the reference point Q to the point X and $\times$ denotes the cross product. The Newton-Euler equations for a rigid body in three dimensional space are (see e.g. [137, section 3.3]):

$$
\begin{aligned}
m_{tot}(\ddot{\mathbf{u}}_Q + \ddot{\theta} \times \mathbf{r}_{QC} + \dot{\theta} \times (\dot{\theta} \times \mathbf{r}_{QC})) &= \mathbf{f}_Q, \\
m_{tot}\mathbf{r}_{QC} \times \ddot{\mathbf{u}}_Q + \Theta_Q^{tot} \ddot{\theta} + \dot{\theta} \times \Theta_Q^{tot} \dot{\theta} &= \mathbf{m}_Q,
\end{aligned}
\tag{2.58}
$$

where m_{tot} is the total mass of the rigid body and Θ_Q^{tot} is its total rotational inertia around point Q. The term "total" is used in this context to denote that for accurate modeling the mass of applied acceleration sensors should be included (see section 2.7.2). The externally applied forces and moments around point Q are denoted as $\mathbf{f}_Q$ and $\mathbf{m}_Q$ respectively. Considering that $\mathbf{u}_Q$ represents small displacements and θ small rotations, and that also their time derivatives are small, one can drop the second order terms in equation (2.58). One can then write the linearized version of the Newton-Euler[7] equations as:

$$\underbrace{\begin{bmatrix} m_{tot}\mathbf{I} & -m_{tot}\tilde{\mathbf{r}}_{QC} \\ m_{tot}\tilde{\mathbf{r}}_{QC} & \Theta_Q^{tot} \end{bmatrix}}_{\mathbf{M}} \underbrace{\begin{bmatrix} \ddot{\mathbf{u}}_Q \\ \ddot{\theta} \end{bmatrix}}_{\mathbf{u}} = \underbrace{\begin{bmatrix} \mathbf{f}_Q \\ \mathbf{m}_Q \end{bmatrix}}_{\mathbf{f}}, \tag{2.59}$$

where $\mathbf{I}$ is the 3×3 identity matrix. This equation has the desired form including the mass matrix $\mathbf{M}$. The dynamic stiffness $\mathbf{Z}(\omega)$ matrix can directly be computed from it (equation (2.22)),

---

[7]Note for the derivation that a cross product $\mathbf{a} \times \mathbf{b}$ can be written as $\tilde{\mathbf{a}}\,\mathbf{b}$, where $\tilde{\mathbf{a}}$ is a skew-symmetric 3×3 matrix. Skew symmetric implies that $\tilde{\mathbf{a}}^T = -\tilde{\mathbf{a}}$, and thus the mass matrix in (2.59) is symmetric. Additionally, note that $\mathbf{a} \times \mathbf{b} = -\mathbf{b} \times \mathbf{a}$.

and since it is only a 6×6 matrix, the admittance $\mathbf{Y}(\omega)$ can be obtained by simply inverting it (no solution for eigenmodes required).

2.7.2 CAD data and sensor mass loading

Another practical aspect, often encountered in the course of this research project, is the proper computation of the total rotational inertia Θ_Q^{tot} around a given point Q. Usually, one gets the rotational inertia of a rigid body $\Theta_{C'}$, which is computed around its center of gravity C' (e.g. from a CAD model) without applied sensor masses. The general definition for the rotational inertia of a body with density ρ around any point Q is (see e.g. [163, section 3.8]):

$$\mathbf{\Theta}_Q = \int_\Omega \rho \left(||\mathbf{r}_{QX}||^2 \mathbf{I} - \mathbf{r}_{QX} \mathbf{r}_{QX}^T \right) dV \qquad \text{with} \quad X \in \Omega, \tag{2.60}$$

where X is some point on the body and Ω is the whole volume of the body, over which the integration is applied, see figure 2.6a. As already said, most often the rotational inertia around the plain bodies center of gravity $\Theta_{C'}$ is known from CAD. But the rotational inertia around a given point of interest Q is sought, e.g. since the body shall be coupled at this point to another structure. Before proceeding, it is important to remember the definition of the center of gravity C', namely:

$$\mathbf{r}_{QC'} = \frac{1}{m_b} \int_\Omega \rho \, \mathbf{r}_{QX} \, dV \qquad \text{with} \quad X \in \Omega, \tag{2.61}$$

where m_b is the total mass of the body without the sensors. The vector $\mathbf{r}_{QC'}$ is also known from the CAD model. Any vector $\mathbf{r}_{QX}$ in equation (2.60) can be written as the vector sum $\mathbf{r}_{QX} = \mathbf{r}_{QC'} + \mathbf{r}_{C'X}$, where $\mathbf{r}_{QC'}$ is constant for all X in the integration. Inserting this in equation (2.60), yields the rotational inertia $\mathbf{\Theta}_Q$ around a general point Q:

$$\begin{aligned}
\mathbf{\Theta}_Q &= \int_\Omega \rho \left(||\mathbf{r}_{QX}||^2 \mathbf{I} - \mathbf{r}_{QX} \mathbf{r}_{QX}^T \right) dV \\
&= \int_\Omega \rho ||\mathbf{r}_{QX}||^2 \mathbf{I} dV - \int_\Omega \rho \, \mathbf{r}_{QX} \mathbf{r}_{QX}^T dV \\
&= \int_\Omega \rho (||\mathbf{r}_{QC'}||^2 \mathbf{I} + \underbrace{2\mathbf{r}_{QC'}^T \mathbf{r}_{C'X} \mathbf{I}}_{\text{vanishes in integral}} + ||\mathbf{r}_{C'X}||^2 \mathbf{I}) dV - \\
&\quad \int_\Omega \rho (\mathbf{r}_{QC'} \mathbf{r}_{QC'}^T + \underbrace{\mathbf{r}_{QC'} \mathbf{r}_{C'X}^T}_{\text{vanishes in int.}} + \underbrace{\mathbf{r}_{C'X} \mathbf{r}_{QC'}^T}_{\text{vanishes in int.}} + \mathbf{r}_{C'X} \mathbf{r}_{C'X}^T) dV \\
&= \mathbf{\Theta}_{C'} + m_b (||\mathbf{r}_{QC'}||^2 \mathbf{I} - \mathbf{r}_{QC'} \mathbf{r}_{QC'}^T),
\end{aligned} \tag{2.62}$$

where the indicated terms drop out due to the definition of the center of gravity in equation (2.61). Therefore, the inertia tensor of the body around a given point Q can be computed from the inertia tensor around the center of gravity $\mathbf{\Theta}_{C'}$ and the position of Q with respect to the center of gravity C' (which is usually both obtained from CAD models):

$$\mathbf{\Theta}_Q = \mathbf{\Theta}_{C'} + m_b (||\mathbf{r}_{QC'}||^2 \mathbf{I} - \mathbf{r}_{QC'} \mathbf{r}_{QC'}^T). \tag{2.63}$$

Lastly, for an accurate model it is also necessary to consider the mass loading of acceleration sensors on the rigid body. The rotational inertia is defined as an integral over the whole body Ω (equation (2.60)). Integrals are additive, and thus one can add the inertia contributions of the sensors (treated as point masses). The resulting total rotational inertia of the rigid body *with* acceleration sensors around point Q is:

$$\mathbf{\Theta}_Q^{tot} = \underbrace{\mathbf{\Theta}_{C'} + m_b(||\mathbf{r}_{QC'}||^2\mathbf{I} - \mathbf{r}_{QC'}\mathbf{r}_{QC'}^T)}_{\text{rot. inertia of body around } Q} + \underbrace{\sum_{i=1}^{n_s} m_s(||\mathbf{r}_{Q\,S_i}||^2\mathbf{I} - \mathbf{r}_{Q\,S_i}\mathbf{r}_{Q\,S_i}^T)}_{\text{rot. inertia of sensors}}, \tag{2.64}$$

where m_s is the mass of a single sensor and n_s is the number of sensors on the rigid body. The vector from point Q to each sensor is denoted as $\mathbf{r}_{Q\,S_i}$. The total mass of the rigid body with attached sensors is then:

$$m_{tot} = m_b + n_s m_s. \tag{2.65}$$

Due to the addition of the sensor masses, the position of the total center of gravity C, will be different from the center of of gravity of the plain rigid body C'. It can be computed by:

$$\mathbf{r}_{QC} = \frac{1}{m_{tot}} \left[m_b \mathbf{r}_{QC'} + \sum_{i=1}^{n_s} m_s \mathbf{r}_{QS_i} \right]. \tag{2.66}$$

With these definitions and the rigid body model in equation (2.59) accurate models of simple substructures can be obtained. Fortunately, the position of the sensors has to be known anyway (for a process called virtual point transformation, as will be seen in section 3.3) and the sensor masses are easily measured, so the procedure can be implemented straightforwardly in software.

2.7.3 Application example: rigid crosses

For experimentally measuring full six degrees of freedom at a connection point of a structure (e.g. a car body or a rubber mount), it was often advantageous to screw a rigid cross to that connection point. The cross is equipped with accelerometers in each corner, and the FRF measurements can be done by impacting on this cross. Instead of modeling the crosses with the FEM or even measuring their FRF experimentally, it is more time efficient to use a rigid body model as described above[8]. The crosses have to be designed such that they behave rigidly in the frequency range of interest, since this is a basic assumption underlying the virtual point transformation explained in section 3.3.

The example shown in figure 2.7 is an aluminium cross that was used for obtaining experimental rubber bearing models in chapter 4. The single cross weighed about 750 gram, where the accelerometers weighed 7.51 gram each. Its first resonance is at approximately 4600 Hz (validated by FEM and experiment) and the maximum frequency of interest was 2000 Hz. The comparison of the driving point accelerance for the rotation around the z-axis in figure 2.7b shows that the analytical models can be just as accurate as experimental models. The inclusion of the sensor masses yields the last bit of desired accuracy. Analytical models are definitely easier to obtain and less prone to errors that could be encountered in experimental models.

---

[8]A coarse FEM model is then merely required for assuring that they behave as a rigid body in the frequency range of interest. A rule of thumb is that the first resonance frequency of the cross should be at least twice the maximum frequency of interest. This will also be shown with the consistency measure in introduced in section 3.4.3.
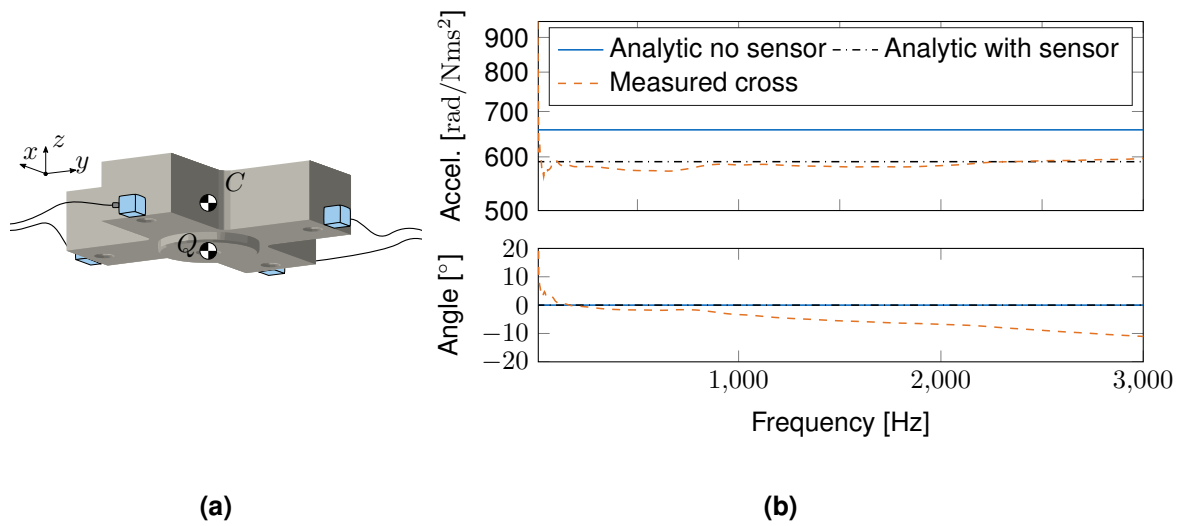
(a)

(b)

Figure 2.7: (a) Schematic depiction of a rigid cross equipped with acceleration sensors (b) Driving point admittance (rotation around z-axis, left figure) of a measurement on the cross vs. the analytical rigid body model with and without consideration of the sensor masses.

Chapter 3

Substructuring

Contents:

> Nothing is particularly hard if you divide it into small jobs.
>
> *Henry Ford*

The contents of this chapter were published in similar form in [54, 57, 60]. The text hereafter has been modified and adapted to the thesis.

The goal of this chapter is to outline how different *substructures* can be coupled to each other, in order to predict the dynamics of a whole assembly. In the previous chapter, different approaches for modeling the dynamic behavior of single substrucutres were explained. It was shown that numerical models from the FEM, experimental tests or analytical rigid body models can represent the dynamics of substructures equally well (provided the underlying modeling assumptions are valid). So each substructure can be modeled with the preferred or most efficient approach. The substructure models can be in different domains, and it was already pointed out that for this thesis the frequency domain is the most important one. The reason for this is found in the complexity of large assembled structures like cars. A typical 'vibro-acoustic' FRF of a modern car is shown in figure 3.1. Vibro-acoustic means that the input quantity was a hammer impact on the car body in the front compartment and the output was a microphone inside the drivers cabin (measuring the dynamic sound pressure response in $[\mathrm{Pa} = \mathrm{N/m^2}]$). The impact measurements were performed with an automatic hammer [100] and 5 averages were used for the estimation of the FRF. As can be seen in the coherence γ^2 in figure 3.1b, the measurements are highly repeatable, resulting in a co-
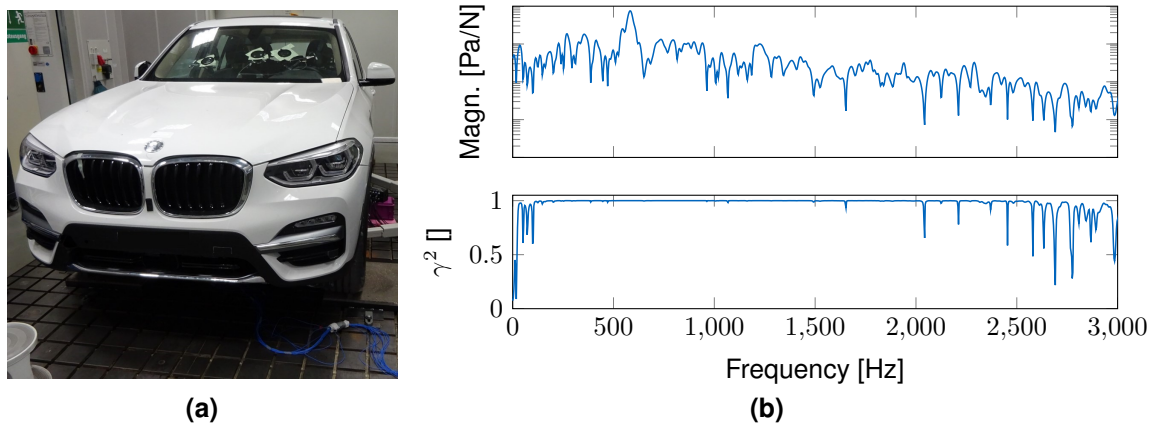
Figure 3.1: (a) Vehicle on a testrig for acoustic FRF measurements. Sensors and automatic hammer are placed under the bonnet in the front compartment and microphones are mounted inside the drivers cabin. (b) Example of a vibro-acoustic FRF from an impact on the car body to a microphone inside the driver's cabin.

herence close to one over almost the entire frequency range (significant drops in coherence can only be seen at frequencies were the overall FRF magnitude is low, and hence the signal to noise ratio is low). Nevertheless, the shape of the FRF is quite complex, and no clear resonances as in figure 2.4 can be found. If fact, the FRF of a whole vehicle is dependent on a myriad of small influences. There are many different contacts between bolted, glued and welded parts, which are hard to model accurately, but crucial for the overall damping of the structure. Additionally, the sound absorption of e.g. interior materials in the drivers cabin, or the dynamic material properties of many different parts might be unknown. Therefore, it is often desirable for an NVH engineer to use an experimentally obtained model for the final transfer path in the car body. All other substructures, like e.g. rubber bearings, carrier structures or the climate compressor, are then virtually coupled to the experimental vehicle model. Also new design concepts can be judged virtually, by changing e.g. the rubber stiffness or the carrier structures in the assembly model (in chapter 11 this will be exemplified). As experimental models of the vehicle are naturally in the frequency domain, in the form of admittance matrices $\mathbf{Y}$, the coupling equations between different substructures will also be formulated in the frequency domain. A process called *frequency based substrucutring* (FBS).

3.1 Frequency based substructuring

The family of dynamic substructuring (DS) methods, have become a well accepted framework for numerically assembling subcomponents, potentially developed by different design teams, and finally predicting the dynamic behavior of the complete product. Variants for coupling in different domains (e.g. the physical, modal and frequency domain) can be derived in a straight forward manner [31] and can equivalently be used for decoupling of structures [4, 186]. For a broad overview of current developments in substructuring generally see e.g. [5]. Getting an accurate physical $\mathbf{M}, \mathbf{C}, \mathbf{K}$ model of a whole car is often infeasible, as explained above. Also, extraction of the modes from an FRF measurement like in figure 3.1b with experimental modal analysis is virtually impossible. Therefore, coupling in the physical or modal domain is not useful for creating the virtual acoustic prototypes that this thesis aims for. The obtained FRFs could potentially be transformed to impulse response functions and
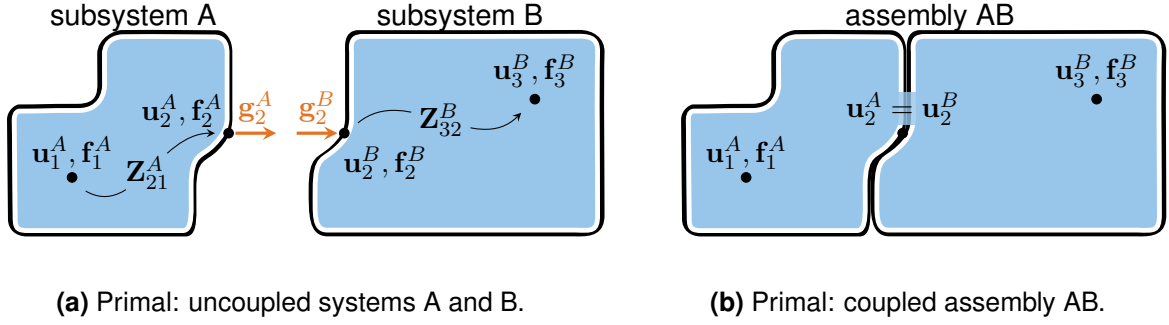
(a) Primal: uncoupled systems A and B.　　　　**(b)** Primal: coupled assembly AB.

Figure 3.2: General overview of the substructuring problem for two substructures in the primal formulation, i.e. based on their dynamics stiffness matrices $\mathbf{Z}^A$ and $\mathbf{Z}^B$.

substructuring could be performed in the time domain [150, 180] (impulse based substructuring), but this approach will not be followed in this thesis. The method of choice, FBS, was first published by Jetmundsen [73] (although similar methods where proposed earlier [30]). It is well suited for inclusion of experimentally obtained substructure models. One advantage of directly using frequency response functions (FRFs) is that the measurement data already contains residual terms from higher order modes.

The coupling operation is first shown in the primal formulation with dynamic stiffness matrices $\mathbf{Z}$, as this is also the most intuitive method and well known from e.g. FEM assembly. Thereafter, the dual formulation with admittance matrices $\mathbf{Y}$ is explained, since this is the most convenient method for including experimental substructure models.

3.1.1　Primal (de-) coupling

Consider the general depiction of two subsystems shown in figure 3.2a. They will be called A and B in the remainder of this chapter. Their DoFs have been grouped into two sets for each substructure: a set of DoFs that are *not* on the coupling interface and thus internal to each substructure (the DoFs $(\star)_1^A$ on substrucutre A and $(\star)_3^B$ on substructure B), and a set of DoFs which *are* on the coupling interface $((\star)_2^A$ and $(\star)_2^B)$. Their dynamic stiffness matrices can thus be partitioned into these DoF sets :

$$\mathbf{Z}^A = \begin{bmatrix} \mathbf{Z}_{11}^A & \mathbf{Z}_{12}^A \\ \mathbf{Z}_{21}^A & \mathbf{Z}_{22}^A \end{bmatrix}, \qquad \mathbf{Z}^B = \begin{bmatrix} \mathbf{Z}_{22}^B & \mathbf{Z}_{23}^B \\ \mathbf{Z}_{32}^B & \mathbf{Z}_{33}^B \end{bmatrix}, \tag{3.1}$$

where the explicit dependence on the frequency ω has been dropped for brevity. With the dynamic displacements $\mathbf{u}$ and external force vectors $\mathbf{f}$ in either group of DoFs, one can write the dynamic equations for both systems. In the coupled configuration, there will also be connection forces $\mathbf{g}_2$ acting on the interface between both substructures, see figure 3.2a:

$$\begin{bmatrix} \mathbf{Z}_{11}^A & \mathbf{Z}_{12}^A & 0 & 0 \\ \mathbf{Z}_{21}^A & \mathbf{Z}_{22}^A & 0 & 0 \\ 0 & 0 & \mathbf{Z}_{22}^B & \mathbf{Z}_{23}^B \\ 0 & 0 & \mathbf{Z}_{32}^B & \mathbf{Z}_{33}^B \end{bmatrix} \begin{bmatrix} \mathbf{u}_1^A \\ \mathbf{u}_2^A \\ \mathbf{u}_2^B \\ \mathbf{u}_3^B \end{bmatrix} = \begin{bmatrix} \mathbf{f}_1^A \\ \mathbf{f}_2^A \\ \mathbf{f}_2^B \\ \mathbf{f}_3^B \end{bmatrix} + \begin{bmatrix} 0 \\ \mathbf{g}_2^A \\ \mathbf{g}_2^B \\ 0 \end{bmatrix}. \tag{3.2}$$

When coupling any two structures to each other, the following two conditions must be fulfilled: *compatibility* of displacements and *equilibrium* of forces. Compatibility states in the above case that $\mathbf{u}_2^A = \mathbf{u}_2^B$. When using the so called 'primal' assembly[1], the two separated

---

[1]The notion of 'primal' assembly is related to the fact that the displacements $\mathbf{u}$ are usually the 'primal' vari-

variables on either side of the interface are replaced by one global variable $\mathbf{u}_2^{AB} := \mathbf{u}_2^A = \mathbf{u}_2^B$, so that the compatibility condition is automatically fulfilled:

$$
\begin{bmatrix} \mathbf{Z}_{11}^A & \mathbf{Z}_{12}^A & \mathbf{0} \\ \mathbf{Z}_{21}^A & \mathbf{Z}_{22}^A & \mathbf{0} \\ \mathbf{0} & \mathbf{Z}_{22}^B & \mathbf{Z}_{23}^B \\ \mathbf{0} & \mathbf{Z}_{32}^B & \mathbf{Z}_{33}^B \end{bmatrix} \begin{bmatrix} \mathbf{u}_1^A \\ \mathbf{u}_2^{AB} \\ \mathbf{u}_3^B \end{bmatrix} = \begin{bmatrix} \mathbf{f}_1^A \\ \mathbf{f}_2^A \\ \mathbf{f}_2^B \\ \mathbf{f}_3^B \end{bmatrix} + \begin{bmatrix} \mathbf{0} \\ \mathbf{g}_2^A \\ \mathbf{g}_2^B \\ \mathbf{0} \end{bmatrix} \tag{3.3}
$$

The next coupling condition is the equilibrium, requiring that the coupling forces on either side of the interface are equal in magnitude, but have opposite sign: $\mathbf{g}_2^A = -\mathbf{g}_2^B$. *Actio est reactio.* Adding the second and third line of (3.3) and considering the equilibrium condition yields the coupled stiffness matrix:

$$
\underbrace{\begin{bmatrix} \mathbf{Z}_{11}^A & \mathbf{Z}_{12}^A & \mathbf{0} \\ \mathbf{Z}_{21}^A & \mathbf{Z}_{22}^A + \mathbf{Z}_{22}^B & \mathbf{Z}_{23}^B \\ \mathbf{0} & \mathbf{Z}_{32}^B & \mathbf{Z}_{33}^B \end{bmatrix}}_{\mathbf{Z}^{AB}} \begin{bmatrix} \mathbf{u}_1^A \\ \mathbf{u}_2^{AB} \\ \mathbf{u}_3^B \end{bmatrix} = \begin{bmatrix} \mathbf{f}_1^A \\ \mathbf{f}_2^A + \mathbf{f}_2^B \\ \mathbf{f}_3^B \end{bmatrix}, \tag{3.4}
$$

which corresponds to the stiffness matrix assembly well known from e.g. finite element modeling. The interface forces vanished from the equations due to the equilibrium condition. This basically corresponds to d'Alemberts principle that "reaction forces ($\mathbf{g}_2^A$ and $\mathbf{g}_2^B$) do not produce any work in the direction compatible with the constraints ($\mathbf{u}_2^A = \mathbf{u}_2^B$)". Formulated loosely, when coupling dynamic stiffness matrices, the coupling process comes down to just "*adding the overlapping matrix parts*". Knowing how to couple two substructures is enough for creating arbitrarily complex assemblies. Each coupled substructuring result can itself be regarded as a single substructure, which could be coupled to yet another component.

As can be seen from (3.4), the uncoupled stiffness $\mathbf{Z}^A$ can be found from "*subtracting*" the dynamic stiffness $\mathbf{Z}^B$ from $\mathbf{Z}^{AB}$. Alternatively, for **decoupling** one could start with the same uncoupled notation as in equation (3.2) including the assembled $\mathbf{Z}^{AB}$ and the *negative* $-\mathbf{Z}^B$, and then perform the same coupling steps, i.e. enforcing equilibrium and compatibility in the shared DoFs $(\star)_2$ and $(\star)_3$.

3.1.2 Dual (de-) coupling

The dual formulation of FBS aims at deriving the admittance of an assembled system $\mathbf{Y}^{AB}$ from the separate admittances of two subsystems $\mathbf{Y}^A$ and $\mathbf{Y}^B$. Consider the situation depicted in figure 3.3a. The admittances of both subsystems $\mathbf{Y}^A$ and $\mathbf{Y}^B$ are known, and their DoF are again grouped into some internal and common DoF on the interface. The admittance of the *uncoupled* substructures can be written in block diagonal form $\mathbf{Y}^{A|B}$. The following equations are the starting point for coupling $\mathbf{Y}^A$ and $\mathbf{Y}^B$, and also aim at clarifying the notation in verbose (3.5) and compact form (3.6):

---

ables for which the equations are being solved in mechanics. The 'dual' variables are the (connection) forces, which can be solved for in a post procesing step. For an interesting discussion regarding the distinction between primal and dual variables in engineering generally, see [165, chapter 2.5]. For further explanation of the distinction between primal and dual variables in dynamic substructuring see the book [5] or the publication [149].
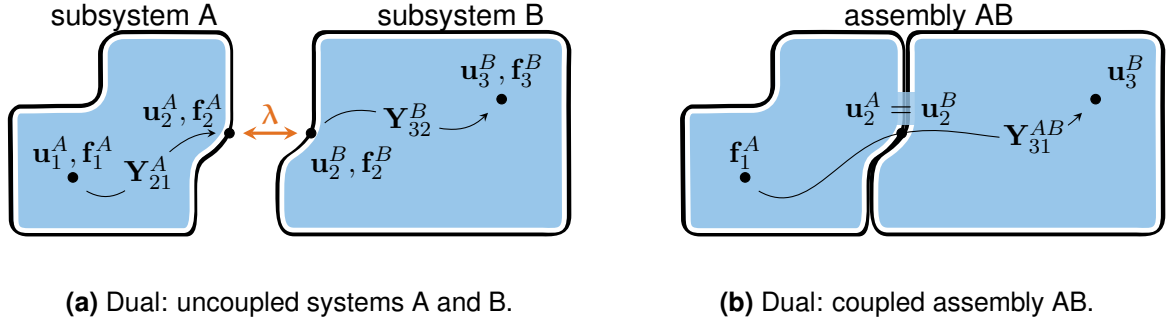
(a) Dual: uncoupled systems A and B.   **(b)** Dual: coupled assembly AB.

Figure 3.3: General overview of the substructuring problem for two substructures in the dual formulation, i.e. based on their admittances $\mathbf{Y}^A$ and $\mathbf{Y}^B$.

$$\begin{bmatrix} \mathbf{Y}_{11}^A & \mathbf{Y}_{12}^A & \mathbf{0} & \mathbf{0} \\ \mathbf{Y}_{21}^A & \mathbf{Y}_{22}^A & \mathbf{0} & \mathbf{0} \\ \mathbf{0} & \mathbf{0} & \mathbf{Y}_{22}^B & \mathbf{Y}_{23}^B \\ \mathbf{0} & \mathbf{0} & \mathbf{Y}_{32}^B & \mathbf{Y}_{33}^B \end{bmatrix} \left(\begin{bmatrix} \mathbf{f}_1^A \\ \mathbf{f}_2^A \\ \mathbf{f}_2^B \\ \mathbf{f}_3^B \end{bmatrix} + \begin{bmatrix} \mathbf{0} \\ \mathbf{g}_2^A \\ \mathbf{g}_2^B \\ \mathbf{0} \end{bmatrix} \right) = \begin{bmatrix} \mathbf{u}_1^A \\ \mathbf{u}_2^A \\ \mathbf{u}_2^B \\ \mathbf{u}_3^B \end{bmatrix}, \tag{3.5}$$

$$\mathbf{Y}^{A|B} \left(\mathbf{f} + \mathbf{g} \right) = \mathbf{u}, \tag{3.6}$$

where $\mathbf{g}$ again denotes the yet unknown reaction forces acting between the two substructures. The two substrucutures have to fulfill *continuity* on the interface again, which can also be written as $\mathbf{u}_2^A - \mathbf{u}_2^B = \mathbf{0}$. The reaction forces $\mathbf{g}$ needed for achieving continuity fulfill *actio est reactio*, i.e. they are equal in magnitude but have opposite signs ($\mathbf{g}_2^A = -\mathbf{g}_2^B$). They can thus be denoted by a single vector of reaction forces $\boldsymbol{\lambda}$. These conditions result in the following set of equations:

$$\mathbf{Y}^{A|B} \left(\mathbf{f} + \underbrace{\mathbf{B}^T \boldsymbol{\lambda}}_{=\mathbf{g}} \right) = \mathbf{u}, \tag{3.7}$$

$$\mathbf{B}\mathbf{u} = \mathbf{0}, \qquad \text{where} \quad \mathbf{B} = \begin{bmatrix} \mathbf{0} & \mathbf{I} & -\mathbf{I} & \mathbf{0} \end{bmatrix}, \tag{3.8}$$

so that in the dual coupling formulation, the reaction forces $\mathbf{g} = \mathbf{B}^T \boldsymbol{\lambda}$ in (3.7) automatically fulfill *actio est reactio*. The statement in (3.8) enforces *continuity*. The matrix $\mathbf{B}$ is commonly called a 'signed Boolean matrix'. Inserting (3.7) in (3.8) and solving for $\boldsymbol{\lambda}$ yields:

$$\boldsymbol{\lambda} = - \left(\mathbf{B}\mathbf{Y}^{A|B}\mathbf{B}^T \right)^{-1} \mathbf{B}\mathbf{Y}^{A|B}\mathbf{f} = - \underbrace{\left(\mathbf{Y}_{22}^A + \mathbf{Y}_{22}^B \right)^{-1}}_{Z_{int}} \underbrace{\mathbf{B}\mathbf{Y}^{A|B}\mathbf{f}}_{\Delta\mathbf{u}_2}, \tag{3.9}$$

where the term $\Delta\mathbf{u}_2$ denotes the interface gap which would result between both structures if they where uncoupled (due to the externally applied forces $\mathbf{f}$). The term $\mathbf{Z}_{int}$ can be interpreted as the 'interface stiffness' that relates the interface gap $\Delta\mathbf{u}_2$ to the reaction forces $\boldsymbol{\lambda}$ needed for 'closing the gap'. Reinserting (3.9) in (3.7) yields the admittance matrix of the assembled system $\mathbf{Y}^{AB}$:

$$\underbrace{\left(\mathbf{Y}^{A|B} - \mathbf{Y}^{A|B}\mathbf{B}^T \left(\mathbf{B}\mathbf{Y}^{A|B}\mathbf{B}^T \right)^{-1} \mathbf{B}\mathbf{Y}^{A|B} \right)}_{=\mathbf{Y}^{AB}} \mathbf{f} = \mathbf{u}. \tag{3.10}$$

In fact primal and dual assembly are mathematically equal, as long as no DoF reduction is performed on the interface [5]. If an interface DoF reduction is performed, then the dual substructuring is weakening the interface condition (mechanically one could think about having flexibility in the directions not covered by the interface reduction, see [148] and section 3.3.3 of this thesis). The primal assembly is artificially stiffening the interface in case an interface reduction is performed (setting all motion in the directions not included in the reduction basis to zero, i.e. a stiffening of the substructures). The primal assembly ensures the fulfillment of the continuity a priory, by choosing a common variable for the interface displacement $\mathbf{u}_2^{AB}$. The dual assembly satisfies the equilibrium a priory by choosing a common variable for the interface forces $\boldsymbol{\lambda}$.

For **decoupling** a substructure B from an assembly AB, one can use the same equations as above, just putting the positive $\mathbf{Y}^{AB}$ and the *negative* $-\mathbf{Y}^B$ into the uncoupled block notation in equation (3.10). As primal and dual assembly are in fact mathematically equivalent, one can deduct that if inserting a negative $-\mathbf{Z}^B$ in the primal formula yields a decoupling of structure B, this means that inserting a negative $\mathbf{Y}^B$ in the dual formula equivalently yields a decoupling of B. A more elaborate and mechanically insightful discussion of decoupling in the dual formulation can be found in [186].

3.2   Interpretation of the dual coupling

This section is intended to answer some questions which are either frequently asked by students (which included the author at the beginning of his project), provide helpful insights for implementation of the method, or just give further understanding of the dual FBS formulation. They could not be found explicitly in other literature and therefore it was decided to include them here.

3.2.1   Redundant rows and columns in dual assembly

Note that the assembled matrix $\mathbf{Y}^{AB}$ in (3.10) still has the same size as the unassembled block matrix $\mathbf{Y}^{A|B}$. Writing down (3.10) in the verbose form indicated in (3.5) yields:

$$\mathbf{Y}^{AB} = \begin{bmatrix} \mathbf{Y}_{11}^A - \mathbf{Y}_{12}^A \mathbf{Z}_{int} \mathbf{Y}_{21}^A & \mathbf{Y}_{12}^A - \mathbf{Y}_{12}^A \mathbf{Z}_{int} \mathbf{Y}_{22}^A & \mathbf{Y}_{12}^A \mathbf{Z}_{int} \mathbf{Y}_{22}^B & \mathbf{Y}_{12}^A \mathbf{Z}_{int} \mathbf{Y}_{23}^B \\ \mathbf{Y}_{21}^A - \mathbf{Y}_{22}^A \mathbf{Z}_{int} \mathbf{Y}_{21}^A & \mathbf{Y}_{22}^A - \mathbf{Y}_{22}^A \mathbf{Z}_{int} \mathbf{Y}_{22}^A & \mathbf{Y}_{22}^A \mathbf{Z}_{int} \mathbf{Y}_{22}^B & \mathbf{Y}_{12}^A \mathbf{Z}_{int} \mathbf{Y}_{23}^B \\ \mathbf{Y}_{22}^B \mathbf{Z}_{int} \mathbf{Y}_{21}^A & \mathbf{Y}_{22}^B \mathbf{Z}_{int} \mathbf{Y}_{22}^A & \mathbf{Y}_{22}^B - \mathbf{Y}_{22}^B \mathbf{Z}_{int} \mathbf{Y}_{22}^B & \mathbf{Y}_{23}^B - \mathbf{Y}_{22}^B \mathbf{Z}_{int} \mathbf{Y}_{23}^B \\ \mathbf{Y}_{32}^B \mathbf{Z}_{int} \mathbf{Y}_{21}^A & \mathbf{Y}_{32}^B \mathbf{Z}_{int} \mathbf{Y}_{22}^A & \mathbf{Y}_{32}^B - \mathbf{Y}_{32}^B \mathbf{Z}_{int} \mathbf{Y}_{22}^B & \mathbf{Y}_{33}^B - \mathbf{Y}_{32}^B \mathbf{Z}_{int} \mathbf{Y}_{23}^B \end{bmatrix}$$

$$(3.11)$$

Notice that the second and third row of $\mathbf{Y}^{AB}$ should be equal as a direct consequence of the continuity ($\mathbf{u}_2^A = \mathbf{u}_2^B$). Take e.g. the first column terms of the second and third row in (3.11) and subtract them from each other:

$$\underbrace{(\mathbf{Y}_{21}^A - \mathbf{Y}_{22}^A \mathbf{Z}_{int} \mathbf{Y}_{21}^A)}_{=\mathbf{Y}_{21}^{AB}} - \underbrace{(\mathbf{Y}_{22}^B \mathbf{Z}_{int} \mathbf{Y}_{21}^A)}_{=\mathbf{Y}_{31}^{AB}} = \mathbf{Y}_{21}^A - \underbrace{(\mathbf{Y}_{22}^A + \mathbf{Y}_{22}^B) \mathbf{Z}_{int}}_{=\mathbf{I}, \quad \text{see (3.9)}} \mathbf{Y}_{21}^A = \mathbf{0}, \qquad (3.12)$$

which proves that these two terms are equal. This can be done similarly for all terms in the second and third row. Additionally, notice that the second and third column in $\mathbf{Y}^{AB}$ are equal, meaning that the external forces on the interface $\mathbf{f}_2^A$ and $\mathbf{f}_2^B$ both have the same effect on the response of the assembled system. It is thus common practice to remove these redundant

$$\mathbf{K}^A = \begin{bmatrix} 2 & -1 & 0 \\ -1 & 2 & -1 \\ 0 & -1 & 1 \end{bmatrix}, \mathbf{K}^B = \pi \begin{bmatrix} 1 & -1 & 0 \\ -1 & 2 & -1 \\ 0 & -1 & 2 \end{bmatrix}$$

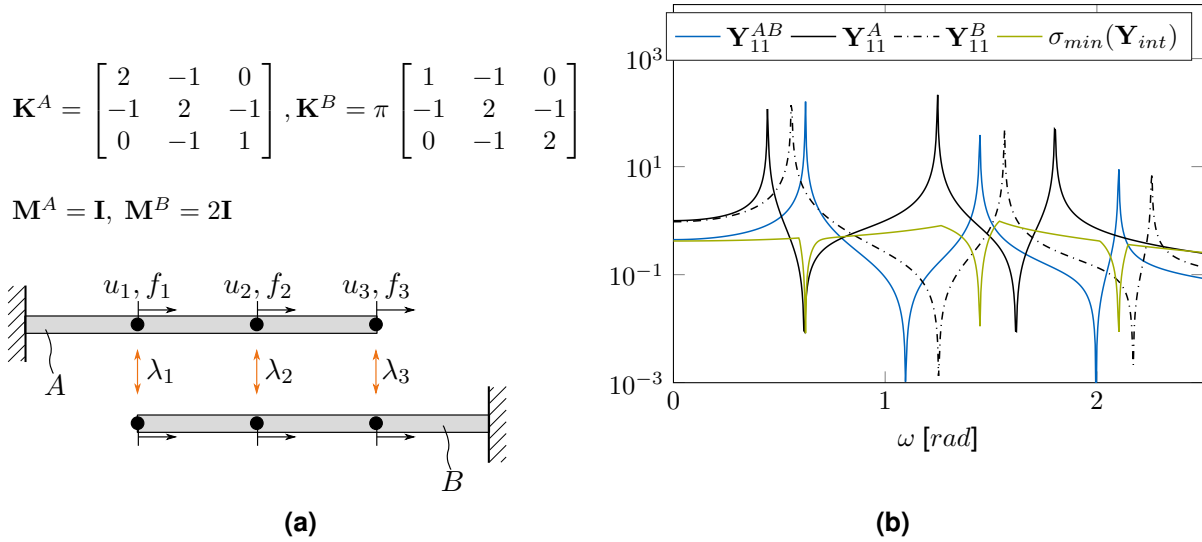$$\mathbf{M}^A = \mathbf{I}, \ \mathbf{M}^B = 2\mathbf{I}$$

(a) **(b)**

Figure 3.4: Simple example for dual FBS. (a) separate subsystems of two discretized bars with their mass and stiffness matrices. (b) FRFs of coupled system Y_{11}^{AB} and uncoupled systems Y_{11}^A, Y_{11}^B. Drops in the smallest singular value of the interface admittance $\sigma_{min}(\mathbf{Y}_{int})$ can clearly detect resonances of the coupled system. At these frequencies the interface forces $\boldsymbol{\lambda}$ become large and drive the separate systems A and B to high response amplitudes.

rows and columns from the final matrix $\mathbf{Y}^{AB}$, thereby also making it invertible again and treating the interface dofs as the common quantities they are:

$$\mathbf{u}_2^A = \mathbf{u}_2^B =: \mathbf{u}_2^{AB}, \qquad \text{and} \qquad \mathbf{f}_2^A + \mathbf{f}_2^B =: \mathbf{f}_2^{AB}. \tag{3.13}$$

This can be implemented in the final software for performing the coupling and decoupling.

3.2.2 Resonances of the coupled system

The resonances of the coupled system will generally be different from the original resonance frequencies of the separate subsystems A and B. Consider the system shown in figure 3.4a. The two bars A and B are discretized with three DoF each and the mass and stiffness matrices are given in figure 3.4a. The corresponding admittance matrices $\mathbf{Y}^A$ and $\mathbf{Y}^B$ are computed from these (no damping) and coupled in all DoF with the dual FBS given in equation (3.10). In figure 3.4b, the driving point FRF at the first degree of freedom for the coupled and both uncoupled systems is shown. It can be seen that the resonances of the coupled system are distinct from the resonances of the uncoupled systems. The resonances of the coupled system can be explained with a singular value decomposition[2] (SVD) of the 'interface admittance' $\mathbf{Y}_{int}$:

$$\mathbf{Y}_{int} = \mathbf{Y}_{22}^A + \mathbf{Y}_{22}^B = \mathbf{U}\boldsymbol{\Sigma}\mathbf{V}^*, \qquad \text{with:}$$

$$\mathbf{U}^*\mathbf{U} = \mathbf{I}, \quad \mathbf{V}^*\mathbf{V} = \mathbf{I}, \quad \boldsymbol{\Sigma} = diag(\sigma_{max}, ..., \sigma_{min}), \qquad \text{so that:} \tag{3.14}$$

$$\mathbf{Z}_{int} = \mathbf{Y}_{int}^{-1} = \mathbf{V}\boldsymbol{\Sigma}^{-1}\mathbf{U}^*,$$

---

[2]Initially, the author was tempted to include an explanation of the SVD in the Appendix of this thesis, like it is done in many other texts. After all, this endeavor was considered to be a futile attempt to write something that is only close to the clarity of the SVD derivation in Strangs textbooks [165, 167], or his MIT open courseware lectures on linear algebra which are freely accessible videos on the internet.

where $(\star)^*$ denotes the hermitian of a matrix (complex conjugate and transposed matrix). The minimum singular value σ_{min} of the interface admittance will exhibit significant drops at the resonances of the coupled system. In figure 3.4b, the value of σ_{min} is also plotted over frequency. The mechanical interpretation is straightforward: if a gap $\Delta\mathbf{u}_2$ between the uncoupled systems has a non-zero contribution in the vector of $\mathbf{U}$ corresponding to the minimal singular value $\sigma_{min}(\mathbf{Y}_{int})$, then the resulting interface force $\boldsymbol{\lambda}$ to close this gap is very large, provided $\sigma_{min}(\mathbf{Y}_{int})$ is very low. This in turn leads to a large response in both systems and thus a resonance of the assembly. This can also be seen as having a large interface stiffness $\mathbf{Z}_{int}$ in this direction, since $\sigma_{max}(\mathbf{Z}_{int}) = (\sigma_{min}(\mathbf{Y}_{int}))^{-1}$, as indicated in equation (3.14).

In case of a single *uncoupled* subsystem resonance, the maximum singular value of the interface $\sigma_{max}(\mathbf{Y}_{int})$ would be large (it is dominated by the substructure in resonance). The interface stiffness in this direction would thus be small. This means that a large gap $\Delta\mathbf{u}_2$, which is a result of the subsystem in resonance, could be countered by a small interface force $\boldsymbol{\lambda}$ and the response of the coupled system stays bounded at this frequency. I.e. resonances of subsystems are not necessarily also a resonance of the coupled system[3].

The fact that the resonances of the new system arise at the points were the interface flexibility has sharp drops in its lowest singular value is unfortunate for experimental measurements, since at frequencies where the response of both substrucutres is low, and thus also the signal to noise ratio in the measurements is low, the random errors in the measurement can lead to matrix components that cancel out mutually leading to small singular values and thus to spurious peaks. This and other challenges related to experimental FBS will be discussed in section 3.4. Also some important error checks will be given to limit these problems in practice.

3.2.3   Practical reason for dual coupling with experimental models

An often encountered question is: Why is the distinction between primal and dual assembly important? After all, they are mathematically equivalent. They only yield different results if an interface reduction is performed, as was already stated and is described in [5]. But there is a practical reason for the dual assembly, when dealing with experimental substructures. If one would prefer to couple the substructures with the primal formulation (3.4), one would have to invert the measured $\mathbf{Y}$ matrices to get the dynamic stiffnesses $\mathbf{Z}$ which can then be coupled:

$$\mathbf{Z}^A = \begin{bmatrix} \mathbf{Y}_{11}^A & \mathbf{Y}_{12}^A \\ \mathbf{Y}_{21}^A & \mathbf{Y}_{22}^A \end{bmatrix}^{-1}, \qquad \mathbf{Z}^B = \begin{bmatrix} \mathbf{Y}_{22}^B & \mathbf{Y}_{23}^B \\ \mathbf{Y}_{32}^B & \mathbf{Y}_{33}^B \end{bmatrix}^{-1}. \tag{3.15}$$

In practice however, there is often only measured inputs at the connection points, but outputs also at internal DoF, resulting in rectangular admittance matrices $\mathbf{Y}$. Say in a practical example one has a vibration source admittance $\mathbf{Y}^A$, which is only measured on its interface DoF. The final receiver B, to which A shall be coupled, is the vehicle. For the vehicle FRF one applied input forces only at the coupling interface, but additionally measured the transfer functions to some microphones and acceleration sensors inside the driver's cabin (this would be internal DoF to B). The admittances look like:

---

[3]Writing this down for e.g. a small system with only one interface DoF and performing a limit calculation is also well possible, but spared at this point. Note that with noisy measurement data, there are spurious peaks developing also at the resonances of the uncoupled substructures [147].

$$\mathbf{Y}^A = \begin{bmatrix} \mathbf{Y}^A_{22} \end{bmatrix}, \qquad \mathbf{Y}^B = \begin{bmatrix} \mathbf{Y}^B_{22} \\ \mathbf{Y}^B_{32} \end{bmatrix}. \tag{3.16}$$

Since $\mathbf{Y}^B$ is rectangular it cannot be simply inverted, as in equation (3.15), for getting the dynamic stiffness $\mathbf{Z}^B$ and performing a primal coupling[4]. With the dual formulation however, one can couple them easily with a slight amendment of the dual FBS formula (3.10). The Boolean matrices for ensuring the compatibility and distributing the interface forces, $\mathbf{B}_u$ and $\mathbf{B}_f$ respectively, would have different shapes since the number of input and output DoF is different now. Writing the dual coupling problem again with the amended matrix shapes yields:

$$\mathbf{Y}^{A|B} = \begin{bmatrix} \mathbf{Y}^A_{22} & \mathbf{0} \\ \mathbf{0} & \mathbf{Y}^B_{22} \\ \mathbf{0} & \mathbf{Y}^B_{32,} \end{bmatrix}, \tag{3.17}$$

$$\mathbf{B}_u \mathbf{u} = \mathbf{0}, \qquad\qquad \text{with } \mathbf{B}_u = \begin{bmatrix} \mathbf{I} & -\mathbf{I} & \mathbf{0} \end{bmatrix} \tag{3.18}$$

$$\mathbf{g} = \mathbf{B}_f^T \boldsymbol{\lambda}, \qquad\qquad \text{with } \mathbf{B}_f = \begin{bmatrix} \mathbf{I} & -\mathbf{I} \end{bmatrix} \tag{3.19}$$

which can be solved the same way as before resulting in the dual coupling:

$$\underbrace{\left(\mathbf{Y}^{A|B} - \mathbf{Y}^{A|B} \mathbf{B}_f^T \left(\mathbf{B}_u \mathbf{Y}^{A|B} \mathbf{B}_f^T \right)^{-1} \mathbf{B}_u \mathbf{Y}^{A|B} \right)}_{=\mathbf{Y}^{AB}} \mathbf{f} = \mathbf{u}. \tag{3.20}$$

Getting this result with primal assembly would also be possible but is quite cumbersome in the equations and is therefore omitted here. The dual formulation as in equation (3.20) is just more elegant and practical, for which credit has to be given to De Klerk who first formulated the coupling in this form [87].

3.3 Virtual point transformation

The content of this section was published in [60]. The text hereafter has been modified and adapted to the thesis.

In the previous section, it was implicitly assumed that the DoFs $\mathbf{u}_2^A$ and $\mathbf{u}_2^B$ are in the same position and direction once the substructures are coupled, see figure 3.3. This way the enforcement of continuity on the interface, equation (3.8), is meaningful. The same is true for the external forces $\mathbf{f}_2^A$, $\mathbf{f}_2^B$ and the coupling forces $\boldsymbol{\lambda}$ on either side of the interface. In numerical modeling with the FEM, the need for compatible interface DoF is usually solved by using the same mesh on either side of the interface. More advanced methods to couple also non-matching finite element meshes would be e.g. the mortar method [140]. When coupling elements like screws or spot welds are part of the connections, one also uses separately modeled connection elements [79]. However, in experimental models the problem is rather

---

[4]Substructure A would be ok, since $\mathbf{Z}^A = \mathbf{Z}^A_{22} = \left(\mathbf{Y}^A_{22} \right)^{-1}$. But for substructure B the driving point admittance $\mathbf{Y}^B_{33}$ could not be determined, unless performing an exmerimental modal analysis (which is not possible for a full vehicle in higher frequencies, as discussed in the beginning of this chapter). The missing off-diagonal term could be obtained from considering reciprocity $\mathbf{Y}^B_{23} = \left(\mathbf{Y}^B_{32} \right)^T$ (i.e. that the admittance matrix must be symmetric), see equation (2.30).
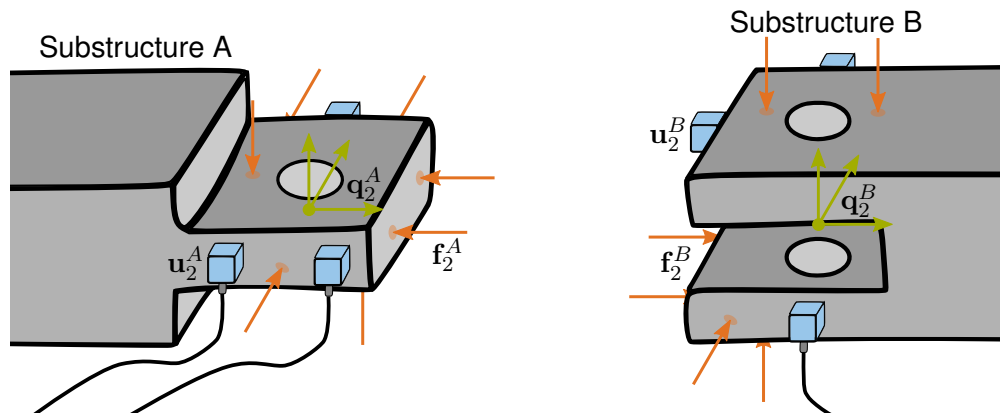
Figure 3.5: Assembly problem in experimental dynamic substructuring. Sensors $\mathbf{u}_2$ and force inputs $\mathbf{f}_2$ on either side of the interface are non-matching.

the non-matching positions of impact and sensor locations, see figure 3.5. Quite often it is not even possible to have sensor and impact positions to be geometrically coinciding on either side of the interface. Thus, they can not be coupled by simply enforcing equality in each DoF, as in numerical analysis and the definition of the interface coupling in experimental FBS therefore remains challenging. The method for modeling the interface DoF of experimental substructures, used in this thesis, is called the 'virtual point transformation' (VPT). Before the underlying transformations and the mechanical interpretation of this coupling variant is explained, a brief overview of other methods described in the literature shall be given.

3.3.1 Coupling interface description with experimental data

One challenge of describing coupling interfaces of experimental substructures properly is measuring and exciting rotational degrees of freedom (RDoF) on the interface. Sensors that can actually measure RDoF have been discussed for a long time and can even be found in textbooks [40, p.166ff] and [104, p.197ff]. However, rotational acceleration sensors are still exotic and not commonly available. An example for the application of a rotational accelerometer, with application to FBS and promising results can be found in [22, 34]. This sensor can measure the rotational acceleration around one axis and weighs around 18.5 gram. Measuring all 3 rotations around one interface point would thus require 3 sensors, or remounting and repeating the measurements 3 times (roving sensor). Despite the challenges of measuring them, including RDoF in the coupling process has been shown to be crucial for accurate results [36, 39, 48, 86, 98, 113]. After all, coupling only the translational directions at a connection point would correspond to a ball joint instead of the needed rigid connection for e.g. the beam shown in figure 3.5.

Therefore, different methods have been developed to implicitly measure and include rotations in the coupling. A large class of methods tries to infer the rotational motion on the interface by using free vibration modes of the substructures to be coupled. They are thus closely related to the component mode synthesis (CMS) techniques, well known from numerical modeling [29, chapter 17]. The '*system equivalent reduction and expansion*' (SEREP) procedure [129] is an elegant way to infer full motion data of the structure (including RDoF on the interface) by measuring with translational sensors only at a few measurement points. An application to experimental DS can be found in [195]. An advantage of these techniques is that the mode identification processes has a 'smoothing effect' on the frequency response functions that are being coupled. It is thereby avoiding some of the numerical instability

issues that are common in FBS [147]. However, a precondition to applying these methods is having a reasonably accurate FEM model of the structure. If a FEM model is available, also the '*system equivalent model mixing*' (SEMM) method [82] could be used for inferring rotational DoF from only a few measurements on the structure.

To account implicitly for the RDoF on the coupling interface, some methods have used multiple connection points on the interface that are simultaneously coupled [36, 103], which has been called '*equivalent multiple point connection*' (EMPC) [86]. However, coupling too many points can result in an overdetermination and a bad conditioning of the interface coupling equations. Some of the equations are then almost redundant and cause numerical instabilities (see the discussion about small singular values on the interface matrix in section 3.2.2). Additionally, the direct use of experimentally obtained data in the FRFs inherently causes numerical instabilities [147]. An interesting depiction of different methods, their problems and remedies can be found in the companion publications [4, 103], where it was found that enforcing the coupling in only a 'weak' least squares sense in many (modal) DoFs, can significantly improve the substructuring results.

The approach used in this thesis is called 'virtual point transformation' (VPT). It can be seen as a combination of the CMS and EMPC methods above. It is using '*interface displacement modes*' (IDMs) which aren't free vibration modes of the whole structure, but rather kinematic assumptions of the local displacement field directly at the interface. The IDMs can be constructed without the need of building a finite element model or performing an experimental modal analysis. However, the transformation of measured FRFs on IDMs can also provide some numerical smoothing if the transformation is overdetermined. This method has first been used in [86] with driving point FRFs and was extended in [155] to allow for different positions in sensors and force impacts, which is making it more feasible experimentally (see figure 3.5). Earlier, in [67] the VPT concept (though under a different name) has already been described for designing a 6 DoF force and acceleration sensor. In [158] the transformation matrices necessary for transforming the measured FRF matrices on generalized IDMs where derived using Moore-Penrose pseudoinverses. This also allowed for a different weighting of physical DoFs in the transformation on the IDMs. In this chapter, the transformation matrices will be derived from a minimization point of view, to more clearly show how the weighting matrices can be utilized to further improve the transformation and coupling process. It will additionally be shown that the transformation of the measured DoFs to the virtual point DoFs has a 'weakening' effect on the interface compatibility (which is fulfilled only in a 'least squares' sense).

3.3.2 Transformation of FRF matrices

As explained above, it is not possible to enforce continuity and equilibrium directly between two experimental substructure models. With the VPT, the measured sensor motion $\mathbf{u}_2$ and the force inputs $\mathbf{f}_2$ are projected on some generalized IDMs. The resulting generalized displacements $\mathbf{q}$ and generalized forces $\mathbf{m}$ are matching on either side of the interface and can thus be coupled as explained in section 3.1. The transformation will take the following form [158]:

$$\mathbf{Y}_{qm} = \mathbf{T}_u \mathbf{Y}_{22} \mathbf{T}_f^T, \tag{3.21}$$

where $\mathbf{Y}_{22}$ denotes the measured FRF matrix in the nonmatching interface dofs $\mathbf{u}_2$, $\mathbf{f}_2$ and $\mathbf{Y}_{qm}$ denotes the transformed FRF matrix in the (matching) generalized coordinates. $\mathbf{T}_u$ and $\mathbf{T}_f^T$ are the transformation matrices:
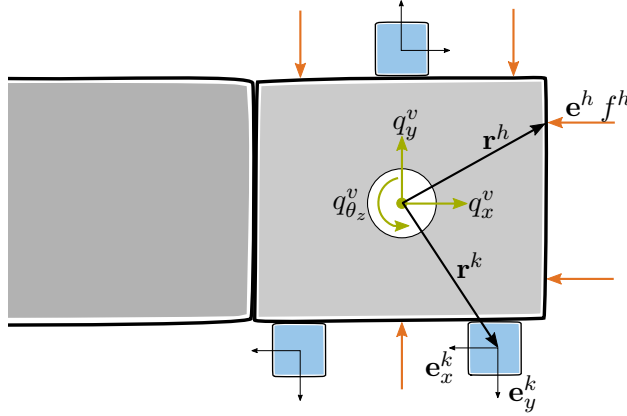
Figure 3.6: General interface connection point. Exemplary quantities for one sensor k and one force input h.

$$\mathbf{q} = \mathbf{T}_u \mathbf{u}_2; \qquad \mathbf{f}_2 = \mathbf{T}_f^T \mathbf{m}. \tag{3.22}$$

The transformation in this section will only concern the interface submatrices $\mathbf{Y}_{22}$, the transformation of the whole matrix $\mathbf{Y}^A$ or $\mathbf{Y}^B$ including also non-transformed internal DoF is straight forward then (see sec. 3.3.3).

Displacement modes

In the case of nonmatching sensor DoFs on the interface $\mathbf{u}_2$, one can choose to represent the interface motion by some general interface displacement modes (IDMs) and the corresponding generalized coordinates $\mathbf{q}$. The number of IDMs is typically lower than the number of measured interface DoFs:

$$\mathbf{u_2} \in \mathbb{C}^{n_u}, \qquad \mathbf{q} \in \mathbb{C}^p, \qquad \text{with} \quad p \leq n_u.$$

Consider the single interface connection point depicted in figure 3.6. When assuming for example that the interface behaves almost rigid in the frequency range of interest, one can compose the generalized coordinates of a translational part $\mathbf{q}_t^v = [q_x^v \; q_y^v \; q_z^v]^T$ and a rotational part $\mathbf{q}_\theta^v = [q_{\theta_x}^v \; q_{\theta_y}^v \; q_{\theta_z}^v]^T$. The superscript $(\star)^v$ denotes the virtual coupling point v, of which there may be multiple on a structure. These coupling points are often called *virtual points* since they can generally be at geometric positions where no physical sensors or inputs are [86, 155, 158]. Such virtual points do not even need to be a material point of the substructure, as for instance the point inside a U-shaped connector in the right part of figure 3.5. Assume the displacement u_x^k measured in x-direction of sensor k (see figure 3.6) shall be computed from the six rigid motion coordinates $\mathbf{q}^v$. The relation between the motion in this single sensor channel and the generalized coordinates can easily be found, provided we know the orientation of the sensor's x-axis $\mathbf{e}_x^k$ and its distance from the virtual point $\mathbf{r}^k$:

$$u_x^k = (\mathbf{e}_x^k)^T \left(\mathbf{q}_t^v + \mathbf{q}_\theta^v \times \mathbf{r}^k \right) = (\mathbf{e}_x^k)^T \begin{bmatrix} 1 & 0 & 0 & 0 & r_z^k & -r_y^k \\ 0 & 1 & 0 & -r_z^k & 0 & r_x^k \\ 0 & 0 & 1 & r_y^k & -r_x^k & 0 \end{bmatrix} \begin{bmatrix} q_x^v \\ q_y^v \\ q_z^v \\ q_{\theta_x}^v \\ q_{\theta_y}^v \\ q_{\theta_z}^v \end{bmatrix} = \mathbf{R}_{u_x^k} \, \mathbf{q}^v, \quad (3.23)$$

where $\mathbf{R}_{u_x^k}$ is a 1×6 matrix relating the generalized coordinates $\mathbf{q}^v$ to the displacement in the sensor's x-channel. Note that this is essentially the same as the rigid body kinematics stated in equation (2.57), where the virtual point would correspond to the reference point Q. The displacements in all sensor channels can be reconstructed for a given $\mathbf{q}^v$ following a similar procedure. Stacking all sensor transformation matrices for all virtual points (see also [158]), yields:

$$\mathbf{u}_2 = \mathbf{R}_u \mathbf{q} \qquad \text{with} \quad \mathbf{R}_u \in \mathbb{R}^{n_u \times p}. \tag{3.24}$$

This can be seen as representing $\mathbf{u}_2$ by a reduced basis contained in the matrix $\mathbf{R}_u$. Note that the reduced basis $\mathbf{R}_u$ may contain arbitrary other interface displacement modes, not just the rigid modes for a *virtual point* as discussed above. Any modes other than the rigid ones that might be of importance can be included as a column in $\mathbf{R}_u$ (see e.g. [133]). However, the general form of (3.24), i.e. the reduction of sensor DoFs, will remain the same.

Displacement transformation

In reality, the response in the sensor channels $\mathbf{u}_2$ will not behave perfectly as indicated in (3.24). This means that one can only represent a measured $\mathbf{u}_2$ with the IDMs up to a certain residual μ, which contains e.g. the non-rigid motion or measurement noise.

$$\mathbf{u}_2 = \mathbf{R}_u \mathbf{q} + \mu \qquad \rightarrow \qquad \mu = \mathbf{u}_2 - \mathbf{R}_u \mathbf{q}. \tag{3.25}$$

However, if the kinematic assumption of the interface motion, contained in $\mathbf{R}_u$, is good enough in the frequency range of interest (e.g. the rigid body assumption on a virtual point as shown above), then the residual μ is likely to be very small and contains mostly measurement noise or results from sensor positioning uncertainties. See e.g. [157, 158] for some indicator functions to check for the validity of the kinematic assumption in a given measurement.

With a given reduction basis $\mathbf{R}_u$, one wants to find the $\mathbf{q}$ that best approximates the measured response $\mathbf{u}_2$. This can be done by minimizing a *cost function* $\Phi(\mathbf{q})$, which is merely the residual μ weighted by a symmetric weighting matrix $\mathbf{W}_u$[5]. The weighting can be chosen from an engineering point of view (some possible choices for $\mathbf{W}_u$ can be found in [60]). The scalar to minimize with the transformation from $\mathbf{u}_2$ to $\mathbf{q}$ is:

$$\Phi(\mathbf{q}) = \tfrac{1}{2}\, \mu^T \mathbf{W}_u \mu = \tfrac{1}{2}(\mathbf{u}_2 - \mathbf{R}_u \mathbf{q})^T \mathbf{W}_u (\mathbf{u}_2 - \mathbf{R}_u \mathbf{q}) \tag{3.26}$$

$$= \tfrac{1}{2}\left(\underbrace{\mathbf{q}^T \mathbf{R}_u^T \mathbf{W}_u \mathbf{R}_u \mathbf{q}}_{\text{quadratic in } \mathbf{q}} - \underbrace{2 \mathbf{u}_2^T \mathbf{W}_u \mathbf{R}_u \mathbf{q}}_{\text{linear in } \mathbf{q}} + \underbrace{\mathbf{u}_2^T \mathbf{W}_u \mathbf{u}_2}_{\text{constant}} \right).$$

If the quaratic term of this function is convex (i.e. the Hessian matrix $\mathbf{R}_u^T \mathbf{W}_u \mathbf{R}_u$ is positive definite), one can simply find the minimum of $\Phi(\mathbf{q})$ by setting its first derivative to zero:

$$\left(\frac{\partial \Phi}{\partial \mathbf{q}} \right)^T = \mathbf{R}_u^T \mathbf{W}_u \mathbf{R}_u \mathbf{q} - \mathbf{R}_u^T \mathbf{W}_u \mathbf{u}_2 \overset{!}{=} \mathbf{0}, \tag{3.27}$$

where it was already assumed that $\mathbf{W}_u$ is symmetric. This means for the sought transformation matrix $\mathbf{T}_u$:

---

[5] Also frequently called *weighted least squares* [165].

$$\mathbf{q} = \underbrace{\left(\mathbf{R}_u^T \mathbf{W}_u \mathbf{R}_u\right)^{-1} \mathbf{R}_u^T \mathbf{W}_u}_{\mathbf{T}_u} \, \mathbf{u}_2, \tag{3.28}$$

where $\mathbf{q}$ represents the 'optimal' solution, which is minimizing the cost function (3.26), and approximates a given $\mathbf{u}_2$ with the IDMs. This transformation matrix is the same as the Moore Penrose pseudoinverse in [158]. The weighting matrix can e.g. be chosen to be a diagonal $n_u \times n_u$ identity matrix, apart from weights lower than 1 for those measurement channels that were found to be very noisy or not as trustworthy during the tests. More choices can be found in [60].

Remark 3.1: The positive definiteness of the Hessian matrix shall get some brief attention here. In simple least squares, the Hessian matrix is $\mathbf{R}_u^T \mathbf{R}_u$, which is always positive definite if the IDMs contained in $\mathbf{R}_u$ are independent, i.e. $\mathbf{R}_u$ has full rank. Thus:

$$\mathbf{R}_u \mathbf{q} \neq \mathbf{0}; \qquad\qquad \forall \mathbf{q} \neq \mathbf{0}$$
$$\mathbf{q}^T \mathbf{R}_u^T \mathbf{R}_u \mathbf{q} =: \mathbf{x}^T \mathbf{x} > 0; \qquad\qquad \forall \mathbf{q} \neq \mathbf{0}$$

The positive definiteness of the Hessian matrix, can also be shown if the weighting matrix $\mathbf{W}_u$ is a symmetric positive definite matrix. Then $\mathbf{W}_u$ can be factored in its (all positive!) eigenvalues $\mathbf{\Lambda} = diag(\lambda_{ii})$ and the orthonormal eigenvectors $\mathbf{Q}$. Thus:

$$\mathbf{q}^T \mathbf{R}_u^T \mathbf{W}_u \mathbf{R}_u \mathbf{q} =: \mathbf{x}^T \mathbf{W}_u \mathbf{x} > 0; \qquad\qquad \forall \mathbf{q} \neq \mathbf{0}$$

Obviously, one could also add multiple weighting matrices to include different quality criteria in the transformation, e.g. $\mathbf{W}_u = \mathbf{W}_{u,1} + \mathbf{W}_{u,2}$; as long as $\mathbf{W}_{u,1}$ and $\mathbf{W}_{u,2}$ are also symmetric positive definite.

Force modes

The same kinematic assumptions as for the displacements are made for the forces. The number of force inputs n_f is typically higher than the number of IDMs p. Their position must also be carefully chosen, so that all IDMs are excited [158].

$$\mathbf{f_2} \in \mathbb{C}^{n_f}, \qquad \mathbf{m} \in \mathbb{C}^p, \qquad \text{with} \quad p \leq n_f.$$

Consider again the example in figure 3.6, with a locally rigid interface on virtual point v. All input forces $\mathbf{f}_2$ will result in a force $\mathbf{m}_t^v$ and a moment $\mathbf{m}_\theta^v$ around the virtual point. For a single force input f^h this can be expressed by:

$$\mathbf{m}^v = \begin{bmatrix} \mathbf{m}_t^v \\ \mathbf{m}_\theta^v \end{bmatrix} = \begin{bmatrix} \mathbf{I} \\ \mathbf{r}^h \times \mathbf{I} \end{bmatrix} \mathbf{e}^h f^h = \mathbf{R}_{fh}^T \, f^h, \tag{3.29}$$

where $\mathbf{R}_{fh}^T$ denotes the 6×1 matrix representing the virtual point load $\mathbf{m}^v$ resulting from a unit force input in f^h and $\mathbf{e}^h$ denotes the direction vector in which the force was applied. The virtual point loads resulting from the other force inputs can be found following a similar procedure. Putting each contribution in a column of $\mathbf{R}_f^T$, one can write
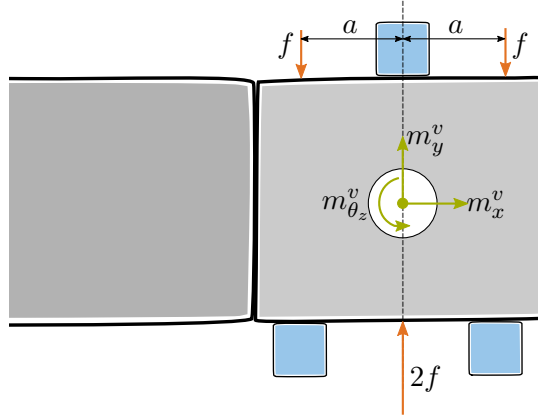
Figure 3.7: Exemplary nullspace vector for input forces.

$$\mathbf{m} = \mathbf{R}_f^T \mathbf{f}_2 \qquad \text{with} \quad \mathbf{R}_f^T \in \mathbb{R}^{p \times n_f}. \tag{3.30}$$

Notice that $\mathbf{R}_f^T$ is written *transposed* since it would directly correspond to the transpose of $\mathbf{R}_u$ in (3.24) if the measured FRF contains only driving point DoF, i. e. if all force inputs would have a corresponding sensor channel in the same geometric position and in the same direction. However, it is a great practical advantage that different DoFs can be used for force inputs and displacement outputs.

Force transformation

In order to transform a measured FRF matrix according to (3.21), a force transformation matrix $\mathbf{T}_f^T$ is needed. It transforms a given load in the generalized forces $\mathbf{m}$, to an equivalent vector of input forces $\tilde{\mathbf{f}}_2$:

$$\tilde{\mathbf{f}}_2 = \mathbf{T}_f^T \mathbf{m}, \tag{3.31}$$

$$\text{where:} \qquad \mathbf{R}_f^T \tilde{\mathbf{f}}_2 \overset{!}{=} \mathbf{m}. \tag{3.32}$$

The problem in (3.31) and (3.32) is fundamentally different from the displacement transformation, stated in (3.25). The requirement in (3.32) is an underdetermined problem and there are infinitely many possible solutions for $\tilde{\mathbf{f}}_2$ that fulfill this requirement. Any vector in the nullspace of $\mathbf{R}_f^T$, lets call an example vector $\tilde{\mathbf{f}}_{2,null}$, could be added to $\tilde{\mathbf{f}}_2$ to produce yet another possible solution to (3.32). For the assumption of a locally rigid interface, all $\tilde{\mathbf{f}}_{2,null}$ would be exciting only flexible modes. Figure 3.7 shows a depiction of such a possible $\tilde{\mathbf{f}}_{2,null}$ which would excite a local bending, which is not contained in the rigid basis.

The question for the transformation is: how to find a solution $\tilde{\mathbf{f}}_2$ from those possible combinations, which is 'good' from an engineering point of view? One can state a standard convex optimization problem where the goal is to minimize a scalar cost function $\Phi(\tilde{\mathbf{f}}_2)$, while the optimum solution $\tilde{\mathbf{f}}_2$ is subject to constraints $\mathbf{g}(\tilde{\mathbf{f}}_2)$:

$$\text{Minimize:} \qquad \Phi(\tilde{\mathbf{f}}_2) = \tfrac{1}{2} \tilde{\mathbf{f}}_2^T \mathbf{W}_f \tilde{\mathbf{f}}_2, \tag{3.33}$$

$$\text{Subject to:} \qquad \mathbf{g}(\tilde{\mathbf{f}}_2) = \mathbf{R}_f^T \tilde{\mathbf{f}}_2 - \mathbf{m} = \mathbf{0}, \tag{3.34}$$

where the force weighting matrix $\mathbf{W}_f$ was introduced for the cost function. Following the same arguments as in the transformation of the displacements, one can state that $\Phi(\tilde{\mathbf{f}}_2)$ has only one global minimum, if the weighting matrix $\mathbf{W}_f$ is positive definite. In the standard optimization formulation for finding a constrained minimum[6], i.e. forming the Lagrangian $\mathcal{L}(\tilde{\mathbf{f}}_2, \boldsymbol{\lambda})$ and search for its stationary point, this yields:

$$\mathcal{L}(\tilde{\mathbf{f}}_2, \boldsymbol{\lambda}) = \Phi(\tilde{\mathbf{f}}_2) + \boldsymbol{\lambda}^T \mathbf{g}(\tilde{\mathbf{f}}_2), \tag{3.35}$$

$$\left(\frac{\partial \mathcal{L}}{\partial \tilde{\mathbf{f}}_2} \right)^T = \mathbf{W}_f \tilde{\mathbf{f}}_2 + \mathbf{R}_f \boldsymbol{\lambda} \overset{!}{=} \mathbf{0}, \tag{3.36}$$

$$\left(\frac{\partial \mathcal{L}}{\partial \boldsymbol{\lambda}} \right) = \mathbf{R}_f^T \tilde{\mathbf{f}}_2 - \mathbf{m} \overset{!}{=} \mathbf{0}, \tag{3.37}$$

where (3.37) is basically enforcing the constraints. Equation (3.36) states that at the optimum, the gradient of $\Phi(\tilde{\mathbf{f}}_2)$ can be expressed as a linear combination of the constraint function gradients. The weights for this linear combination are in $\boldsymbol{\lambda}$. This effectively means that, at the optimum $\tilde{\mathbf{f}}_2$, there is no 'direction' $\Delta \tilde{\mathbf{f}}_2$ that could improve the value of $\Phi(\tilde{\mathbf{f}}_2)$ without changing/violating one of the constraints in $\mathbf{g}(\tilde{\mathbf{f}}_2)$ (see e.g. also [165, pp.603ff] or any standard text on optimization). Using (3.36) to solve for $\tilde{\mathbf{f}}_2 = -\mathbf{W}_f^{-1} \mathbf{R}_f \boldsymbol{\lambda}$ and inserting this in equation (3.37) to solve for the Lagrange multipliers $\boldsymbol{\lambda}$, yields:

$$\boldsymbol{\lambda} = -(\mathbf{R}_f^T \mathbf{W}_f^{-1} \mathbf{R}_f)^{-1} \mathbf{m}, \tag{3.38}$$

which, reinserted in equation (3.36), means for the 'optimal' solution $\tilde{\mathbf{f}}_2$:

$$\tilde{\mathbf{f}}_2 = \underbrace{\mathbf{W}_f^{-1} \mathbf{R}_f (\mathbf{R}_f^T \mathbf{W}_f^{-1} \mathbf{R}_f)^{-1}}_{\mathbf{T}_f^T} \mathbf{m}, \tag{3.39}$$

where $\mathbf{T}_f^T$ is the transformation matrix for transforming a VP load $\mathbf{m}$ to an equivalent $\tilde{\mathbf{f}}_2$ in the force DoFs (which were actually physically measured in $\mathbf{Y}_{22}$). Note that it is easy to verify that this solution $\tilde{\mathbf{f}}_2$ satisfies the constraints (3.34). The above transformation matrix can also directly be seen as a right Moore-Penrose pseudoinverse as used in [158]. Effectively, the weighting matrix could be used to 'penalize' impact positions which were e.g. not as trustworthy as the others (e.g. due to bad coherences there or hard to reach points on the structure). Penalizing means in this context, that these entries in $\tilde{\mathbf{f}}_2$ for representing a given $\mathbf{m}$ should be small. In order to do this one could choose $\mathbf{W}_f$ to be a diagonal identity matrix apart from numbers *larger* than 1 on the diagonal entry for the force inputs which are not trusted as much. Note that this is in contrast to the displacement transformation were a *lower* number than 1 should be chosen for the untrusted measurement channels. More possible choices for defining the force weighting matrix can be found in [60].

3.3.3 Virtual point transformation as a weakening of compatibility

In the last subsection, the transformation matrices for projecting the interface DoFs $\mathbf{u}_2, \mathbf{f}_2$ on the generalized DoFs $\mathbf{q}, \mathbf{m}$ were derived. Substructure A's full admittance matrix $\mathbf{Y}^A$ may thus be transformed to virtual point DoF on the interface without changing the internal DoF:

---

[6]A great resource for getting an intuitive understanding of constrained optimization with the concept of a Lagrangian function is the 50 minute lecture from the MIT open course ware by Auroux [8].

$$\tilde{\mathbf{Y}}^A = \begin{bmatrix} \mathbf{Y}_{11}^A & \mathbf{Y}_{1m}^A \\ \mathbf{Y}_{q1}^A & \mathbf{Y}_{qm}^A \end{bmatrix} = \begin{bmatrix} \mathbf{I} & \mathbf{0} \\ \mathbf{0} & \mathbf{T}_u^A \end{bmatrix} \begin{bmatrix} \mathbf{Y}_{11}^A & \mathbf{Y}_{12}^A \\ \mathbf{Y}_{21}^A & \mathbf{Y}_{22}^A \end{bmatrix} \begin{bmatrix} \mathbf{I} & \mathbf{0} \\ \mathbf{0} & (\mathbf{T}_f^A)^T \end{bmatrix}, \tag{3.40}$$

where $\tilde{\mathbf{Y}}^A$ denotes the transformed substructure matrix. An analogous expression would yield $\tilde{\mathbf{Y}}^B$, the transformed admittance matrix of substructure B. The two transformed matrices can directly be coupled to each other, as shown in section 3.1.2. The rigid modes on both sides were created with the virtual points being in the same position, so the generalized DoFs on either side of the interface are matching:

$$\tilde{\mathbf{Y}}^{AB} = \tilde{\mathbf{Y}}^{A|B} - \tilde{\mathbf{Y}}^{A|B}\mathbf{B}^T \left(\mathbf{B}\tilde{\mathbf{Y}}^{A|B}\mathbf{B}^T \right)^{-1} \mathbf{B}\tilde{\mathbf{Y}}^{A|B},$$

$$\text{where} \qquad \tilde{\mathbf{Y}}^{A|B} = \begin{bmatrix} \tilde{\mathbf{Y}}^A & \mathbf{0} \\ \mathbf{0} & \tilde{\mathbf{Y}}^B \end{bmatrix}. \tag{3.41}$$

This is generally what is done when coupling with experimental substructures in this thesis. It will now be shown that coupling the virtual point transformed matrices of A and B corresponds to a weakening of the interface compatibility condition.

Assume the non-transformed (i. e. measured) admittance matrices, written in block diagonal form $\mathbf{Y}^{A|B}$ as in (3.20) shall be coupled. However, compatibility is only enforced in directions of the generalized DoFs $\mathbf{q}$ and reaction forces are only the generalized forces $\mathbf{m}$:

$$\mathbf{Y}^{A|B} \underbrace{(\mathbf{f} + \mathbf{B}_f^T\boldsymbol{\lambda})}_{=\mathbf{g}} = \mathbf{u}, \qquad \text{where} \quad \mathbf{B}_f = \begin{bmatrix} \mathbf{0} & \mathbf{T}_f^A & -\mathbf{T}_f^B & \mathbf{0} \end{bmatrix}, \tag{3.42}$$

$$\mathbf{B}_u\mathbf{u} = \mathbf{0}, \qquad \text{where} \quad \mathbf{B}_u = \begin{bmatrix} \mathbf{0} & \mathbf{T}_u^A & -\mathbf{T}_u^B & \mathbf{0} \end{bmatrix}. \tag{3.43}$$

Inserting (3.42) in (3.43) yields[7]:

$$\boldsymbol{\lambda} = - \underbrace{\left(\mathbf{B}_u\mathbf{Y}^{A|B}\mathbf{B}_f^T \right)^{-1}}_{Z_{int}} \underbrace{\mathbf{B}_u\mathbf{Y}^{A|B}\mathbf{f}}_{\Delta\mathbf{q}} \tag{3.44}$$

$$= - \underbrace{\left(\mathbf{Y}_{qm}^A + \mathbf{Y}_{qm}^B \right)^{-1}}_{Z_{int}} \underbrace{\begin{bmatrix} \mathbf{0} & \mathbf{T}_u^A & -\mathbf{T}_u^B & \mathbf{0} \end{bmatrix}}_{=\mathbf{B}_u} \mathbf{Y}^{A|B}\mathbf{f}$$

Reinserting $\boldsymbol{\lambda}$ in (3.42) yields the 'weakly coupled' admittance $\mathbf{Y}_{weak}^{AB}$:

$$\underbrace{\left(\mathbf{Y}^{A|B} - \mathbf{Y}^{A|B}\mathbf{B}_f^T \left(\mathbf{B}_u\mathbf{Y}^{A|B}\mathbf{B}_f^T \right)^{-1} \mathbf{B}_u\mathbf{Y}^{A|B} \right)}_{\mathbf{Y}_{weak}^{AB}} \mathbf{f} = \mathbf{u}. \tag{3.45}$$

Notice that $\mathbf{Y}_{weak}^{AB}$ has the same size as the non-transformed block matrix $\mathbf{Y}^{A|B}$. However, as opposed to $\mathbf{Y}^{AB}$ in (3.10), when writing down $\mathbf{Y}_{weak}^{AB}$ in the verbose 4×4 block matrix notation (shown in section 3.2.1) we would notice that the second and third row are not identical. This means that the displacements $\mathbf{u}_2^B$ and $\mathbf{u}_2^A$ are not perfectly coupled, but remain uncoupled

---

[7]Notice that the matrices $\mathbf{B}_u$ and $\mathbf{B}_f$ for requiring compatibility and equilibrium are not 'signed boolean' anymore now. This makes the naming 'B-matrix' somewhat meaningless, but this notation is so common that it will be kept.

in the residual directions of the transformation μ. Inserting (3.28) in (3.25), we can write for the interface residuals μ:

$$\mu = (\mathbf{I} - \mathbf{R}_u \mathbf{T}_u)\, \mathbf{u}_2. \tag{3.46}$$

These 'residual motions' μ may be present on either side of the interface as a part of the real motion $\mathbf{u}_2 = \mathbf{R_u q} + \mu$. However, when transforming the residual parts μ in (3.46) on the IDMs, we see that of course $\mathbf{T}_u \mu = \mathbf{0}$. When looking at the last part of (3.44), this means that the residual motions on either side are not producing any reaction force $\boldsymbol{\lambda}$ and are thus remaining uncoupled.

This weakly coupled $\mathbf{Y}^{AB}_{weak}$ may then be transformed to the generalized DoFs via:

$$\tilde{\mathbf{Y}}^{AB} = \begin{bmatrix} \mathbf{I} & \mathbf{0} & \mathbf{0} & \mathbf{0} \\ \mathbf{0} & \mathbf{T}_u^A & \mathbf{0} & \mathbf{0} \\ \mathbf{0} & \mathbf{0} & \mathbf{T}_u^B & \mathbf{0} \\ \mathbf{0} & \mathbf{0} & \mathbf{0} & \mathbf{I} \end{bmatrix} \mathbf{Y}^{AB}_{weak} \begin{bmatrix} \mathbf{I} & \mathbf{0} & \mathbf{0} & \mathbf{0} \\ \mathbf{0} & (\mathbf{T}_f^A)^T & \mathbf{0} & \mathbf{0} \\ \mathbf{0} & \mathbf{0} & (\mathbf{T}_f^B)^T & \mathbf{0} \\ \mathbf{0} & \mathbf{0} & \mathbf{0} & \mathbf{I} \end{bmatrix}, \tag{3.47}$$

which can be verified to be the same matrix $\tilde{\mathbf{Y}}^{AB}$ from equation (3.41). This result is pointing out two important assumptions when two virtual point transformed admittances are coupled:

- Substructures are left uncoupled in the directions not contained in the IDMs.

- All important motion is contained in the IDMs and thus external excitations and motions in directions not contained in the IDMs are negligible or not of special interest.

The result of (3.45) can also be used to purposely couple two substructures only in specific directions or modes, while leaving their full set of DoFs in the resulting model (e.g. for structures containing relatively loose joints in certain directions). In fact, this is an important insight for understanding how to couple e.g. gyroscopic effects. These can be important for substructures with internally rotating parts, while their FRFS were measured in an idle state (like e.g. the climate compressor). The gyroscopic effects are coupled to only the directions that are actually tilting the rotation axis (this will be explained in chapter 5).

The findings of past publications, such as '*that the lack of RDOF data underestimates in frequency the correct predictions [of the coupled system resonances, M.H.].*' [36], can be clearly attributed to the weakening effect on the interface compatibility when leaving out the rotational IDMs.

Mayes and Allen have clearly shown in [4, 103] that solving the compatibility condition in experimental substructuring only in a least squares way (called 'MCFS' in these publications), can dramatrically improve the results. This is also an encouraging result for the coupling of substructures in a 'weak' manner as in the projection developed in [86, 155, 158] and described here.

3.4 Error checks for accurate experimental substructure models

The VPT yields experimental substructure models that are compatible with other structures on the interface. Thus, for coupling them, it does not matter if these structures are obtained from experiments or from numerical/analytical modeling. However, it is crucially important to check the quality and physical validity of each model before coupling them via FBS. The
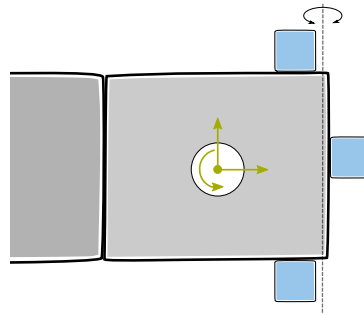
Figure 3.8: Example of bad sensor placement. Sensors are close to a common line through their center points. Rotations around this axis can barely be observed and random measurement noise in the sensor channels is amplified.

measurements have to be conducted with great care. E.g. in [20] it is shown that a wrong positioning of 35mm or a wrong orientation of $15°$ will change the FRF from source to microphones in the vehicle by roughly 5dB. In section 2.6, some checks that should be performed on pure FRF measurements were already proposed. After performing the VPT of the experimental models, there are additional valuable checks for obtaining most accurate experimental models. These shall be mentioned here.

3.4.1 Observability of interface displacement modes

Especially when applying the VPT for the first time, it is a common error that the sensors and impact positions are not setup correctly in order to observe and excite all rigid motion on the interface. If three triaxial acceleration sensors are placed on the interface (nine DoFs) it is still possible that the observability of the rigid motions is bad, e.g. if the sensors all lie close to a straight line through their centers (see figure 3.8). The problem in this case is that a rigid rotation around this line/axis would result in almost no signal in the sensor channels. This direction may thus be severely contaminated by measurement noise. Also small positioning errors of the sensors would cause large bias errors in the estimated rotation around this axis. The same is true for the force application points. They must be able to excite all rigid interface modes without the need for extremely high forces to excite specific rigid body loads. A quick and handy check is the condition number of the IDM matrices $\mathbf{R}_u$ and $\mathbf{R}_f$. In the case that one direction cannot be observed or excited properly, the resulting condition number in the corresponding IDM matrix would be very high. As a rule of thumb, it turned out that the condition number of the IDM matrix should be below 1000 in any case[8]. Otherwise one should rethink the positioning of sensors and impacts. In case of a good distribution of sensors and forces around the virtual point, the condition number of the IDM matrices should be in the order of 100 or below. Consider e.g. the rigid cross already discussed in section 2.7.3 (see figure 3.9 for the applied sensors and force input points). It was specifically designed, so that the sensors and impacts can observe and excite all rigid motion very well. As a result, the condition numbers of the IDM matrices are comparably low, $cond(\mathbf{R}_u) = 18.6$ and $cond(\mathbf{R}_f) = 26.6$.

---

[8](All guidelines here for measuring displacements in meter and rotations in radians)
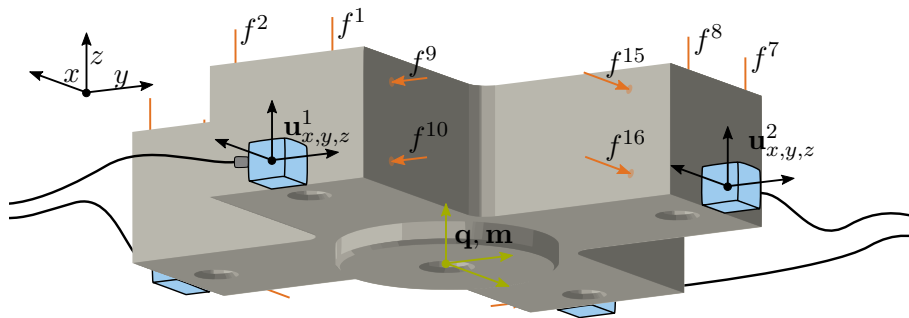
Figure 3.9: Rigid cross with measured sensor accelerations $\mathbf{u}$, applied hammer impacts $\mathbf{f}$, transformed rigid body DoF $\mathbf{q}$ and forces and moments $\mathbf{m}$ around virtual point (indicated as green point).

3.4.2 Noisy channels effect on the virtual point transformation

As mentioned in in section 2.7.3, before performing the measurement, one should also check the noise level in the single sensor channels. During impact measurements on the cross in figure 3.9, it was found that the noise in one sensor channel was around $50dB$ higher than for all others. Interchanging cables and connectors on the data acquisition system led to the conclusion that it was actually an issue in one channel on the sensor. The FRFs measured with this sensor channel reflected the significantly higher noise level. In figure 3.10a, two different FRFs that should be equal (due to symmetry of the cross) are compared: one measured with the noisy channel and the other with an intact sensor[9]. Due to over determination of the VPT (12 sensor channels transformed to only 6 rigid DoF), it was not necessary to keep the defect sensor channel in the transformation. In this case, it is recommended to take this channel completely out of the transformation (deleting the corresponding row from $\mathbf{Y}_{uf}$ and $\mathbf{R}_u$). The result of a virtual point transformed FRF which is particularly influenced by the response in the noisy channel is shown in figure 3.10b, once for keeping and once for neglecting the broken sensor channel. The condition number of the sensor IDM matrix $\mathbf{R}_u$ did only deteriorate slightly by neglecting the data measured with this channel, hence throwing this sensor out of the transformation was possible. Otherwise, it would have been an option to put a lower weight on the diagonal weighting matrix $\mathbf{W}_u$ for this sensor channel. One can also observe the 'smoothing' effect that the VPT inherently has on the data, even when keeping the broken sensor channel in the transformation (compare the 'noisiness' of the purely measured FRF in figure 3.10a to the virtual point transformed FRF in figure 3.10b).

3.4.3 Consistency of the transformation

Even with perfect observability of all rigid IDMs on the interface and low noise in all channels, it is still possible that the transformation is not valid, since e.g. the interface simply does not behave rigidly over the whole frequency range. Therefore, one should check the consistency of the transformation, as defined in [158]. A filter matrix $\mathbf{F}_u$ that filters out all motions not contained in the reduced basis $\mathbf{R}_u$, and a filter matrix $\mathbf{F}_f$ that filters out all excitations not contained in the reduced basis $\mathbf{R}_f$, is defined:

---

[9]This measurement was performed on an assembly of two crosses with a rubber bearing in between (see figure 4.1). Hence, the FRF matrices are not just flat lines as would be expected for a freely hung up cross which is just a rigid body. But this does not matter for the point being made here about good experimental models.
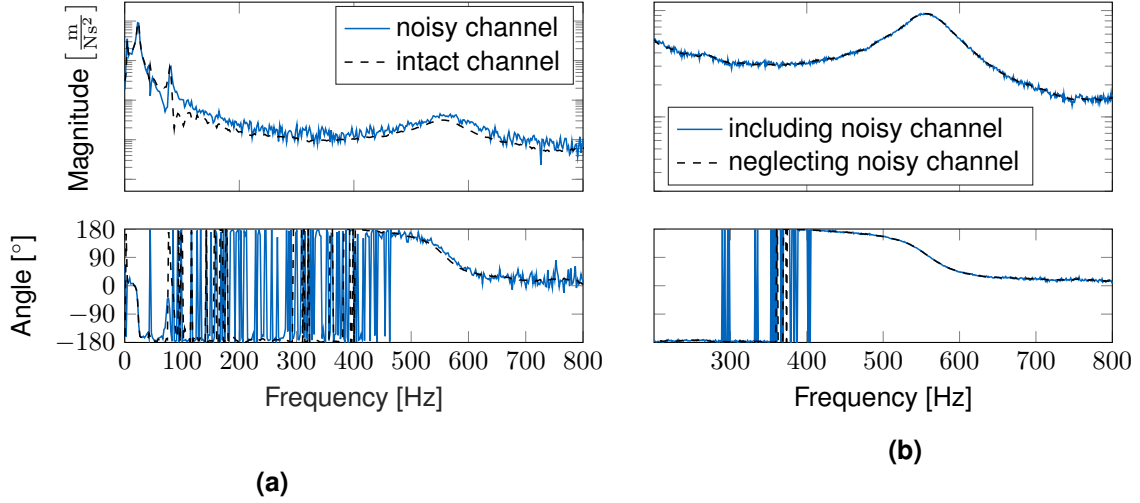
Figure 3.10: (a) FRF measured with a noisy channel compared to intact channel. (b) Virtual point transformed FRF for a rotational DoF which is particularly affected by the noisy channel. Once for keeping the broken sensor channel in the transformation and once for neglecting the data measured with it.

$$\tilde{\mathbf{u}} = \mathbf{R}_u\mathbf{q} = \underbrace{\mathbf{R}_u\mathbf{T}_u}_{=\mathbf{F}_u}\mathbf{u}, \qquad \tilde{\mathbf{f}} = \mathbf{T}_f^T\mathbf{m} = \underbrace{\mathbf{T}_f^T\mathbf{R}_f^T}_{=\mathbf{F}_f^T}\mathbf{f}, \qquad (3.48)$$

where $\tilde{\mathbf{u}}$ and $\tilde{\mathbf{f}}$ represent the filtered motions and forces respectively. If the interface was indeed perfectly rigid, then the mesured FRF matrix would be invariant to these filtering operations, i.e. filtering out the non-rigid motion of $\mathbf{u}$ would not change the vector, since it does not contain any non-rigid motion anyway ($\mu = \mathbf{0}$ in equation (3.25)). Also the response to a force vector $\mathbf{f}$ would be the same as to the filtered force vector $\tilde{\mathbf{f}}$. The forces $\tilde{\mathbf{f}}$ might differ in their individual entries of single forces from $\mathbf{f}$, but are effectively applying the same load to the virtual point in the reduced basis as $\mathbf{f}$ does (same forces and moments in case of a rigid interface). To check the consistency of the sensor transformation one can therefore check if:

$$\text{Sensor consistency:} \qquad \tilde{\mathbf{Y}} = \mathbf{F}_u\mathbf{Y} \qquad \overset{?}{=} \mathbf{Y}, \qquad (3.49)$$

$$\text{Impact consistency:} \qquad \tilde{\mathbf{Y}} = \mathbf{Y}\mathbf{F}_f^T \qquad \overset{?}{=} \mathbf{Y}. \qquad (3.50)$$

These checks are best performed by defining coherence-like functions that allow to compare the similarity of two complex numbers (the filtered and unfiltered entries of the FRF matrix). The coherence-like functions yield a value of 1 for perfect equality of the two numbers and a value close to 0 if they are very different. Two of many possible choices for comparing two complex numbers a and b are:

$$coh_\theta(a,b) = \frac{(a+b)(a^*+b^*)}{2(aa^*+bb^*)}, \qquad (3.51)$$

$$coh_A(a,b) = 1 - \frac{(||a|| - ||b||)^2}{||a||^2 + ||b||^2} = \frac{2||a||\,||b||}{||a||^2 + ||b||^2}, \qquad (3.52)$$
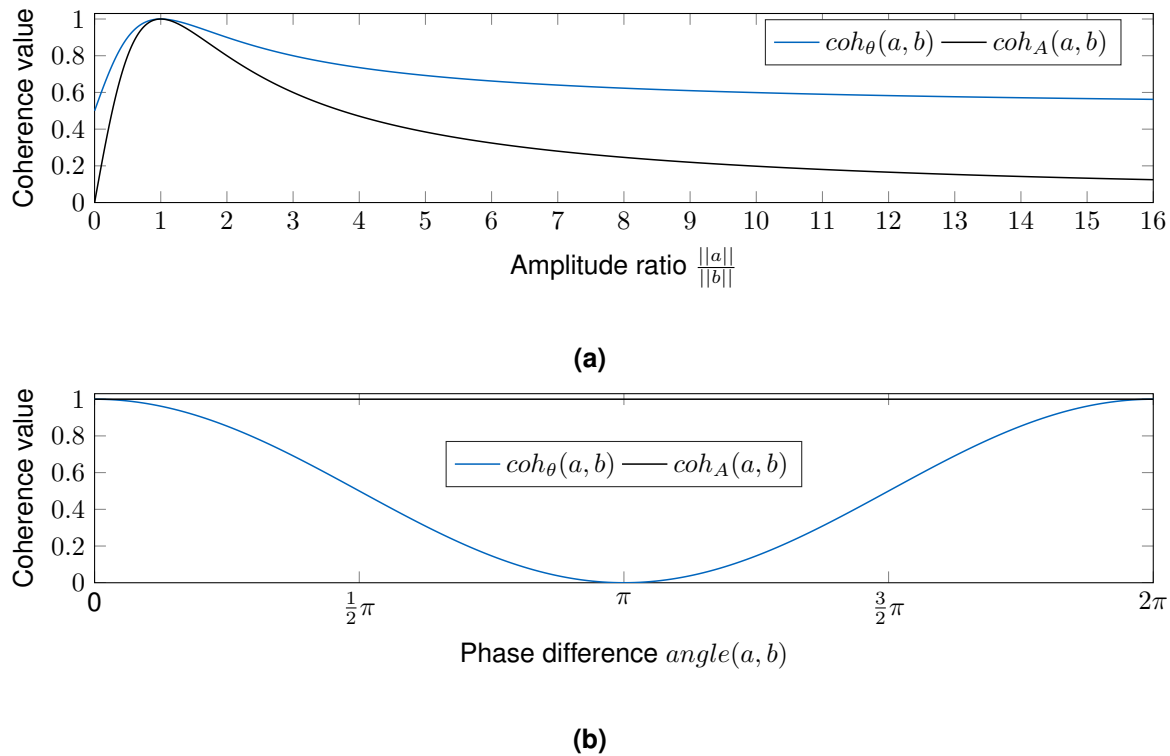
(a)

(b)

Figure 3.11: Depiction of the defined coherence functions for comparing the similarity of two complex numbers a and b. (a) Differnces in complex amplitude between a and b. (b) Differences in phase angle between a and b.

where coh_θ is the coherence-like function already defined in [157, 158]. It is more sensitive to phase differences. The coherence-like function coh_A is a bit more sensitive to differences in amplitude between the numbers a and b. The behavior of these functions for differences in angle and amplitude of a and b can be seen in figure 3.11.

Each of these functions can then be choosen to depict the consisteny of the sensor and impact transformation,

$$consist_\theta(\tilde{Y}_{ij}, Y_{ij}) = coh_\theta(\tilde{Y}_{ij}, Y_{ij}), \qquad consist_A(\tilde{Y}_{ij}, Y_{ij}) = coh_A(\tilde{Y}_{ij}, Y_{ij}), \tag{3.53}$$

Sensor consistency: $\tilde{\mathbf{Y}} = \mathbf{F}_u \mathbf{Y}$, $\tag{3.54}$

Impact consistency: $\tilde{\mathbf{Y}} = \mathbf{Y} \mathbf{F}_u^T$. $\tag{3.55}$

These can then be checked over the whole frequency range for individual FRF matrix entries Y_{ij} or averaged over the frequency range of interest and plotted in a tile-like overview plot for all matrix entries. In figure 3.12a, the sensor consistency of a single entry Y_{ij} from the measured FRF matrix on the freely hung-up cross (figure 3.9) is shown. It can be seen that the consistency is good until around 2000 Hz. In this case, this is not a problem since the frequency range of interest was only up to 2000 Hz and it was well known that the first flexible mode of the cross would be in the region of 4600 Hz. It is also important to have some engineering judgment while checking these consistency functions. E.g. FRF matrix entries where the applied force simply does not excite the specific sensor channel will not only show a poor coherence γ^2, but also a poor consistency of the VP transformation. This is not a problem. Also drops in the consistency close to anti-resonances are rather natural. Low consistencies over the whole frequency range for one sensor channel, and consistencies
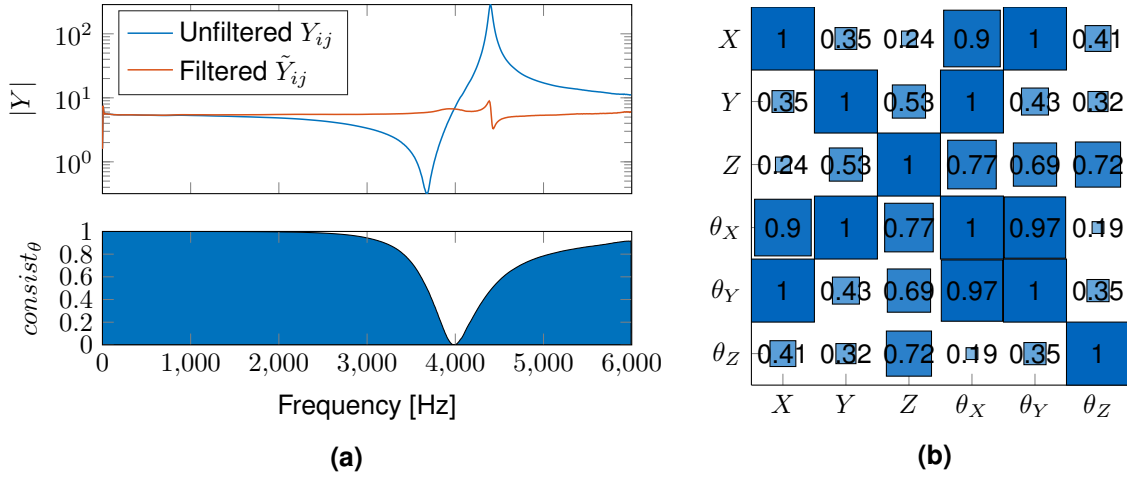
Figure 3.12: (a) Consistency of the VPT of one FRF measurement on the rigid crosses (input f_1 and output z-direction of adjacent sensor, see figure 3.9). (b) Symmetry $symm_\theta(Y_{ij}, Y_{ji})$ of virtual point transformed FRF matrix of rigid cross. Averaged over the frequency range 0-2000Hz.

that never quite reach the value 1 for all other sensor channels on the same virtual point, usually mean that the position or orientation of this sensor channel is not fitting the assumed position and orientation used for constructing $\mathbf{R}_u$. Looking at the plausibility of an operational deflection shape animation helps fixing these issues.

3.4.4 Symmetry of FRF matrix

Interchanging the output DoF i and input DoF j on an FRF matrix yields the same FRF, i.e. $Y_{ij} = Y_{ij}$. This is also known as 'reciprocity' principle and can directly be seen from equation (2.30) for the synthesis of an FRF matrix entry. For usual FRF measurements this is not really a valid check, since the inputs and outputs (i.e. hammer impact and sensor positions) are typically not all in the same position and directions so they do not really represent the same DoF (see figure 3.5). After performing the VPT however, the transformed matrices give the relation between virtual point inputs and outputs defined around the same point and in the same directions. They should thus be symmetric. This symmetry can be tested with the coherence functions defined above,

$$symm_\theta(Y_{ij}, Y_{ji}) = coh_\theta(Y_{ij}, Y_{ji}), \qquad symm_A(Y_{ij}, Y_{ji}) = coh_A(Y_{ij}, Y_{ji}), \tag{3.56}$$

This frequency dependent value for the symmetry can then be averaged over the frequency range of interest and plotted in a tile plot for each entry of the transformed FRF matrix. In figure 3.12b, the symmetry for the virtual point transformed experimental FRF of the rigid cross is shown. Note that, at first sight, it looks like the symmetry is bad for many entries, but in fact most of the rigid body DoF on this cross are uncoupled from each other. E.g. a force in z-direction (see figure 3.9) would cause only a response acceleration in z-direction. The x- and y -translation and all rotations should be zero, and are mostly noise and thus comparatively low in magnitude. The only directions which are coupled for the free cross is the x-translation and the rotation θ_y, as well as y-translation and the rotation θ_x, since the center of gravity C of the cross does not correspond to the virtual point Q (see figure 2.7a). These entries show almost perfect symmetry in figure 3.12b and thus this model would be considered valid. Note that one could also force symmetry on the transformed matrix by

$\mathbf{Y}_{sym} = \mathbf{Y}^T + \mathbf{Y}$. But to the authors experience this does not improve any results, and one should rather try to obtain a symmetric matrix by performing a good measurement.

3.4.5 Passivity of FRF matrix

Another property that the virtual point transformed FRF matrix should fulfill is passivity. A passive structure without any internal energy sources must only dissipate energy and not produce any. The phase requirements for driving point FRFs were already discussed in section 2.6.2. However, the right phase relations on driving point FRF matrix entries are not sufficient for assuring that the structure behaves passive. The principal requirement is that the power input to a passive system must always be positive, i.e. there can be no net power output from the system. This can be expressed in the frequency domain as: The real part of *any* external input force $\mathbf{m}$ times the velocity $\dot{\mathbf{q}}$ resulting from it must be positive (scalar product). Assuming we have a mobility FRF matrix, i.e. the velocity as output, one can say that for a passive system:[10]

$$Real\left(\mathbf{m}^*\,\dot{\mathbf{q}}\right) = Real\left(\mathbf{m}^*\,\mathbf{Y}_{\dot{q}m}(\omega)\,\mathbf{m}\right) \geq 0 \qquad \forall \omega, \mathbf{m}, \tag{3.57}$$

where $(\star)^*$ indicates the hermitian, and $\mathbf{Y}_{\dot{q}m}$ represents the virtual point transformed, interface FRF matrix in mobility format. Note that this requirement can be violated even if the passivity requirements on the driving points are fulfilled. The topic of FRF matrices passivity has had some attention in the past. Especially with respect to Substructuring. E.g. in [164] the authors give a good discussion about the passivity requirement for a **symmetric** FRF matrix. They show that for passivity, the real part of the mobility FRF matrix needs to be positive definite, which would translate to corresponding requirements for receptance and accelerance. Also in [24], this requirement is shown for symmetric FRF matrices with modal damping. Ín [24], the authors propose to perform an eigenvalue decomposition on the real part of the FRF matrix and then replace all the negative eigenvalues (the ones associated with the negative damping) by zero. Here it is tried to not limit the property to symmetric matrices since, as we have seen in the previous subsection, the resulting matrices from the virtual point transformation are in general not perfectly symmetric. In [96], the authors show that experimental modal analysis (EMA) methods, which are pure curve fitting tools, also fit measurement errors and thus produce slightly non-passive estimates for the modal properties (eigenvalues and eigenvectors). They propose an elegant method for a minimal correction of mode shape vector entries, so that the passivity of the main diagonal entries Y_{ii} in equation (2.30) is valid again (see section 2.6.2). One of the goals with the VPT is to save the extra step of an EMA, in order to be applicable to complex structures without clear modal behavior. Hence, the following discussion is included in this thesis.

Passivity from the SVD

In order for the passivity requirement in (3.57) to hold, it is useful to look at the singular value decomposition of the virtual point mobility matrix:

$$\mathbf{Y}_{\dot{q}m} = \mathbf{U}\boldsymbol{\Sigma}\mathbf{V}^*, \qquad \text{where} \quad \mathbf{U}, \mathbf{V} \in \mathbb{C}^{n_q \times n_q}, \quad \boldsymbol{\Sigma} \in \mathbb{R}^{n_q \times n_q}. \tag{3.58}$$

where n_q is the number of VP interface DoF. The left and right singular vector matrices $\mathbf{U}$ and $\mathbf{V}$ are complex unitary matrices (i.e. their column vectors are orthogonal to each other

---

[10]These definitions are well known in electrical engineering. The real part is called active or "real" power (really consumed by the device). The imaginary part is called the "complex" or reactive power (cyclically absorbed and released by the device).

and have unit length). Notice that it was *not* assumed that the virtual point matrix $\mathbf{Y}_{\dot{q}m}$ is symmetric. This is generally not the case for experimental FRF matrices after VPT (see e.g. figure 3.12b), so $\mathbf{U} \neq \mathbf{V}$. The singular values from the SVD, σ_i in $\mathbf{\Sigma}$, are always *positive* real [51, p. 80]. Any input force vector $\mathbf{m}$ can be expressed with the complete basis $\mathbf{V}$, i.e. as a combination of the unit basis vectors $\mathbf{v}_i$. So it is sufficient to show passivity for each input vectors $\mathbf{v}_i$. Assume a force $\mathbf{m} = \mathbf{v}_i$ is applied, then:

$$\mathbf{Y}_{\dot{q}m}\mathbf{v}_i = \mathbf{U}\mathbf{\Sigma}\mathbf{V}^*\mathbf{v}_i = \mathbf{u}_i\sigma_i. \tag{3.59}$$

All singular values σ_i are positive. So for satisfying the general statement of passivity in equation (3.57) for any possible $\mathbf{m}$, it needs to hold that:

$$Real\left(\mathbf{v}_i^* \, \mathbf{u}_i\right) \geq 0 \qquad \forall i = 1, ..., n_q. \tag{3.60}$$

The criterion holds for all mobility FRF matrices, but can be generalized to the other representations as before:

$$\angle\left(\mathbf{v}_i^* \, \mathbf{u}_i\right) \begin{cases} \in [-180°, 0°] & \text{for an admittance/receptance FRF} \\ \in [-90°, 90°] & \text{for a mobility FRF} \\ \in [0°, 180°] & \text{for an accelerance FRF} \end{cases} \qquad \forall i, \tag{3.61}$$

Passivity from real part of mobility matrix

One can also play with the general formulation of equation (3.57). For any complex number a, one can say that:

$$Real(a) = \frac{1}{2}Real(a + a^*), \tag{3.62}$$

which means for the condition in (3.57):

$$\begin{aligned} 0 \leq \quad & Real\left(\mathbf{m}^* \, \mathbf{Y}_{\dot{q}m} \, \mathbf{m}\right) \\ = & \frac{1}{2}Real\left(\mathbf{m}^* \, \mathbf{Y}_{\dot{q}m} \, \mathbf{m} + \mathbf{m}^*\mathbf{Y}_{\dot{q}m}^* \, \mathbf{m}\right) \\ = & \frac{1}{2}Real\left(\mathbf{m}^* \, \left(\mathbf{Y}_{\dot{q}m} + \mathbf{Y}_{\dot{q}m}^*\right) \, \mathbf{m}\right). \end{aligned} \tag{3.63}$$

Now one needs to verify that the matrix $\left(\mathbf{Y}_{\dot{q}m} + \mathbf{Y}_{\dot{q}m}^*\right)$ is positive definite, which is easy to verify since it is Hermitian. One could check if all eigenvalues are positive, or one could look at the LU-factorization and check if there are any negative pivots occuring (this maybe more effective numerically).

Chapter 4

Experimental rubber element models

Contents:

> Research is like looking for the needle in a haystack. But sometimes while searching the needle, you will find the handsome daughter of the farmer. Then you do some math to prove it was clear from the beginning that it would work.
>
> *Prof. Wolfgang A. Wall,*
> *during a FEM lecture*

The contents of this chapter were published in similar form in [54]. The text hereafter has been modified and adapted to the thesis.

A crucial part of this project was the development of sufficiently accurate dynamic models for rubber mounts, since most of the isolation concepts for the structure borne sound were based on them. Unfortunately, commercial off-the-shelf rubber isolators often come with no additional information other than the *static* stiffness in three translational directions. Hydraulic testing machines can be used to obtain frequency dependent *dynamic* stiffnesses of rubber isolators in translational DoF. Alternatively, DS based methods can be used, which can additionally identify the dynamic stiffness in rotational DoF while requiring only standard vibration testing equipment. In this chapter, results of two substructuring methods will be compared to those from a hydraulic machine. Both of the presented methods use the rigid crosses, already presented in section 2.7.3 and section 3.4, mounted to the bottom and top

of the isolators. *Frequency based substructuring* (FBS) requires knowing the fixtures dynamics to decouple them. *Inverse substructuring*, also called *in-situ decoupling*, does not require knowing the fixtures dynamics, but is assuming negligible mass and a special stiffness matrix topology of the rubber isolator. Both methods produce accurate results for translational DoF up to the kilo Hertz range, which is confirmed by comparison to measurements on the hydraulic machine. However, FBS does not rely on specific assumptions about the isolator, like inverse substructuring. The limits of inverse substructuring's underlying assumptions are shown theoretically and in the measurements presented here. We propose two extensions to compensate for the assumptions and present their results. However, FBS seems to be more appropriate for including the identified rubber element models in a larger substructured assembly. The advantage of FBS over inverse Substructuring is also confirmed in this chapter, with a small example. The experimental rubber element models, obtained with either method, are tested in a substructuring prediction of a coupled frequency response function (FRF) which is compared to reference measurements. Therefore, the FBS based rubber models will be used for the applications shown in chapter 11 and 12.

4.1   Review of rubber dynamics and outline of the chapter

Optimizing the vibration behavior of a mechanical system frequently requires knowledge about rubber isolators' dynamic properties. They have thus been the subject of many studies over the past years. The following discussion gives an overview of the dynamic properties of rubber, the goal of the methdods presented in this chapter, and how it relates to existing work in the field.

4.1.1   Dynamic behavior of rubber isolators

The vibration stiffness of rubber isolators depends on many different factors, such as static preload [1], temperature [52, 76, 151], vibration frequency [35, 80, 88, 184] and vibration amplitude [65, 69, 127, 151].

- **Static Preload:** Changes in dynamic stiffness due to static preload are mainly caused by significant non-linear changes of the isolators geometry, e.g. a stiffening due to increased cross sectional area of the preloaded rubber isolator. From the results of this study and also the results reported in [1], they start affecting the isolator properties if the material strain ε from the static preload exceeds approximately $\varepsilon > 5\%$.

- **Temperature:** The rubber temperature has a significant influence on the dynamic properties of the material, which is mainly caused by the constitutive change from the "rubber region" to the "glassy region" in the material, see e.g. [76, 151].

- **Frequency:** With varying excitation frequency ω, a rubber isolator also changes its stiffness [1, 35, 80, 88, 184]. Partly, this is due to changes in the material properties, like the complex Youngs modulus. However, this effect seems to be not prominent in the typical frequency range of interest for noise and vibration engineering. E.g. in [88], it was found that the rubber material could well be modeled with frequency independent material parameters (up to about 1000Hz). In [88], the dominant effects changing the isolator stiffness were continuum (anti-) resonances in the rubber geometry (found at about 1200Hz in [88]). See e.g. [1] for a simulation and depiction of the internal resonances in a given rubber isolator element. Especially for frequencies up to the kilo Hertz range these effects are important to consider.

- **Amplitude:** The overall vibration amplitude in the time domain is changing the dynamic stiffness of rubber isolator elements [65, 69, 127, 151]. Rubber generally behaves stiffer if the maximum transient displacement in time is small. For example, in a harmonic shaker test with only one excitation frequency ω and a vibration amplitude A, the overall transient vibration in time is smaller than for a superposition of multiple excitation frequencies which still contain the single excitation at frequency ω with amplitude A. E.g. in case of an impact or many excitation orders of a motor, the maximum vibration amplitude in time is higher, and the rubber material behaves softer compared to the case where it would be tested with a shaker that is stepping through the single excitation frequencies and amplitudes individually. This "material softening" with higher transient displacements can be attributed to the elastomer molecule chains in the material, which start to unfold from a compact packaging in the undeformed position, to a more flexible structure for large dynamic displacements. For a detailed discussion of this effect see [65].

For modeling the dynamic behavior of rubber isolators with given geometry, many researchers investigated methods for identifying the frequency dependent stiffness and damping (usually represented by a complex modulus) of the rubber material. In [88], the authors compare different formulations for the complex modulus whose parameters are fitted to FRF measurements on a rubber specimen placed between two masses. The results are validated by using the identified modulus in a FE-model of the same setup.

In [1] and [85, section 7.3], the authors follow a similar approach: Experimentally obtained material parameters are used for a non-linear FE-model of the rubber bushing. The FE-model is then subjected to a non-linear preloading step. Subsequently, a harmonic vibration is superimposed on the static preload in a linearized analysis. Thereby, a frequency and preload dependent super-element with six DoF on the upper and lower connection is constructed (i.e. twelve DoF in total).

4.1.2 Goal: experimental identification of rubber isolator models using substructuring

Methods for identifying the material properties, like modulus and loss factor of the rubber, are very valuable if the intent is to model and modify the geometry of the rubber mount for a specific application. However, the goal in this chapter is not to model the material of the rubber, but more globally, to identify the dynamic properties of readily available isolator elements with different materials and geometries. Since, in general, the manufacturers do not provide material properties nor CAD models of the isolators, it is often impossible to build trustful numerical models of rubber mounts. Therefore the models in this chapter shall be obtained experimentally. Thereby, one is saving the effort of identifying all material properties and setting up a model for each geometry. This also avoids possible errors due to approximations inherent in numerical models and constitutive laws. The experimental models shall then be used in a larger substructured model, e.g. the suspension concept for vibration sources in a car. The rubber element models should consider effects that depend on the excitation frequency ω, like frequency dependent material properties and internal resonances of the isolators, since the sources contain high frequency excitations, typically seen for example in an electric motor. Another goal of this study was to develop models of the rubber mounts which contain six degrees of freedom on either end of the connection, so that a complete description of the vibration transmission from the source to the receiver is possible. Consider the depiction of a rubber element in figure 4.1c, where $\mathbf{q}_1$ is the vector containing the 6 rigid body motions (3 translations plus 3 rotations) on the upper connection

of the rubber element. The upper connection is indicated by the subscript $(\star)_1$. Likewise, $\mathbf{m}_1$ is a vector containing the three forces and three moments that can be applied at the upper connection. The desired rubber isolator model is determined by the frequency dependent 12×12 dynamic stiffness matrix $\mathbf{Z}^I(\omega)$, that relates the rigid motions to the forces and moments on both connections, $(\star)_1$ & $(\star)_2$:

$$\underbrace{\begin{bmatrix} \mathbf{Z}_{11}^I(\omega) & \mathbf{Z}_{12}^I(\omega) \\ \mathbf{Z}_{21}^I(\omega) & \mathbf{Z}_{22}^I(\omega) \end{bmatrix}}_{\mathbf{Z}^I(\omega)} \begin{bmatrix} \mathbf{q}_1^I(\omega) \\ \mathbf{q}_2^I(\omega) \end{bmatrix} = \begin{bmatrix} \mathbf{m}_1^I(\omega) \\ \mathbf{m}_2^I(\omega) \end{bmatrix} \tag{4.1}$$

where the superscript $(\star)^I$ denotes that the quantity belongs to the "isolator". E.g. $\mathbf{Z}_{21}^I$ is the 6×6 submatrix that relates a motion at the upper connection $\mathbf{q}_1^I$ to the reaction forces and moments at the lower connection, i.e. $\mathbf{m}_2^I = \mathbf{Z}_{21}^I \mathbf{q}_1^I$ for the case that $\mathbf{q}_2^I = \mathbf{0}$. This rubber mount model can then be used for assembling a larger substructured model and allows for testing different noise reduction concepts, e.g. by playing with different combinations of available rubber isolators. The temperature is assumed to be constant, but the method for obtaining the rubber element models described in this chapter can be applied at different temperatures. The tests can also be performed for different transient vibration amplitudes, though this is a little harder to achieve (discussed in the conclusion). For the specific rubber isolators used in this chapter, the expected effects of static preload were not considered to be relevant since the expected material strain ε from the preload was well below 5%.

4.1.3 Existing work on experimental rubber mount models

Some studies (e.g. [32, 97, 189]) investigate the rubber isolators dynamic stiffness only in the axial direction (the vertical direction in figure 4.1c). The authors of [97] for example perform shaker and hammer measurements on a mass sitting on top of the rubber mount. They compare different methods for identifying the complex stiffness of the mount in this single DoF configuration. It is proposed to use a complex stiffness, which is a piecewise frequency dependent polynomial, fitted to the measurement data. Thereby, the entry for the axial direction of the matrix $\mathbf{Z}_{11}^I$ from equation (4.1) is determined.

Verheij in his PhD thesis of 1982 [184, section 2] designed a test rig for obtaining the transfer isolator stiffness $\mathbf{Z}_{21}^I$ in six degrees of freedom. Similar to the methods compared in this chapter, the rubber mount is fitted between two rigid masses whose properties are known. The rubber mount stiffness is then determined from the transmissibility, i.e. the ratio of the accelerations measured on either mass. This approach is an approximation valid for a certain minimum weight of the masses on top and bottom (an analytical error analyis is carried out in [184, section 2]). Additionally, this rubber mount model is only valid for assuming a negligible mass of the rubber mount itself. In [184], also depictions and summaries are given, which show the different terms in the matrix $\mathbf{Z}_{21}^I$ that should be equal or vanish for different standard shapes of rubber isolators (e.g. cylindrical, block rectangular, etc.).

Recently, some research was focused on identifying isolator properties from pure frequency response function (FRF) measurements of an assembly containing the rubber elements [107, 109, 123]. This method is therefore coined *in-situ* identification. The method is mathematically equivalent to (and relies on the same assumptions as) the method developed in [188, 201], where it is called *inverse substructuring*. However, the mathematical developments in [188, 201] are lengthier and arguably more intricate than in [107, 109, 123]. Either way, these methods assume a special topology of the isolator stiffness matrix and negligible mass of the rubber isolators, which is further explained in section 4.3.1 and appendix A. In [78, 94, 111, 112, 135] the same assumptions are used to identify the properties of the

structures connected by the isolators. However, in [78] the equations are reformulated so that only a smaller sub-matrix needs to be inverted, which makes the operation less sensitive to measurement noise.

In [80], a method to identify the full dynamic rubber mount stiffness $\mathbf{Z^I}$ from equation (4.1) was proposed. That method can be understood as a substructure-based decoupling technique using the same assumptions and theoretical basis as the frequency based substructuring (FBS) technique applied in this chapter. Therefore, although the mathematical derivation is done in a much simpler manner in the present chapter, it is to be assumed that both methods are theoretically equivalent. It seems like the method in [80] uses more matrix inversions of measured data than the FBS method presented here, making it potentially more vulnerable to measurement errors. Comparisons to dynamic stiffnesses obtained from a hydraulic testing machine are also shown in [80] and good agreement is found, though some "smoothing" of the frequency dependent stiffness needs to be applied due to detrimental effects of measurement noise. In the formulation of the FBS approach the VPT is used, which inherently applies an overdetermination of many measurements to mitigate random measurement errors. In [80], a minimum number of measurements was used which could explain the need for smoothing there, which we found to be unnecessary over most parts of the frequency range. In addition to the fact that a more systematic and compact explanation of the decoupling technique is proposed, also a comparison to the so-called inverse substructuring approach is given. The comparison includes the theory (section 4.3) and an experimental validation of their appropriateness for substructuring assemblies (section 4.5).

4.1.4   Outline of the chapter

Section 4.2 describes the experimental FRF measurements for obtaining the desired 12×12 matrices as well as the validation measurements on the hyropulse. Section 4.3 describes and compares a FBS approach and an inverse substructuring approach for obtaining rubber isolators dynamic stiffnesses $\mathbf{Z}^I$. The identified stiffnesses are then compared to that obtained from a hydraulic testing machine. Especially, the assumptions underlying inverse substructuring are examined. In section 4.4, we propose some enhancements to the methods for overcoming the shortcomings identified in section 4.3. In section 4.5, the resulting rubber mount models are used for predicting the dynamics of a different assembly, to assess the models' appropriateness for being used in substructuring. The conclusions and recommendations for the use of the rubber models are given in section 4.6.

4.2   Experimental data

This section gives an overview of the performed measurements and introduces the notation used throughout the chapter. This includes the dynamic models of the rubber mounts between two rigid crosses section 4.2.1 and an explanation of the validation measurements performed on a servo hydraulic testing machine (section 4.2.2).

4.2.1   Experimental measurement setup

As hammer impacting directly at the end of a rubber isolator I is practically infeasible, it was attached to two fixtures in the form of crosses, which are assumed to be rigid bodies in the
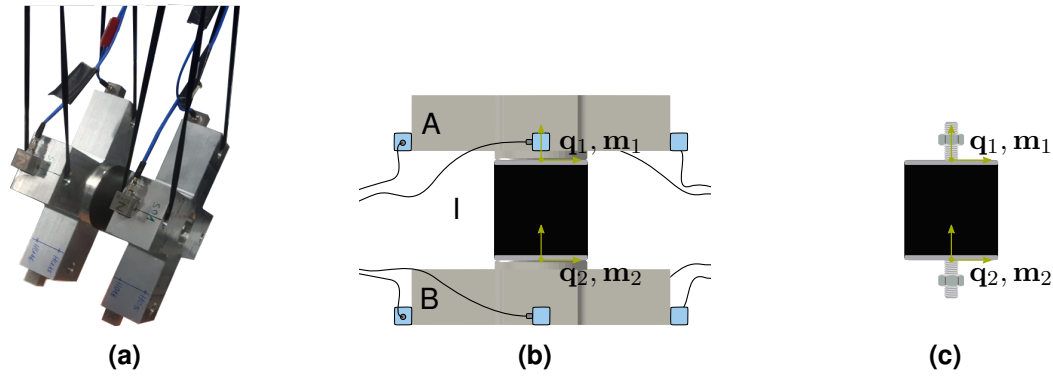
Figure 4.1: (a) Measurement setup: rubber isolator between upper and lower fixture hung up with rubber bands. (b) Schematic: free-free measurement of isolator I between fixtures A and B, resulting in the FRF matrix of the assembled system $\mathbf{Y}^{AIB}$. (c) Admittance $\mathbf{Y}^I$ of the sole rubber isolator which is to be determined. Vectors $\mathbf{q}_1$ and $\mathbf{q}_2$ describe the rigid body responses at the top and bottom of the rubber isolator respectively. Vectors $\mathbf{m}_1$ and $\mathbf{m}_2$ contain the translational and rotational excitations.

frequency range of interest. An upper cross A and a lower cross B, resulting in the assembly AIB (see figure 4.1b).

The crosses were designed so that one can apply hammer impacts that excite all translations and rotations at the connection to the rubber isolator. The sensors are mounted at well-defined positions which can observe all translations and rotations of the cross (cf. figures 4.1a and 3.9). During the impact measurements on the freely suspended assembly AIB (cf. figure 4.1a), 16 points on the upper cross A and 16 points on the lower cross B were excited with hammer impacts (see also figure 3.9). Responses were measured with 4 triaxial accelerometers on either cross, resulting in a 24×32 FRF matrix $\mathbf{Y}_{uf}^{AIB}$, so that

$$\mathbf{u} = \mathbf{Y}_{uf}^{AIB}\, \mathbf{f}, \tag{4.2}$$

where $\mathbf{u}$ indicates the responses in all 24 sensor channels and $\mathbf{f}$ denotes the excitation amplitudes at all impact positions. The rubber temperature during the measurements was $21°$C. Each FRF was estimated from at least 3 averages with an H1-estimator. The DoF on the upper cross will be given the subscript $(\star)_1$ and the ones on the lower cross the subscript $(\star)_2$. The measured FRF is partitioned as:

$$\mathbf{Y}_{uf}^{AIB} = \begin{bmatrix} \mathbf{Y}_{11} & \mathbf{Y}_{12} \\ \mathbf{Y}_{21} & \mathbf{Y}_{22} \end{bmatrix}_{uf}^{AIB}. \tag{4.3}$$

The measured FRF matrix $\mathbf{Y}_{uf}^{AIB}$ is transformed with the VPT (see section 3.3) to $\mathbf{Y}_{qm}^{AIB}$ which relates translational and rotational responses $\mathbf{q}$ to applied loads and moments $\mathbf{m}$,

$$\mathbf{Y}_{qm}^{AIB} = \mathbf{T}_u \mathbf{Y}_{uf}^{AIB} \mathbf{T}_f^T. \tag{4.4}$$

The overdetermination involved in transforming the 24×32 FRF matrix $\mathbf{Y}_{uf}^{AIB}$ to the 12×12 FRF matrix $\mathbf{Y}_{qm}^{AIB}$ helps reducing random measurement and positioning errors, see [158] or figure 3.10. For the rest of the chapter the subscript $(\star)_{qm}$ will be dropped, assuming all DoF are the rigid body motions in the two virtual points.

Analytical model of the crosses

The crosses where designed to behave like a rigid body in the frequency range of interest, which is an important precondition for the validity of the VPT. The crosses dynamics where

	freq. range [Hz]	freq. resolution [Hz]	vibration amplitude [mm]
lower	$3 - 200$	1	0.1
medium	$20 - 400$	10	0.03
higher	$100 - 900$	20	0.01

Table 4.1: Test cycles performed on the rubber isolator with the hydropulse machine.
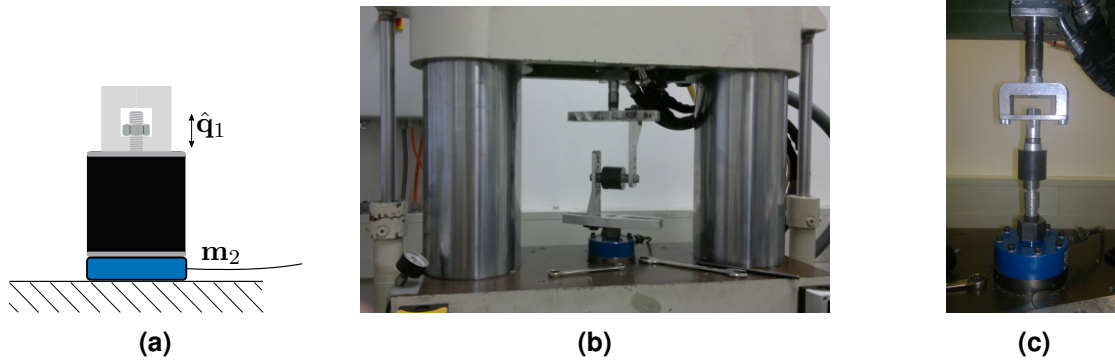

Figure 4.2: Overview of the hydropulse measurements. (a) Measurement principle with controlled vibration $\hat{\mathbf{q}}_1$ on the top and force measurement $\mathbf{m}_2$ at the bottom. This corresponds to measuring single entries in the off-diagonal stiffness matrix $\mathbf{Z}_{21}$. (b) Measurement setup for radial stiffness measurement. (c) Measurement setup for axial stiffness measurement.

modeled by their mass and rotational inertia from the CAD model, and an additional correction for the mass of the sensors (see section 2.7). The rigid body assumption was found to be reasonable up to 2000Hz, as can be seen in the consistency of the VPT that was already shown as an example in figure 3.12a.

4.2.2 Validation measurements on hydropulse

For validation of the two methods, the rubber isolators where tested on a servo hydraulic testing machine, or in short: "hydropulse". The machine controls the vibration amplitude and frequency $\hat{\mathbf{q}}_1$ on the upper connection bolt of the rubber mount, and measures the reaction force $\mathbf{m}_2$ on the lower connection (see figure 4.2a for a schematic depiction of the measurement principle). The controlled vibration amplitude is measured within the hydraulic cylinder at the top of the machine. The fixtures needed for mounting the rubber isolators in the machine are considered to be rigid in the frequency range of interest. If this assumption holds, then the displacement of the upper isolator connection bolt is the same as the one controlled in the hydraulic cylinder. The rubber mount stiffnesses were measured in the axial (z-direction in figure 3.9) and radial direction (since the rubber mount is axis-symmetric, any direction in $x - y$ plane in figure 3.9). The setups for the radial and axial measurements can be seen in figure 4.2b and figure 4.2c respectively. During the measurements, the preload of the rubber isolators can be adjusted, so that the dynamic stiffnesses are measured around this operating point. In all reference measurements shown, the preload was $20N$ (radial and axial). Depending on the frequency range of interest, the vibration amplitude was adjusted. In total, 3 different frequency ranges where tested with stepped sine testing (see table 4.1).

4.3 Substructuring methods for identification of rubber isolator properties

The goal of this section is to introduce the two methods that were investigated for obtaining the dynamic properties of a rubber isolator from the virtual point transformed FRF matrix $\mathbf{Y}^{AIB}$. In section 4.3.1, the specific assumptions for the inverse substructuring method are explained and the results are compared to the hydropulse measurements. In section 4.3.2, these assumptions are tested for validity by comparing them to the results obtained from a decoupling of the crosses (via FBS), which does not rely on any assumptions about the isolator. In section 4.3.3 some general observations regarding the results of the two substructuring approaches are discussed.

4.3.1 Inverse substructuring

The description in this section is following [111]. Assume the dynamic stiffness matrix of the rubber isolator $\mathbf{Z}^I$ shall be coupled to the upper and lower cross, $\mathbf{Z}^A$ and $\mathbf{Z}^B$. This corresponds to the FBS coupling in the primal formulation shown in section 3.1.1, and yields the coupled impedance matrix $\mathbf{Z}^{AIB}$

$$\mathbf{Z}^{AIB} = \begin{bmatrix} \mathbf{Z}_{11}^A + \mathbf{Z}_{11}^I & \mathbf{Z}_{12}^I \\ \mathbf{Z}_{21}^I & \mathbf{Z}_{22}^B + \mathbf{Z}_{22}^I \end{bmatrix}. \tag{4.5}$$

When coupling two substructures via a resilient isolator, the assembled $\mathbf{Z}^{AIB}$ will always have the form of equation (4.5). Experimentally, one can measure the FRF matrix and invert it to obtain the dynamic stiffness of the assembly $\mathbf{Z}^{AIB} = (\mathbf{Y}^{AIB})^{-1}$. Inverse substructuring uses the fact that the off-diagonal terms in (4.5) are a property of the rubber isolator alone:

$$\mathbf{Z}_{21}^{AIB} = \mathbf{Z}_{21}^I, \qquad\qquad \mathbf{Z}_{12}^{AIB} = \mathbf{Z}_{12}^I. \tag{4.6}$$

In the recent publications on the identification of rubber mounts [107, 109, 123], it is assumed that:

$$\mathbf{Z}_{11}^I \approx -\mathbf{Z}_{12}^I \approx -\mathbf{Z}_{21}^I \approx \mathbf{Z}_{22}^I. \tag{4.7}$$

For the identification of the rubber mount, the fully populated 6×6 submatrices $\mathbf{Z}_{12}^I$ or $\mathbf{Z}_{21}^I$ are used to recreate the full 12×12 rubber stiffness matrix $\mathbf{Z}^I$ by placing the off-diagonal submatrices with a negative sign on the main diagonal, for example:

$$\mathbf{Z}^I \approx \begin{bmatrix} -\mathbf{Z}_{12}^I & \mathbf{Z}_{12}^I \\ \mathbf{Z}_{21}^I & -\mathbf{Z}_{21}^I \end{bmatrix} \tag{4.8}$$

This method for modeling the rubber element will be referred to as **inverse substructuring (IS)** model in the validation section 4.5. This method is also known as the in-situ identification as explained earlier. Note that $\mathbf{Z}_{21}$ and $\mathbf{Z}_{12}$ could be used interchangeably, since according to the assumptions underlying inverse substructuring they should be equal[1]. The statement in equation (4.7) is an assumption, and is not generally true for arbitrary numbers of DoF with possible cross couplings on the rubber isolator. Additionally, it is assumed that the joint element (i.e. the rubber mount) has negligible mass. The assumptions underlying this inverse substructuring approach are further elaborated in appendix A. In [107, 109, 123],

---

[1] For the general case without any assumptions, they should be the transposes of each other.
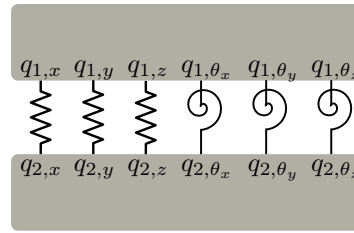
Figure 4.3: Schematic depiction of the assumed "DoF to DoF " topology of the joint elements for the inverse substructuring diagonal (ISD) approach.

this method was used for rubber isolators with a maximum of 2 DoF on either connection point (the axial displacement and one rotation around a radial axis, which would correspond to the displacement in the z direction and e.g. the rotation around the x axis in figure 3.9). These two DoF have no cross coupling, so the underlying assumptions had no effect, see appendix A with the example of a beam element stiffness matrix.

The statement in (4.7) would be valid if the isolator connected the DoF of the two virtual points with the special topology shown in figure 4.3, i.e. each DoF on one side of the interface is only coupled to one DoF on the other side and there are no cross couplings with any other DoF . The depiction of springs in figure 4.3 is just for didactic purposes. Of course there can be any kind of frequency dependent stiffness and damping properties inherent in the links depicted as mere springs. If such a model is assumed, then the stiffness matrix of the rubber isolator has the properties stated in equation (4.7). Additionally, due to the DoF to DoF coupling (figure 4.3), $\mathbf{Z}_{11}^{I}$ and therefore also $\mathbf{Z}_{12}^{I}$ would be diagonal matrices. The model for the rubber isolator could then be obtained by approximating the rubber stiffness matrix by e.g.:

$$\mathbf{Z}^{I} \approx \begin{bmatrix} -diag(\mathbf{Z}_{12}^{I}) & diag(\mathbf{Z}_{12}^{I}) \\ diag(\mathbf{Z}_{21}^{I}) & -diag(\mathbf{Z}_{21}^{I}) \end{bmatrix}. \tag{4.9}$$

This method for modeling the rubber element will be referred to as **inverse substructuring diagonal (ISD)** model in the validation section 4.5. Either way, using equation (4.8) or (4.9), one can approximate the whole rubber isolator by simply *inverting* the measured FRF matrix of the assembly $\mathbf{Y}^{AIB}$ to $\mathbf{Z}^{AIB}$, and utilizing the off-diagonal blocks $\mathbf{Z}_{12}^{AIB}$ and $\mathbf{Z}_{21}^{AIB}$ alone (provided that the assumptions hold). The name inverse substructuring given in [188, 201] probably stems from this inversion of the measured admittance $\mathbf{Y}^{AIB}$.

In this case, one can also derive the dynamic stiffnesses of the two separate substructures A and B from the measurements:

$$\begin{bmatrix} \mathbf{Z}_{11}^{A} & \mathbf{0} \\ \mathbf{0} & \mathbf{Z}_{22}^{B} \end{bmatrix} = \begin{bmatrix} \mathbf{Z}_{11}^{A} + \mathbf{Z}_{11}^{I} & \mathbf{Z}_{12}^{I} \\ \mathbf{Z}_{21}^{I} & \mathbf{Z}_{22}^{B} + \mathbf{Z}_{22}^{I} \end{bmatrix} - \underbrace{\begin{bmatrix} \mathbf{Z}_{11}^{I} & \mathbf{Z}_{12}^{I} \\ \mathbf{Z}_{21}^{I} & \mathbf{Z}_{22}^{I} \end{bmatrix}}_{\text{from (4.8) or (4.9)}}. \tag{4.10}$$

This comes with the great practical advantage that it is not necessary to know anything about the dynamic properties of the two structures A and B which are coupled by the isolator. Thus, one is able to identify the dynamic properties of all involved substructures A, B and I separately from only one set of measurements performed on the assembly AIB.

Also the hydropulse identifies the off-diagonal stiffness terms $\mathbf{Z}_{21}^{I}$ (see figure 4.2) of the isolator in the axial and radial direction. In figure 4.4, the hydropulse measurements (details listed in table 4.1) are compared to the results from the inverse substructuring approach in axial direction. In the figure, both entries containing this axial-axial stiffness from the two off-diagonal matrices $\mathbf{Z}_{12}$ and $\mathbf{Z}_{21}$ are shown. In figure 4.5, the results in the radial direction are compared.
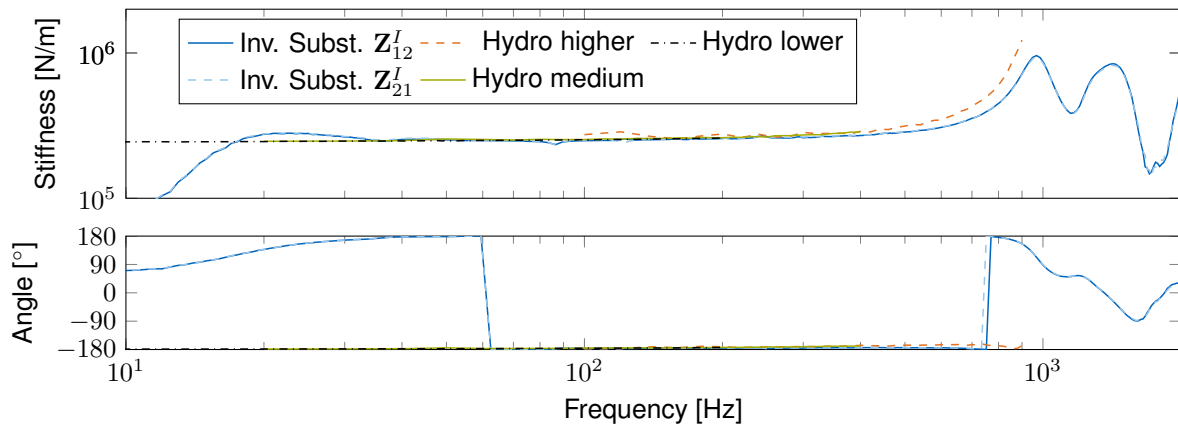
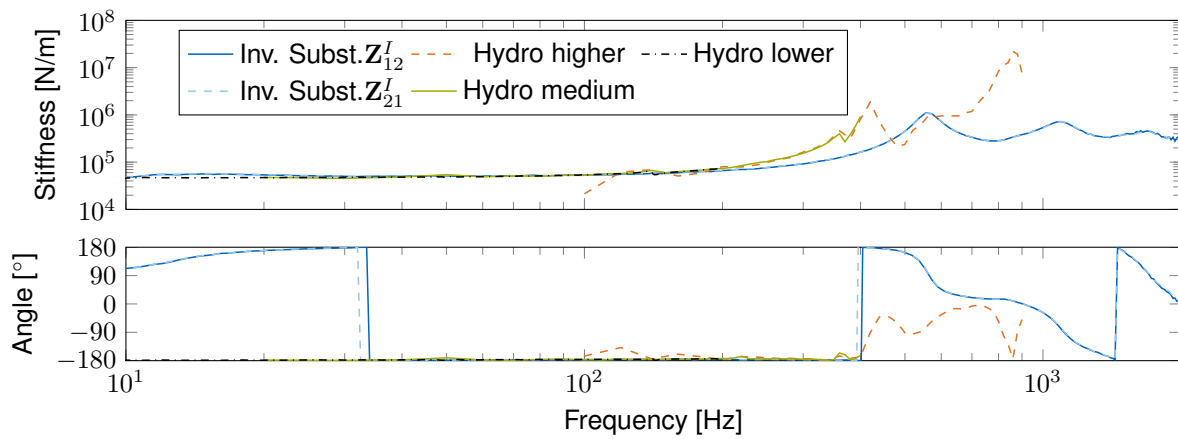**Figure 4.4:** Axial direction: Comparison of hydropulse with inverse substructuring results.

Figure 4.5: Radial direction: Comparison of hydropulse with inverse substructuring results.
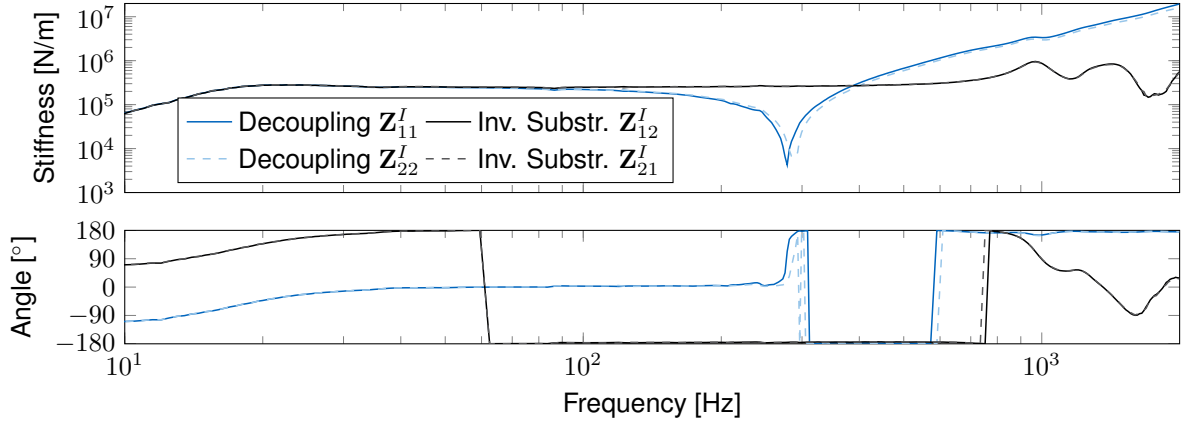
Figure 4.6: Axial direction: Comparison of off-diagonal ($\mathbf{Z}_{12}^I$, $\mathbf{Z}_{21}^I$) and diagonal ($\mathbf{Z}_{11}^I$, $\mathbf{Z}_{22}^I$) entries.

As can be seen in figure 4.4, the magnitude of the axial stiffness identified from the inverse substructuring fits the hydropulse measurements well for frequencies above 30Hz. The phase, which is important for a good damping estimate, is more difficult. This is assumed to be due to slight phase errors in the FRF measurements (this will be further discussed in sections 4.3.3 and 4.4.3). For the radial direction in figure 4.5, the magnitude of the stiffness also fits well for lower frequencies. However, for higher frequencies the deviation of stiffness magnitude between hydropulse and the inverse substructuring is higher (which is also further discussed in section 4.3.3).

4.3.2 Primal disassembly & review of inverse substructuring assumptions

The dynamic stiffness of upper and lower cross, $\mathbf{Z}^A$ and $\mathbf{Z}^B$ respectively, is known from analytical rigid body modeling (see section 2.7). Therefore, it is straightforward to perform the decoupling of both crosses in the primal FBS formulation:

$$\begin{bmatrix} \mathbf{Z}_{11}^I & \mathbf{Z}_{12}^I \\ \mathbf{Z}_{21}^I & \mathbf{Z}_{22}^I \end{bmatrix} = \begin{bmatrix} \mathbf{Z}_{11}^A + \mathbf{Z}_{11}^I & \mathbf{Z}_{12}^I \\ \mathbf{Z}_{21}^I & \mathbf{Z}_{22}^B + \mathbf{Z}_{22}^I \end{bmatrix} - \begin{bmatrix} \mathbf{Z}_{11}^A & \mathbf{0} \\ \mathbf{0} & \mathbf{Z}_{22}^B \end{bmatrix}. \tag{4.11}$$

Obviously, the entries on the off-diagonals are unchanged by the decoupling, but it is now possible to investigate the assumptions underlying the inverse substructuring approach, e.g. by comparing the main- and off-diagonal entries.

Negligible mass assumption

In figure 4.6, the axial stiffness values taken from the diagonal ($\mathbf{Z}_{11}^I$ and $\mathbf{Z}_{22}^I$) are compared to those from the off diagonal terms. If the assumption of negligible rubber element mass holds, then they should be the same apart from a negative sign, i.e. a $180°$ phase shift (see equation (4.7)). This is true for the low frequency spectrum up to around 100Hz. For higher frequencies, there is a clear resonance (showing as a dip in the stiffness magnitude) visible in the entries of the main diagonal. A quick investigation of this resonance can be done assuming the rubber isolator to be a lumped mass and stiffness model. When using the static axial stiffness and half of the rubber isolator mass m_r (including bolts and nuts, see figure 4.1c), one can compute the resonance of a single DoF oscillator resulting in 257Hz. The actual resonance appearing in figure 4.6 is at 278Hz. The higher value may be attributed to dynamic stiffening of the rubber and the fact that the mass of the rubber isolator
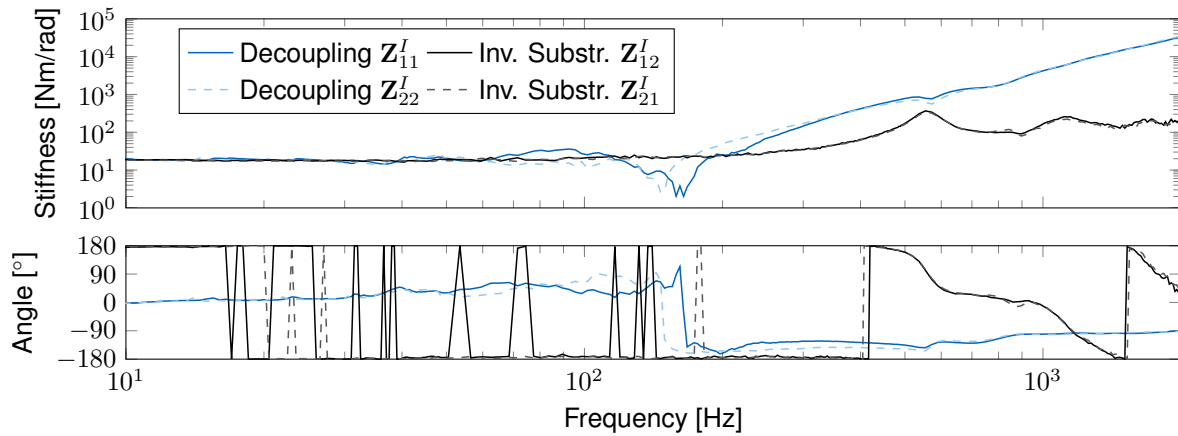
Figure 4.7: Rotation around z: Comparison of off-diagonal ($\mathbf{Z}_{12}^I$, $\mathbf{Z}_{21}^I$) and diagonal ($\mathbf{Z}_{11}^I$, $\mathbf{Z}_{22}^I$) entries.

is not lumped but continuously distributed. The slope of the main diagonal entries for higher frequencies in figure 4.6 is indicating a quadratic increase of stiffness with frequency, typical for a "mass line". The results for the radial directions show similar behavior.

In figure 4.7, the off-diagonal and main diagonal entries for the rotational stiffness around the z-axis are compared. Similar effects can be observed here: up to around 100Hz, the off-diagonal terms deviate only in a 180 phase shift from the main diagonal entries, as expected. So, it may be argued that the rubber isolator mass could play a significant role for the rubber mount stiffness at higher frequencies.

No cross-coupling

In figure 4.8, the coupling stiffness between the x-translation and y-rotation in the main diagonal submatrices $\mathbf{Z}_{11}$ and $\mathbf{Z}_{22}$ are compared. When looking at an animation of the operational deflection shapes of the experiments, one can observe that there is a clear coupling between the radial directions and the rotation around the axis perpendicular to it. This is by no means surprising since it is the normal behaviour of e.g. a beam. See also the stiffness matrix of a 3 dimensional beam element in appendix A. However, this would violate the no-cross coupling assumption of the inverse substructuring diagonal (ISD) approach in equation (4.9) (see figure 4.3).

4.3.3   Discussion: stiffness from both substructuring methods compared to hydropulse

In this section, some of the observations that can be made from comparing the stiffnesses identified by the two methods to the stiffnesses measured on the hydropulse shall be discussed.

Rigidity of Hydropulse fixtures

It is not sure whether the fixture, connecting the amplitude controlled hydraulic cylinder with the rubber isolators upper bolt, is behaving rigidly in the whole frequency-range (see the discussion in section 4.2.2). This may be an explanation for the deviations between the inverse substructuring results and the hydropulse measurements at higher frequencies. Especially
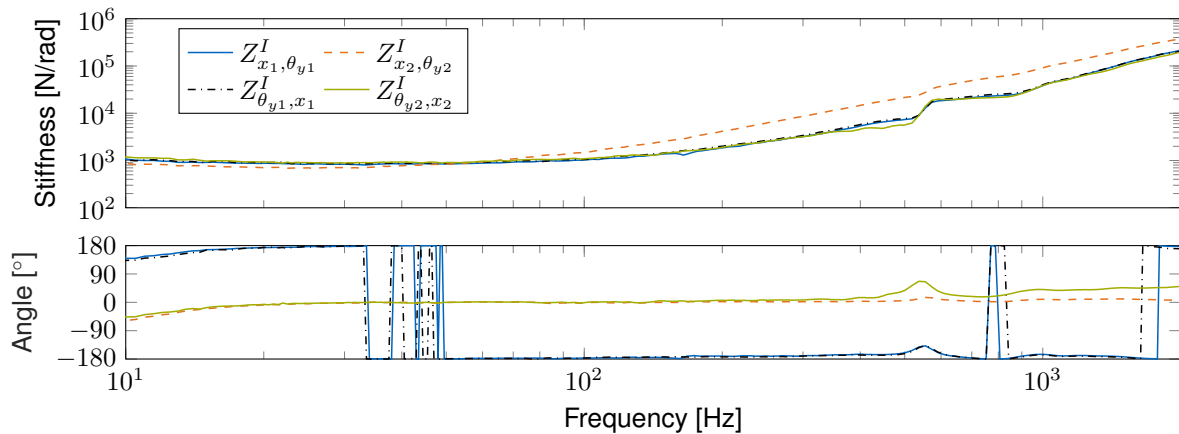
Figure 4.8: Coupling stiffness between translations in x direction and rotations around y axis.

the rigidity of the fixture that holds the rubber isolator during the radial stiffness measurements seems to be questionable for high frequencies (see figure 4.2b and the results in figure 4.5).

Non-linear effects in dynamic behavior of rubber isolators

The rubber temperature for all tests performed was kept constant. The frequency dependent effects due to internal (anti-)resonances are automatically included in the rubber mount models obtained from FBS or inverse substructuring (see these effects at high frequencies in figure 4.4 and 4.5). The remaining two effects which are hard to control with the methods presented in this chapter are:

- **Preload:** When testing the freely hung-up rubber mounts with crosses (see figure 4.1a) there is no preload on the rubber isolator. As has been mentioned in section 4.2.2, the measurements on the hydropulse have been performed with a static preload of 20N. They have also been tested with a preload of 120N, which was the expected static load from the later assembly (shown in chapter 12). This did not yield significantly different results compared to the 20N preload. In [1], it was found that only the axial direction stiffness is susceptible to preload, but only for large deformations. In [1], tests were performed with a material strain of $\varepsilon = 6\%$, 12% or 18%. The deviations from the stiffness with no preload compared to the $\varepsilon = 6\%$ preload deformation were still very limited. Especially when compared to the stiffness changes over frequency due to the internal resonances in the isolator. The expected static deformation of the rubber bearings in this test was in the order of $\varepsilon = 1.5\%$, so these effects were not considered to be important.

- **Amplitude:** Rubber generally behaves stiffer if the maximum transient displacement in time is small (see section 4.1.1), e.g. in a harmonic test with only one excitation frequency like on the hydropulse (see table 4.1). In [69], it is shown that this change of stiffness is more prominent for higher frequencies than for lower frequencies. This effect might explain the higher stiffness measured with the hydropulse in the high-frequency-range when compared to inverse substructuring (see figure 4.4 and 4.5).

Phase errors and damping estimates

The phase of a driving point, i.e. a main diagonal entry in the stiffness matrix $\mathbf{Z}^I$, should be between $0°$ and $180°$ for a rubber isolator with positive damping (see the discussion in section 2.6.2 or [164]). Put differently, the imaginary part ($i\omega d$) of these terms should always be positive, since the damping d is always positive. In the results of the substructure decoupling (e.g. the main diagonal entries from $\mathbf{Z}^I_{11}$ and $\mathbf{Z}^I_{22}$ in figure 4.6), there seems to be an error of a few degrees in the phase over the whole frequency range. The phase is not between $0°$ and $180°$ for the low frequency range (below 40Hz) and for a higher frequency band (300 to 600Hz), which is not a physical behaviour as it would indicate negative damping. For the rotation around the z-axis (cf. figure 4.7) the phase error is more apparent and the magnitude seems more affected by noise than in the axial direction. The raw measured FRFs before VPT are also showing these errors in the identified phase. An accelerance driving point FRF ($\left[\frac{m}{Ns^2}\right]$) should always have a positive phase for a positive damping (see section 2.6.2). A quick check on a FRF in the measured matrix $\mathbf{Y}^{AIB}_{uf}$ which is approximately a driving-point (impact f_{10} and the coressponding channel of the adjacent sensor, see figure 3.9) shows a negative phase of about $2°$ at 500Hz which is growing to approximately $7°$ at 2000Hz. The VPT seems to be helpfull by averaging out the different phase errors of single sensors, but also here some driving point FRFs in $\mathbf{Y}^{AIB}_{qm}$ have a negative phase (growing from about $-0.8°$ at 500Hz to $-2°$ at 2000Hz). Manufacturers specify different maximum phase errors for their sensors (values found on the internet are ranging from $2.5°$ to $10°$). However, manufacturer specifications for the sensors used in this chapter could not be found. The decoupling of the cross masses amplifies slight errors in the phase even more, which we will explain and attempt to remedy in section 4.4.3.

4.4 Variants and extensions to the methods

In this section, suggestions to remedy to some of the previously identified shortcomings of the methods are made. Namely, this will be a correction term for the neglected rubber isolator mass in inverse substructuring (section 4.4.1), a correction to account for the cross coupling between translational and rotational directions which is otherwise neglected in inverse substructuring (section 4.4.2) and a way to bound the phase errors in the identified rubber element models (section 4.4.3). The performance of the rubber element models with and without these modifications is going to be evaluated in section 4.5, by using them in substructuring and validate them against a reference measurement.

4.4.1 ISD: correction terms for the rubber isolator mass

In figures 4.6 and 4.7, we saw that the mass of the rubber element itself had an influence on the stiffness of the main diagonal elements. In this subsection, we try to account for the neglected mass of the rubber element (IS and ISD models), with a simple mass correction that is lumping half of the rubber elements mass on either virtual point. The total mass of the rubber elements m_r can be measured on a scale. The dimensions of the threaded stud, the halved rubber clylinder and the position and weight of the nut can also be measured. The density of steel and rubber is known from literature. The position of the center of gravity G as well as the rotational inertia around the virtual point Θ_V can then be calculated from elementary geometric shapes. The threaded stud and the rubber where therefore modeled as cylinders and the nut was treated as a point mass. The lumped mass matrix for a halved rubber element as seen in figure 4.9 can then be stated as:
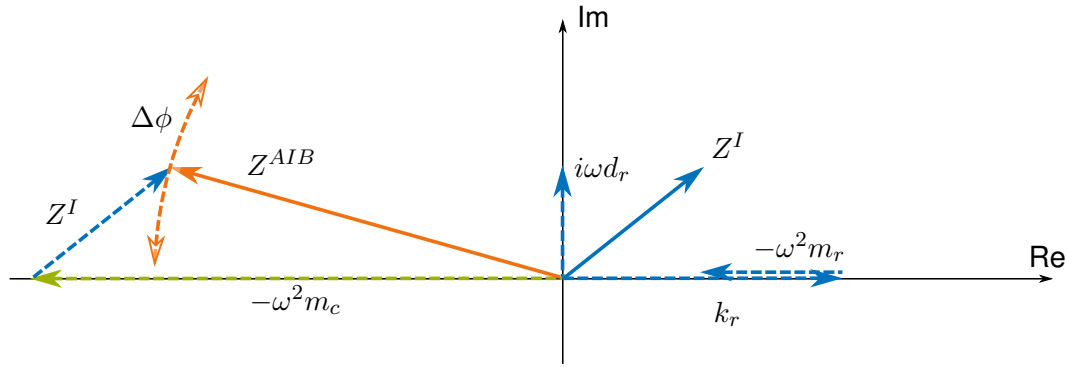
Figure 4.9: Half of the rubber element, which is used for creating a lumped mass correction for the inverse substructuring rubber element model.

$$\mathbf{M}_r = \begin{bmatrix} \frac{m_r}{2}\mathbf{I} & -\frac{m_r}{2}\tilde{\mathbf{r}}_{V,G} \\ \frac{m_r}{2}\tilde{\mathbf{r}}_{V,G} & \boldsymbol{\Theta}_V \end{bmatrix}. \tag{4.12}$$

The mass correction term can then be applied to e.g. the ISD model for the rubber bearings:

$$\mathbf{Z}^I = \underbrace{\begin{bmatrix} -diag(\mathbf{Z}_{12}^{AIB}) & diag(\mathbf{Z}_{12}^{AIB}) \\ diag(\mathbf{Z}_{12}^{AIB}) & -diag(\mathbf{Z}_{12}^{AIB}) \end{bmatrix}}_{\text{ISD model}} \underbrace{-\omega^2 \begin{bmatrix} \mathbf{M}_r & \mathbf{0} \\ \mathbf{0} & \mathbf{M}_r \end{bmatrix}}_{\text{correction}}. \tag{4.13}$$

4.4.2 ISD: accounting for cross coupling stiffness

In figure 4.8, we saw that the rubber bearings have a cross coupling stiffness between the radial displacements (x and y direction in figure 3.9) and the rotation around the radial axis perpendicular to that. This is the normal behaviour that is also known from beam theory (see appendix A). In this subsection, we are concerned about the coupling terms between the translation and the rotation. They show up on the off-diagonal terms of $\mathbf{Z}_{12}^{AIB}$ and $\mathbf{Z}_{21}^{AIB}$. However, they are placed with the wrong sign in the main diagonal matrices $\mathbf{Z}_{11}$ and $\mathbf{Z}_{22}$ by following the IS approach in equation (4.8) (compare to the full stiffness matrix of a 3 dimensional beam in the appendix). Since the rubber bearings are cylindrical, all coupling terms between rotation and translation (e.g. $Z_{x_1,\theta_{y1}}$ and $Z_{y_1,\theta_{x1}}$) are equal in magnitude, and possibly differing in sign.

The sign and position of the translation-rotation coupling-stiffness terms could then be defined in a matrix $\mathbf{P}$:

$$\mathbf{P} = \begin{bmatrix} \cdot & \cdot & \cdot & \cdot & \ominus & \cdot & \cdot & \cdot & \cdot & \cdot & \ominus & \cdot \\ \cdot & \cdot & \cdot & \oplus & \cdot & \cdot & \cdot & \cdot & \cdot & \oplus & \cdot & \cdot \\ \cdot & \cdot & \cdot & \cdot & \cdot & \cdot & \cdot & \cdot & \cdot & \cdot & \cdot & \cdot \\ \cdot & \oplus & \cdot & \cdot & \cdot & \cdot & \ominus & \cdot & \cdot & \cdot & \cdot & \cdot \\ \ominus & \cdot & \cdot & \cdot & \cdot & \cdot & \oplus & \cdot & \cdot & \cdot & \cdot & \cdot \\ \cdot & \cdot & \cdot & \cdot & \cdot & \cdot & \cdot & \cdot & \cdot & \cdot & \cdot & \cdot \\ \cdot & \cdot & \cdot & \oplus & \cdot & \cdot & \cdot & \cdot & \cdot & \oplus & \cdot & \cdot \\ \cdot & \cdot & \cdot & \ominus & \cdot & \cdot & \cdot & \cdot & \cdot & \ominus & \cdot & \cdot \\ \cdot & \cdot & \cdot & \cdot & \cdot & \cdot & \cdot & \cdot & \cdot & \cdot & \cdot & \cdot \\ \cdot & \oplus & \cdot & \cdot & \cdot & \cdot & \cdot & \ominus & \cdot & \cdot & \cdot & \cdot \\ \ominus & \cdot & \cdot & \cdot & \cdot & \cdot & \oplus & \cdot & \cdot & \cdot & \cdot & \cdot \\ \cdot & \cdot & \cdot & \cdot & \cdot & \cdot & \cdot & \cdot & \cdot & \cdot & \cdot & \cdot \end{bmatrix}, \tag{4.14}$$

where a $\cdot$ represents zero and the plus and minus represent a positive and negative one (the representation was chosen for a clearer overview). The plain ISD model for the rubber element stiffness matrix may thus be modified by:

Figure 4.10: Schematic depiction of the complex stiffness values on the main diagonal and the decoupling process in the primal formulation. The rubber element stiffness, damping and mass are denoted as k_r, d_r and m_r respectively, resulting in the complex rubber element stiffness Z^I (blue arrows in complex plane). The cross mass is denoted as m_c (green arrow) and the measured complex stiffness of the assembly is denoted as Z^{AIB}, including possible phase errors $\Delta\phi$ (orange arrows) in the measurements.

$$\mathbf{Z}^I = \underbrace{\begin{bmatrix} -diag(\mathbf{Z}_{12}^{AIB}) & diag(\mathbf{Z}_{12}^{AIB}) \\ diag(\mathbf{Z}_{12}^{AIB}) & -diag(\mathbf{Z}_{12}^{AIB}) \end{bmatrix}}_{\text{ISD model}} + \underbrace{P_{ij}Z_{ij}^{AIB}\mathbf{P}}_{\text{correction}} \qquad \text{with: } \mathbf{P}(i,j) \neq 0. \qquad (4.15)$$

The indices i, j can be chosen to take the matrix entry from $\mathbf{Z}_{12}^{AIB}$ or $\mathbf{Z}_{21}^{AIB}$ which looks physically most meaningful or has the best signal to noise ratio. However, as an error check, one should always verify if all these entries have identical magnitude and possibly differing sign as in equation (4.14) (see e.g. figure 4.8).

The representation of the cross coupling terms in equation (4.14) is valid for a cylindrical rubber bearing. For different shapes (e.g. cubic rubber blocks) similar expressions can be derived, which has already been done in [184, section 2.2].

4.4.3 Frequency based substructuring: reducing phase errors

As discussed in section 4.3.3, the magnitude of the estimated stiffness seems to match well with the measurements performed on the hydropulse. The phase however, which is important for the damping estimate, is not physically meaningfull over parts of the frequency range at the driving points. In order to explain the reason for the phase errors, we need to get a clearer grasp on the operations involved in the decoupling and the raw measurements.

Amplification of phase errors by the method

In figure 4.10, we show a schematic depiction of the decoupling process in the primal formulation on a driving point. The dynamic stiffness of the crosses is only their mass ($-\omega^2 m_c$) if we model them as a rigid body. It is subtracted from the measured stiffness of the whole assembly Z^{AIB} to get the stiffness of the rubber element Z^I, see equation (4.11). The rubber element stiffness at a driving point should always have a positive imaginary part, since the damping term $\mathrm{i}\omega d$ is always positive. However, the measured Z^{AIB} is subject to modeling and measurement errors, which induce an error on the phase, denoted as $\Delta\phi$ in figure 4.10. If the mass of the cross has the largest contribution to the measured stiffness of the assembly Z^{AIB} (which is the case either for crosses that are very heavy or for high frequencies ω), then even slight phase errors $\Delta\phi$ will have a large influence on the identified damping of
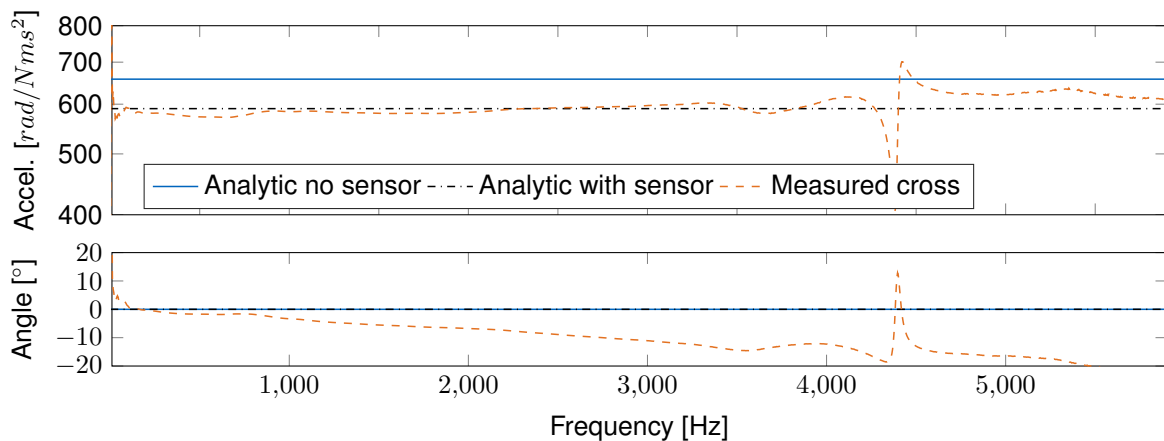
Figure 4.11: Driving point accelerance (rotation around z-axis, cf. figure 3.9) of the measured aluminium cross vs. the analytical cross model from section 2.7 with and without consideration of the sensor masses

the rubber isolator. In this case, the phase of Z^{AIB} approaches $180°$, and even small phase errors $\Delta\phi$ are large enough to cause Z^{AIB} having a negative imaginary part. Then also the estimated damping for the rubber mount will be negative, which is unphysical. In general, it can be said that the initial small phase errors $\Delta\phi$ in the measurements of the coupled system Z^{AIB} are being amplified to large phase errors of Z^I during the decoupling process, especially for high frequencies.

Phase errors in raw measurement data

After explaining this amplification of a wrong phase, we will now further investigate the actual phase drifts in the experimental models. Figure 4.11 shows the accelerance of the analytic cross model ($\mathbf{M}^{-1}$ from equation (2.59)), once with and once without the correction term for the sensor's masses. It is compared with a measurement of the crosses accelerance, i.e. the crosses hung up freely without the rubber isolator in between. It can be seen that the magnitude of the accelerance fits well, especially if the correction terms for the sensor masses are included. However, the phase of the measurement is not as expected (just a constant $0°$), but seems to deviate more and more from $0°$ for higher frequencies. This phase drift is assumed to be due to multiple reasons. One is thought to be a constant time delay between the signals of the sensor channels and the force channel. A constant time delay between the signal of two channels will show in the FRF between them as a linearly increasing phase drift with frequency [44]. Note the linear frequency axis in figure 4.11 instead of a logarithmic axis as in the other plots. This way one can see that indeed the phase of the measured crosses seems to decrease linearly with frequency, apart from a deviation at the first cross resonance at $4489 Hz$ and very low frequencies. In [44, 178], the authors use a phase correction term, which is linearly increasing with frequency, on a driving point measurement to compensate for this effect. In the case of [178], this resulted in a valid estimation of damping and thus a meaningful calculation of structural power flow. However, in the example presented here, there are multiple measurements involved which are not only pure driving points as in [44, 178]. If the time delay which causes the linear phase deviation in figure 4.11 was only due to a *constant* time delay between the channels of the measurement equipment, then the phase drift should be the same for a fixed combination of the hammer channel and one sensor channel (i.e. same phase drift on Y_{ij} for all impact positions j measured with the same sensor channel $i = const.$). However, this is not the

	longitudinal	transversal	one sample delay
$4cm$	$4.57°$	$9.29°$	$21.97°$
$10cm$	$11.42°$	$23.22°$	

Table 4.2: Estimation of phase drift at $2000Hz$, resulting from different sources of time delays. The time delays are calculated for a distance of $4cm$ or $10cm$ and with the speed of either a longitudinal or transversal wave in aluminum. The resulting phase error at $2000Hz$ from a one sample glitch in the measurement system at a sampling rate of $32768Hz$ is also given.

case for the measurements performed for this chapter. It is assumed, that the time delays are also related to the time it takes for the elastic wave to travel from the impact to the sensor position. This time delay obviously also changes with the position of the hammer impact. Further investigations are possible, but a small plausibility calculation is provided here. The distance from an impact position to a sensor varied between roughly $4-10cm$. The speed for a transversal and longitudinal wave in aluminum can be approximated with $3100\frac{m}{s}$ and $6300\frac{m}{s}$ respectively. The resulting phase drift at $2000Hz$ due to the time delays from the elastic wave traveling through the material are listed in table 4.2. An estimate for the phase error which would result from a glitch of one sample on the data acquisition system is also provided (the sampling rate in the measurements was $32768Hz$). It can be seen that the resulting phase drifts at $2000Hz$ are all of the same order of magnitude as we see them in the measurements shown in figure 4.11. If the errors were due to random sample glitches in the measurement system, then we would have seen a linear drop in the coherence of the measurements, which was not the case. Thus, it is believed that the effect can be explained by the elastic waves travel-time and constant time delays in the measurement equipment. Note that the travel time for a wave in the material is of course not an error in the measurements. It is rather the assumption of local rigidity with the virtual point transformation that is violated in this case. For a truly rigid structure, the wave speed would be infinity and the time delays would therefore be zero.

Attenuating phase errors in practice

A remedy to the phase errors which was found to work best is described in the following. After performing the measurements on the assembly to get $\mathbf{Y}^{AIB}$, one can perform the same measurement on the freely hung up crosses (same impacts and sensor positions as for the case with the rubber bearings in between, see figure 3.9) to obtain $\mathbf{Y}^{AB}$. This can then be inverted to the *measured* stiffness $\mathbf{Z}^{AB}$ of the crosses alone, and then used in the decoupling from the assembly $\mathbf{Z}^{AIB}$, equation (4.11). In this case, the measured stiffness $\mathbf{Z}^{AB}$ is already containing similar phase errors as in the measurement of $\mathbf{Z}^{AIB}$. After all, the measurement equipment and impact positions were the same, so possible time delay issues between sensor channels during the measurement are affecting $\mathbf{Z}^{AB}$ and $\mathbf{Z}^{AIB}$ equally. Therefore, the phase error on the identified rubber mount stiffness $\mathbf{Z}^{I}$ is being reduced, since e.g. a negative imaginary part in $\mathbf{Z}^{AB}$ is being subtracted from a similar negative imaginary part in $\mathbf{Z}^{AIB}$. Figure 4.12 shows the rubber mount driving point stiffness in the axial direction. Indeed, the phase errors for the higher frequencies can be removed to a large extent by decoupling the measured instead of the analytically modeled cross stiffness $\mathbf{Z}^{AB}$. Especially between approximately 300 and 600 Hz the damping estimate is now physically meaningfull, since now the identified driving point stiffness of the rubber mount phase is between $0-180°$.

What might also be seen as an advantage of this variant, is that the mass of the sensors is automatically being considered, since they are part of the measured system. So no analytic modeling (section 2.7) has to be done. In theory, it is also more precise, since the crosses
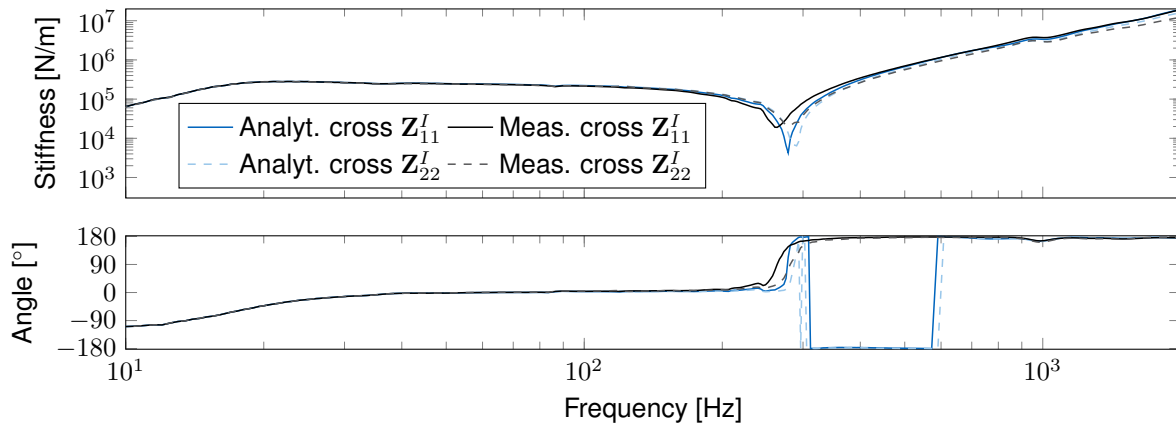
Figure 4.12: Driving point stiffness in axial direction: Comparison of decoupling the measured crosses vs. decoupling analytical cross model (see section 2.7). Phase errors are reduced by decoupling a measured model of the crosses.

were hung up with rubber bands. These rubber bands are not part of the description in the analytical model, but are very well included in the measurements of the crosses when hung up freely. The measurement effort however increases twofold.

Note that at lower frequencies, below ca. 30Hz in figure 4.12, the phase and the rubber stiffness is dropping which is un-physical. It is believed that this effect is due to the bad visibility of the flexible modes, that contain the rubber stiffness. At the lower frequencies the whole FRF is dominated by the rigid body modes of the whole assembly AIB.

4.5 Validation: rubber isolator models in substructuring

The goal of developing the rubber isolator models is to use them in a larger assembly of subcomponents which are coupled via substructuring. Here, the predicted FRF of an assembly, which includes the rubber models, is then compared to a reference measurement of that assembly. The accordance between reference and prediction can be seen as a quality indicator for the different rubber mount models.

The crosses used for measuring $\mathbf{Y}^{AIB}$ and then identifying the rubber elements stiffness were made of aluminum. Here, crosses ($\tilde{A}$ and $\tilde{B}$) with the same geometry, but this time made of steel, are connected to the rubber isolators as a validation measurement. The different methods for obtaining the rubber isolator stiffness are then used to predict the accelerance FRF $\mathbf{Y}^{\tilde{A}I\tilde{B}}$ of the rubber element coupled to the steel crosses. Either primal or dual substructuring can be used to couple an analytical model of the steel crosses to the different rubber isolator models. Figure 4.13 shows a comparison of the reference and predictions for driving point FRFs (i.e. input and output on the upper cross). As expected, these FRFs start with a horizontal line, representing the rigid body motion of the whole assembly $\tilde{A}I\tilde{B}$ in the corresponding direction. This is followed by the resonances and subsequently a horizontal line which is just the rigid body motion of a single cross. This is also expected, since for higher frequencies the rubber stiffness is negligible compared to the dynamic stiffness of the crosses mass. Figure 4.14 shows a comparison of the reference and predictions for the transfer FRFs (i.e. input on the upper cross and output on the lower cross). For higher frequencies these FRFs tend towards zero which is the desired 'dynamic isolation'. This is what the engineer usually wants to achieve between source and receiver with the use

of rubber isolators. Notice the highly damped peaks at higher frequencies (approx. 700Hz) caused by the internal resonances in the rubber isolator.

In the axial direction both rubber models (from FBS (left column) or inverse substructuring (right column) in figures 4.13 and 4.14) seem to be well able to predict the FRF of the coupled system. For inverse substructuring, the mass correction (as proposed in section 4.4.1) does not seem to make a significant difference when compared to the model without the correction term. This is not a surprise, since the weight of a single steel cross was 2.2kg compared to the overall weight of a rubber bearing of only 150g. In the radial direction, the models from FBS perform noticeably better, since the frequencies of the resonances are all accurately predicted. For the inverse substructuring models, the correction term for the cross coupling (see section 4.4.2) seems to improve the results, though the overall result is still worse then for FBS. The same can be said for the rotation around a radial direction. Decoupling the measured instead of the analytically modeled cross model in the FBS approach seemingly improves the damping estimate in the radial translation and rotation directions (which can be seen by the height of the first resonance peak and the phase curve). For the axial direction however it seems like the damping estimate is actually worse for decoupling the measured crosses instead of the analytically modeled crosses. This should be further investigated.

4.6 Conclusion and recommendations

This chapter investigated the performance of two groups of experimental techniques for identifying 12-DoF dynamic models of rubber isolators: Frequency based substructuring (FBS) and inverse substructuring (IS). The results suggest that it is possible to identify valid stiffness magnitudes up to the kilo-Hertz frequency range with both methods. It is thereby possible to obtain dynamic stiffness values of rubber isolators in more degrees of freedom and up to a higher frequency range than usually possible, even with an expensive hydropulse testing machine. The axial and radial stiffness values have been successfully validated against hydropulse measurements. No smoothing or curve fitting had to be applied on the measurement data. Careful examination of the measurements and the averaging inherent to the virtual point transformation (section 4.2.1) was sufficient.

One important advantage of the IS method compared to FBS is that no dynamic model of the connected structures is needed to determine the dynamics of the isolator. For the FBS approach, the quality of the identified rubber model depends on the accuracy of the dynamic model of the fixtures. That is one of the reason why, in this work, the fixtures were taken as crosses that could be assumed rigid in the frequency range of interest. Thereby, an accurate dynamic model could be easily obtained analytically.

The limits of the assumptions underlying the inverse substructuring method were investigated. First, the mass of the rubber isolators seems not negligible on the main diagonal stiffness entries (figure 4.6). However, the influence of the neglected rubber mass on the models performance in substructuring depends on the ratio of the rubber mass compared to the mass of the system to which the rubber isolators are assembled later. If the rubber mass is negligible compared to this mass, then the assumption would not cause big deviations in the substructuring results, as can also be seen in the results presented in section 4.5. Second, the coupling stiffness for radial displacements and the rotations around the perpendicular axis are not zero (see figure 4.8). This is clearly understandable, considering that the topology of the identified rubber isolator stiffness matrix is similar to that of a three dimensional beam element (see appendix A). With plain inverse substruturing, some of the translation-rotation coupling terms are either placed with the wrong sign on the main diagonal blocks, or neglected completely for the inverse substructuring that accounts only for
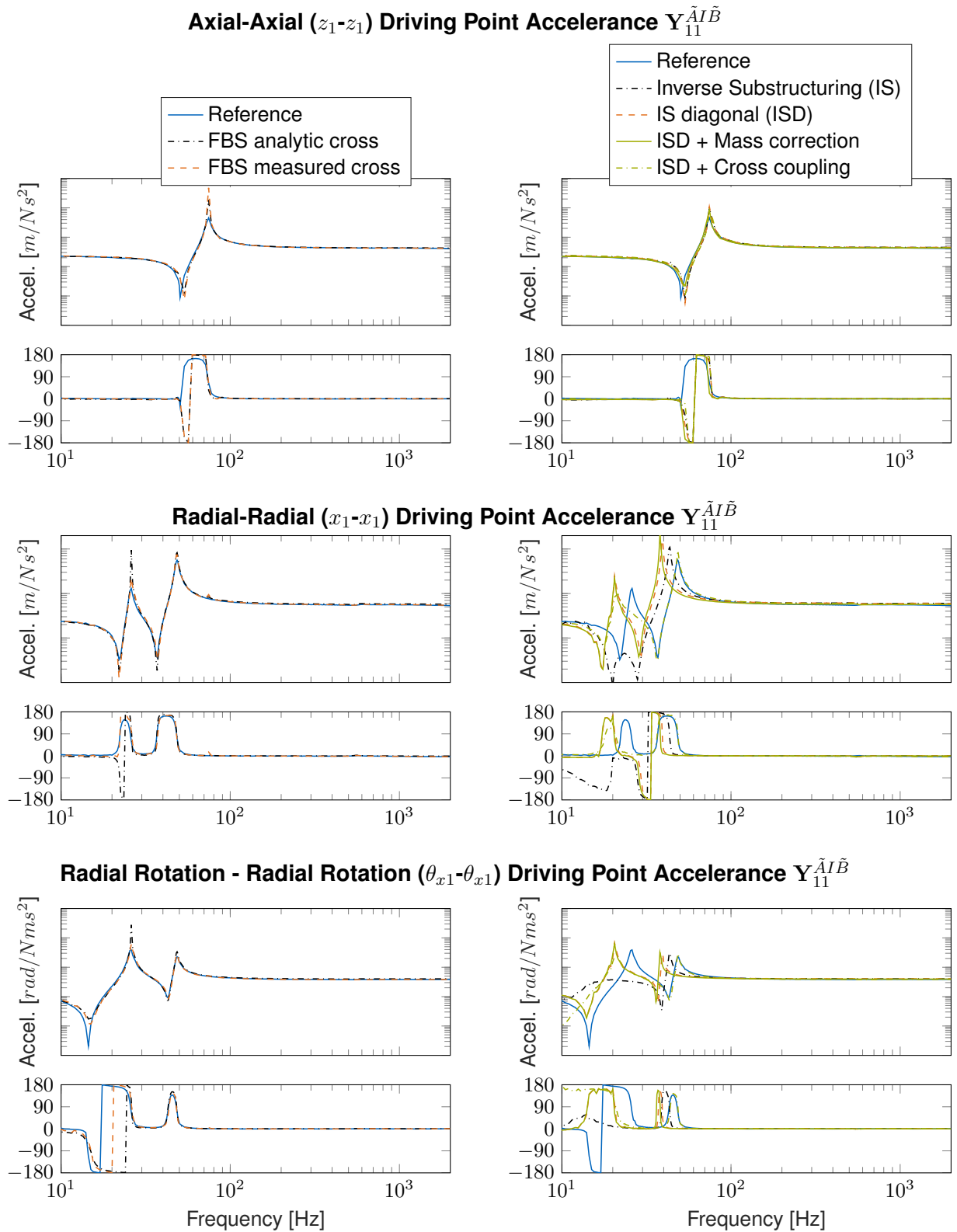
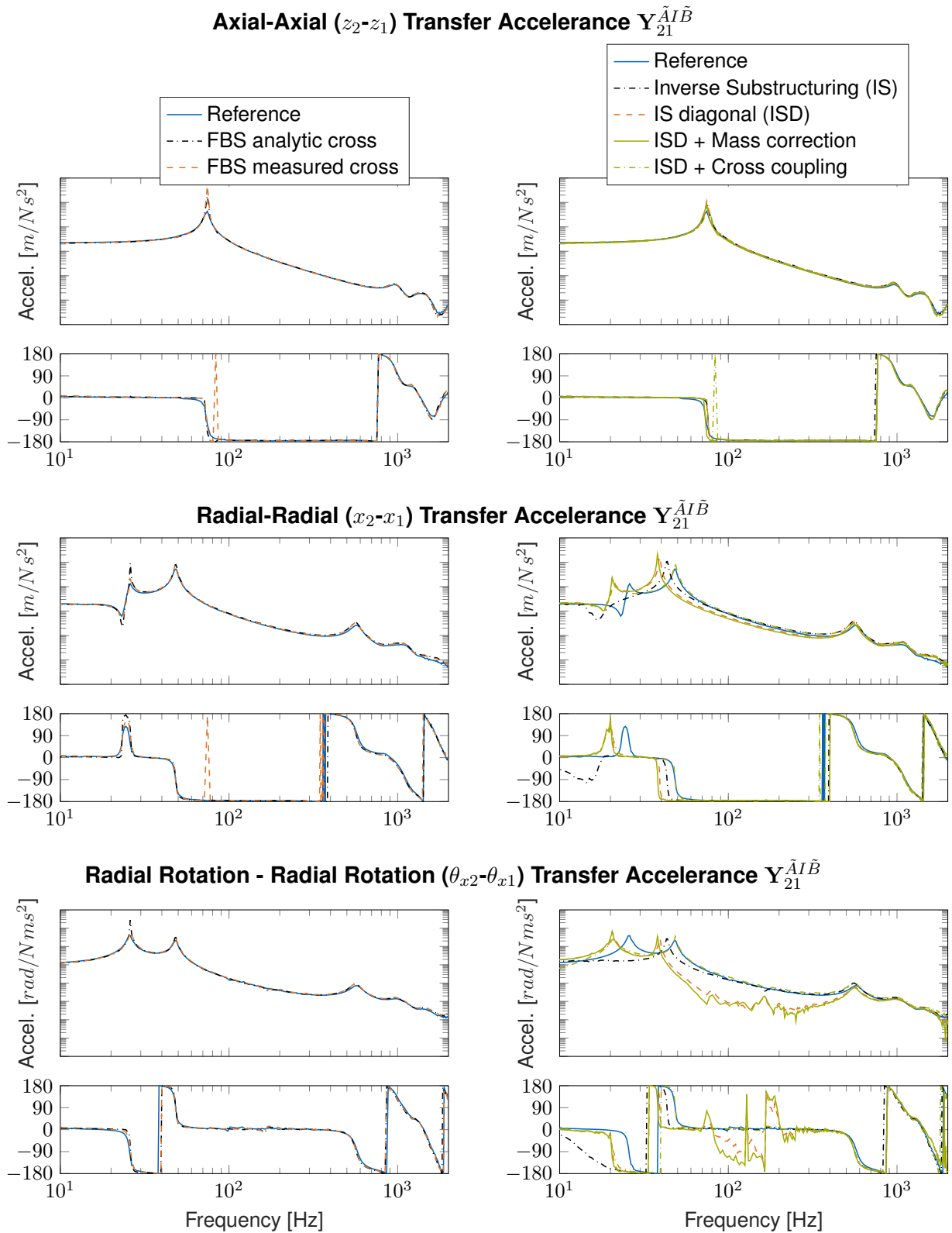**Figure 4.13:** Rubber isolator models performance in substructuring for driving point FRFs. The left column shows the results with the FBS rubber isolator models (equation (4.11)), either decoupling the measured or the analytically modeled aluminum crosses. The right column shows the results of inverse substructuring (IS) models (equation (4.8)) and ISD models (equation (4.9)). Also the extension of ISD with the mass correction (equation (4.13)) and with the compensation for the cross coupling (equation (4.15)) is shown.

Axial-Axial (z_2-z_1) Transfer Accelerance $\mathbf{Y}_{21}^{\tilde{A}I\tilde{B}}$

Radial-Radial (x_2-x_1) Transfer Accelerance $\mathbf{Y}_{21}^{\tilde{A}I\tilde{B}}$

Radial Rotation - Radial Rotation (θ_{x2}-θ_{x1}) Transfer Accelerance $\mathbf{Y}_{21}^{\tilde{A}I\tilde{B}}$

Figure 4.14: Rubber isolator models performance in substructuring for predicting transfer FRFs. The left column shows the results with the FBS rubber isolator models (equation (4.11)), either decoupling the measured or the analytically modeled aluminum crosses. The right column shows the results of inverse substructuring (IS) models (equation (4.8)) and ISD models (equation (4.9)). Also the extension of ISD with the mass correction (equation (4.13)) and with the compensation for the cross coupling (equation (4.15)) is shown.

the diagonal terms (IS and ISD in figures 4.13 and 4.14). Additionally, the rotation-rotation coupling stiffness terms for the radial directions, are placed with a wrong magnitude and sign on the main diagonal blocks. This seemingly affects the assembly results of the inverse substructuring models (see figures 4.13 and 4.14). It is therefore recommended to use a classical decoupling, i.e FBS, to obtain rubber element models that can be used for modeling a larger assembly and the full six DoF shall be used on either connection of the isolator.

For the specific usecase in this chapter, it was not important to consider the effect of preload (see section 4.1.1 and 4.3.3). However if it was, the tests suggested in this chapter would have to be amended. The rubber temperature was kept constant, but the models can easily be obtained at different temperatures with the same procedure. Obtaining the stiffness for different vibration amplitudes is harder, since it would require adjusting the hammer impact magnitudes in a precise manner. A solution to this could be the use of an automatic impacting device, like the low-cost design proposed in [100].

The models developed in this chapter have shown their value in other applications already (see chapter 11 and 12). Therefore, the chapter shall be concluded with a few recommendations for conducting the measurements and designing the tests for obtaining the rubber models:

- **Cross Design:** The crosses should generally be as light as possible. The influence of phase errors can be effectively attenuated, if the mass of the cross structures is decreased (see section 4.4.3). Additionally, the crosses should also fulfill the rigidity assumption that is the basis for the virtual point transformation (VPT, see section 4.2.1). This means for the first flexible eigenfrequency to be approximately 2-3 times higher than the desired frequency range of the rubber mount model. The VPT assumption also presumes, that the stiffness against local deformation in the vicinity of the hammer impacts is high. So especially the region around the hammer impacts should be "bulk material".

- **Cross model**: If possible, a direct measurement of the free-free crosses $\mathbf{Y}^A$ and $\mathbf{Y}^B$, which is later transformed to virtual points, is to be preferred over an analytical model of the crosses. In this way, the structures being decoupled ($\mathbf{Y}^A$ and $\mathbf{Y}^B$) already contain the same phase error, as the ones present in the measurements of $\mathbf{Y}^{AIB}$ (see the discussions in section 4.4.3). Thereby, similar measurement errors are subtracted from one another, and the resulting phase error in $\mathbf{Y}^I$ is reduced (see figure 4.12).

- **Non rigid fixtures**: In theory, one could also use structures other than the rigid crosses presented here. As long as their dynamic stiffness is known, they can still be decoupled to obtain the rubber models. However, for obtaining the rotational degrees of freedom, one will likely use either the virtual point transformation or a finite difference approach, for each of which the assumption of at least local rigidity is mandatory. Additionally, for non-rigid fixtures, one might run into signal to noise issues if one of the structures has an antiresonance at a connection point. In this case, no energy can be inserted into the rubber at the antiresonance frequency. See the results reported in [107] for using a plate and a beam on the connection points to the rubber element.

- **Low frequency stiffnesses**: If the measurements are performed with standard accelerometers, the signal to noise ratio (SNR) for frequencies below approx. 20Hz can be too low, resulting in noisy measurements. Additionally, in the low frequency region (below approximately $30Hz$) the stiffness of the rubber models can drop (see e.g. figure 4.4), which is unphysical. This could be a problem of low frequency rigid body resonances of the whole assembly AIB in the rubber bands (see figure 4.1a), a

decreased SNR at lower frequencies, or undetected overload issues during the measurements. However, from experience and also the results that can be seen in the hydropulse measurements (e.g. figures 4.4 and 4.5), the rubber isolators stiffness is almost constant for lower frequencies[2]. So from experience, it is a valid assumption to extrapolate the determined rubber mount stiffness from a frequency range of e.g. 50-100Hz back to the low frequency range of 0-50Hz. This is further confirmed by the comparison of the rubber models with and without this low frequent extrapolation in chapter 12 (see figures 12.10 and 12.12). Similarly, also Verheij suggested in [184, section 2.4] to extrapolate the stiffness from 80-160Hz back to the range below 80Hz.

---

[2]This may be different for rubber isolators with internal fluid channels. Their intrinsic eigenfrequency is lower due to the higher dynamic mass of the accelerated fluid.

Chapter 5

Gyroscopic effects

Contents:

Shift happens...

unknown Master student

The contents of this chapter were published in similar form in [55]. The text hereafter has been modified and adapted to the thesis.

Frequency response functions (FRFs) often serve as a basis for predicting sound and vibration levels at a receiver position, with a known excitation at a source position. As explained in chapter 3, dynamic substructuring allows to build the FRFs of a complex assembly from the measured or modeled FRFs of its subcomponents. However, in the case of subcomponents with revolving parts, the task is further complicated due to gyroscopic effects. These cause a changing FRF matrix of the subcomponent depending on its operating speed. A correct approach would require measuring the FRFs of the rotating machinery at each operating speed, which is a difficult and tedious task. Thus, the unmeasured gyroscopic effects are often neglected, but not always negligible, in practice. In this chapter a dynamic substructuring based approach is proposed, which allows to analytically couple the gyroscopic reaction moments to an FRF matrix that describes the idling subcomponent. Gyroscopic terms only influence subcomponent motions that are tilting the rotation axis. The proposed method will thus be interpreted and derived as a coupling in the subspace of this tilting motion. An analytical testcase is used to exemplify and validate the proposed method in section 5.1. The tilting angles can be determined from an overdetermined set of measured sensor motions, via the virtual point transformation (see section 3.3). The gyroscopic effects can be coupled to the full FRF matrix, by coupling only in the tilting subspace of the matrix, as will be shown in section 5.2. Thereby, an FRF matrix with a large set of DoF can be augmented with a speed dependent gyroscopic term. This is based on the kinematic assumption of rigidity. The validity of this assumption certainly influences the solution, which will be shown on the example in section 5.3. However, in practice the gyroscopic effects mainly influence the FRF matrix in the lower frequency region, where the rigidity assumption is mostly valid. The necessity of including gyroscopic correction terms to the compressor in free-free conditions will be checked in section 5.4.

Chen [25] has designed a dedicated testrig which experimentally proved the validity of the proposed method. This was done by coupling the gyroscopic effects to an FRF that was

measured on the idling testrig, and validating the results with a reference FRFs measured on the operating testrig. Reichart [144] has investigated the need for this correction term on a compressor testrig design. It was found that on a testrig which does not allow for compressor rigid body motion, the gyroscopic effects can be neglected. Janssens and Verheij noted in their paper [71] about operational load indentification[1]:

"Further, the source mobility $\mathbf{Y}^A$ also may be affected by the operational conditions. For instance in rotating machinery the dynamics in a stationary case can differ from the running case. Common linear theory as in Section 2.1 will fail for such situations. In these situations, a remedy is to look in more detail to the source generating mechanism inside the source, as is also suggested in [49]. Little is known about how often such effects play a role in practice."

In this chapter however, it will be shown that the gyroscopic effects can be included in linear theory. Literature can be found on modal testing of rotating structures, which aims at extracting the modal properties of a rotating structure from a set of measurements. See e.g. [23] for a comprehensive review on the topic. However, the measured FRFs of the structure will still change depending on the operating speed of the machine. Also a change of rotation direction (forward or backward) will alter the measured FRFs. An approach solely based on testing is thus very time consuming. To make matters worse, it is non-trivial to get a clean FRF measurement on a machine while it is in operation. All sorts of operational excitations, coming from the internals of the machine, are masking the sensor response to e.g. a shaker input. Some techniques are available for performing these measurements, like e.g. the operating system identification (OSI) method [85], but the involved signal processing and averaging prolongs the FRF determination time. These issues are removed by the proposed approach, since FRF measurements can be done on the idle machine, and the gyroscopic effects are analytically modeled, by knowing the operational speed and rotational inertia of the rotating parts.

5.1 Coupling gyroscopic effects

The FBS approach explained in section 3.1 allows to couple the dynamic behavior of two separate structures. This approach can equivalently be used for coupling non-measured gyroscopic effects to an FRF matrix measured on the idle component. To make the derivations more tangible, the theory shall be discussed on an example, namely a wind turbine like structure, shown in figure 5.1a. The windturbine is mounted on a flexible support, allowing it to rotate around the longitudinal axis (spring stiffness c_γ, angle γ) and to tilt forward (spring stiffness c_β, angle β). The vector of unconstrained DoF is $\mathbf{q} = \begin{bmatrix} \gamma & \beta \end{bmatrix}^T$. The system consists of two bodies, the tower (mass m_t, inertia tensor $\boldsymbol{\Theta}_t$) and the rotor (mass m_r, inertia tensor $\boldsymbol{\Theta}_r$) with their centers of mass being at height h_t and h_r respectively[2]. The rotor can rotate at varying operational speeds Ω. For simplicity, the distance of the rotors' center of mass to the vertical axis is assumed to be zero. Hence, the system is in equilibrium position for $\mathbf{q}^{equil.} = \begin{bmatrix} 0 & 0 \end{bmatrix}^T$, where the springs are undeformed. For studying the vibrations around this

---

[1]Notation adapted to this thesis.

[2]Since in this thesis noise and vibrations shall be studied with linear theory, it is assumed that the motions of this system are small and both rotational inertia tensors $\boldsymbol{\Theta}_t$ and $\boldsymbol{\Theta}_r$ are constant over time. For the tower and rotor, this is valid if the motions $\mathbf{q}$ are small. Thereby, the inertial coordinate systems I and the tower fixed coordinate system T shown in figure 5.1a are equal. For the rotor, one is additionally assuming that the rotational inertia measured in the inertial frame of reference I is constant while the rotor is revolving. This is true for typical 3 bladed designs, and for the e-compressor as well, see remark 5.1.
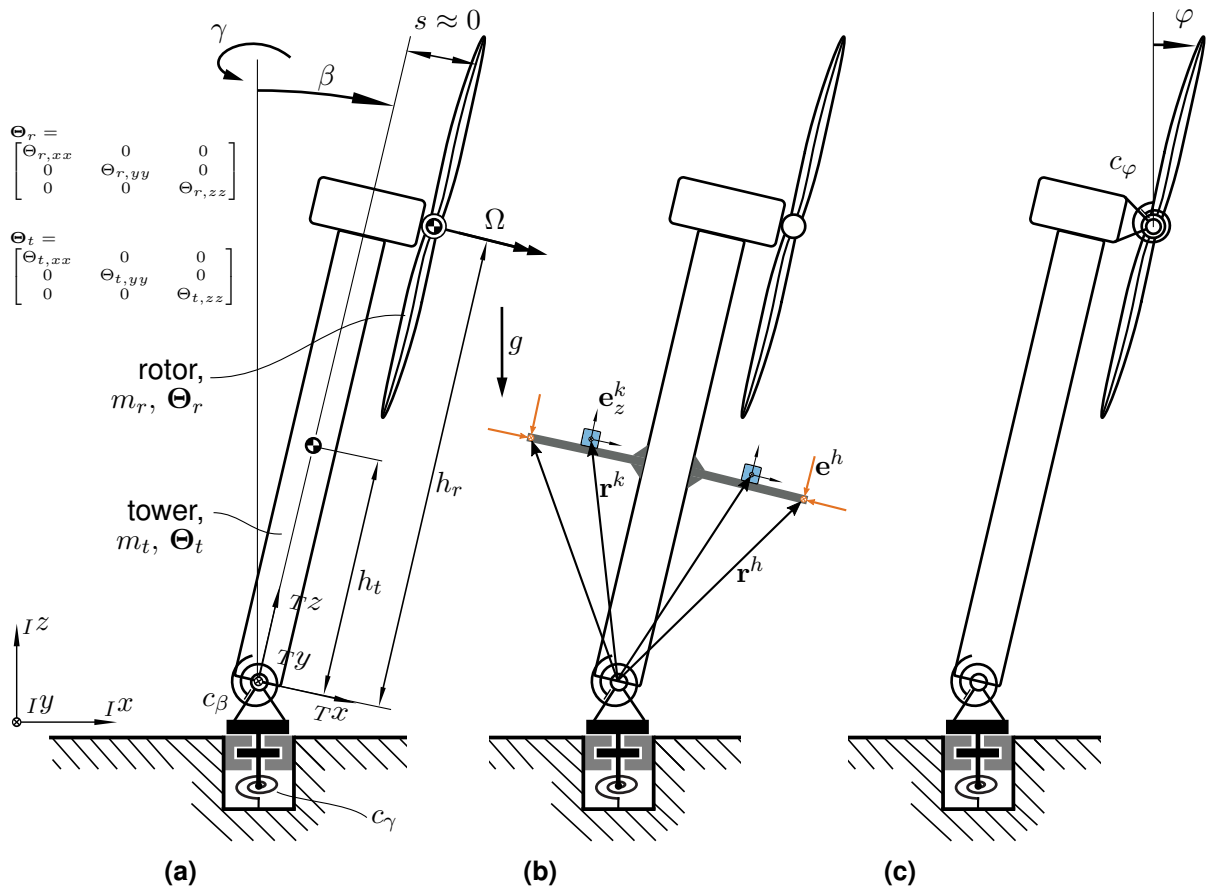
Figure 5.1: Example of windturbine for the coupling of gyroscopic effects. (a) Dimensions and symbols. (b) Applied acceleration sensors and force inputs. (c) Flexibility c_φ between rotor and tower.

equilibrium position, the linearized equations of motion can be written as:

$$\underbrace{\left(-\omega^2\mathbf{M} + i\omega\mathbf{G} + \mathbf{K}\right)}_{=:\mathbf{Z}^{op}(\omega)} \mathbf{q} = \mathbf{m}, \tag{5.1}$$

with the system matrices for this example being[3]:

$$\mathbf{M} = \begin{bmatrix} \Theta_{t,zz} + \Theta_{r,zz} & 0 \\ 0 & \Theta_{t,yy} + \Theta_{r,yy} + m_t h_t^2 + m_r h_r^2 \end{bmatrix},$$

$$\mathbf{G} = \begin{bmatrix} 0 & -\Omega\Theta_{r,xx} \\ \Omega\Theta_{r,xx} & 0 \end{bmatrix}, \qquad \mathbf{K} = \begin{bmatrix} c_\gamma & 0 \\ 0 & c_\beta - (m_t h_t + m_r h_r)g \end{bmatrix}. \tag{5.2}$$

External moments in the respective DoFs are denoted by $\mathbf{m}$. Matrices $\mathbf{M}, \mathbf{G}, \mathbf{K}$ denote the mass, gyroscopic and stiffness matrix respectively. Note that the gyroscopic matrix $\mathbf{G}$ is skew symmetric, i.e. the reciprocity property of FRFs is not valid for systems with rotating components. The system matrices can be combined in the dynamic stiffness $\mathbf{Z}^{op}(\omega)$, where the superscript $(\star)^{op}$ indicates that the matrix is dependent on the operating conditions, i.e. the speed of the rotor Ω. The excitation frequency is denoted by ω, which will be omitted for clarity of notation. The admittance matrix which could be measured on the idling system is $\mathbf{Y}^0$, where the superscript $(\star)^0$ denotes the idling component. However, one is interested interested in obtaining the admittance matrix of the operating system $\mathbf{Y}^{op}$. The individual FRFs needed can be written as:

$$\mathbf{Y}^0 = \left(-\omega^2\mathbf{M} + \mathbf{K}\right)^{-1}, \qquad \mathbf{Y}^{op} = \left(-\omega^2\mathbf{M} + i\omega\mathbf{G} + \mathbf{K}\right)^{-1}, \qquad \mathbf{Y}^{gy} = (i\omega\mathbf{G})^{-1}. \tag{5.3}$$

The gyroscopic effects, not measured on the idle component, can be seen as an additional substructure admittance $\mathbf{Y}^{gy}$ which can be coupled to the idle component $\mathbf{Y}^0$ in a post processing step via FBS. The two matrices to be coupled and the Boolean matrix $\mathbf{B}$ for the compatibility can be inserted in the FBS equation (3.10):

$$\mathbf{Y}^{A|B} = \mathbf{Y}^{0|gy} = \begin{bmatrix} \mathbf{Y}^0 & \mathbf{0} \\ \mathbf{0} & \mathbf{Y}^{gy} \end{bmatrix}, \qquad \text{and} \qquad \mathbf{B} = \begin{bmatrix} \mathbf{I} & -\mathbf{I} \end{bmatrix}, \tag{5.4}$$

with which one obtains for the coupled matrix $\mathbf{Y}^{op}$:

$$\mathbf{Y}^{op} = \mathbf{Y}^0 - \mathbf{Y}^0 \left(\mathbf{Y}^{gy} + \mathbf{Y}^0\right)^{-1} \mathbf{Y}_0, \tag{5.5}$$

where the redundant DoFs have already been removed (see section 3.2.1). Note that in equation (5.5) the roles of $\mathbf{Y}^0$ and $\mathbf{Y}^{gy}$ could be interchanged (removing the other redundant DoFs in the coupled equation). One can show that the FBS result in (5.5) is equivalent to directly assembling the operational dynamic stiffness $\mathbf{Z}^{op} = \mathbf{Z}^0 + \mathbf{Z}^{gy}$ and inverting it. One needs to show that:

$$\underbrace{\left(\mathbf{Z}^0 + \mathbf{Z}^{gy}\right)^{-1}}_{\mathbf{Z}^{op}} = \mathbf{Y}^0 - \mathbf{Y}^0 \left(\mathbf{Y}^{gy} + \mathbf{Y}^0\right)^{-1} \mathbf{Y}_0 \tag{5.6}$$

In order to show this, it is useful to note that:

---

[3]The system of equations can be derived by setting up all energies of the system and applying the Lagrange formalism to it [136]. These equations of motion can then be linearized around the equilibrium state $\mathbf{q}^{equil.}$, in order to obtain the system matrices.

$$\mathbf{Y}^0 \left(\mathbf{Y}^{gy} + \mathbf{Y}^0\right)^{-1} = \left(\mathbf{Y}^{gy} \, \mathbf{Z}^0 + \mathbf{I}\right)^{-1}, \tag{5.7}$$

which can be verified by left multiplying both sides of the above equation with the term $\left(\mathbf{Y}^{gy} \, \mathbf{Z}^0 + \mathbf{I}\right)$. A proof that was already used in [147]. Inserting equation (5.7) to the right side of equation (5.6) yields:

$$\begin{aligned}
\mathbf{Y}^0 - \mathbf{Y}^0 \left(\mathbf{Y}^{gy} + \mathbf{Y}^0\right)^{-1} \mathbf{Y}_0 &= \left(\mathbf{I} - \left(\mathbf{Y}^{gy} \, \mathbf{Z}^0 + \mathbf{I}\right)^{-1}\right) \mathbf{Y}^0 \\
&= \left(\mathbf{Y}^{gy} \, \mathbf{Z}^0 + \mathbf{I}\right)^{-1} \left(\mathbf{Y}^{gy} \, \mathbf{Z}^0 + \mathbf{I} - \mathbf{I}\right) \mathbf{Y}^0 \\
&= \left(\mathbf{Y}^{gy} \, \mathbf{Z}^0 + \mathbf{I}\right)^{-1} \mathbf{Y}^{gy} \\
&= \left(\mathbf{Z}^0 + \mathbf{Z}^{gy}\right)^{-1} \qquad\qquad \square
\end{aligned}$$

where the last two lines can again be proven by using the identity in equation (5.7). This completes the desired proof to show that equation (5.6) is true. Note that a similar result for the coupling of gyroscopic terms was found in [23, appendix C], though not derived from FBS but from pure linear algebra.

Remark 5.1: Note that above it was implicitly assumed that the rotor's inertia tensor $\boldsymbol{\Theta}_r$ is independent of the actual rotation angle Ωt (i.e. $\Theta_{r,zz} = \Theta_{r,yy} = const.$) and that frame of reference T is a principal axes system for the inertia tensor ($\boldsymbol{\Theta}_r$ is a diagonal matrix). These properties are true for components which are often referred to as 'isotropic rotating component' [23]. The gyroscopic matrix $\mathbf{G}$ of the above example is representative for these isotropic rotation components, as can be seen from the Euler equations for the rotor (second line of equation (2.58)):

$$\boldsymbol{\Theta}_r \, \ddot{\boldsymbol{\theta}}_{op} + \dot{\boldsymbol{\theta}}_T \times \boldsymbol{\Theta}_r \, \dot{\boldsymbol{\theta}}_{op} = \mathbf{m},$$

where $\dot{\boldsymbol{\theta}}_{op} = [\Omega \quad \beta \quad \gamma]^T$ is the angular velocity of the rotor, and $\dot{\boldsymbol{\theta}}_T = [0 \quad \beta \quad \gamma]^T$ is the angular velocity of the tower fixed coordinate system T. In a linear analysis, one considers only small rotations and a constant rotor operating speed, i.e. $\gamma \ll 1$, $\beta \ll 1$ and $\Omega = const.$, which means $\ddot{\boldsymbol{\theta}}_{op} = [0 \quad \dot{\beta} \quad \dot{\gamma}]^T$. Inserting this in the above Euler equations for the rotor yields:

$$\begin{bmatrix} 0 \\ \Theta_{r,yy}\ddot{\beta} \\ \Theta_{r,zz}\ddot{\gamma} \end{bmatrix} + \begin{bmatrix} (\Theta_{r,zz} - \Theta_{r,yy})\dot{\beta}\dot{\gamma} \\ \Omega\Theta_{r,xx}\dot{\gamma} \\ -\Omega\Theta_{r,xx}\dot{\beta} \end{bmatrix} = \begin{bmatrix} 0 \\ m_\beta \\ m_\gamma \end{bmatrix}.$$

With the degrees of freedom $\mathbf{q} = \begin{bmatrix} \gamma & \beta \end{bmatrix}^T$ and linearizing for only small perturbations (i.e. assuming small $\dot{\beta}$ and $\dot{\gamma}$ and neglecting terms of higher order), we get the same gyroscopic matrix $\mathbf{G}$ as in (5.2).

5.2 Coupling gyroscopic effects to measured FRFs

The gyroscopic effects contained in the 2×2 matrix $\mathbf{Y}^{gy}$ can be analytically modeled by knowing the rotational inertia of the rotor around its rotation axis, i.e. $\Theta_{r,xx}$, and the opera-

tional speed of the component Ω. So far, the system matrices $\mathbf{Y}^0$ and $\mathbf{Y}^{op}$ were also both 2×2 matrices and the DoF were only the two rotations that actually tilted the rotational axis in space, so the gyroscopic effects could be directly coupled. However, in practice the matrices $\mathbf{Y}^0$ and $\mathbf{Y}^{op}$ will likely contain a larger set of DoF and the gyroscopic effects shall only be coupled in the DoF subspace that is tilting the rotational axis of the rotor. This will be explained in the following.

Consider the situation depicted in figure 5.1b. The wind turbine is equipped with a rigid fixture on which some sensors (indexed with k) are mounted and some force inputs (indexed with h) can be applied. Usually, the set of measurements is performed on the idling component and the single measurement channels, grouped in the vector $\mathbf{u}$, do not directly correspond to the tilting angles of the rotor axis $\mathbf{q}$. Likewise, the applied forces, grouped in the vector $\mathbf{f}$, do not directly correspond to the tilting moments of the rotor axis $\mathbf{m}$. Consider the *kinematic assumption* of rigidity for the wind turbine to be valid. Then the linearized response in e.g. the z-channel of sensor k due to a small β and γ is:

$$u_z^k = \left(\mathbf{e}_z^k\right)^T \left(\begin{bmatrix} 0 & \beta & \gamma \end{bmatrix}^T \times \mathbf{r}^k\right) = \left(\mathbf{e}_z^k\right)^T \begin{bmatrix} r_z^k & -r_y^k \\ 0 & r_x^k \\ -r_x^k & 0 \end{bmatrix} \begin{bmatrix} \beta \\ \gamma \end{bmatrix}. \tag{5.8}$$

The resulting moments $\mathbf{m}^h$ in the axis tilting directions, due to one force input f^h are:

$$\mathbf{m}^h = \begin{bmatrix} m_\beta^h \\ m_\gamma^h \end{bmatrix} = \begin{bmatrix} r_z^h & 0 & -r_x^h \\ -r_y^h & r_x^h & 0 \end{bmatrix} \mathbf{e}^h f^h, \tag{5.9}$$

where $\mathbf{r}$ denotes the position vectors of sensors / forces and $\mathbf{e}$ denotes their unit direction vectors (see figure 5.1b). Similar to (5.8) and (5.9), one finds general expressions between all sensor channels / force inputs ($\mathbf{u}$ and $\mathbf{f}$) and the tilting angles / tilting moments ($\mathbf{q}$ and $\mathbf{m}$). This is equivalent to the VPT explained in section 3.3, when the IDM matrices are constructed with only considering the tilting rotation angles. Thus, for the wind turbine example, one can find the FRF matrix $\mathbf{Y}_{uf}^0$, measured between force impacts and sensor channels, from the 2×2 FRF matrix in the subspace of the tilting angles $\mathbf{Y}_{qm}^0$:

$$\mathbf{u} = \mathbf{R}_u \mathbf{q}, \qquad\qquad \mathbf{m} = \mathbf{R}_f^T \mathbf{f}, \qquad\qquad \mathbf{Y}_{uf}^0 = \mathbf{R}_u \mathbf{Y}_{qm}^0 \mathbf{R}_f^T, \tag{5.10}$$

$$\mathbf{q} = \underbrace{\left(\mathbf{R}_u^T \mathbf{R}_u\right)^{-1} \mathbf{R}_u^T}_{=:\mathbf{T}_u} \mathbf{u}, \qquad \mathbf{f} = \underbrace{\mathbf{R}_f \left(\mathbf{R}_f^T \mathbf{R}_f\right)^{-1}}_{=:\mathbf{T}_f^T} \mathbf{m}, \tag{5.11}$$

where $\mathbf{R}_u$ and $\mathbf{R}_f$ contain the kinematic assumption for relating the tilting angles and tilting moments to the set of measured channels. As in section 3.3, the matrices $\mathbf{T}_u$ and $\mathbf{T}_f^T$ are the pseudo inverses of $\mathbf{R}_u$ and $\mathbf{R}_f$ (i.e. $\mathbf{T}_u \mathbf{R}_u = \mathbf{T}_f \mathbf{R}_f = \mathbf{I}$, with the weighting matrices $\mathbf{W}$ chosen to be the identity.).

$\mathbf{T}_u$ transforms measured signals $\mathbf{u}$ to the tilting angles $\mathbf{q}$, and $\mathbf{T}_f^T$ determines a minimal set of forces $\mathbf{f}$ for producing a specific tilting moment $\mathbf{m}$. The subscript $(\star)_{uf}$ refers to the FRF matrix being measured between force inputs and sensor channels. The subscript $(\star)_{qm}$ denotes a FRF matrix being measured in the subspace of the tilting angles, i.e. the 2×2 matrices that have been treated in section 5.1. The goal is to predict the FRF matrix of the operating system $\mathbf{Y}_{uf}^{op}$ from the measured FRF matrix of the idling component $\mathbf{Y}_{uf}^0$ and the known gyroscopic admittance $\mathbf{Y}_{qm}^{gy}$. The FBS coupling needs to ensure compatibility between the tilting angles of the idling component (inferred from the measured sensor channels $\mathbf{u}$ via (5.11)) and the tilting angles of the 'gyroscopic substructure' $\mathbf{Y}_{qm}^{gy}$. This compatibility is stated in equations (5.12) and (5.13). The gyroscopic reaction moments needed for ensuring compatibility are denoted as $\boldsymbol{\lambda}$. The reaction moments have to be projected to an

equivalent set of forces for applying them to the measured FRF $\mathbf{Y}^0_{uf}$ (via $\mathbf{T}^T_f$, which is stated in (5.12)). The formulation of the coupling is stated as:

$$\mathbf{Y}^{0|gy}\,\left(\mathbf{f} + \mathbf{B}^T_f \boldsymbol{\lambda}\right) = \begin{bmatrix} \mathbf{Y}^0_{uf} & \mathbf{0} \\ \mathbf{0} & \mathbf{Y}^{gy}_{qm} \end{bmatrix} \left(\begin{bmatrix} \mathbf{f}^0 \\ \mathbf{0} \end{bmatrix} + \begin{bmatrix} \mathbf{T}^T_f \boldsymbol{\lambda} \\ -\boldsymbol{\lambda} \end{bmatrix} \right) = \begin{bmatrix} \mathbf{u}^0 \\ \mathbf{q}^{gy} \end{bmatrix} = \mathbf{u}, \qquad (5.12)$$

with:

$$\begin{aligned} &\mathbf{B}_u \mathbf{u} = \mathbf{0}, \\ &\text{where} \quad \mathbf{B}_u = \begin{bmatrix} \mathbf{T}_u & -\mathbf{I} \end{bmatrix}, \qquad \text{and} \qquad \mathbf{B}_f = \begin{bmatrix} \mathbf{T}_f & -\mathbf{I} \end{bmatrix}. \end{aligned} \qquad (5.13)$$

This coupling corresponds to the weak coupling already shown in section 3.3.3 (see equation (3.45)). The coupling of two substructures is performed only in the subspace of the axis tilting directions. Solving the system in equation (5.12) (e.g. by inserting into equation (3.45)), results in:

$$\mathbf{Y}^{op}_{uf} = \mathbf{Y}^0_{uf} - \mathbf{Y}^0_{uf}\mathbf{T}^T_f \left(\mathbf{Y}^{gy}_{qm} + \mathbf{T}_u\mathbf{Y}^0_{uf}\mathbf{T}^T_f\right)^{-1}\mathbf{T}_u\mathbf{Y}^0_{uf}. \qquad (5.14)$$

Only the resulting part of the full DoF matrix $\mathbf{Y}^{op}_{uf}$ has been stated, since this was the desired outcome. Note that there are no external moments on the 'gyroscopic substructure', only the reaction moments $\boldsymbol{\lambda}$ for enforcing compatibility (see the 'zero' entry in the external forces $\mathbf{f}$ in (5.12)).

Remark 5.2: For the example of the wind turbine, the above result is equal to just expanding the matrix of the operational system from (5.5), which is restated here:

$$\mathbf{Y}^{op}_{qm} = \mathbf{Y}^0_{qm} - \mathbf{Y}^0_{qm} \left(\mathbf{Y}^{gy}_{qm} + \mathbf{Y}^0_{qm}\right)^{-1} \mathbf{Y}^0_{qm}$$

The expansion of a matrix to the sensor channels and force inputs can be done via:

$$\mathbf{Y}^{op}_{uf} = \mathbf{R}_u \mathbf{Y}^{op}_{qm} \mathbf{R}^T_f \qquad\qquad \mathbf{Y}^0_{uf} = \mathbf{R}_u \mathbf{Y}^0_{qm} \mathbf{R}^T_f$$

Starting from (5.14) with the definitions of the transformation matrices in (5.11) it is easy to show:

$$\mathbf{Y}^{op}_{uf} = \mathbf{Y}^0_{uf} - \mathbf{Y}^0_{uf}\mathbf{T}^T_f \big(\mathbf{Y}^{gy}_{qm} + \underbrace{\mathbf{T}_u\mathbf{Y}^0_{uf}\mathbf{T}^T_f}_{=\mathbf{Y}^0_{qm}}\big)^{-1}\mathbf{T}_u\mathbf{Y}^0_{uf}$$

$$= \mathbf{Y}^0_{uf} - \underbrace{\mathbf{Y}^0_{uf}\mathbf{T}^T_f}_{=\mathbf{R}_u\mathbf{Y}^0_{qm}} \left(\mathbf{Y}^{gy}_{qm} + \mathbf{Y}^0_{qm}\right)^{-1} \underbrace{\mathbf{T}_u\mathbf{Y}^0_{uf}}_{=\mathbf{Y}^0_{qm}\mathbf{R}^T_f}$$

$$= \mathbf{R}_u \underbrace{\left(\mathbf{Y}^0_{qm} - \mathbf{Y}^0_{qm}\left(\mathbf{Y}^{gy}_{qm} + \mathbf{Y}^0_{qm}\right)^{-1}\mathbf{Y}^0_{qm}\right)}_{\mathbf{Y}^{op}_{qm}} \mathbf{R}^T_f \qquad\qquad \square$$

(a) $c_\varphi = 1000$ **(b)** $c_\varphi = 100$

Figure 5.2: FRF between impact point h in y-direction and sensor k in y-direction (cf. figure 5.1b). Comparison of idle FRF Y_{uf}^0, reference solution Y_{uf}^{op} which is obtained for solving the full system without the kinematic assumption of rigidity, and the dynamic substructuring result $Y_{uf}^{op,DS}$, obtained with equation (5.14).

5.3 Analysis of kinematic assumptions

In the previous section, it was shown that the suggested FBS approach yields the exact solution, provided the kinematic assumption of rigidity, for relating the axis tilting motion to the sensor motion, is valid. This section shall highlight the importance of this assumption for the quality of the results. Consider the situation in figure 5.1c, with a spring c_φ between the tower and the rotor. Assume the FRF measurements $\mathbf{Y}_{uf}^0$ between the sensors and impacts on the tower as shown in figure 5.1b, shall still be used for coupling the gyroscopic effects $\mathbf{Y}_{qm}^{gy}$. The kinematic assumption of a rigid connection between the sensors and the rotor axis will be deteriorated as c_φ is reduced. In fact, the system has three coordinates now $\mathbf{q} = [\gamma\ \beta\ \varphi]^T$, where φ describes the absolute angle of the rotor as it tilts over. For a very stiff c_φ, the coordinates β and φ will be almost identical, which means the kinematic assumption of rigidity is valid. However, for a reduced c_φ the kinematic assumption can become unacceptably violated. The result for an arbitrary choice of parameters[4] is shown in figure 5.2. It can be seen that the response of the idle system shows only one resonance peak, since in the case shown, with an excitation in the y-direction, one is only exciting a rotation around the z-axis (i.e. the coordinate γ). The rotations of the two free coordinates (β and φ) are decoupled from each other in the idle case. The gyroscopic reaction moments introduce a DoF coupling and their resonances start to show up in this FRF as we introduce a rotor velocity $\Omega \neq 0$. Due to the significant difference between idle and operational FRF, it can be argued that a consideration of the gyroscopic effects in this case is essential for an accurate estimate of the FRF at different operating speeds. The results for differing stiffnesses c_φ (cf. figure 5.2a and figure 5.2b) also show that an accurate consideration of the structure kinematics is vital for good results.

(a) electric climate compressor
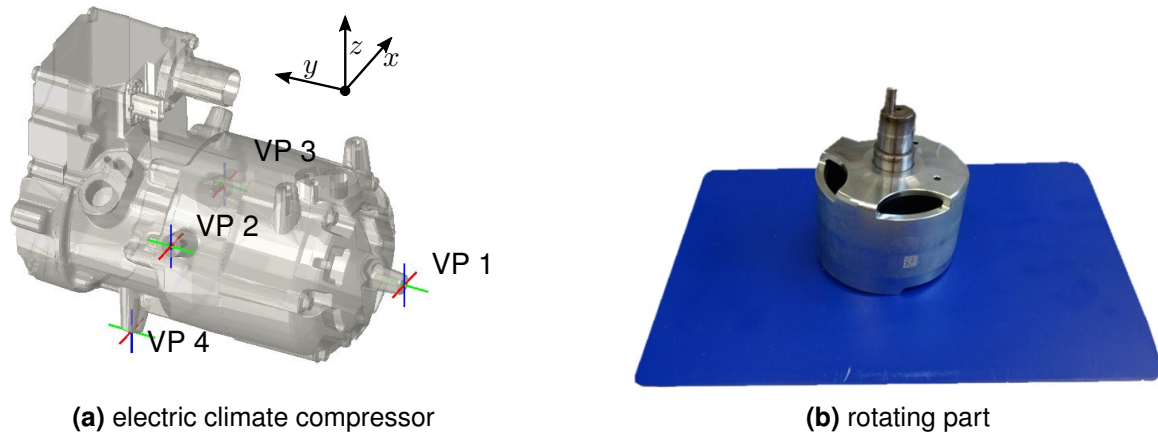
(b) rotating part

Figure 5.3: Schematic depiction of the compressor with the four virtual points for coupling indicated as VP. The rotating part of the compressor was disassembled, weighed on a scale and the dimensions were taken with a caliper. Thereby the rotational inertia of the rotating part could be estimated from superposition of simple geometric shapes (disks, hollow cylinders, etc.).

5.4 Free-free compressor

For obtaining an accurate substructured FRF of the compressor assembled to a vehicle, or accurate blocked forces (see section 6.2) for a source description, it is important that the FRF of the compressor is valid. In general, one would make an error when coupling the compressor to a structure or computing blocked forces with an FRF that was recorded on the idling component. Reichart [144] has shown that on a relatively stiff compressor testrig, which does not allow for compressor rigid body motion, the gyroscopic effects can be neglected. This becomes clear from the basic equations of linear dynamics in the frequency domain:

$$\left(-\omega^2\mathbf{M} + i\,\omega(\mathbf{C} + \mathbf{G}) + \mathbf{K}\right)\mathbf{u}(\omega) = \mathbf{f}(\omega), \tag{5.15}$$

where $\mathbf{M}, \mathbf{C}, \mathbf{G}, \mathbf{K}$ are the mass, damping, gyroscopic and stiffness matrix respectively. For higher frequencies the mass term $-\omega^2\mathbf{M}$ in the equations dominates the dynamic stiffness. For a stiff design without rigid body motion, the stiffness term $\mathbf{K}$ will dominate in the lower frequency region. However, in case of a freely hung up compressor (e.g. for obtaining the blocked forces, as will be done in chapter 11) or for a compressor which shall be suspended with relatively soft rubber bushings (which will be the case in the vehicle example in chapter 11), the gyroscopic effects might have to be considered.

The necessity for coupling the gyroscopic terms for these cases, will be checked in this section. Therefore, the FRF of the idle compressor was modeled from its rigid body properties (taken from the CAD model), since it was known that the compressor can be modeled as a rigid in the lower frequency region. It was intended to couple the compressor at 4 points, which are all treated as a full virtual point with six DoF, resulting in a 24×24 compressor FRF matrix ready for FBS coupling (see figure 5.3a). The gyroscopic effects can be modeled by the rotational inertia and operational speed of the rotating parts. These were estimated from the weight and geometric dimensions of the compressor rotor, see figure 5.3b. The speed dependent gyroscopic matrix $\mathbf{Y}_{qm}^{gy}$ can then be coupled to the full FRF matrix of the compressor, via equation (5.14). Some of the resulting FRFs for the minimum and maximum speed of the compressor can be seen in figure 5.4. It can be seen that for higher operational

---

[4]All parameter appearing in the system matrices of (5.2) are set to 1 apart from: $c_\gamma = c_\beta = 10; h_r = 2, \Omega = 10$.

Compressor speed 8600rpm

Compressor speed 860rpm
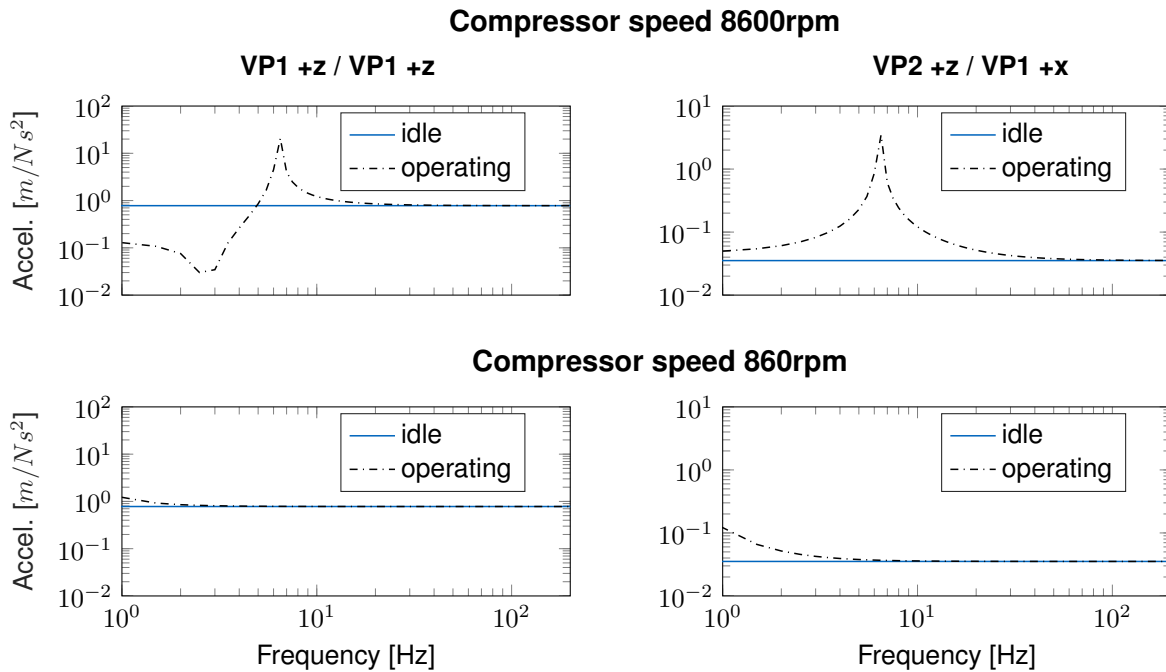
Figure 5.4: Compressor FRFs for maximum and minimum operational speed, 8600rpm and 860rpm, for certain DoF which can be seen in figure 5.3a.

speeds the gyroscopic effects clearly influence the FRFs at lower frequencies[5] up to about 30Hz. For higher frequencies they become negligible again, due the the dominating mass term in the dynamic equations (see equation (5.15)).

5.5 Conclusion

It was shown how gyroscopic effects of rotating components in a substructure can significantly alter its dynamic behavior. The proposed method can be used as a comparatively easy way for considering these gyroscopic effects in a dynamic model, without the need for performing a new set of measurements for each operating speed. It is well suited for providing the doubting engineer with evidence regarding the importance of gyroscopic effects in a specific design. The presented method could prove particularly valuable for components that are relatively compact, e.g. electric motors and compressors in stiff housings. Though not shown in this chapter, the kinematic assumptions, for inferring the rotor tilting angles from a set of measurement channels, doesn't have to be rigidity. If e.g. a finite element model of the component is available, one might determine the modal participation of important modes from a set of measurements and get the tilting angles from those modal participations (reduction matrices $\mathbf{R}_u$ and $\mathbf{R}_f$ would change). Also the general idea of this chapter, namely to use concepts from dynamic substructuring for coupling a non-measurable physical effect to a measured substructure, may also be transferable to other problems.

For the compressor though, it was decided to not consider the gyroscopic effects further in the analyses. The reason for this decision is that the important excitation frequencies

---

[5]This effect can be felt very clearly, when trying to tilt the freely hanging compressor while it is in operation. This personal experience was one of the reasons for the author to investigate this effect in more detail. Note that this manual experiment was of course done with all necessary personal precautions, but not trying it was not an option due to curiosity of the author.

of the compressor start at the first operational order. As the rotational speed of the compressor is increased, the gyroscopic effects gain importance (see figure 5.4). At the same time however, the first order of the compressor increases as well. For 8600rpm the first compressor order is at ca. 143Hz, which is well above the frequency where the gyroscopic effects still have a significant influence on the FRFs, see figure 5.4. The same is true for all other operational speeds and therefore it was chosen to not consider these effects anymore. Nevertheless, it is reassuring to have clarity on this point.

Part II

Independent modeling of structural source excitation

Chapter 6

Transfer path analysis

Contents:

> You shouldn't do things differently just
> because they're different. They need to
> be... better.

Elon Musk

The contents of this chapter were published in similar form in [59]. The text hereafter has been modified and adapted to the thesis.

In part I, it was shown how to obtain the transfer functions of a whole assembly, from coupling the FRF matrices of the sub-components. The FRF matrices of the sub-components can be obtained from either experiment or analytic/numerical models (see chapter 2). For predicting the expected sound and vibration of the assembly, it is now important to investigate the origin of the vibrations, namely the vibration source. The general problem can be described by the situation shown in figure 6.1a. An assembly AB contains a vibration source A which is subject to internal loads $\mathbf{f}_1^A$. These forces are transferred to the DoF $\mathbf{u}_3^B$ in the receiver, via the transfer function $\mathbf{Y}_{31}^{AB}$ of the coupled system:

$$\mathbf{u}_3^B = \mathbf{Y}_{31}^{AB}\mathbf{f}_1^A. \tag{6.1}$$

In the specific case of this thesis, the source A is an electric climate compressor, but it could be any other active component. The internal forces $\mathbf{f}_1^A$ are caused by imbalance in the rotor, the motor pole-pairs passing each other, compression shocks in the refrigerant fluid, high frequency excitations from the inverter, etc. However, in many practical cases, the source is a supplier part or is developed by a different department. The exact mechanisms creating the internal forces $\mathbf{f}_1^A$ and the location of their DoF might then be unknown or cumbersome to model. It is therefore desirable for an NVH engineer to find another more abstract, yet complete description of the source. This is a typical situation where transfer path analysis (TPA) can be employed.

TPA has established in industry as a tool for NVH trouble shooting. A broad review and comparison of methods in a unified notation can be found in [159]. There, important pioneering publications are referenced and put in context. In general, with TPA one studies machines that are actively exciting a final assembly and thereby causing noise and vibrations. As one of the first applications, Verheij described the transmission of vibrations from a ship engine to the hull by interface forces transmitted over the rubber isolators [184]. TPA is nowadays

(a) Source receiver problem

(b) Classical TPA

(c) Blocked source
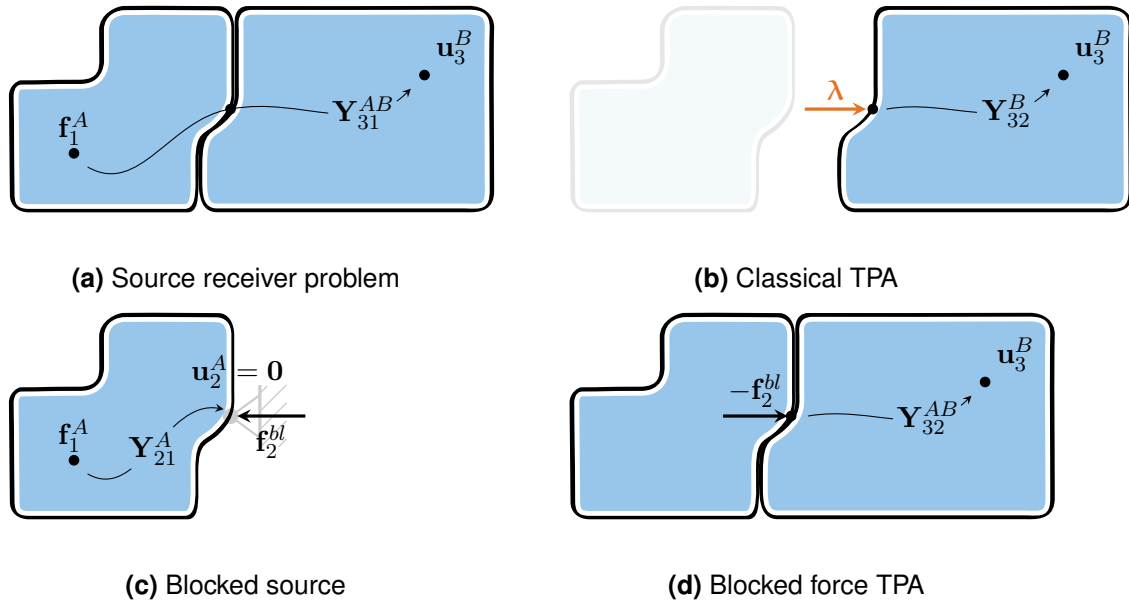
(d) Blocked force TPA

Figure 6.1: Overview of the source receiver problem and the description of the vibration transmission on the interface by classic and the blocked force TPA.

commonly applied in NVH engineering of vehicles [139, 183]. Classically, TPA has been used as trouble shooting tool, using interface forces to understand the transmission of vibrations from the source to the receiver. A current trend is to use approaches which describe the source independently from a specific receiver via blocked forces [39, 93, 160]. A popular method for obtaining the blocked forces is the in-situ method [120], which will also be used in this thesis.

6.1 Classical TPA

All excitation from the source has to enter the receiver over the interface DoF, subscript $(\star)_2$. The classic approach to TPA describes the excitation that source A excerts on the receiver B, via the interface forces $\boldsymbol{\lambda}$ (see figure 6.1b):

$$\mathbf{u}_3^B = \mathbf{Y}_{32}^B \, \boldsymbol{\lambda}, \tag{6.2}$$

where $\mathbf{Y}_{32}^B$ is the transfer function of the receiver B alone, i. e. decoupled from the source. The above statement is the response on structure B for the case that the interface forces $\boldsymbol{\lambda}$ are known (e.g. from substructuring, equation (3.9)). It is assumed that the receiver B is a purely passive structure with no external forces (i.e. $\mathbf{f}_2^B$ and $\mathbf{f}_3^B$ are zero in the verbose equation (3.5)). With classical TPA, one compares the contribution of each interface force, contained in the vector $\boldsymbol{\lambda}$, to the final vibration response $\mathbf{u}_3^B$. A common way of trouble shooting NVH problems is to decreas the coupling stiffness between source and receiver in the interface DoF with the highest contribution to the response $\mathbf{u}_3^B$. This is done by e.g. introducing (softer) rubber bearings in these connection points and directions [139]. When the internal DoF and their exciation $\mathbf{f}_1^A$ are known, the interface forces can be computed by equation (3.9). As already discussed, this is most often not the case so different methods for obtaining $\boldsymbol{\lambda}$ can be applied in practice. An overview of methods can be found in [159].

6.2 Blocked force TPA

As already mentioned, the classical TPA approach is often used as a trouble-shooting tool in the late development phase. The identified interface forces λ cannot be used for simulating a substantial design optimization of the receiver B. They are dependent on a specific version of B. This can be seen from equation (3.9), where the formula for computing λ also contains the admittance of the receiver $\mathbf{Y}^B$. In practice, this means that the interface forces that were once identified in a specific design are not valid for a modified design. This makes intuitive sense. Consider an initial connection between source and receiver that is dynamically 'stiff'. The interface forces λ will have a certain magnitude. If the coupling stiffness is decreased, the magnitude of the interface forces will diminish (or ultimately tend to zero if the connection is loosened completely).

This is a typical case where using the so-called 'blocked force' or 'component based' TPA should be used. Consider the following thought experiment: The operating source is rigidly clamped on its interface so that the interface vibration $\mathbf{u}_2^A$ is zero, see figure 6.1c. The reaction forces in the clamped support are called 'blocked forces' $\mathbf{f}_2^{bl}$ and ensure that:

$$\mathbf{0} \stackrel{!}{=} \mathbf{u}_2^A = \mathbf{Y}_{21}^A \mathbf{f}_1^A + \mathbf{Y}_{22}^A \mathbf{f}_2^{bl}. \tag{6.3}$$

If $\mathbf{f}_2^{bl}$ could be applied as an *external* load in the interface between source and receiver (remember this is just a thought experiment) then they would act on the source, just like before, as a perfect clamping support. The motion on the interface of the assembly AB would thus also be zero:

$$\mathbf{0} \stackrel{!}{=} \mathbf{u}_2^{AB} = \mathbf{Y}_{21}^{AB} \mathbf{f}_1^A + \mathbf{Y}_{22}^{AB} \mathbf{f}_2^{bl}. \tag{6.4}$$

However, if the assembly AB has no motion on the interface, and there is no other vibration source on the receiver B, then also the vibration at all other points in the receiver $\mathbf{u}_3^B$ would be zero:

$$\mathbf{0} \stackrel{!}{=} \mathbf{u}_3^B = \mathbf{Y}_{31}^{AB} \mathbf{f}_1^A + \mathbf{Y}_{32}^{AB} \mathbf{f}_2^{bl}. \tag{6.5}$$

The blocked forces act like a noise cancellation on the source. Another way to get to this result is to see that the interface gap $\Delta \mathbf{u}_2$ in equation (3.9), and thus also the Lagrange multipliers λ would be zero. This is the theoretical basis for the blocked force concept (or in fact all equivalent force concepts in TPA, see [159]). Of course, the discussion so far was just a thought experiment (artificially applying the blocked forces to the interface DoF of the assembly AB is usually not possible). However, since the assembly AB is modelled as a linear time invariant system, it is allowed to add and subtract the effect of the blocked forces from the original problem in equation (6.1) without modifying the outcome (superposition principle):

$$\mathbf{u}_3^B = \mathbf{Y}_{31}^{AB} \mathbf{f}_1^A + \overbrace{\mathbf{Y}_{32}^{AB} \mathbf{f}_2^{bl} - \mathbf{Y}_{32}^{AB} \mathbf{f}_2^{bl}}^{=\mathbf{0}}. \tag{6.6}$$

Using the blocking effect on the original excitation $\mathbf{f}_1^A$ from equation (6.5), one finds that:

$$\boxed{\mathbf{u}_3^B = -\mathbf{Y}_{32}^{AB} \mathbf{f}_2^{bl}.} \tag{6.7}$$

Notice that the derivation did not specify which particular receiver structure B is used. The blocked forces are thus a valid source description for *any* receiver B. Also note that the blocked forces are a property of the source alone, see equation (6.3). A thorough derivation

of the concept, as well as different methods for obtaining the blocked forces in practice, are described in [159] and a theoretical comparison of these methods is given in [149].

> **Remark 6.1**: An important assumption for the derivation of the blocked force concept, is that the internal source excitation $\mathbf{f}_1^A$ is independent of the source mounting, i.e. the receiver B. This is (to the authors experience) a good assumption for the climate compressor and electric motors, but it may not be justified for other sources. Consider a gearbox whose housing is rigidly connected to a stiff receiver. Due to manufacturing tolerances, the housing is slightly deformed after assembly with the receiver. The resulting misalignment of the gears would be an important mechanism changing the internal loads $\mathbf{f}_1^A$, which is **dependent** on the specific receiver (how much is the housing deformed by the mounting?). Care has to be taken so that this assumption is not violated.

> **Remark 6.2**: The blocked force concept, as well as another component based TPA concept commonly called 'free velocites', are special cases of the two equivalent representations of a forced vibration developed in [18]. They are in fact equivalent to the developments in [18], for the special case where the receiver structure has no external excitations. However, in [18] the framework is extended to cases where one is also interested in the vibration on the source itself, or for cases where there are multiple sources. The paper is an interesting read for those involved with method development in the TPA field.

6.3   Example: in-situ determination of blocked forces

The method used for obtaining the blocked forces in this thesis is called the in-situ blocked force method, to the authors knowledge first introduced in [120]. There, the source is mounted to a structure R which is, in its dynamical behavior, already similar to the final design, see figure 6.2a. The reciever structure R could be a testrig, the final receiver itself, or an early prototype of the final receiver.

Thereby, detrimental effects from a possible violation of the blocked force assumption in remark 6.1 is reduced. The author thinks that this is one of the reasons, why the in-situ approach often yields better results than other approaches for determining the blocked forces. In the example shown in figure 6.2b, the testrig R is equipped with additional sensors that record the vibration while the source is in operation $\mathbf{u}_4^R$. The compressor is connected with 3 bolts to the receiver. The receiver consists of connectors which are themselves bolted to a plate. The plate is bolted to four steel arms which are clamped to a rigid test bed. The test bed is floating on air-springs. Each of the 3 compressor connection points could be treated as a virtual point as described in section 3.3, so the blocked force vector $\mathbf{f}_2^{bl}$ would contain 18 forces and moments in total. This approach can be necessary for describing the high frequent behavior, but can cause stability issues in the solution (this is further treated in chapter 8). In this chapter, the compressor was treated as a rigid body, so only one virtual point is defined in the middle of the compressor housing and in total 6 blocked forces have to be determined. The FRFs from hammer impacts at the interface (see lower right part of figure 6.2b) to all acceleration sensors, i.e. FRF matrices $\mathbf{Y}_{42_f}^{AR}$ and $\mathbf{Y}_{32_f}^{AR}$, are determined by
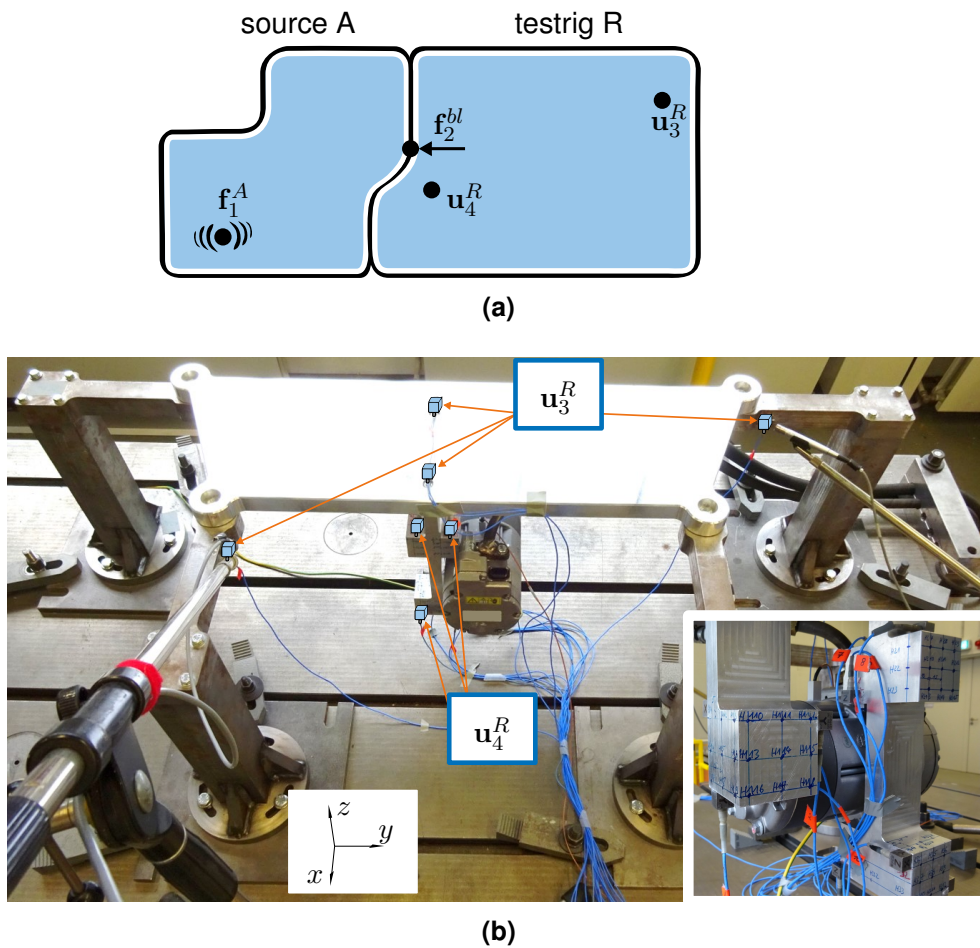
Figure 6.2: Overview of the performed in-situ determination for the blocked forces. a) schematic overview b) picture of the testrig, with attached climate compressor. Lower right part of the figure gives an overview of the connection points between compressor and the testrig, including the sensors for recording $\mathbf{u}_4^R$ and the positions for applying hammer impacts.

hammer impact testing. The hammer inputs are then transformed to virtual point loads, by:

$$\mathbf{Y}_{32_m}^{AR} = \mathbf{Y}_{32_f}^{AR}\mathbf{T}_f^T, \qquad\qquad \mathbf{Y}_{42_m}^{AR} = \mathbf{Y}_{42_f}^{AR}\mathbf{T}_f^T. \qquad (6.8)$$

The number of input columns is thereby reduced from 76 in $\mathbf{Y}_{42_f}^{AR}$ to 6 in $\mathbf{Y}_{42_m}^{AR}$. The transformed matrices with the 6 virtual point loads as input are simply stated as $\mathbf{Y}_{42}^{AR}$ and $\mathbf{Y}_{32}^{AR}$ in the following[1]. The sensors for identifying the blocked forces on the interface $\mathbf{u}_4^R$ were placed as close as possible to the interface with the source, i.e. the compressor (see lower right part of figure 6.2b). This is in accordance with the findings in [192], where the authors investigated the optimal placement of sensors for 'observing' the blocked forces and found that close to the interface generally yields the best results. In total, the vector $\mathbf{u}_4^R$ consisted of 36 signals from 12 triaxial accelerometers. When artificially applying the blocked forces $\mathbf{f}_2^{bl}$ to the interface, they would have to cancel out all vibration on the receiver (as discussed in section 6.2):

$$\mathbf{0} \overset{!}{=} \underbrace{\mathbf{Y}_{41}^{AR}\mathbf{f}_1^A}_{\mathbf{u}_4^R} + \mathbf{Y}_{42}^{AR}\mathbf{f}_2^{bl}, \qquad (6.9)$$

which means for the calculation of the blocked forces,

$$\boxed{\mathbf{f}_2^{bl} = -\left(\mathbf{Y}_{42}^{AR}\right)^+ \mathbf{u}_4^R,} \qquad (6.10)$$

where $(\star)^+$ indicates the least squares pseudo inverse. The pseudo inverse has to be used since the system of equations is overdetermined ($\mathbf{Y}_{42}^{AR}$ is a 36×6 matrix). The pseudo inverse can either be built with least squares, or with a regularized inverse to suppress the detrimental effects of measurement noise even more than with least squares. Some variants for regularizing the inverse problem will be explained and compared in chapter 8.

An initial check that can be done with the computed blocked forces is often called **On-Board validation** (see e.g. [168]). The blocked forces, computed with the signals $\mathbf{u}_4^R$ on the testrig, can be used to predict the vibration at other sensors $\mathbf{u}_3^R$ which were also attached to the testrig (see figure 6.2). These signals were recorded during the same operational measurements as $\mathbf{u}_4^R$, but were not used for the calculation of the blocked forces in equation (6.10). The response in these channels is predicted with the blocked forces, similar to equation (6.7). If the description of the interface is complete, this should yield vibration levels equivalent to the ones actually recorded during the measurement. Comparing the measured $\mathbf{u}_3^R$ and the TPA prediction with the blocked forces, i.e.:

$$\mathbf{u}_3^R \overset{?}{=} -\mathbf{Y}_{32}^{AR}\mathbf{f}_2^{bl}, \qquad (6.11)$$

then serves as an initial validity check of the computed blocked forces. In case the description of the interface loads is inappropriate, e.g. since an important transfer path on the interface was neglected, this would manifest in a bad predictability of the measured $\mathbf{u}_3^R$. Figure 6.3 exemplarily shows the on-board validation for one of the channels in $\mathbf{u}_3^R$, in a third octave plot, a narrowband plot and a hearing comparison in two separate sound files. The prediction is found to be good (also in the other channels), so the blocked forces are assumed to describe the excitation of the compressor sufficiently. Another valuable check for testing the 'completeness' of the interface description can be given by the interface completeness criterion (ICC), as introduced in [113]. Note that the two negative signs in the blocked force identification (6.10) and prediction of responses with the blocked forces (6.11)

---

[1]In chapter 8, each connection is treated as a full virtual point, hence the larger number of impacts.

(a)

(b)

(c)
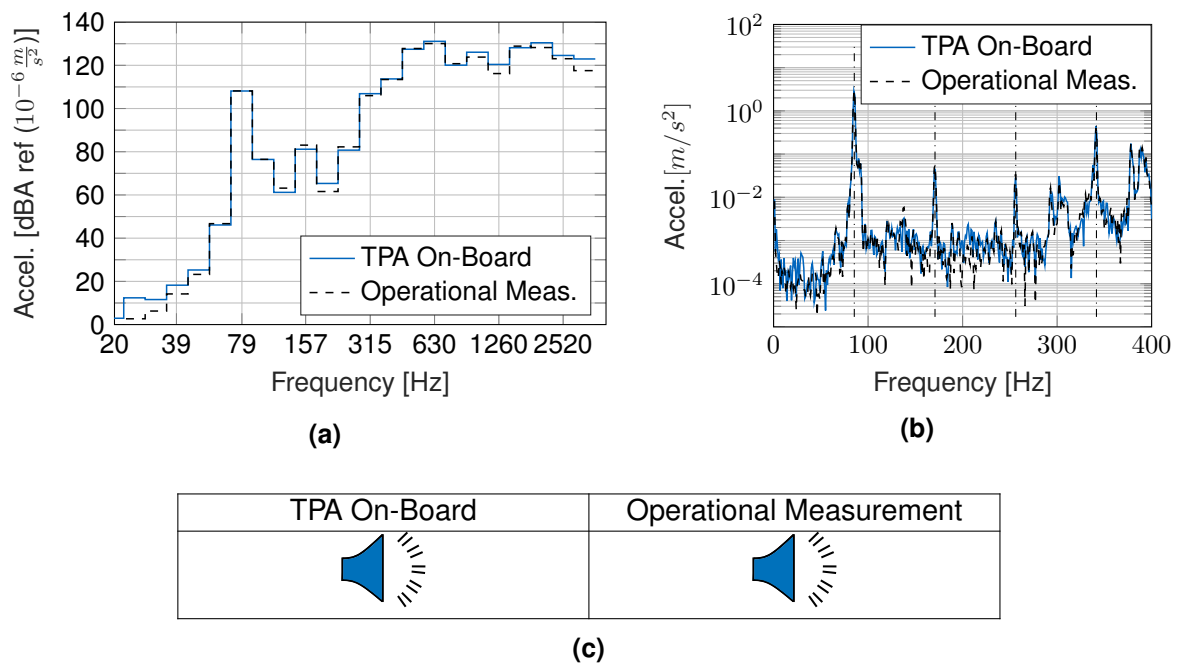
Figure 6.3: On Board validation of in-situ TPA measurements. The operational data was captured at 60% of the compressors maximum rotational speed (first order at $86Hz$). The blocked forces are calculated according to equation (6.10) from the data recorded with accelerometers $\mathbf{u}_4^R$. All plots are showing the prediction for one sensor in the set of $\mathbf{u}_3^R$ (global z-direction of left most sensor in figure 6.2b). (a) Third Octave plot of operational measurement and the prediction via the blocked forces (left and right part of equation (6.11) respectively). (b) Narrow band plot, vertical lines indicate the compressor orders. (c) Sound file of TPA prediction and operational measurement. For audio playback, click on the respective loudspeaker symbol (Adobe Acrobat reader version 9.0 or newer is needed).

are annihilating each other. In the rest of this thesis, the negative sign in the identification and prediction is therefore often dropped for simplicity.

6.4   Computing blocked forces from long time records

So far, all equations and quantities have been stated in the frequency domain, i.e. $\mathbf{u}_4^R$ meant the frequency dependent amplitudes $\mathbf{u}_4^R(\omega)$, which are obtained from a recorded time signal $\mathbf{u}_4^R(t)$. The frequency resolution of the Fourier transform $\mathbf{u}_4^R(\omega)$ depends on the timeblock length T which is taken from a longer time record $\mathbf{u}_4^R(t)$, see equation (2.19). For a time block length $T = 1s$, one would have a frequency resolution of $1Hz$, for $T = 2s$ a frequency resolution of $0.5Hz$, and so on. Of course the frequency resolutions of $\mathbf{Y}_{42}^{AR}$ and $\mathbf{u}_4^R$ have to be equal to perform the operation in equation (6.10) for each frequency.

However, if the frequency resolution of the measured $\mathbf{Y}_{42}^{AR}$ is $1Hz$, as is the case in this example, then also the timeblocks that are taken from $\mathbf{u}_4^R(t)$ must be one second long. Simply taking the long time signal $\mathbf{u}_4^R(t)$ and transforming it to the frequency domain would require to increase the frequency resolution of the inverted matrix $\mathbf{Y}_{42}^{AR}$. Since this would require to invert the matrix at more frequencies, it would result in longer program run-times. Additionally, the blocked force result would not be meaningful for e.g. a run-up of the compressor. If a longer time period shall be included in the blocked force estimation (e.g. for a runup of the compressor), then the signal is cropped into N_b, possibly overlapping, time blocks and the blocked forces are computed for each of these timeblocks individually, see figure 6.4. The frequency dependent signal $\mathbf{u}_4^R(\omega, b)$ and computed blocked forces $\mathbf{f}_2^{bl}(\omega, b)$ are thus also dependent on the specific time block b for which they were computed.
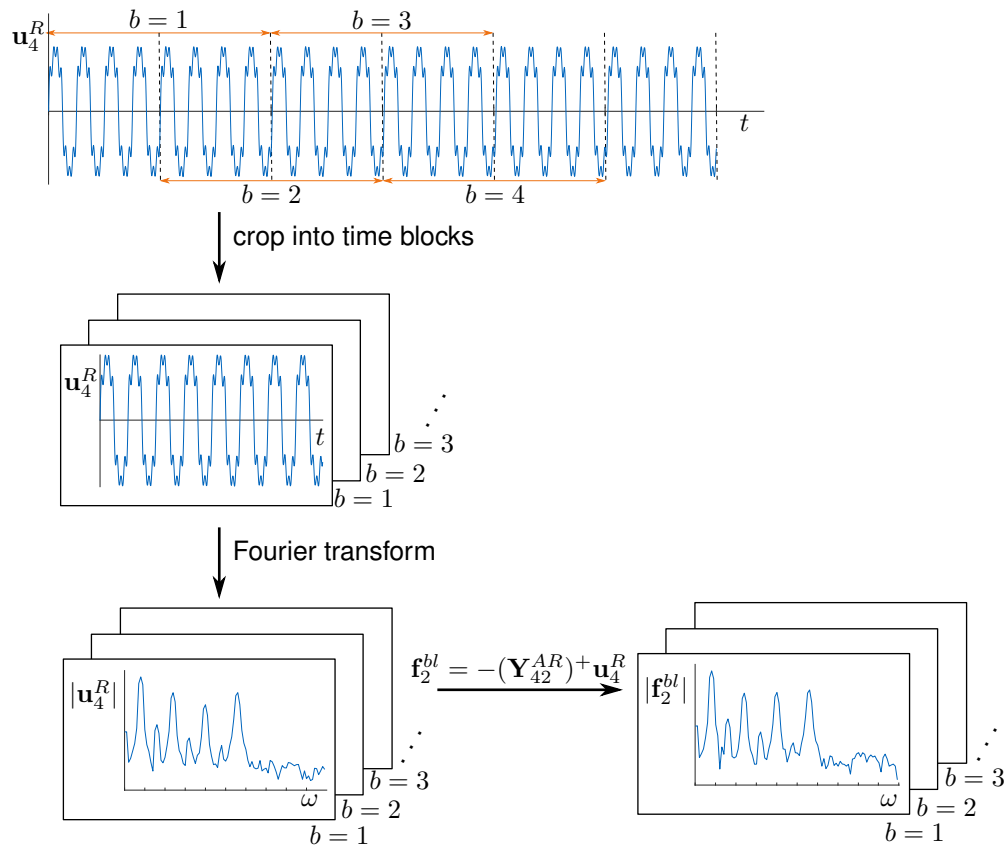
Figure 6.4: Schematic depiction of the blocked force computation for longer operational sequences. The original time signal in all channels $\mathbf{u}_4^R$ is cropped in to N_b possibly overlapping time blocks. These are transformed to the frequency domain where a set of blocked forces is computed for each time block from the operational signal.

Chapter 7

Auralization of TPA results

Contents:

> A good acoustic engineer uses his ears
> as a primary instrument for analysis;
> the measurement technology merely
> serves to confirm already-formed
> presumptions.
>
> *Maarten V. van der Seijs in [157]*

Ultimately, all efforts in NVH engineering are dedicated to maximize the comfort and quality perception of the product user. The inputs to the human hearing system are air pressure fluctuations at both ears in the time domain. However, so far all computations for the coupling of substructures and the computation of the blocked forces were stated in the frequency domain. The numerical evaluation in the frequency domain offers great advantages for computation (a differential equation can be treated as an algebraic equation). Also for understanding issues in the design phase, the frequency domain is well suited (phenomena can be attributed to e.g. resonances). Nevertheless, a result plot in the frequency domain can never fully convey the human impression of the analysis results. For example, humans can perceive frequency differences in individual tones up to 3Hz at a frequency around 1000Hz. This minimum perceivable tone difference increases towards higher frequencies [153, 190]. The field of psycho-acoustics [42] has made great advances in describing the hearing impression of signals represented in the frequency domain by defining quantities such as e.g. loudness, sharpness, roughness and tonality. However, in order to make the results more tangible to non-acoustic experts it was found indispensable to present results in terms of sound files that can be played back in an adequate environment. E.g. when communicating analysis results to vehicle development project managers. Hearing examples greatly simplify the discussions during the NVH development of new products [12, 187, 200]. This invariably means to provide the TPA results in the time domain. This chapter treats the proper handling of this issue. For an undistorted hearing experience, at least a binaural hearing needs to be provided, i.e. at least two channels [46, 132]. Everything in this chapter will be explained on the basis of one input and output channel for clarity of the presentation, but is generally applicable to multiple input and output channels.

The most complete overview on auralization that the author could find is [187]. From [187, chapter 9]:

"If the source signal and the system's transfer function or impulse response are obtained separately, the resulting output signal can be calculated by convolution. The convolution can be processed in various ways, either directly in the time domain by using FIR filters or by using FFT convolution. In the latter case, however, it should be kept in mind that FFT requires fixed block lengths and is related to periodic signals. Time windows might be required for reducing artefacts from discontinuities."

This chapter will summarize the experiences of the author with the use of FFT (cyclic) convolution and FIR filters (non-cyclic convolution). Additionally, some specialties related to the inverse force identification in the blocked force approach will be explained. The author wants to thank Dr. Maarten van der Seijs, Dr. Georg Eisele, and Prof. Bernhard Seeber for the personal communication on this issue.

7.1 Literature on auralization for TPA

Reichart [144] identified the direct airborne radiation of the compressor via its emitted sound power. The sound power lacks information of the signals phase. Thus a method for auralization that assigns a random phase to the individual components was applied [11]. However, the influence of the time windows and the tonal spectrum of the compressor made the auralization difficult. Benner [14] investigated the use of overlapping Hanning windows (see section 7.4) and using time window lengths that were adapted to fit the order frequency of the compressor. The latter approach provided insight but proved infeasible for practical application. Auweraer [181] applies a time domain convolution for auralization. In [182] the authors propose a cyclic convolution for stationary machine operating conditions and a non-cyclic convolution for transient operating conditions, e.g. a run-up.

7.2 Cyclic and non-cyclic convolution

It is not the intent of this chapter to go into full detail on digital signal processing (see e.g. [99]). The basics of the needed computations for creating TPA results in the time domain will be explained in this section. Therefore, a short numeric example in Matlab™ notation is given (following [165, chapter 4]). Assume a simple one degree of freedom system with a discrete impulse response $Y(n)$ and a force input $f(n)$, represented in matrix notation as:

$$Y(n) = \begin{bmatrix} 2 & 3 & 1 \end{bmatrix}, \qquad f(n) = \begin{bmatrix} 5 & 3 & 2 \end{bmatrix}. \tag{7.1}$$

The answer to a single unit impulse, $Y(n)$, is 3 samples long. That means a force input $f(n)$ with 3 impulses will create a response, $u(n)$, that is 5 samples long. It can be obtained by convolution with the impulse response:

$$u(n) = \sum_{\tau=1}^{n} Y(n+1-\tau)\, f(\tau), \qquad \text{resulting in:} \tag{7.2}$$

$$u(n) = \begin{bmatrix} 10 & 21 & 18 & 9 & 2 \end{bmatrix}. \tag{7.3}$$

This is commonly called standard FIR-filtering or non-cyclic convolution. FFT convolution, also called cylclic convolution, is assuming that the force input $f(n)$ is periodically repeating after a number of samples (see section 2.3). Assume this is the case and:

$$f(n) = \begin{bmatrix} \dots & \vdots & 5 & 3 & 2 & \vdots & 5 & 3 & 2 & \vdots & \dots \end{bmatrix}. \tag{7.4}$$

The result of this force input $f(n)$ could be split into overlapping blocks of the responses to the repeating input blocks in $f(n)$ which were computed in equation (7.3). These need to be added in the overlapping parts, to yield the response for a periodic excitation:

$$
\begin{array}{rcccccccc}
u(n) = & \dots & 10 & 21 & 18 & 9 & 2 & \dots & \\
+ & & & \dots & 10 & 21 & 18 & 9 & 2 & \dots \\
+ & & & & & \dots & & & \\
= & & & \dots & 19 & 23 & 18 & \dots &
\end{array}
\tag{7.5}
$$

where the response of the previous input block overlaps with the response of the new input block. This part is cyclically repeating since each input block of the force is the same. The result of this repeating part of the answer can be obtained by using the computationally more efficient approach via the FFT. Again in Matlab™ notation this would mean:

$$Y(\omega) = \texttt{fft}(Y(n)), \qquad\qquad f(\omega) = \texttt{fft}(f(n)), \tag{7.6}$$

$$u(\omega) = Y(\omega) \,.* \, f(\omega), \qquad\qquad u(n) = \texttt{ifft}(u(\omega)), \tag{7.7}$$

assuming the input of equation (7.1) this would result in:

$$u(n) = \begin{bmatrix} 19 & 23 & 18 \end{bmatrix}, \tag{7.8}$$

which is equal to the periodically repeating part of the overlapping block responses that one would get from a partitioned non-cyclic convolution (equation (7.5)). This approach is computationally very efficient and fits perfectly into the framework for the blocked force evaluations based on individual frequency blocks (see figure 6.4).

7.3 TPA Auralization by cyclic convolution

As mentioned, the cyclic convolution is computationally very efficient but is assuming a periodically repeating force input. For the case of the compressor, this means one is assuming that the operating speed is very stable and each time block is covering an integer number of cycles. For investigating the appropriateness of this assumption, the blocked force workflow shall be re-enacted on a simple example in this chapter. The time signal used here was recorded while the compressor was running with 90% of its maximum speed in a freely hung up condition (7740rpm). For the sake of presentation, the signal of one accelerometer channel attached to the compressor was extracted, low-pass filtered (8-pole Butterworth filter, cut off frequency 1000Hz), and used as "operational signal" u^A, see figure 7.1.

Assume this signal was recorded on a simple analytically modeled source A that shall be used for force identification, see figure 7.2a. With its FRF Y^A (see figure 7.2c)[1] and the operational signal u^A, this means for the blocked forces f^{bl}:

$$f^{bl} = \left(Y^A\right)^{-1} u^A, \tag{7.9}$$
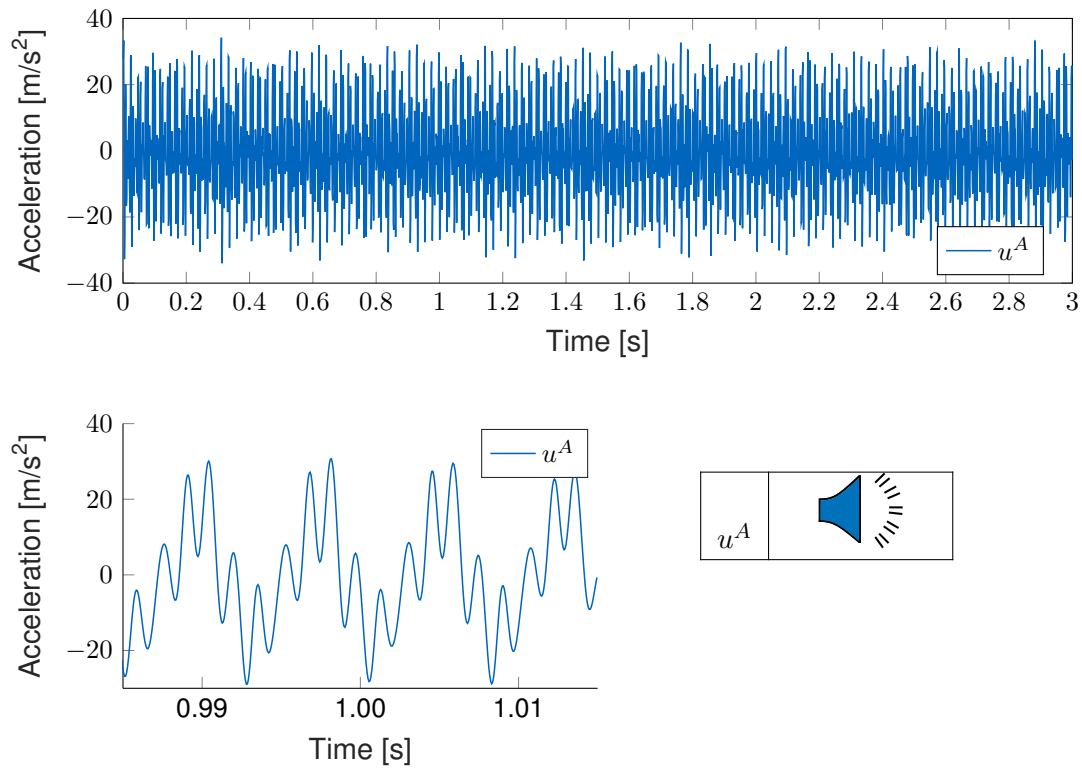
Figure 7.1: Acceleration signal of the freely hung up compressor at 90% of its maximum speed (7740rpm, 129Hz first order). This will be used as example signal u^A used for the blocked force calculation.

(a)   **(b)**   **(c)**
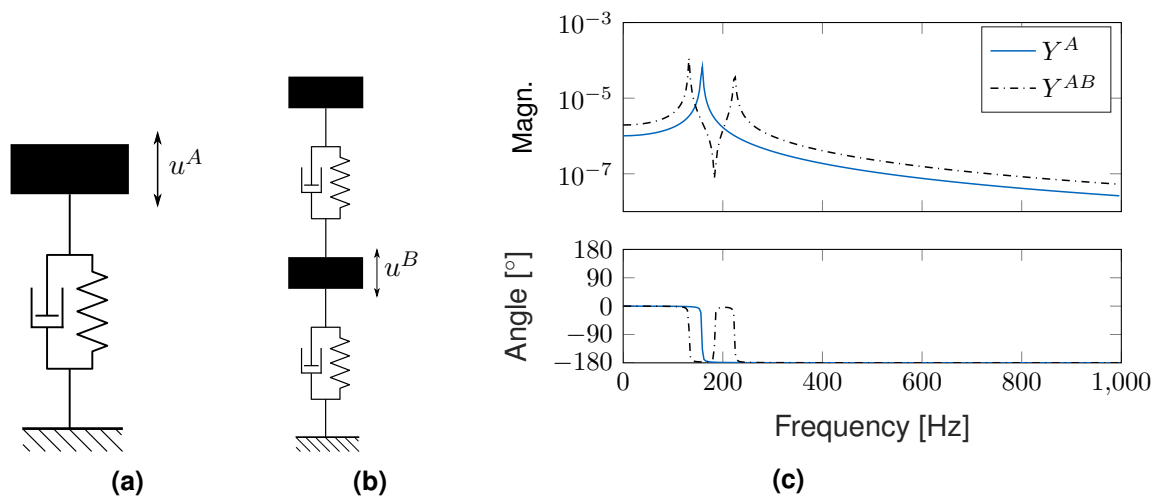
Figure 7.2: Schematic drawing of (a) source with operating signal u^A and FRF Y^A, (b) source attached to receiver with FRF Y^{AB} and response u^B that is to be predicted by blocked force TPA, and (c) the FRFs Y^A and Y^{AB}.

where the above equation is in the frequency domain. The identified blocked forces f^{bl} shall be transferred to a design where the source is attached to a receiver, yielding the modeled source receiver assembly AB, see figure 7.2b. The vibration u^B that would be recorded on this assembly with FRF Y^{AB} (see figure 7.2c) can be computed in the frequency domain as:

$$u^B = Y^{AB} f^{bl}. \tag{7.10}$$

The FRFs Y^A and Y^{AB} are modeled with a frequency resolution of 1Hz. For performing the blocked force identification and transfer (equation (7.9) and (7.10)), the operational signal u^A is cut into 1 second long time blocks. These are transformed to the frequency domain, resulting in frequency blocks with a resolution of also 1Hz. The computations are then performed per frequency and block (see figure 6.4). This results in a response u^B in multiple frequency blocks. For the cyclic convolution, one is assuming that each of these blocks is equal, or at least very similar. The time blocks are successively cut out of the long time signal u^A with no overlap between the individual blocks. For the auralizing the signal u^B with the cyclic convolution, two approaches will be compared:

- **Repeated Block:** Only the first time block of the signal u^A is extracted and processed. The back transformed time block of u^B is then repeated 7 times, so the resulting audio file is 7 seconds long.

- **Subsequent Blocks:** The first 7 time blocks of the signal u^A are extracted and processed. The 7 back transformed time blocks of u^B are appended to each other, so the resulting audio file is 7 seconds long.

The resulting signals and auralizations can be seen in figure 7.3. It can be clearly seen and heard that the resulting audio files are contaminated by jumps in the time signal, which occur at the bounds of the time blocks. These result in spurious clicks in the audio signal. For the results of the repeated block, the jumps result from a violation of the assumption that the compressor is performing an integer number of operational cycles in the time block (leakage). For the subsequent blocks of the signal, also small variations in the operational speed of the compressor come into play, which results in even larger jumps at the time block bounds. Note also that the predicted time signal of u^B is larger at the beginning of each new time block, and smaller at the end of a time block. This phenomenon is also related to leakage. In the cyclic convolution the computation is assuming that the signal is periodic. The identified forces f^{eq} need to enforce the jumps at time block bounds so the forces are large at the beginning and end of the time block. This can be seen when plotting one time block of the identified forces, see figure 7.4.

---

[1]Notice that these simple FRFs are in displacement over force format. This is however not impairing the general results of the derivations in this chapter.
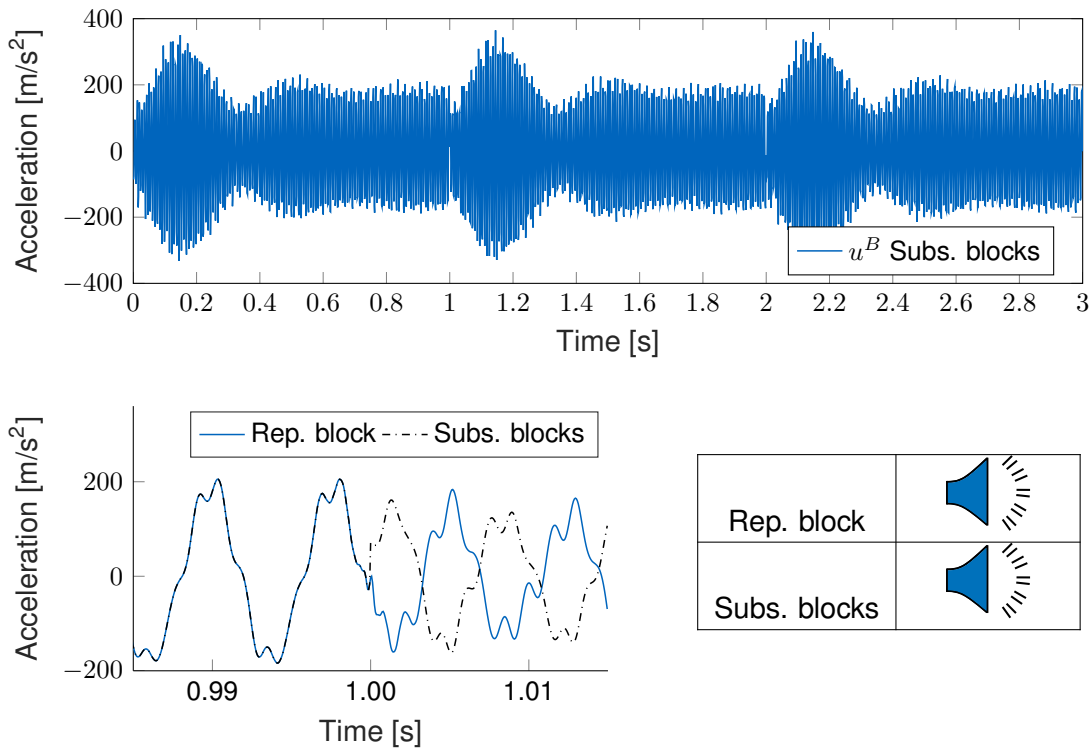
Figure 7.3: Results of the cyclic convolution. Clear "clicks" can be heard in the audio and observed in the timeplots at the bounds between individual time blocks.
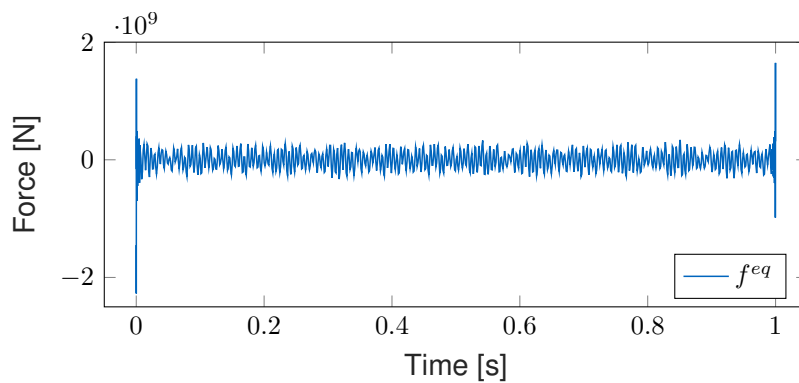
Figure 7.4: Time block of the identified blocked forces f^{bl} for the rectangular windows cut from the signal for u^A. Large increases at the start and end of the force block are needed to force the signals discontinuity at the time block bounds.
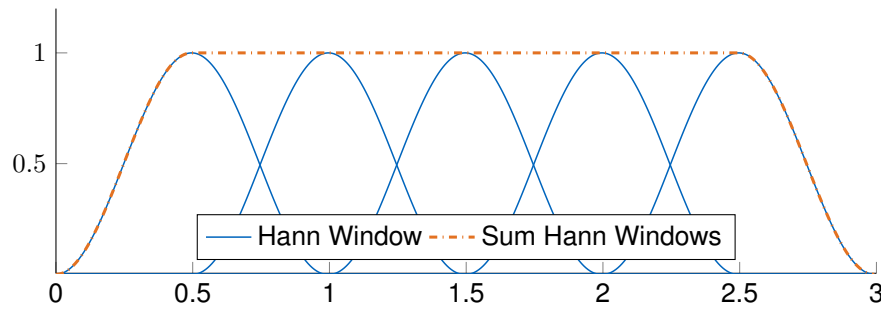
Figure 7.5: Overlapping Hanning windows and sum of the windows

Remark 7.1: One solution for creating sound files without "clicks" is to process the whole operational signal u^A in only one large time block and transforming this into the frequency domain. Since the frequency resolution is then increased, also the FRF needs to be adjusted to the larger frequency resolution (e.g. by interpolation). Nevertheless, this approach results in very large program run times and is infeasible in practice, where a larger matrix $\mathbf{Y}_{42}^{AR}$ needs to be inverted. The number of matrices to be inverted (at each frequency!) simply becomes too large.

Benner [14] investigated using an order tracking algorithm [116], for identifying the exact speed of the compressor in each time block and adjust the time block length accordingly, so that the leakage phenomenon is not an issue anymore. However, especially for lower operational speeds of the compressor, the order frequency is very unstable (see [14]). The frequency resolution adjustments to the FRF matrix in each block were found to be infeasible in practice.

7.4 TPA Auralization by cyclic convolution with overlap-add

A well known remedy to leakage is the application of windows to the time blocks. They typically force the signal to zero at the beginning and end of the time blocks. A Hanning window of length N is defined by:

$$w(n) = 0.5 - 0.5 \cos\left(\tfrac{2\pi n}{N}\right). \tag{7.11}$$

Assume the sum of the overlapping windows is equal to one. Then the reassembly of the windowed time blocks into a long time series comes down to time correct adding of the single blocks. When superposing two consecutive Hanning windows that overlap by a shift of $\frac{N}{2}$, i.e. 50% of the time block length, the sum of the windows is equal to one:

$$
\begin{aligned}
w(n) + w\left(n + \tfrac{N}{2}\right) &= 0.5 - 0.5 \cos\left(\tfrac{2\pi n}{N}\right) + 0.5 - 0.5 \cos\left(\frac{2\pi(n+\frac{N}{2})}{N}\right) \\
&= 1 - 0.5 \cos\left(\tfrac{2\pi n}{N}\right) + 0.5 \cos\left(\tfrac{2\pi n}{N}\right) \\
&= 1,
\end{aligned} \tag{7.12}
$$

since the cosine is point symmetric around half a period. The sum of consecutive Hanning windows that overlapp by half of the window length N is thus equal to one, apart from a fade-in and fade-out at the beginning and end of the time series, see figure 7.5. Applying

a window with this property to overlapping time blocks, resulting from frequency domain data, is called constant overlap add (short COLA) [3, 50, 61, 101], and is often used for creating sound files without spurious clicks at the block bounds. For the example treated in this section, two different approaches are compared:

- **Pre Hanning windowing:** The sources operational signal u^A is cut into 50% overlapping blocks and a Hanning window is applied. The force identification and response prediction is done per block in the frequency domain (equation (7.9) and (7.10)). The resulting frequency blocks for u^B are transformed back to the time domain and added with the same 50% overlap to yield the time signal for the response u^B that can be auralized.

- **Post Hanning windowing:** The sources operational signal u^A is cut into 50% overlapping blocks and *no* window is applied to them. The force identification and response prediction is done per block in the frequency domain (equation (7.9) and (7.10)). The resulting frequency blocks for u^B are transformed back to the time domain and a Hanning window is applied to them. They are added with the same overlap to yield the time signal for the response u^B that can be auralized.

The results of these two approaches can be seen and heard in figure 7.6. It can be seen that for the post Hanning windowed results, the results still show the cyclical increases and decreases that are related to the leakage effect (as explained in section 7.3). This is due to the fact that the blocked forces are still computed with unwindowed time blocks. The signal is nevertheless free of spurious clicks, since the Hanning windows that are applied to the resulting blocks of u^B are forcing any possible jumps in the signal to zero. The resulting sound file sounds like a signal with a beating phenomenon.

For the pre Hanning windowed results in figure 7.6, it can be seen that the cyclic increases and decreases are eliminated. The leakage phenomenon is remedied by applying the Hanning window to the source signal u^A before the identification of the blocked forces. Nevertheless, the resulting time blocks of u^B are not zero anymore at the beginning and end of the block. This results in small, but still well audible clicks in the operational signal. Note the slight jump in the signal at 1.5 seconds in figure 7.6.

7.5   Filtering of discontinuities at timeblock bounds

The signal resulting from the pre-Hanning windowed time blocks was leakage free (see section 7.4). This was considered promising, so it was tried to remove the small but audible jumps in the time signal by two different approaches:

- **Polynomial fitting:** 5 samples left and right of each timeblock bound were taken (so in total 11 samples) and a fourth order polynomial was least squares fitted to the initial data.

- **Low pass filtering:** Since the jumps introduce an impulse like signal, containing higher frequencies, the whole reconstructed time series of u^B was again low pass filtered (8-pole Butterworth filter, cut off frequency 1000Hz).

The results of these filtering approaches on the timeblock bounds can be seen and heard in figure 7.7. Both approaches can dampen the spurious clicks in the audio file to a large extent, where the low pass filtering approach seems to be more successful from the hearing examples. Nevertheless, with both approaches the slight clicks at the time block bounds
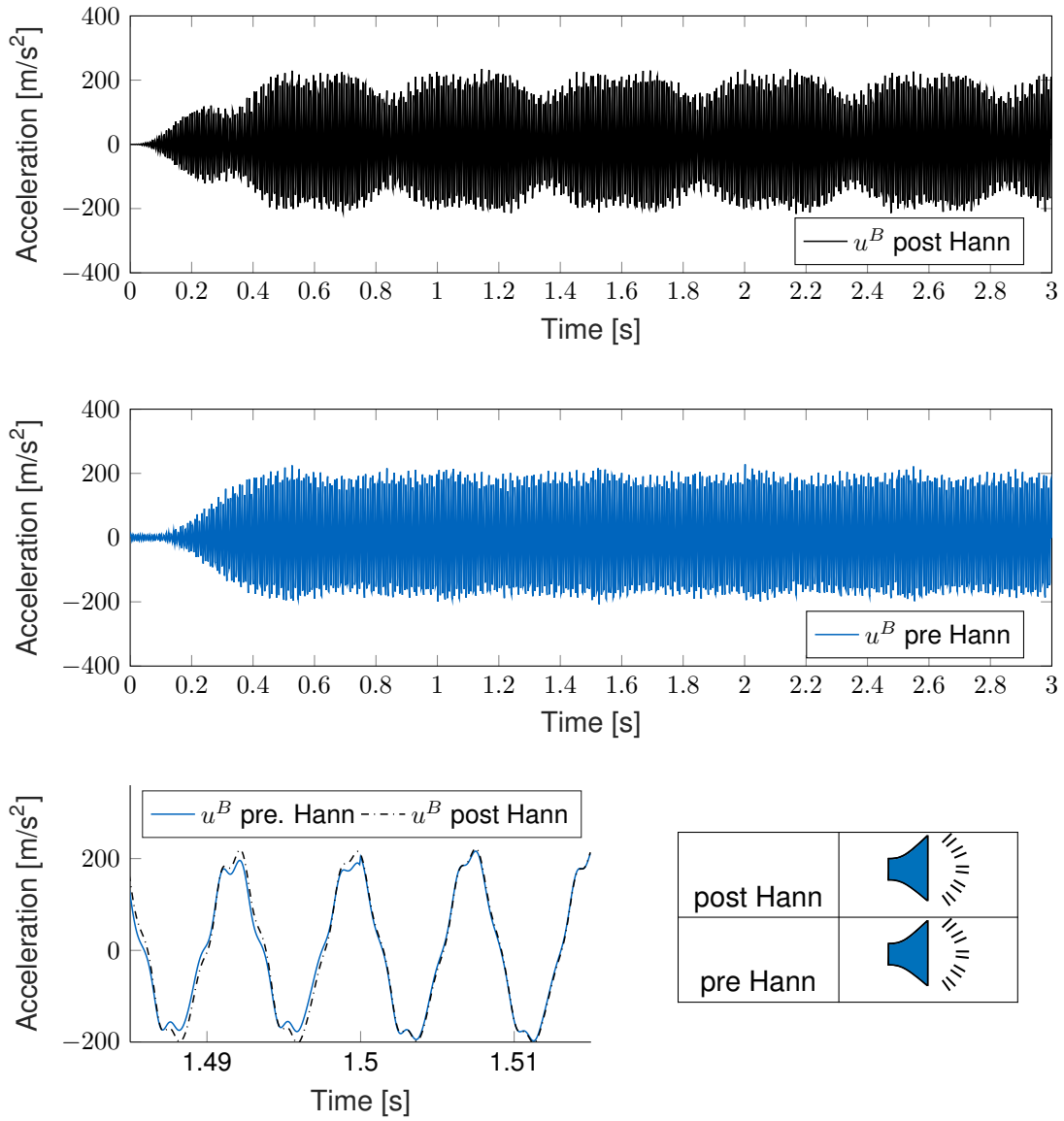
Figure 7.6: Cyclic convolution results with overlap add and the "pre" Hanning windowing on u^A and "post" Hanning windowing on u^B.
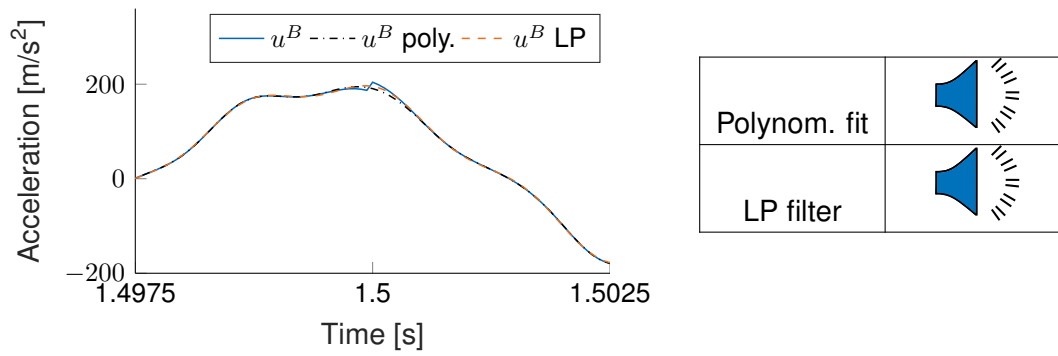
Figure 7.7: Filtering of discontinuities at the time block bounds. Once with a least squares fitted fourth order polynomial over 11 samples, and second with a low pass filter applied to the whole time series.

can still be heard[2]. The anomalies at the block bounds in the time signal are virtually non-visible in the time plots after both filtering approaches (this has been checked at all time block bounds). The fact that the human ear can still capture them, still amazes the author. This was one of the reasons for the quote at the chapter beginning.

7.6 TPA Auralization by non-cyclic convolution

Obviously, the approach of non-cyclic convolution to the auralization task is still an option. Here no assumption about the periodicity of the signal has to be made, so it is generally also applicable to transient sounds like rattling, or a run-up of a motor. The frequency domain operations of the blocked force TPA can be combined in one operation, yielding the transmissibility $T^{AB|A}$:

$$u^B(\omega) = \underbrace{Y^{AB}(\omega)\left(Y^A(\omega)\right)^{-1}}_{=:T^{AB|A}(\omega)} u^A(\omega). \qquad (7.13)$$

This operation in the frequency domain can be executed in the time domain by transforming the transmissibility to a finite impulse response (FIR) filter and performing a non-cyclic convolution with the time signal u^A, to obtain directly the time signal of u^B:

$$u^B(t) = \int_{\tau=0}^{t} T^{AB|A}(t-\tau)u^A(\tau)d\tau. \qquad (7.14)$$

For a computationally efficient implementation of this convolution, a block-wise FFT based convolution [45, 75, 114] can be used (which is strongly recommended for better performance). In this block-wise computation, it is possible to adapt the transmissibility over time, due to e.g. changing transfer functions of the system during an operational cycle (see [194] for the example of a steering system). When the impulse response of the transmissibility $T^{AB|A}$ is plotted over time, see figure 7.8, one notices that, unlike the expected exponentially decaying oscillation, the impulse response is increasing again towards the end of the time block. This is related to the inverse force identification involved in the TPA approach. From a physical point of view, the forces f^{bl} which are identified by the inverse FRF have

---

[2]Generally it was found that very simple ear plug headphones give a clearer impression on these clicks, than over-ear headphones or loudspeakers.
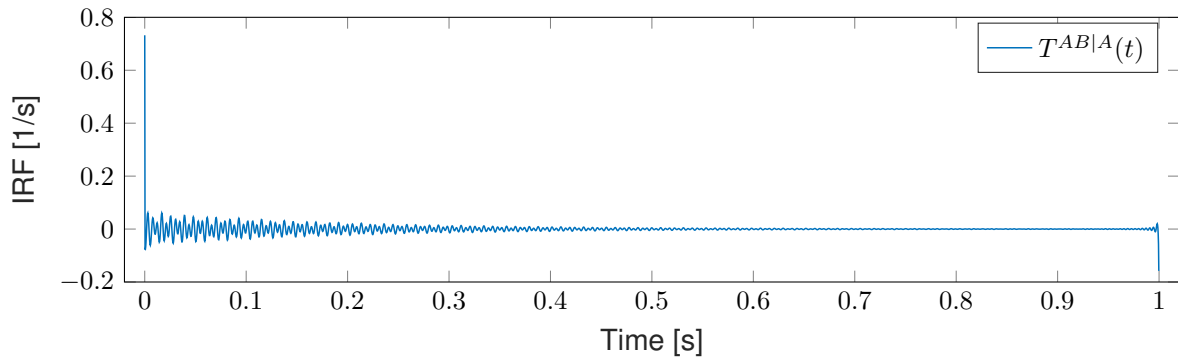
Figure 7.8: Impulse response function of the transmissibility $T^{AB|A}(t)$.
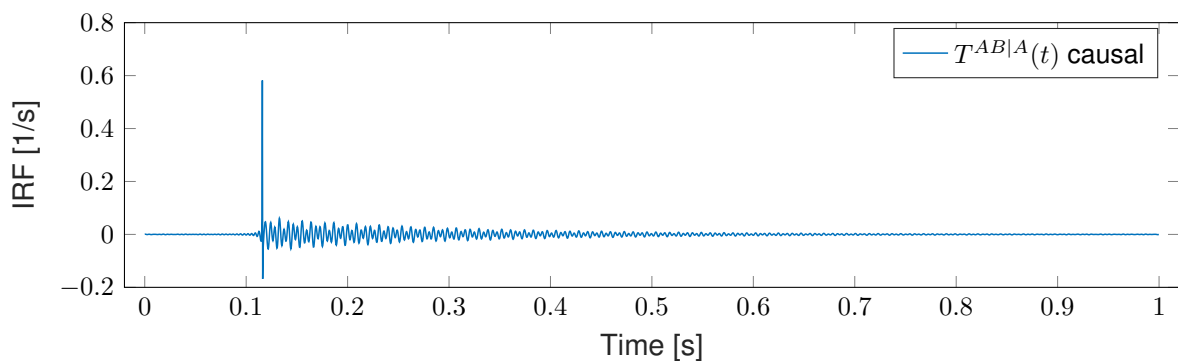
Figure 7.9: Impulse response function of the transmissibility $T^{AB|A}(t)$ with a time shift applied to make the filter causal again.

to act *first* in time *before* one observes a signal response u^A. This phenomenon is called a non-causal filter in control theory. To remedy this issue, one can apply a slight time-shift to make the filter causal again, as also mentioned in [181]. Applying a time-shift of 0.1s directly to the IRF, results causal impulse response is shown in figure 7.9.

The results of the non-cyclic convolution with the causal and non-causal FIR filter are shown in figure 7.10. The resulting sound files do not contain any spurious clicks. However, it seems that the convolution with the causal filter yields a sound that is closer to the one from the pre-Hanning windowed approach (see figure 7.10). Note that as the FIR filter in this case has a length of 1 second and the non-cyclic convolution is not assuming a steady state. Hence the first and last second of the resulting time signal u^B cannot be used for auralization, since the signal is fading in and out of the FIR filter.

7.7 Conclusion and final notes

The block-wise auralization with cyclic convolution was found to be hindered by discontinuities at time block bounds. These disturb the auralized audio files by spurious "clicks". This is related to the non-periodic operational state of the compressor (and most likely any other imaginable machine). From the authors experience, the constant overlap add (COLA) approach with Hanning windows often produces sound files without the spurious clicks when an on-board validation is auralized. For a transfer validation, like shown here on a simple ex-
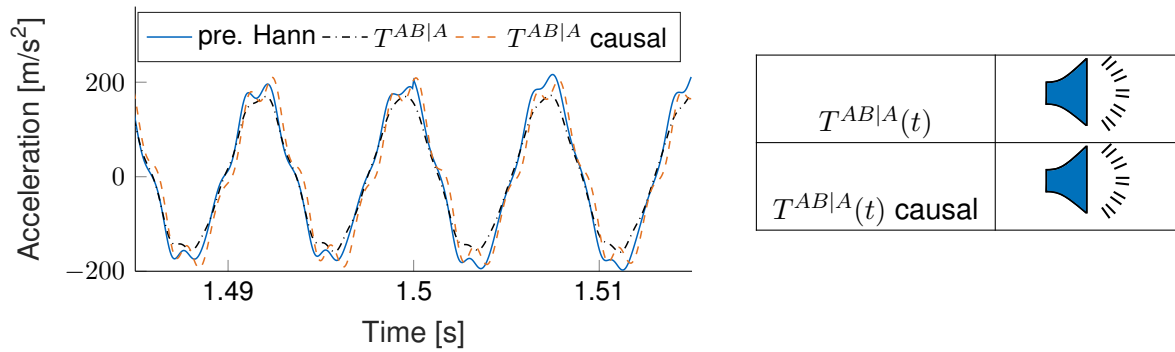
Figure 7.10: Results of the non cyclic convolution with the impulse response $T^{AB|A}(t)$ and the impulse response that was made causal by applying a slight time shift.

ample, it does not yield satisfactory results. The exact reason for this difference in on-board and transfer validation is not yet clear and is up to further investigation. The non-cyclic convolution was found to be the only reliable method for creating sound files that are free of signal processing artifacts such as the clicks. Due to the inverse force identification involved in the TPA method, the resulting filter showed a non causal behavior. This was remedied by applying a time-shift to the resulting filter.

The simple example in this chapter had only one input and output channel, but the time domain auralization is also applicable to multiple input and output channels. For an in-situ blocked force identification on a testrig assembly AR with transfer to a new receiver assembly AB, this can be written as:

$$\mathbf{p}_3^B = \underbrace{\mathbf{Y}_{32}^{AB}\left(\mathbf{Y}_{42}^{AR}\right)^+}_{=:\mathbf{T}^{AB|AR}} \mathbf{u}_4^R \tag{7.15}$$

where the transmissibility matrix $\mathbf{T}^{AB|AR}$ can be transformed to a FIR filter matrix, made causal by a time shift, and convoluted with the testbench time signal $\mathbf{u}_4^R(t)$, to yield the predicted sound in the final receiver $\mathbf{p}_3^B(t)$:

$$\mathbf{p}_3^B(t) = \int_{\tau=0}^{t} \mathbf{T}^{AB|AR}(t-\tau)\mathbf{u}_4^R(\tau). \tag{7.16}$$

To the authors experience, it is best to first use all available checks in the frequency domain and make sure that the results make sense there. After that the final step of the auralization, equation (7.16), can be taken. The auralization with the non-cyclical convolution has the additional advantage that it also allows to auralize non-stationary machine sounds, like run-ups or rattling of components.

Two practical notes for aiding the interpretation of the sound files provided in this document should be made:

Conversion to sound files and comparability of individual sound files

All sound files embedded in this document are in MP3 format, which is a lossy compression but was chosen to keep the file size of this document low. Both, the MP3 format and the lossless WAV format, allow the time signal values to vary only in a range of $[-1, 1]$. Therefore, the time series results of the TPA auralizations have to be scaled and shifted such that this dynamic range of $[-1, 1]$ is fully used. It is thus not possible to convey information about

the absolute sound pressure level in the form of an MP3 or WAV file. In order to make the TPA results comparable to each other, the same scaling has to be applied to all individual time series. All results of u^B in this chapter are created with the same scaling and are thus comparable to each other. In the rest of this thesis, only the sound files in one tabular frame are comparable to each other (see e.g. the comparison between the reference measurement and on-board validation in figure 6.3).

Listening to and interpreting the sound examples

An valuable tool during the hearing comparisons in this thesis can be provided by spectrum analyzers which are available for all smartphones in the respective app stores. Placing the spectrum analyzer next to the loudspeaker while listening to the sound files can provide additional information about the spectral content of the signals. However, most loudspeakers have their own transfer function and distort the sound somewhat with respect to the real sound which was recorded/predicted. According to [42], headphones, even rather cheap ones, typically have a flat transfer function and give more accurate hearing impressions than loudspeaker boxes.

Chapter 8

Regularization methods for blocked force TPA

Contents:

> The singular value decomposition (SVD) is the swiss army knife of engineering.
>
> *Prof. Klaus Diepold,*
> *panel discussion with Cleve Moler [118]*

The method which is predominantly used for obtaining the blocked forces $\mathbf{f}_2^{bl}$ in this thesis is the in-situ TPA method, as explained in chapter 6. A matrix (pseudo-) inverse is used for the blocked force determination: $\mathbf{f}_2^{bl} = (\mathbf{Y}_{42}^{AR})^+ \mathbf{u}_4^R$. This inverse makes the method potentially sensitive to measurement noise in the vibration signals. Relatively small noise levels in $\mathbf{u}_4^R$ can get amplified to large errors in the computed blocked forces $\mathbf{f}_2^{bl}$, if the problem is ill-posed and has a high condition number. This might be a cause for obtaining different blocked forces, even when measuring the same source component in the same operational condition but on different test rigs. In theory (which often means: *without noise*), this should not be the case. This effect potentially distorts the predicted sound and vibration when applying the blocked forces to a modified receiver design. A possible remedy is to replace the pseudo-inverse $(\mathbf{Y}_{42}^{AR})^+$ by a regularized inverse $(\mathbf{Y}_{42}^{AR})^{\#}$, which is less sensitive to measurement noise and yields more stable and transferable results. This is important for reliable sound prediction in early NVH engineering or target setting for collaboration with component suppliers.

Section 8.1 summarizes the standard solutions to inverse problems, like the classical pseudo-inverse. These solutions can be sensitive to measurement noise amplification, and related terms like "ill-posed" and the "condition number" are introduced in section 8.2. The effects on the blocked force computation are shown by an experimental example of the e-compressor in section 8.3. Thereby, it is also shown that common quality checks on the blocked forces (like the on-board validation, see section 6.3) can lack the sensitivity to detect this issue. The background on regularization methods and some tools for investigating the properties of inverse problems are explained in section 8.4. The principle of some regularization strategies is then explained and applied to the compressor example in section 8.5. The comparison of different regularization schemes is an excerpt of the methods compared in Felix Benners master thesis [15]. Some of these techniques are used for the application examples at the end of this thesis. A summary and some practical recommendations on regularization are given in section 8.6.

8.1   Standard solutions of inverse problems

For solving inverse problems, different approaches can be used. For the in-situ blocked force TPA, the inverse problem (for each frequency) is:

$$\mathbf{f}_2^{bl} = (\mathbf{Y}_{42}^{AR})^+ \mathbf{u}_4^R, \qquad \text{with:} \quad \mathbf{u}_4^R \in \mathbb{C}^m, \ \mathbf{Y}_{42}^{AR} \in \mathbb{C}^{m \times n}, \ \mathbf{f}_2^{bl} \in \mathbb{C}^n \text{ and } m \geq n. \tag{8.1}$$

The pseudo inverse of the matrix is indicated by the superscript 'plus'. Common approaches for computing it are explained in the following.

Regular inverse

If the number of indicator channels is equal to the number of sought forces, i.e. $m = n$, the regular inverse of the FRF matrix can be used for computing the blocked forces:

$$\mathbf{f}_2^{bl} = \left(\mathbf{Y}_{42}^{AR}\right)^{-1} \mathbf{u}_4^R. \tag{8.2}$$

This solution requires the matrix $\mathbf{Y}_{42}^{AR}$ to have full rank. Most often this is the case, due to the presence of some measurement noise, but the matrix is often ill-conditioned which causes stability issues in the results (see section 8.2).

Least squares inverse

In the literature on TPA and inverse force identification, it is almost always suggested to use an overdetermined problem [33, 68, 71, 72, 77, 141, 172, 174, 192, 193], i.e. $m > n$. In fact, the author could not find a single publication that advised against using overdetermination. In [174], it is found that, up to an over-determination of $\frac{m}{n} \approx 1.5$, the results of the inverse force identification can be improved. In [192], it is suggested to use *at least* a factor of over-determination of 1.5. To the authors experience an over-determination of factor 2 should be used if channel count is not a limitation, lower then 1.5 should be avoided. Solving an overdetermined problem, is often done by the least squares method. There is less degrees of freedom in the forces than in the measured responses, $m > n$, so the solution to $\mathbf{f}_2^{bl}$ can only reproduce the measured responses $\mathbf{u}_4^R$ up to a certain residual μ:

$$\mathbf{u}_4^R = \mathbf{Y}_{42}^{AR} \mathbf{f}_2^{bl} + \mu \tag{8.3}$$

The least squares solution is the blocked force vector which minimizes the square norm of this residual $||\mu||^2$. This is the same procedure as in the virtual point transformation of the sensor signals (see section 3.3.2), yielding:

$$\mathbf{f}_2^{bl} = \left[(\mathbf{Y}_{42}^{AR})^* \, \mathbf{Y}_{42}^{AR} \right]^{-1} (\mathbf{Y}_{42}^{AR})^* \, \mathbf{u}_4^R, \tag{8.4}$$

for the computation of the blocked forces.[1] This method requires the matrix $\mathbf{Y}_{42}^{AR}$ to have at least full column rank, i.e. $rank(\mathbf{Y}_{42}^{AR}) = n$. Otherwise, the inverse in equation (8.4) does not exist.

SVD based pseudo-inverse

The SVD based pseudo-inverse removes the requirement of full column rank on the matrix, i.e. a solution for the blocked forces can be found even if $rank(\mathbf{Y}_{42}^{AR}) < n$. Additionally, it allows for a deeper insight into the behavior of the inverse problem, as will be seen in the following sections. The SVD of the FRF matrix always yields [165, 167]:

$$\mathbf{Y}_{42}^{AR} = \mathbf{U}\mathbf{\Sigma}\mathbf{V}^*, \tag{8.5}$$

with:

$$\mathbf{U} \in \mathbb{C}^{m \times m}, \qquad \mathbf{\Sigma} \in \mathbb{R}_+^{m \times n} \qquad \mathbf{V} \in \mathbb{C}^{n \times n}, \quad \text{and} \tag{8.6}$$

$$\mathbf{U}^*\mathbf{U} = \mathbf{I}, \qquad \mathbf{\Sigma} = \begin{bmatrix} \sigma_1 & \cdots & 0 \\ \vdots & \ddots & \\ 0 & & \sigma_n \\ \hdashline 0 & \cdots & 0 \\ \vdots & \ddots & \\ 0 & & 0 \end{bmatrix} \qquad \mathbf{V}^*\mathbf{V} = \mathbf{I}. \tag{8.7}$$

The matrix $\mathbf{U}$ contains a set of orthonormal vectors $\mathbf{u}_i$ in its columns, i.e. vectors that all have unit length and are orthogonal with respect to each other. They form a complete basis for representing any vibration that could possibly be recorded by the sensor channels in $\mathbf{u}_4^R$. Similarly, the matrix $\mathbf{V}$ contains a set of orthonormal vectors $\mathbf{v}_i$, which form a complete basis for all possible blocked forces $\mathbf{f}_2^{bl}$. The upper $n \times n$ part of the singular value matrix $\mathbf{\Sigma}$ contains the singular values σ_n on its diagonal. The lower $(m-n) \times n$ part of $\mathbf{\Sigma}$ contains only zeros. The singular values are by definition all positive or zero and ordered in descending magnitude [51]:

$$\sigma_1 \geq \sigma_2 \geq ... \geq \sigma_n \geq 0. \tag{8.8}$$

If one of the singular values is zero, the matrix is rank deficient. The SVD based pseudo-inverse is:

$$\mathbf{f}_2^{bl} = \mathbf{V}\mathbf{\Sigma}^+\mathbf{U}^* \, \mathbf{u}_4, \tag{8.9}$$

---

[1]As in section 3.3.2, one might also use a weighting matrix in the computation of the least squares solution, then commonly called weighted least squares [165]. Thereby, the residual in individual channels might be weighted more compared to others. This might be useful e.g. in case of different physical units contained in $\mathbf{u}_4^R$, e.g. accelerations and strains, or if individual channels exhibit significantly lower vibrations levels in operation which are nevertheless well above the noise floor [71].

with,

$$\mathbf{\Sigma}^+ = \begin{bmatrix} \frac{1}{\sigma_1} & \cdots & 0 & 0 & \cdots & 0 \\ \vdots & \ddots & & \vdots & \ddots & \\ 0 & & \frac{1}{\sigma_n} & 0 & & 0 \end{bmatrix}. \tag{8.10}$$

If the matrix is rank deficient, i.e. one of the singular values is zero, $\sigma_i = 0$, then the corresponding term $\frac{1}{\sigma_i}$ in equation (8.10) is replaced by zero. The singular value $\sigma_i = 0$ means that a vibration $\mathbf{u}_4^R$ which is in the same direction as the basis vector $\mathbf{u}_i$ (the i-th column vector in $\mathbf{U}$) cannot be reproduced by a blocked force component in the direction of the vector $\mathbf{v}_i$. A vibration in the direction of $\mathbf{u}_i$ is in the nullspace of the matrix. If the matrix has full rank ($rank(\mathbf{Y}_{42}^{AR}) = n$), it is easy to show that the SVD based pseudo-inverse yields the same result as the least squares solution:

$$\left[(\mathbf{Y}_{42}^{AR})^*\mathbf{Y}_{42}^{AR}\right]^{-1}(\mathbf{Y}_{42}^{AR})^* = \left[(\mathbf{U}\mathbf{\Sigma}\mathbf{V}^*)^*\mathbf{U}\mathbf{\Sigma}\mathbf{V}^*\right]^{-1}(\mathbf{U}\mathbf{\Sigma}\mathbf{V}^*)^* = \mathbf{V}\mathbf{\Sigma}^+\mathbf{U}^*. \tag{8.11}$$

One could say that the SVD-based pseudo-inverse finds the solution with a minimal residual $||\mu||^2$, which is equivalent to the least squares solution if the problem has full rank. In case the problem is rank deficient, the SVD solution has a minimal residual $||\mu||^2$ with the minimum blocked forces $||\mathbf{f}_2^{bl}||$. The components of the blocked forces in the null space of $\mathbf{Y}_{42}^{AR}$, are set to zero.

8.2 Ill-posed problems

Before introducing the term of an ill-posed inverse problem, it is useful to define well-posed problems. According to [63], a well-posed problem means that small changes in the observed data also cause small changes in the solution, i.e. if:

$$\mathbf{f}_2^{bl} = (\mathbf{Y}_{42}^{AR})^+ \, \mathbf{u}_4^R \qquad \text{and} \quad \tilde{\mathbf{f}}_2^{bl} = (\mathbf{Y}_{42}^{AR})^+ \, \tilde{\mathbf{u}}_4^R, \tag{8.12}$$

with only a small difference in the input data, $\mathbf{u}_4^R \approx \tilde{\mathbf{u}}_4^R$, then also the computed solution should be similar $\mathbf{f}_2^{bl} \approx \tilde{\mathbf{f}}_2^{bl}$. Think about the fact that all measurements are subject to measurement noise, i.e.:

$$\mathbf{u}_4^R = \hat{\mathbf{u}}_4^R + \mathbf{e}_u, \tag{8.13}$$

where $\mathbf{u}_4^R$ is the recorded signal, $\hat{\mathbf{u}}_4^R$ is the noise free signal and $\mathbf{e}_u$ is random measurement noise. If the problem is ill-posed, this would mean that the random measurement noise $\mathbf{e}_u$ could completely alter the solution for the blocked forces. The solution of the inverse problem can be split (it is a linear problem) into the noise free blocked force solution $\hat{\mathbf{f}}_2^{bl}$ and the noise solution $\mathbf{e}_f$:

$$\mathbf{Y}_{42}^{AR} \underbrace{\left(\hat{\mathbf{f}}_2^{bl} + \mathbf{e}_f\right)}_{=\mathbf{f}_2^{bl}} = \underbrace{\hat{\mathbf{u}}_4^R + \mathbf{e}_u}_{=\mathbf{u}_4^R}. \tag{8.14}$$

The so-called condition number is representative for a "worst case" scenario regarding the relative amplification of the measurement noise $\mathbf{e}_u$ to blocked force noise $\mathbf{e}_f$. For this worst case, assume all of the noise free operational signal $\hat{\mathbf{u}}_4^R$ is in the direction corresponding to the first and largest singular value σ_1:

$$\hat{\mathbf{u}}_4^R \quad \hat{=} \quad ||\hat{\mathbf{u}}_4^R|| \, \mathbf{u}_1, \tag{8.15}$$

where $\mathbf{u}_1$ is the first column vector of the matrix $\mathbf{U}$ from the SVD in equation (8.5). Then the solution for the blocked forces, according to (8.9), would be:

$$\hat{\mathbf{f}}_2^{bl} = \mathbf{v}_1 \frac{||\hat{\mathbf{u}}_4^R||}{\sigma_1}. \tag{8.16}$$

In fact, this is the $\hat{\mathbf{f}}_2^{bl}$ solution with the lowest possible magnitude, for an observed vibration with amplitude $||\hat{\mathbf{u}}_4^R||$. For an FRF matrix, the vector $\mathbf{u}_1$ is often very similar to the mode shape of the closest frequency mode [2]. The vector $\mathbf{v}_1$ represents the set of forces that excite this mode shape. Mechanically speaking, this direction is the most "flexible" direction of the system at a given frequency, since a small force input in the direction $\mathbf{v}_1$ can cause a high response in the direction $\mathbf{u}_1$ (amplified with the highest singular value σ_1). Therefore, the lower bound for the blocked forces magnitude of the noise free signal is:

$$||\hat{\mathbf{f}}_2^{bl}|| \geq \frac{1}{\sigma_1}||\hat{\mathbf{u}}_4^R||. \tag{8.17}$$

The worst case scenario for the noise amplification would be, if all the noise $\mathbf{e}_u$ is in the mechanically "stiffest" direction, i.e $\mathbf{u}_n$. So the upper bound for the blocked force noise is:

$$||\mathbf{e}_f|| \leq \frac{1}{\sigma_n}||\mathbf{e}_u||. \tag{8.18}$$

Taken together, one can define an upper bound for the maximum amplification of the relative error in the acceleration signals to a relative error in the force signals:

$$\underbrace{\frac{||\mathbf{e}_f||}{||\hat{\mathbf{f}}_2^{bl}||}}_{\text{relative error } \mathbf{f}_2^{bl}} \leq \underbrace{\frac{\sigma_1}{\sigma_n}}_{=cond(\mathbf{Y}_{42}^{AR})} \underbrace{\frac{||\mathbf{e}_u||}{||\hat{\mathbf{u}}_4^R||}}_{\text{relative error } \mathbf{u}_4^R}. \tag{8.19}$$

This maximum amplification of relative errors is called the condition number of the matrix $cond(\mathbf{Y}_{42}^{AR})$. An ill-posed problem is typically regarded as one where this maximum amplification of errors is high, i.e. systems $\mathbf{Y}_{42}^{AR}$ with a high condition number. One could also say that the condition number is an upper limit to how much the SNR is decreased during the data inversion.

In [63], one makes the distinction between *rank-deficient* and *ill-posed* problems. A rank-deficient problem would be one, where the effective rank of $\mathbf{Y}_{42}^{AR}$ is smaller than n, i.e. the number of blocked forces to compute. This would be the case if e.g. the FRF matrix $\mathbf{Y}_{42}^{AR}$ was measured on a system which is essentially behaving like a rigid body in the frequency range of interest, but more than six forces shall be identified. This could be identified by observing a group of 6 large singular values in the matrix, followed by a "gap" till the rest of the smaller singular values follow. These problems could be solved by either modelling the system with an appropriate number of degrees of freedom, or using regularization (see section 8.5).

An ill-posed problem is one where there is no clear "gap" between groups of singular values. Rather the ratio between subsequent singular values is approximately constant and they are sequentially getting lower and lower. The problems in this thesis are often found to be ill-posed, which can be seen in large parts of the frequency region in figure 8.2, which is a plot of all singular values over frequency. Only in the lower frequency region in figure 8.2 one could argue that the problem is rank deficient.
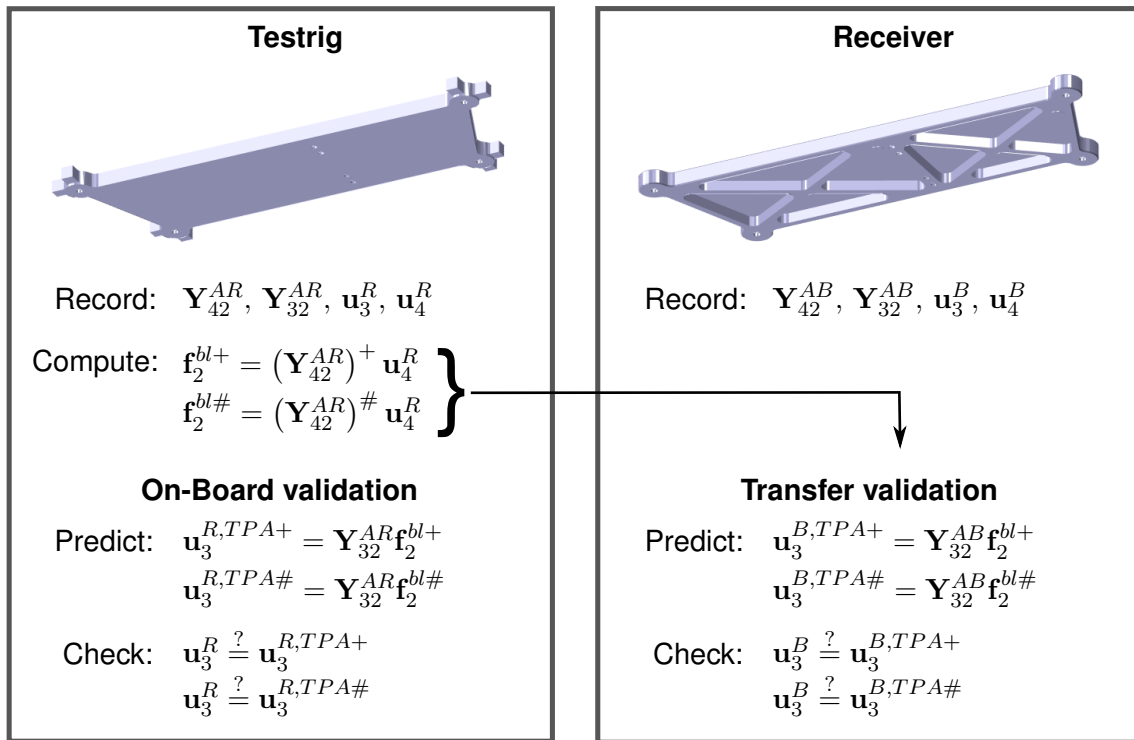
Testrig	**Receiver**
Record: $\mathbf{Y}_{42}^{AR}$, $\mathbf{Y}_{32}^{AR}$, $\mathbf{u}_3^R$, $\mathbf{u}_4^R$	Record: $\mathbf{Y}_{42}^{AB}$, $\mathbf{Y}_{32}^{AB}$, $\mathbf{u}_3^B$, $\mathbf{u}_4^B$

Compute: $\mathbf{f}_2^{bl+} = \left(\mathbf{Y}_{42}^{AR}\right)^+ \mathbf{u}_4^R$
$\mathbf{f}_2^{bl\#} = \left(\mathbf{Y}_{42}^{AR}\right)^\# \mathbf{u}_4^R$

On-Board validation

Predict: $\mathbf{u}_3^{R,TPA+} = \mathbf{Y}_{32}^{AR}\mathbf{f}_2^{bl+}$
$\mathbf{u}_3^{R,TPA\#} = \mathbf{Y}_{32}^{AR}\mathbf{f}_2^{bl\#}$

Check: $\mathbf{u}_3^R \overset{?}{=} \mathbf{u}_3^{R,TPA+}$
$\mathbf{u}_3^R \overset{?}{=} \mathbf{u}_3^{R,TPA\#}$

Transfer validation

Predict: $\mathbf{u}_3^{B,TPA+} = \mathbf{Y}_{32}^{AB}\mathbf{f}_2^{bl+}$
$\mathbf{u}_3^{B,TPA\#} = \mathbf{Y}_{32}^{AB}\mathbf{f}_2^{bl\#}$

Check: $\mathbf{u}_3^B \overset{?}{=} \mathbf{u}_3^{B,TPA+}$
$\mathbf{u}_3^B \overset{?}{=} \mathbf{u}_3^{B,TPA\#}$

Figure 8.1: Depiction of the different plate designs mounted to the configuration shown in figure 6.2. Left plate is made of full material and considered to be the "testrig". The right plate is milled out in certain regions and significantly lighter and considered the final "receiver". The blocked forces are computed on the testrig plate with a pseudo- and a regularized- inverse. The resulting blocked forces are validated by performing an on-board validation on the testrig design and a transfer validation to the receiver design. The flow of evaluations is shown in the figure.

8.3   Example: noise amplification in e-compressor blocked forces

The example case, for the rest of this chapter, is the same setup as in section 6.3. In figure 6.2, one can see the test design containing the compressor. Unlike in section 6.3, in this section there are two different designs of the plate. They can be seen in figure 8.1. The blocked forces of the compressor shall be computed with one of the plates and then transferred to the setup with the other plate. Thereby, the transferability of the blocked forces from one design to the other is checked and the success of different regularization strategies can be studied. One of the plate designs will be considered to be the testrig (left part of figure 8.1). The blocked forces are identified in this configuration and are used for predicting the vibration levels on the testrig itself (on-board validation) and on the receiver design (transfer validation). In both tested designs, the compressor measurements were taken under the same operational conditions (speed, pressures, temperature, oil amount, etc.). Different to section 6.3, the blocked forces in this chapter are *not* containing only 3 forces and 3 moments in the center of gravity of the compressor. In this chapter, each of the three connection points is treated as a full virtual point, so in total $\mathbf{f}_2^{bl}$ contains 18 entries and the matrix $\mathbf{Y}_{42}^{AR}$ has 18 non-zero singular values. The singular values of the matrices $\mathbf{Y}_{42}^{AR}$ and $\mathbf{Y}_{42}^{AB}$ are plotted over frequency in figure 8.2 together with their condition numbers. The problem is still overdetermined, since $\mathbf{u}_4^R$ contained 36 channels (over-determination factor of 2).
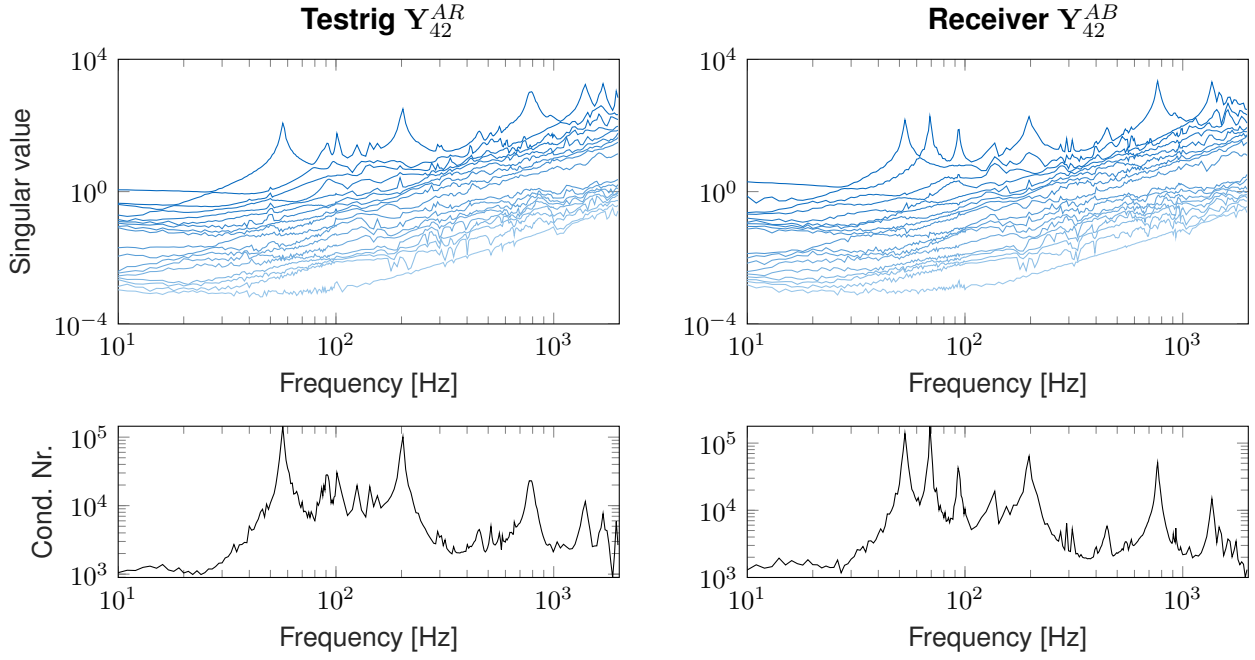
Figure 8.2: Singular values and condition numbers over frequency for $\mathbf{Y}_{42}^{AR}$ and $\mathbf{Y}_{42}^{AB}$.

8.3.1 On-board and transfer validation results

The compressor was tested with a predetermined set of operating conditions on each of the designs. For simplicity, only the results of the compressor running at 80% of its maximum speed (or 6880rpm) are shown in this section. The first order of the compressor is at ca. 115 Hz. The general findings are similar for all other tested operating conditions. During the operational measurements, the signals $\mathbf{u}_4^R$ were recorded. The blocked forces were identified with and without regularization, which will be denoted with $\mathbf{f}_2^{bl+}$ for the unregularized pseudo-inverse and $\mathbf{f}_2^{bl\#}$ for the regularized inverse (see the evaluation flow in figure 8.1). The method used for the regularization is the SNR based Tikhonov regularization, which will be explained in section 8.5.3. It is not necessary to understand its implementation for now, as it serves only to demonstrate the effects of regularization at this point in the chapter.

In figure 8.2, the singular values and the condition numbers of the matrices $\mathbf{Y}_{42}^{AR}$ and $\mathbf{Y}_{42}^{AB}$ are plotted over the frequency range from zero to 2000 Hz. In the left half of figure 8.3, the on-board validation on the testrig $\mathbf{u}_3^R$ is shown. For simplicity, the on-board validation is shown only for one channel in the set of $\mathbf{u}_3^R$ (triaxial sensor to the very right in figure 6.2b, channel in the global y-direction). Again, the principal findings are similar for all receiver channels. In the third octave plot in the left part of figure 8.3, one can see that both TPA predictions $\mathbf{u}_3^{R,TPA+}$ and $\mathbf{u}_3^{R,TPA\#}$ match the validation measurement $\mathbf{u}_3^R$ quite well. The prediction with the standard pseudo-inverse $\mathbf{u}_3^{R,TPA+}$ shows some larger deviations from the reference measurement at frequencies which are not excited by one of the compressor orders. E.g. in the frequency region below 115 Hz, the solution computed with the pseudo-inverse $\mathbf{u}_3^{R,TPA+}$ is too high in amplitude, whereas the regularized solution $\mathbf{u}_3^{R,TPA\#}$ matches the validation $\mathbf{u}_3^R$ better. However, the vibration levels at these frequencies are still more than 40dB lower than the dominant first order peak at 115Hz where the pseudo and regularized inverse predict the vibration levels equally well. The sound files provided in the lower left part of figure 8.3 confirm that the dominant parts of the signal can be reproduced by both approaches, as the predictions sound very similar to the on-board validation $\mathbf{u}_3^R$.

The same validation channel is used for the transfer validation (see right part of figure 8.1).
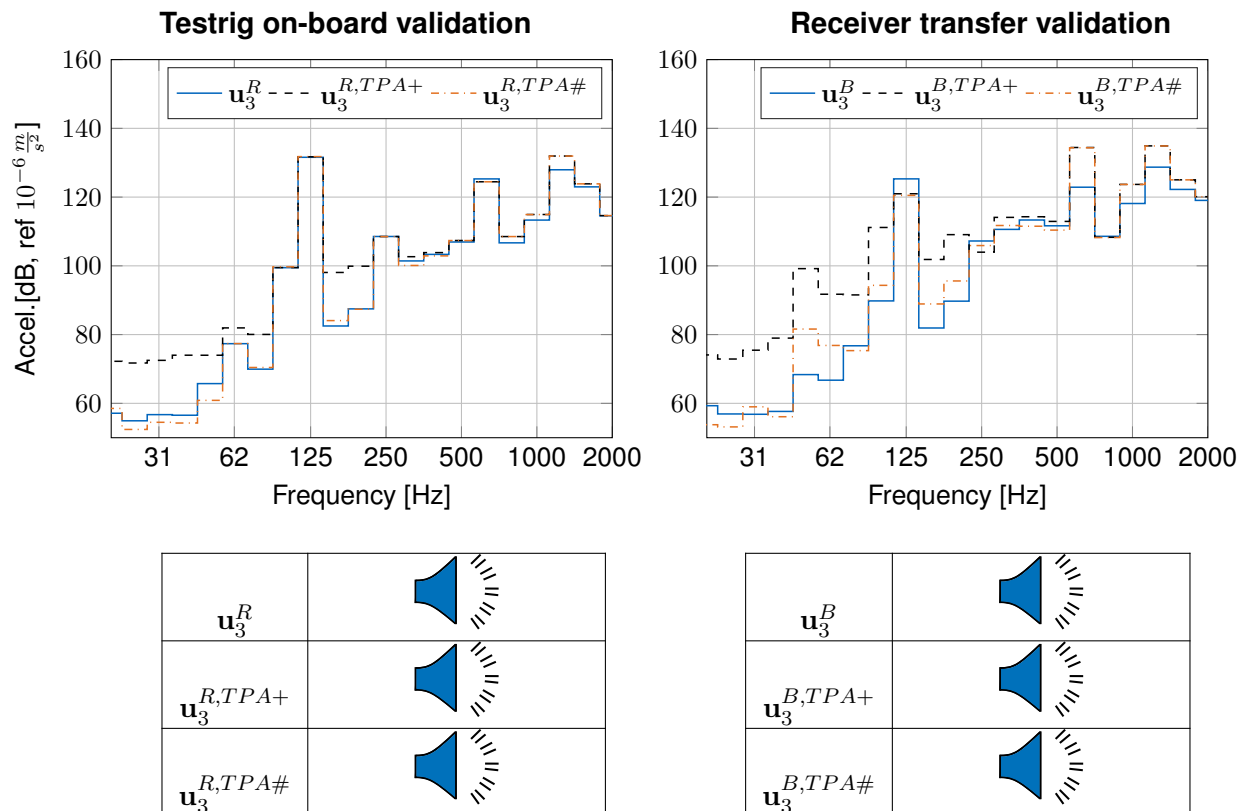
Figure 8.3: Third octave plots of blocked force predictions with validation measurements in the range $0 - 2000$Hz. Sound files of predictions and validation measurements are provided below. All sound files were created with the FIR-filter approach explained in chapter 7 (only the on-board validation would have yielded no artificial clicks with the overlap-add method). *Left part*: On-board validation of blocked forces on the testrig. *Right part*: transfer validation of blocked forces from the testrig transfered to the receiver design.
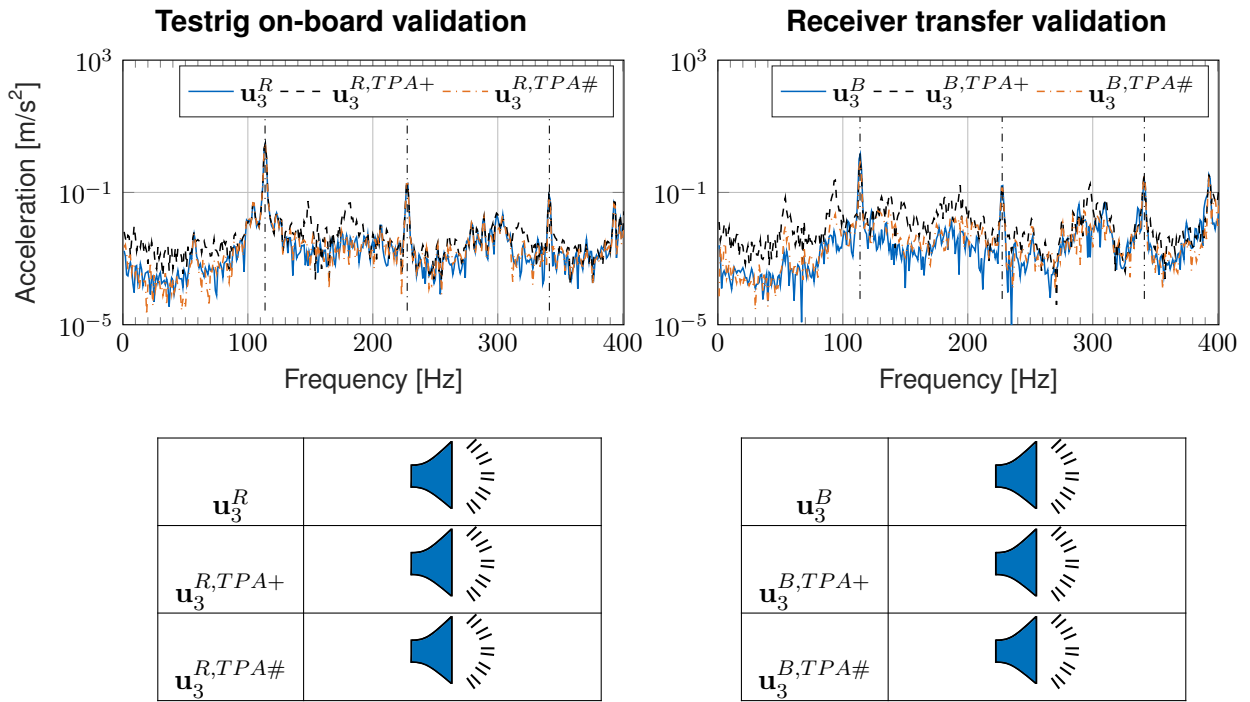
Figure 8.4: Narrow band plots of blocked force predictions with validation measurements in the range $0 - 400$Hz. Sound files of predictions and validation measurements provided below. Vertical dashed lines indicate the order frequencies of the compressor. All sound files had to be created with the FIR-filter approach explained in chapter 7 to avoid spurious clicks in the signals. *Left part*: On-board validation of blocked forces on the testrig. *Right part*: transfer validation of blocked forces from the testrig transfered to the receiver design.

The results are shown in the right part of figure 8.3. The difference between the predictions with the regularized and non-regularized blocked forces are more prominent here. The predicition $\mathbf{u}_3^{B,TPA+}$ is too high in magnitude, especially in the lower frequency region. This is now clearly audible in the sound predictions in the lower right part of figure 8.3. The prediction $\mathbf{u}_3^{B,TPA+}$ contains clearly audible low frequent sound, which is neither present in the regularized solution $\mathbf{u}_3^{B,TPA\#}$ nor in the validation measurement $\mathbf{u}_3^B$. Nevertheless, both blocked force predictions are too high in the upper frequency region.

In figure 8.4, a focus on the frequency region $0 - 400$ Hz is plotted in narrow band representation. The sound files in the lower right part of the figure make this low frequent difference between the regularized and non-regularized transfer predictions even more apparent. In the narrow band frequency plot of the transfer validation (upper right part of figure 8.4), one can observe distinct frequencies where the standard pseudo-inverse solution is significantly higher than the reference measurement.

8.3.2 Interpretation of the results

In the narrow band on-board validation (left part of figure 8.4), there are two distinct frequencies where the non-regularized $\mathbf{u}_3^{R,TPA+}$ is significantly higher than the reference $\mathbf{u}_3^R$. These are around 148Hz and 182Hz. These frequencies do not show as resonances in the testrig FRF matrix $\mathbf{Y}_{42}^{AR}$. At these frequencies, the FRF matrix is rather showing a drop in some lower singular values, which are the dynamically 'stiff' directions. This could be interpreted as an anti-resonance of the system in certain directions. As explained in section 8.2, the random measurement noise $\mathbf{e}_u$ (equally distributed), is amplified to high blocked force errors

in the 'stiff' directions. This is causing errors in the on-board validation, see e.g. the left part of figure 8.2 and figure 8.3, in the lower frequency region. However, to the authors experience, this amplification of measurement noise $\mathbf{e}_u$ to blocked force noise $\mathbf{e}_f$ is usually not an issue in the on-board validation. The on-board validation usually looks good, since the blocked force noise $\mathbf{e}_f$ which is high in the stiff directions of $\mathbf{Y}_{42}^{AR}$, then gets multiplied with the FRF matrix of the *same system* $\mathbf{Y}_{32}^{AR}$, which typically has the same stiff directions. So the resulting noise contamination of $\mathbf{u}_3^{TPA}$ is typically very limited again.

During a transfer validation, the picture can be different. When inspecting the results of the blocked force transfer closer, one finds that the frequencies where the over-prediction with the standard pseudo-inverse is dominant, often correspond to the eigenfrequencies of the receiver design $\mathbf{Y}_{42}^{AB}$. In the upper right part of figure 8.4, one can see that $\mathbf{u}_3^{B,TPA+}$ is significantly too high at e.g. 54Hz, 94Hz and 194Hz. All these frequencies are eigenfrequencies of the final receiver design, which can be seen in the increase of the first singular value of $\mathbf{Y}_{42}^{AB}$ in figure 8.2. Unfortunately, there is no guarantee that the mechanically stiff directions of the testrig $\mathbf{Y}_{42}^{AR}$, where the blocked force noise was amplified, will also be stiff directions on the final receiver $\mathbf{Y}_{32}^{AB}$. In the worst case, the receiver has a resonance that is excited by the blocked force noise.

Effectively, the sensor channel noise $\mathbf{e}_u$ is then amplified twice: first in a stiff direction of the testrig and second in a resonance direction of the final receiver. This noise amplification can cause problems as shown in the right part of figure 8.4. In fact, the spurious noise, which can be heard in the hearing examples of $\mathbf{u}_3^{B,TPA+}$ in figure 8.4, sounds similar to an auralization of the FRF's in $\mathbf{Y}_{32}^{AB}$ in this frequency range (not shown here).

In figure 8.5, the blocked force estimates computed on both configurations are shown. It can be observed that the blocked forces computed on both configurations are equal at the order frequencies of the compressor (as they should, since the blocked forces are a property of the compressor and independent of the receiver). The frequency regions between the order frequencies contain mostly inverted measurement noise. The magnitude of this inverted measurement noise becomes lower with increasing frequency. This corresponds to the increase in the lower singular values of the FRF matrix over frequency (see figure 8.2). Regularization of the inverse problem provides a way to filter out the noise in the stiff directions of the testrig, and therefore limit the detrimental effect of measurement noise on sound predictions for a new receiver. In figure 8.5 one can see that the regularized result for the blocked forces is equal at the order frequencies of the compressor, but significantly lower at the frequencies between the orders, where the noise is prominent. These effects and issues will be explained in the following section.

8.4   Theoretical background on regularization for inverse force estimation

In the last sections, it was explained and exemplified how particularly the small singular values of $\mathbf{Y}_{42}^{AR}$ can amplify the unavoidable measurement noise $\mathbf{e}_u$ during inversion. Regularization methods reduce the noise amplification in these dynamically *stiff* directions in a (hopefully) sensible way. Thereby, a more stable solution for the blocked forces and the transfer validation results is obtained. This section explains some basic background necessary for understanding the working principles of different regularization strategies. In [64], regularization methods are grouped into three different groups:

1. **Direct regularization:** These methods compute a regularized solution, with no foreknowledge of the actual data to invert ($\mathbf{u}_4^R$ or $\mathbf{e}_u$). They thus find a regularized solution
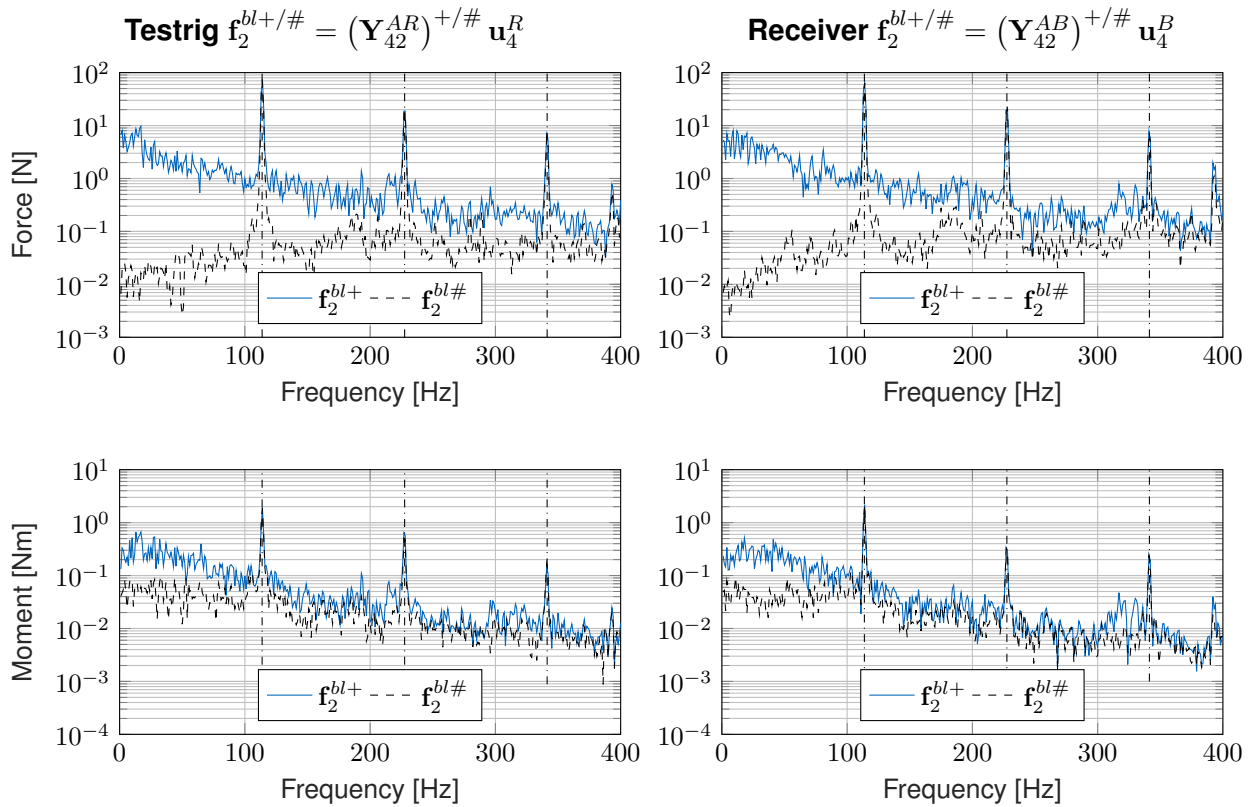
Figure 8.5: Narrow band plots of computed blocked forces. Vertical dashed lines indicate the order frequencies of the compressor. The plotted forces represent the norm of the x, y, z translational forces on the front connection point of the compressor (Left connection point, in the lower right part of figure 6.2b). The plotted moments represent the norm of the moments around the x, yz axis at the same connection point.

Direct regularization	**Parameter choice**	**Iterative regularization**
$(\mathbf{Y}_{42}^{AR})^{\#} = f\left(\mathbf{Y}_{42}^{AR}\right)$	$(\mathbf{Y}_{42}^{AR})^{\#} = f\left(\mathbf{Y}_{42}^{AR}, \mathbf{u}_4^R, \mathbf{e}_u\right)$	$(\mathbf{Y}_{42}^{AR})_i^{\#} = f\left(\mathbf{Y}_{42}^{AR}, \mathbf{u}_4^R, \mathbf{e}_u, i\right)$
Weighted least squares (LS)	Tikhonov SNR	Iterative Tikhonov
Truncated SVD (TSVD)	Tikhonov error balance	Landweber iterations
Tikhonov regularization	L-curve method	
	Cross validation	
	Discrepancy principle	
	Minimal covariance LS	

Table 8.1: Overview of regularization methods grouped according to [64].

with the *same* regularized inverse matrix $(\mathbf{Y}_{42}^{AR})^{\#}$ for all operational data $\mathbf{u}_4^R$.

2. **Parameter choice:** These methods provide a rule for computing the regularized solution depending on the measured data $\mathbf{u}_4^R$ and (an estimate of) $\mathbf{e}_u$.

3. **Iterative regularization:** These methods are computing a regularized solution in each iteration, and a stopping criterion defines the best solution. The advantage of these methods is that often no decomposition of the matrix is required. This is a computational advantage when dealing with very large problems.

Direct regularization and parameter choice methods are also called *a priori* and *a posteriori* regularization methods in the literature [145]. In table 8.1, different methods are classified according to this grouping. In Benners master thesis [15], many of the methods shown in table 8.1 are tested on the same e-compressor example as shown here. The intention of this chapter is mainly to explain the working principles of different regularization strategies, so individual implementations can be understood in a common framework and notation. The methods from [15] which particularly highlighted the differences between individual regularization principles will be presented in section 8.5. Before that, some basics for understanding regularization methods are explained.

8.4.1 Singular value truncation and Tikhonov regularization

In section 8.1, the SVD based pseudo-inverse was explained. If $\mathbf{Y}_{42}^{AR}$ has singular values that are equal to zero (i. e. there is a null-space), the blocked force solution is set to zero in the null-space directions (equation (8.10)). With the **truncated SVD (TSVD)** the blocked force solution is additionally set to zero in directions corresponding to singular values below a lower threshold l_σ, i.e.:

$$\mathbf{\Sigma}^+ = \begin{bmatrix} \frac{1}{\sigma_1} & \cdots & 0 & 0 & \cdots & 0 \\ \vdots & \ddots & & \vdots & \ddots & \\ 0 & & \frac{1}{\sigma_n} & 0 & & 0 \end{bmatrix}, \qquad \text{with: } \frac{1}{\sigma_i} \overset{!}{=} 0, \quad \text{for: } \sigma_i \le l_\sigma. \tag{8.20}$$

Thereby, the solution in the dynamically stiffest directions is artificially set to zero. Choosing l_σ depends on either experience of the NVH engineer or some fixed rule. The TSVD is often implemented in commercial tools for classical TPA, but (to the authors experience) choosing the lower threshold l_σ is often done by trial and error, until the on-board validation of the TPA

synthesis yields the best results. As explained in section 8.3, a good on-board validation is not necessarily enough for obtaining good results when blocked forces shall be transferred to a new design.

Tikhonov regularization is redefining the plain minimization of the residual $||\mu||^2$, which lead to the least squares and SVD pseudo-inverse solution. Additionally to the minimization of the residual, the blocked force magnitude shall not become to large (e.g. due to noise amplification). The Tikhonov regularization, the blocked forces are estimated by the minimization problem,

$$\text{minimize:} \quad ||\mathbf{u}_4^R - \mathbf{Y}_{42}^{AR}\mathbf{f}_2^{bl}||^2 + \alpha||\mathbf{f}_2^{bl}||^2, \tag{8.21}$$

where α is usually called the regularization parameter.[2] After solving equation (8.21), one obtains for the forces:

$$\mathbf{f}_2^{bl} = \left[(\mathbf{Y}_{42}^{AR})^*\mathbf{Y}_{42}^{AR} + \alpha\mathbf{I}\right]^{-1}(\mathbf{Y}_{42}^{AR})^*\mathbf{u}_4, \tag{8.22}$$

which can easily be verified since (8.21) is a positive definite and quadratic problem, so one can take the first derivative and set it to zero. Choosing α can be done by various methods. Some will be shown in section 8.5. Generally in literature it is noted that,

"Choosing the parameter α wisely is often the hardest part." [165, section 8.2].

Also according to [152], the pivotal point in Tikhonov regularization is to find a suitable and stable manner of determining α.

8.4.2 Filter Factors

The standard SVD based pseudo-inverse in (8.9) can be written as a sum over the singular values:

$$\mathbf{f}_2^{bl+} = \sum_{i=1}^{p}\mathbf{v}_i\frac{1}{\sigma_i}\left(\mathbf{u}_i^*\mathbf{u}_4^R\right), \qquad \text{with } p = rank(\mathbf{Y}_{42}^{AR}), \tag{8.23}$$

where $\mathbf{u}_i$ and $\mathbf{v}_i$ are the column vectors of the matrices $\mathbf{U}$ and $\mathbf{V}$ respectively. The effect of regularization strategies can be visualized with the definition of filter factors [64]. The Tikhonov solution (8.22) can be written as:

$$\mathbf{f}_2^{bl\#} = \sum_{i=1}^{p}\mathbf{v}_i\frac{\sigma_i}{\sigma_i^2 + \alpha}\left(\mathbf{u}_i^*\mathbf{u}_4^R\right), \tag{8.24}$$

which can be rewritten as:

---

[2]Just for general interest, the Tikhonov regularization is often found in this generalized form:

$$\text{Find } \mathbf{f} \text{ to minimize: } ||\mathbf{u} - \mathbf{Y}\mathbf{f}||^2 + \alpha||\mathbf{d} - \mathbf{A}\mathbf{f}||^2,$$

where $\mathbf{A}$ is a matrix that either comes from a physical model or acts as a weighting on the sought solution $\mathbf{f}$. The vector $\mathbf{d}$ can be used, if there exists some pre-knowledge of what the solution $\mathbf{f}$ should look like, and therefore also minimize this deviation. E.g. in state estimation for control applications, one is often assuming that the state of a system in a new time step should not deviate wildly from the state in the previous time step. The factor α can be used to control the strength of this additional term in the solution of the inverse problem. If $\alpha \to \infty$, then the solution of $\mathbf{f}$ needs to obey $\mathbf{A}\mathbf{f} = \mathbf{d}$. The rest of the solution is then minimizing the $||\mathbf{u} - \mathbf{Y}\mathbf{f}||^2$ in the nullspace of $\mathbf{A}$.
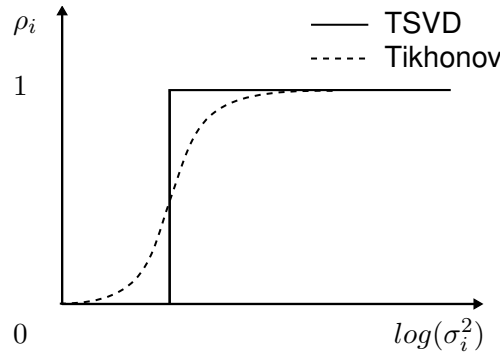
Figure 8.6: Schematic depiction of filter factors for the TSVD and Thickhonov regularization.

$$\mathbf{f}_2^{bl\#} = \sum_{i=1}^{p} \mathbf{v}_i \frac{\rho_i}{\sigma_i} \left(\mathbf{u}_i^* \mathbf{u}_4^R \right) \qquad \text{with} \quad \rho_i = \frac{\sigma_i^2}{\sigma_i^2 + \alpha}. \tag{8.25}$$

The filter factors ρ_i take a value between zero and one (α is always positive). The least squares solution in the direction $\mathbf{v}_i$ is filtered (reduced) by the factor ρ_i. If the filter factor ρ_i is equal to one for all singular values, one obtains the least squares solution. For the TSVD the filter factor would be one for all singular values above l_σ, and zero for all below. The filtering of singular values for the TSVD and the Tikhonov regularization is schematically shown in figure 8.6.

In the problems treated in this thesis, the Tikhonov regularization can be interpreted as adding the same amount of artificial *flexibility* to each force input direction of the system. The regularized system is more flexible particularly in the previously very stiff directions (small singular values). Larger singular values are only marginally affected by this, but the small singular values are significantly changed and the error amplification (but also the true solution) in these directions is filtered out significantly.

8.4.3 Regularization error and the L-curve

Regularization yields a solution $\mathbf{f}_2^{bl\#}$ which differs from the least squares solution $\mathbf{f}_2^{bl+}$. A new *regularization error* is introduced, while the *data error* resulting from amplified measurement noise $\mathbf{e}_u$ is reduced. The overall error in the estimated blocked forces $\mathbf{e}_f$ is composed of these two contributions [165, section 8.2]:

$$||\mathbf{e}_f|| = ||\hat{\mathbf{f}}_2^{bl} - \mathbf{f}_2^{bl\#}|| = || \underbrace{\hat{\mathbf{f}}_2^{bl} - \hat{\mathbf{f}}_2^{bl\#}}_{\text{Regularization error}} + \underbrace{\hat{\mathbf{f}}_2^{bl\#} - \mathbf{f}_2^{bl\#}}_{\text{Data error}} ||, \tag{8.26}$$

where $\hat{\mathbf{f}}_2^{bl}$ denotes the true blocked forces that would have been computed from a noise free signal,

$$\hat{\mathbf{f}}_2^{bl} = (\mathbf{Y}_{42}^{AR})^+ \hat{\mathbf{u}}_4^R, \tag{8.27}$$

and $\hat{\mathbf{f}}_2^{bl\#}$ are the forces computed from a noise free signal with the regularized inverse matrix:

$$\hat{\mathbf{f}}_2^{bl\#} = (\mathbf{Y}_{42}^{AR})^\# \hat{\mathbf{u}}_4^R. \tag{8.28}$$

The term $\mathbf{f}_2^{bl\#}$ denotes the actual result of the computation, namely the blocked forces computed from the noisy signal $\mathbf{u}_4^R$ with the regularized matrix.
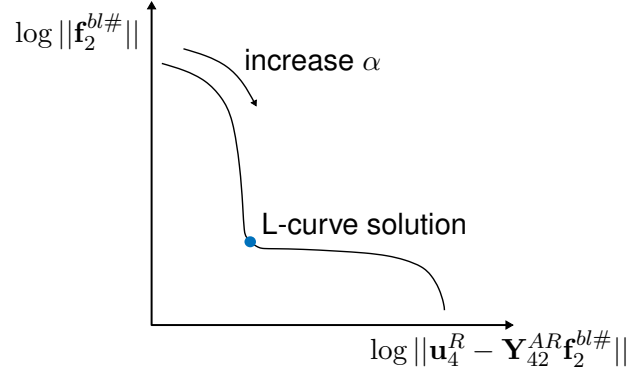
Figure 8.7: The L-curve resulting from computing the solution $\mathbf{f}_2^{bl\#}$ for different values of α. Notice the log-log scale.

$$\mathbf{f}_2^{bl\#} = (\mathbf{Y}_{42}^{AR})^{\#}\mathbf{u}_4^R. \tag{8.29}$$

The goal of all regularization strategies is to balance the *regularization error* and the *data error* such that the overall error $||\mathbf{e}_f||$ is minimized. Of course, both of these errors cannot be computed or compared directly. For doing this, one would need to know the noise free solution, which would render the whole discussion of this chapter pointless.

However, for starting with a low regularization parameter α which is slowly increased, one can often observe a fast decrease in the magnitude of $||\mathbf{f}_2^{bl\#}||$ if the least squares solution $\mathbf{f}_2^{bl+}$ is contaminated by amplified measurement noise. Simultaneously, the residual of the regularized solution $||\mu^{\#}||$ will increase with an increasing α.

$$||\mu^{\#}|| = ||\mathbf{u}_4^R - \mathbf{Y}_{42}^{AR}\mathbf{f}_2^{bl\#}||. \tag{8.30}$$

Both quantities, the residual $||\mu^{\#}||$ and the solution magnitude $||\mathbf{f}_2^{bl\#}||$, can be computed for different values of α. When they are plotted into a figure for increasing values of α, this results in the so called L-curve plot, see a schematic depiction in figure 8.7. This curve can be used for parameter choice in the Tikhonov regularization. It is assumed that the solution with an optimal balance of the regularization and data error is found were the curvature of the L-curve is greatest, see figure 8.7. One parameter choice method is thus to compute the solution for many different values of α and then find the point with the strongest curvature in the L-curve to find the optimal value of α. For an easy to read, but insightful overview of the L-curve see [62].

In figure 8.8, the L-curves for the inverse force identification at different frequencies are shown (109 - 119 Hz). It can be observed that for some frequencies, both the residual $||\mu^{\#}||$ and the blocked force magnitude $||\mathbf{f}_2^{bl\#}||$ is high (see the three curves in the upper right part of figure 8.7). These are the three discrete frequencies around the first compressor order (115Hz), where the signal to noise ratio is high. For an increase of α one can observe only a small initial drop in the blocked force magnitude. Further increasing α mainly results in an increased residual $||\mu^{\#}||$. In the lower left corner of figure 8.8 one finds the frequencies where both the residual and the blocked force magnitude is low. At these frequencies, the operational signal is low since they are not at a compressor order (see e.g. figure 8.4). For an increase of α one can observe a large initial drop in the blocked force magnitude. The L-curve method would thus suggest using a larger regularization parameter α at the frequencies with a lower signal to noise ratio (SNR). Conversely, for frequencies with a high SNR a lower α should be chosen.
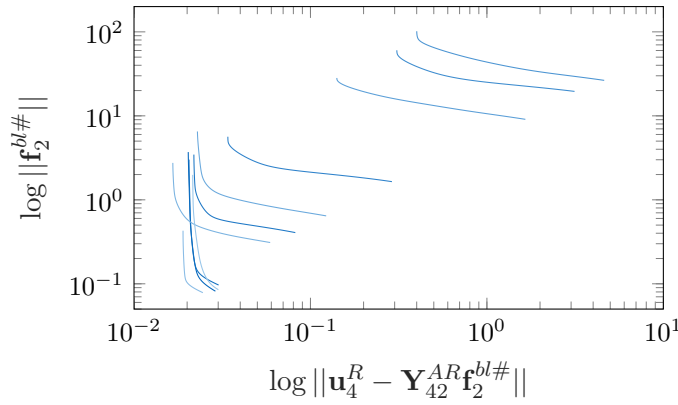
Figure 8.8: Exemplary plot of L-curves for the problem introduced in section 8.3. L-curves are plotted for frequencies from 109Hz - 119Hz, the first order of the compressor was around 115Hz. The regularization parameter α was varied from 10^{-7} to 10^{-1} with 200 steps and a logarithmic spacing.

8.4.4   The discrepancy principle

The idea behind the discrepancy principle is to avoid an *over-fitting* to noisy data, by having an estimate of the measurement noise $\mathbf{e}_u$ [165, section 8.2]. The estimate of $\mathbf{e}_u$ could e.g. be obtained by recording the signal in all channels while the source is switched off. If the residual $||\mu||$ would be lower than the measurement noise magnitude $||\mathbf{e}_u||$, one could expect to perform just a mathematical fit of the blocked forces to measurement noise. Therefore, the residual of the problem should only be smaller than some multiple η of the measurement noise magnitude $||\mathbf{e}_u||$:

$$||\mathbf{u}_4^R - \mathbf{Y}_{42}^{AR}\mathbf{f}_2^{bl\#}|| \leq \eta||\mathbf{e}_u||, \tag{8.31}$$

where η is a scalar parameter to control the degree up to which the noise shall be fitted. The main idea of the discrepancy principle is to chose the regularization parameter such that the residual approximately equal to $\eta||\mathbf{e}_u||$ [64].

8.5   Comparison of regularization methods for e-compressor TPA

Sections 8.2 and 8.3 explained of how measurement noise can affect blocked force predictions. Section 8.4 introduced the basic concepts to understand how regularization methods work and how their effect on force identification can be visualized. In this section, different regularization strategies are introduced and applied to the compressor example. The compared methods are by no means exhaustive, as there have been many methods suggested in the field of noise handling in inverse problems. Therefore, a short literature review shall be given first.

8.5.1   Literature review on noise handling in inverse force identification

One of the first regularization applications to force identification in the frequency domain is Powell [141] in 1984. He used the condition number and the SVD to identify ill-posed problems. Based on the coherence of the FRF matrix, he defines a threshold for filtering small singular values. His method is a TSVD which can be classified as a direct regularization method (see table 8.1).

For inverse force identification at lower frequencies, it is reported that strain/force FRFs yield better results than acceleration/force [33, 68]. According to [68], this relates to the fact that at lower frequencies only a small number of modes is contributing to the response. The contribution from higher frequency modes is barely contained in acceleration signals and can be better observed with strain measurements. The generally more complex mode shapes of high frequency modes create a larger strain. In [77], these findings in favor of using strains are confirmed on a range of analytical examples. In [77], it is recommended to use the condition number of the FRF matrix as an indicator for the accuracy of the force identification, which is also found by [174]. In the literature, it is generally recommended to use overdetermination of the problem (see section 8.1). In [71, 72], an estimated error matrix E_{ij} for the measurement errors of each FRF matrix entry Y_{ij} is computed, using the FRF magnitude, the number of averages and the coherence (see [13]). The largest singular value of this error matrix is used as a threshold for rejecting small singular values in the inversion of the FRF matrix (TSVD). Compared to the least squares solution, significant improvements in the on-board validation are reported. The authors of [71, 72] also propose to compute a covariance matrix of the indicator signals $\mathbf{u}_4^R$. The covariance matrix is computed from multiple time blocks recorded during stationary operation of the source. The covariances of $\mathbf{u}_4^R$ can be propagated to covariances of $\mathbf{f}_2^{bl}$ and $\mathbf{u}_3^B$. From the propagated variances, confidence intervals for the predicted receiver responses $\mathbf{u}_3^B$ can be computed and plotted with the results. A valuable indication for the predictions trustworthiness[3].

In the companion papers [172, 173], different regularization methods of the inverse problem are compared on an analytical and experimental case of a plate. In [172], two TSVD methods are proposed for the regularization. One lower threshold l_σ is also based on the largest singular value of the error matrix, just like in [71, 72]. The other rejection threshold in [172] is based on the variance of the operational signal $\mathbf{u}_4^R$. The regularized results are improved compared to the least squares solution. Nevertheless, the authors suggests in [172] that a criterion based on both errors, would be required, since neither one is universally applicable. In the second paper [173], the authors used two Tikhonov regularization techniques, where α is chosen via ordinary cross validation [64], or an iterative regularization technique. These methods were found to yield better results than the TSVD methods tested in [172]. In [26, 81], the authors compare the Generalized Cross Validation (GCV) and L-curve method for inverse source identification. A recent review on inverse force identification techniques can be found in [152]. For methods identifying forces in the time domain see Sturms PhD thesis [169].

8.5.2 Truncated singular value decomposition (TSVD)

The concept of the TSVD was already introduced in section 8.4.1. The lower threshold l_σ is often found in a manual process, by tuning l_σ until the on-board validation $\mathbf{u}_3^{R,TPA\#}$ matches the measurement $\mathbf{u}_3^R$ as well as possible. In classical interface force TPA, the on-board validation was the only validation one could do anyway. This manual approach was also applied here, see left part of figure 8.9, and for this operational condition of the compressor, yielded $l_\sigma = 2 \cdot 10^{-2}$.

While tuning l_σ in the on-board validation, it was found that the prediction with $\mathbf{f}_2^{bl\#}$ is higher than the prediction with $\mathbf{f}_2^{bl+}$ at the first compressor order (ca. $+1dB$ in some channels). When increasing l_σ further, e.g. to $l_\sigma = 6 \cdot 10^{-2}$, this over prediction increased to ca. $+3dB$. It seems that the solution in the stiff directions is canceling out part of the solution $\mathbf{u}_3^R$ at the

---

[3]In fact the authors of [71] don't compute blocked forces, but a set of forces that are called pseudo-forces which can be seen as a generalization of the blocked force concept [159].
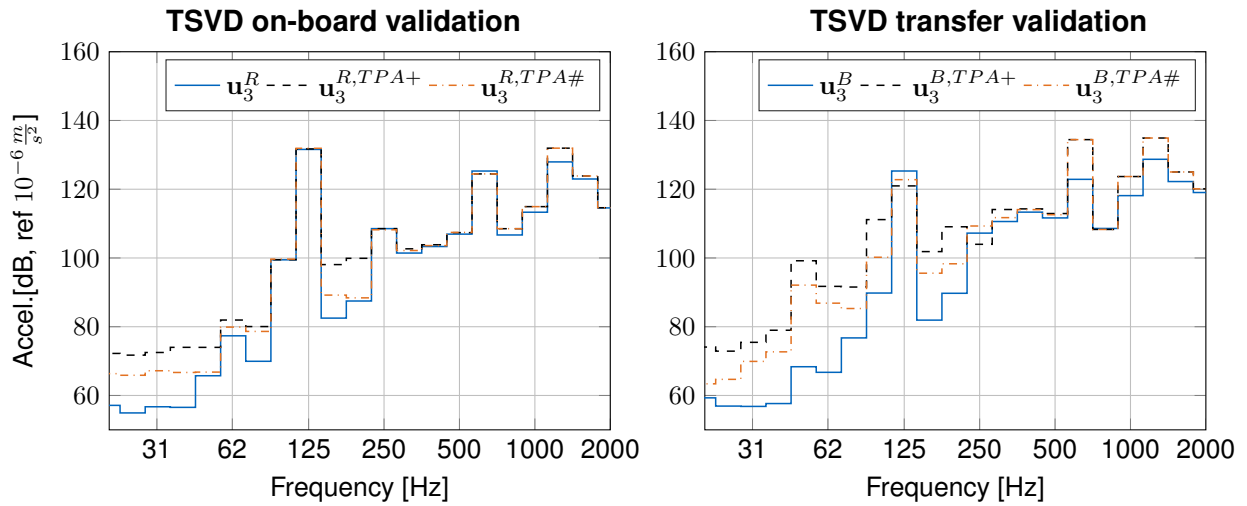
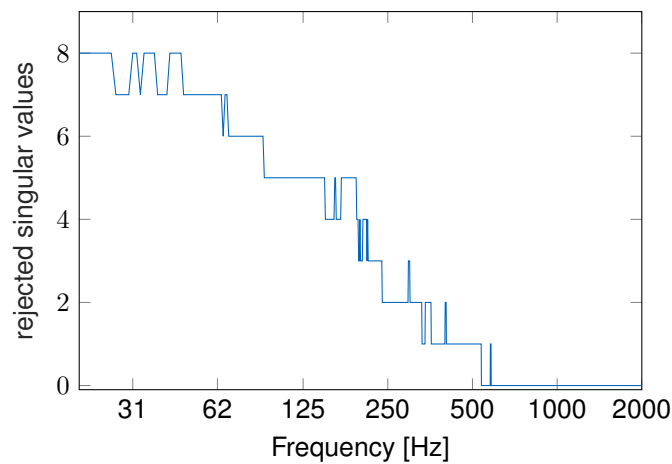**Figure 8.9:** On-board and transfer validation results for the TSVD

Figure 8.10: Number of rejected singular values for the TSVD regularization with $l_\sigma = 2 \times 10^{-2}$.

first order (opposite phase). In the transfer validation (right part of figure 8.9) one can see that this regularization method is not yielding optimal results. Choosing one fixed rejection threshold l_σ is effectively applying same regularization at all frequencies, irrespective of the signal to noise ratio. Additionally, as the singular values are increasing over frequency (see figure 8.2), one fixed l_σ is effectively only regularizing in the lower frequency region. This can be seen from the number of rejected singular values over frequency in figure 8.10. Another disadvantage of the method is the manual labor required for chosing l_σ at each operating condition, which is prone to human errors and a repetitive task.

8.5.3 Tikhonov: parameter choice from signal to noise

Wernsen suggested a filter in his thesis [193], which also takes the operational signal into account. This method could thus be grouped into the parameter choice methods in table 8.1. The method is based on the frequency dependent signal to noise ratio (SNR), which is estimated from the operational signal of the compressor $\mathbf{u}_4^R$ and the signal $\mathbf{e}_u$ recorded in the same channels but with the compressor switched off (see figure 8.11):
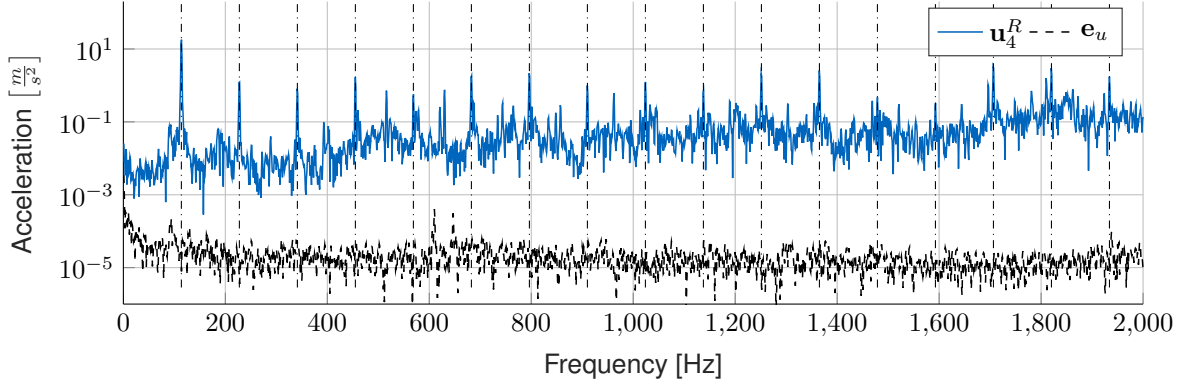
Figure 8.11: Signal $\mathbf{u}_4^R$ recorded during operation and noise $\mathbf{e}_u$ recorded with compressor switched off (exemplary channel). Dashed vertical lines indicate the compressor orders.

$$SNR = \frac{||\mathbf{u}_4^R||}{||\mathbf{e}_u||}. \tag{8.32}$$

With Wernsen's filter the regularization parameter α is defined as the inverse of the signal to noise ratio.

$$\alpha = \frac{1}{SNR}. \tag{8.33}$$

This regularization was found to work well for the climate compressor, due to the tonal excitation. The main excitation of the compressor is at the order-frequencies, see figure 8.11 where the SNR is high. Thus, the solution at the compressor orders is only marginally regularized. Conversely, at all non-order-frequencies, the SNR is low and the regularization parameter α is high, so the measurement noise is not amplified to spuriously large forces This can be seen by plotting the filter factors for this regularization, see figure 8.12. Note how the filter factors drop at multiples of $50Hz$ which is the ground frequency of the power grid. For the channel shown in figure 8.11, one can not see a strong increase in background noise, but in other channels there is probably some grounding issue. The recorded noise $\mathbf{e}_u$ is higher at these frequencies. At the lower frequencies, there are 6 singular values that are not filtered. These are corresponding to the rigid modes of the compressor. This regularization method was used for obtaining the regularized solutions in section 8.3. So the results for applying this filter can be seen and heard in figure 8.3, 8.4 and 8.5.

8.5.4 Tikhonov: parameter choice from error balancing

In section 8.4.3, it was explained how the regularization introduces a new *regularization error* next to the *data error*. In [165, section 8.2], Strang suggested to derive upper bounds for both of these errors, and set them equal to obtain an α that achieves a balance between both.

Upper bound regularization error

The regularization error is defined as $||\hat{\mathbf{f}}_2^{bl} - \hat{\mathbf{f}}_2^{bl\#}||$, see equation (8.26). The regularization affects the smallest singular value σ_n most. Thus the regularization error is greatest if all of the noise free signal $\hat{\mathbf{u}}_4^R$ would be in this mechanically stiffest direction $\mathbf{u}_n$, i. e. if:
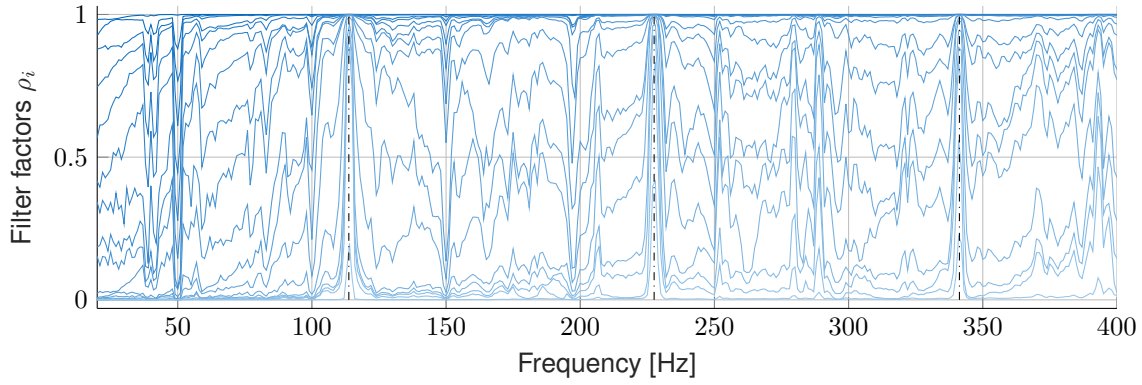
Figure 8.12: Filter factors ρ_i for individual singular values obtained by choosing α according to Wernsen's signal to noise ratio filter (8.33). Note that $\rho_1 \geq \rho_2 \geq ... \geq \rho_n$. Vertical dashed lines indicate the order frequencies of the compressor.

$$\hat{\mathbf{u}}_4^R =: ||\hat{\mathbf{u}}_4^R||\, \mathbf{u}_n. \tag{8.34}$$

The noise-free blocked force solution without and with regularization, $\hat{\mathbf{f}}_2^{bl}$ and $\hat{\mathbf{f}}_2^{bl\#}$, are:

$$\hat{\mathbf{f}}_2^{bl} = \mathbf{v}_n \frac{1}{\sigma_n}||\hat{\mathbf{u}}_4^R|| \qquad\qquad \hat{\mathbf{f}}_2^{bl\#} = \mathbf{v}_n \frac{\sigma_n}{\sigma_n^2 + \alpha}||\hat{\mathbf{u}}_4^R||, \tag{8.35}$$

which means for an upper bound of the regularization error:

$$||\hat{\mathbf{f}}_2^{bl} - \hat{\mathbf{f}}_2^{bl\#}|| \quad \leq \quad \left(\frac{1}{\sigma_n} - \frac{\sigma_n}{\sigma_n^2 + \alpha} \right) ||\hat{\mathbf{u}}_4^R|| \quad \leq \quad \frac{\alpha}{\sigma_n^3}\, ||\hat{\mathbf{u}}_4^R|| \tag{8.36}$$

Upper bound data error

The data error is defined as $||\hat{\mathbf{f}}_2^{bl\#} - \mathbf{f}_2^{bl\#}||$, see equation (8.26). This error depends on the amount of noise $\mathbf{e}_u$. The data error is greatest for a yet unknown relation between α and "a" singular value σ_i, which is to be found. If all the operational signal is in this direction, we get:

$$\hat{\mathbf{f}}_2^{bl\#} = \mathbf{v}_i \frac{\sigma_i}{\sigma_i^2 + \alpha}||\hat{\mathbf{u}}_4^R|| \qquad\qquad \mathbf{f}_2^{bl\#} = \mathbf{v}_i \frac{\sigma_i}{\sigma_i^2 + \alpha}||\hat{\mathbf{u}}_4^R + \mathbf{e}_u||. \tag{8.37}$$

with these definitions, the maximum data error is:

$$||\hat{\mathbf{f}}_2^{bl\#} - \mathbf{f}_2^{bl\#}|| \quad = \quad ||\mathbf{f}_2^{bl\#} - \hat{\mathbf{f}}_2^{bl\#}|| \quad \approx \quad \frac{\sigma_i}{\sigma_i^2 + \alpha}\, ||\mathbf{e}_u||. \tag{8.38}$$

Since the measurement noise $\mathbf{e}_u$ is fixed (it was recorded), the first term needs to be maximal for finding an upper bound of the data error, i. e. :

$$\sigma_i = \sqrt{\alpha} \qquad \text{for maximizing:} \quad \frac{\sigma_i}{\sigma_i^2 + \alpha}. \tag{8.39}$$

For the upper bound of the data error this means (insert (8.39) in (8.38)):

$$||\hat{\mathbf{f}}_2^{bl\#} - \mathbf{f}_2^{bl\#}|| \leq \frac{1}{2\sqrt{\alpha}}\, ||\mathbf{e}_u|| \tag{8.40}$$
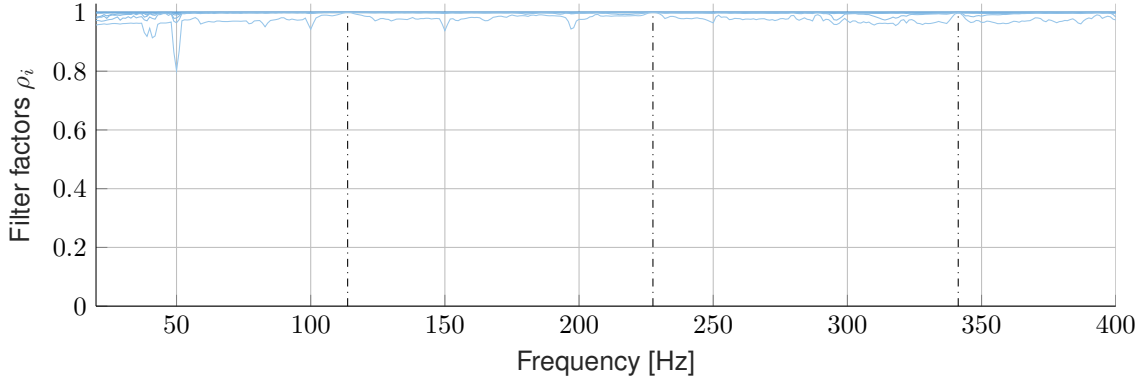
Figure 8.13: Filter factors ρ_i for individual singular values obtained by choosing α according to the error balance, equation (8.42). Vertical dashed lines indicate the order frequencies of the compressor.

Choosing the regularization parameter for error balance

The upper bounds for both errors are set equal in order to obtain a balance of both errors in the regularization:

$$\frac{1}{2\sqrt{\alpha}}\,||\mathbf{e}_u|| = \frac{\alpha}{\sigma_n^3}\,||\hat{\mathbf{u}}_4^R||, \tag{8.41}$$

which means for the α that achieves this balance:

$$\alpha \quad = \quad \left(\sigma_n^3\,\frac{||\mathbf{e}_u||}{2||\hat{\mathbf{u}}_4^R||}\right)^{2/3} \quad \approx \quad \left(\sigma_n^3\,\frac{1}{2\,SNR}\right)^{2/3}, \tag{8.42}$$

where it was assumed that $||\hat{\mathbf{u}}_4^R|| \approx ||\mathbf{u}_4^R||$, since the noise free signal is unknown. Equation (8.42) is the same solution as found in [165, section 8.2]. The SNR can be computed as in equation (8.32). Note that, with this method, the regularization parameter α becomes lower if the smallest singular value σ_n gets lower, in order to keep the regularization error low. As with Wernsen's method, α becomes larger for a lower SNR.

When inspecting the results of this parameter choice, one finds that the solution is virtually the same as the unregularized solution. This parameter choice results in a too weak regularization, see the filter factors in figure 8.13. Apparently, it puts too much emphasis on keeping the regularization error low.

8.5.5 Tikhonov: parameter choice from discrepancy principle

In [115], the problem of finding a regularization parameter α that satisfies:

$$||\mathbf{u}_4^R - \mathbf{Y}_{42}^{AR}\mathbf{f}_2^{bl\#}|| \overset{!}{\leq} M \qquad\qquad\qquad ||\mathbf{f}_2^{bl}|| \leq F \tag{8.43}$$

is approximated by:

$$\alpha = \left(\frac{M}{F}\right)^2, \tag{8.44}$$

where it is shown in [115] that this choice for α violates the constraints in (8.43) maximally by a factor of $\sqrt{2}$. For the discrepancy principle (8.31), one requires that:

$$||\mathbf{u}_4^R - \mathbf{Y}_{42}^{AR}\mathbf{f}_2^{bl\#}|| \overset{!}{\leq} M = \eta||\mathbf{e}_u||. \tag{8.45}$$

One does not want any bound on the blocked force solution, so one can choose F to equal the natural upper bound on the blocked force magnitude:

$$F = \frac{||\hat{\mathbf{u}}_4^R||}{\sigma_n} \tag{8.46}$$

which yields:

$$\alpha = \eta^2 \left(\frac{\sigma_n}{SNR}\right)^2 \tag{8.47}$$

This regularization choice is also not regularizing enough. The results are again almost identical to the results of the normal pseudo-inverse, and are therefore not shown here. The author thinks that using the recordings when the compressor is switched off as an error estimate for $\mathbf{e}_u$ might be the problem. One can observe in figure 8.11 that even at the non-order frequencies the operational signal is still a lot higher than the noise $\mathbf{e}_u$. This issue should be investigated further. It could be related to leakage in the FFT transformation or to machine precision errors in the 24 bit discretization of the measurement system (the discretization error is higher for larger overall vibration levels in the time domain).

8.5.6 Tikhonov: parameter choice from L-curve

The L-curve was introduced in section 8.4.3. The parameter choice based on the L-curve method finds the α in the "corner" of the L-curve, i.e. where the curvature is maximum. It is assumed that there the transition from a dominant data error to a dominant regularization error occurs. The method was first proposed by Hansen [63]. For an easy to read and insightful overview of the L-curve method see [62]. In the application here, the method was executed with a set of 70 values for α at each frequency. These 70 values were in a range of:

$$\alpha \in \left[\tfrac{\sigma_n}{10},\ \sigma_1\right], \tag{8.48}$$

with a logarithmic spacing. The regularized solution was computed for each of these α values. In the resulting L-curves the curvature at each point was computed by using a circle fit with 3 neighboring points (i.e. 3 consecutive values of α). The point of maximum curvature is chosen by the L-curve method, see figure 8.14 for a depiction of this process at a few frequencies. Note how the point of maximum curvature occurs at low α values for the curves in the upper right part of figure 8.14. These frequencies are around the first order, and thus α should be low. At the non-order frequencies (the curves in the lower left part of figure 8.14), the point of maximum curvature occurs for higher values of α.

The resulting filter factors are plotted in figure 8.15. It can be seen that the filtering is not as stable as with the SNR-filter in figure 8.12. From other applications [26, 81], it is known that the L-curve method is well applicable to rather well-posed problems where data noise $\mathbf{e}_u$ is the dominant problem. However, the predictions for the transfer validation show similar improvements as the SNR filter, which can be seen and heard in figure 8.16. The regularization at higher frequencies was overall very low. When plotting the L-curves for higher frequencies, one could clearly see that mostly the lowest α was chosen. The L-curve method takes more time to compute, since many different values of α have to be tested at each fre-
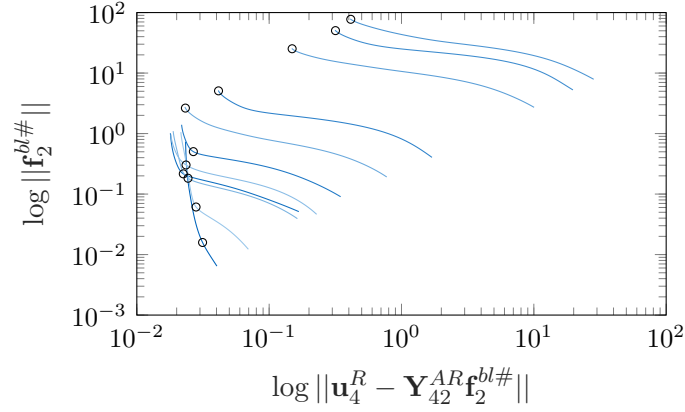
Figure 8.14: L-curves and points of maximum curvature (black circles) for frequencies from 109Hz - 119Hz. The first order of the compressor was around 115Hz. The regularization parameter α was varied from $\frac{\sigma_n}{100}$ to σ_1 with 70 steps and a logarithmic spacing.
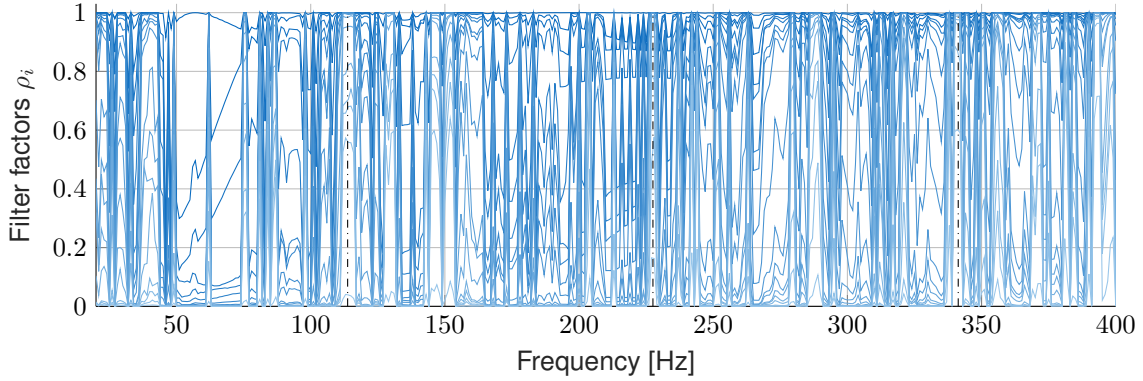
Figure 8.15: Filter factors ρ_i for individual singular values obtained by the L-curve method. Vertical dashed lines indicate the order frequencies of the compressor.

quency[4]. The L-curve method can be executed without an estimate of the measurement noise $\mathbf{e}_u$, which can be seen as an advantage.

8.5.7 Iterative Tikhonov: Discrepancy principle as stopping criterion

The idea behind an iterative Tikhonov regularization is to start with filter factors that correspond to a large regularization α_1. The filter factors are iteratively decreased until a certain stopping criterion is fulfilled. The starting value α_1 chosen here was:

$$\alpha_1 = \left(\frac{\sigma_1}{SNR}\right)^2. \tag{8.49}$$

In the first iteration $k = 1$, all filter factors are corresponding to α_1. During the iterations with increasing k the filter factors are converging to 1, i.e. the regularization is reduced, according to the rule:

$$\rho_i^k = 1 - \left(1 - \frac{\sigma_i^2}{\sigma_i^2 + \alpha_1}\right)^k, \tag{8.50}$$

---

[4]The overall run-time on the authors laptop was still reasonable (ca. 20 minutes).
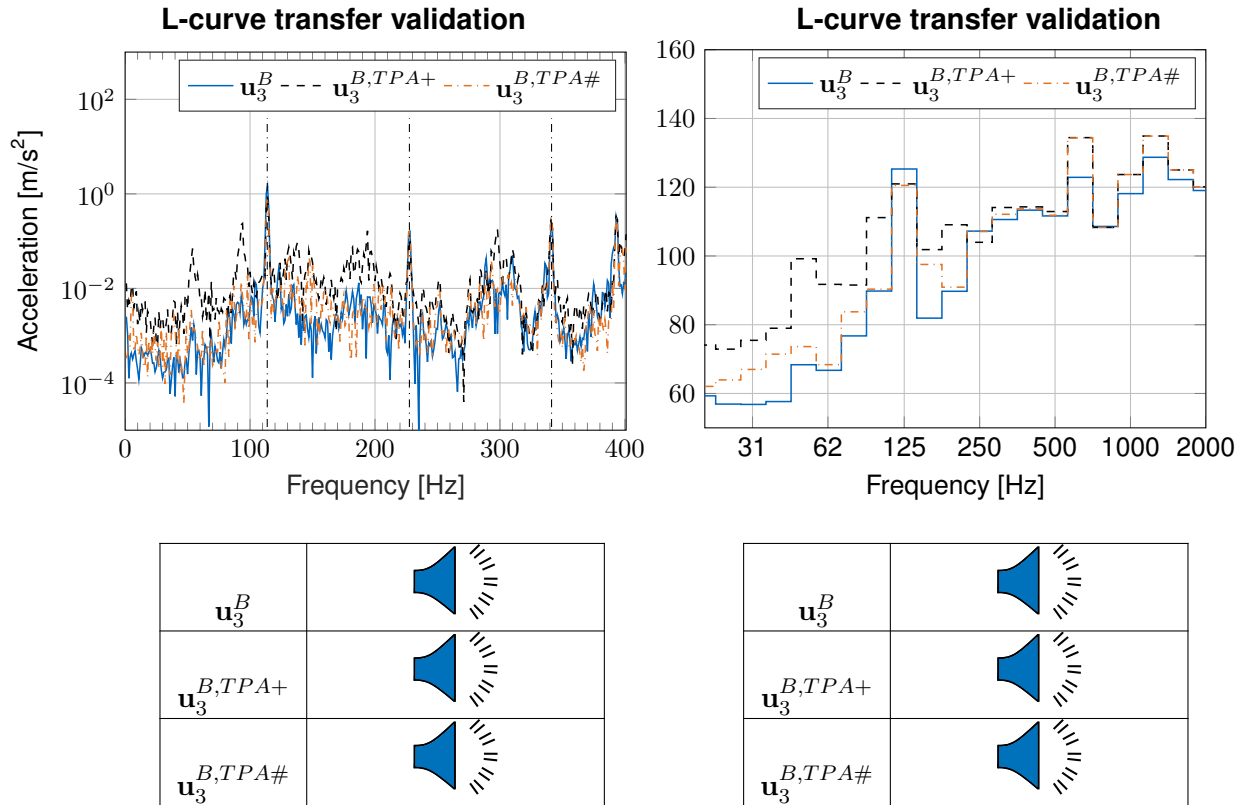
Figure 8.16: Blocked force predictions with validation measurements for the L-curve method. *Left part*: Narrow band signals from 0-400Hz. *Right part*: Broad band signals from 0-2000Hz.

where ρ_i^k is the filter factor for singular value i in iteration k. It is easy to verify that for $k = 1$ the filter factors correspond to a standard Tikhonov regularization with α_1. The convergence behavior of the filter factors is further discussed in [15]. The iterations are stopped after a stopping criterion is fulfilled. This could be done with the discrepancy principle as stated in equation (8.31). However, it was found that even with the least squares solution $\mathbf{f}_2^{bl+}$, the residual is higher than the noise level. The least squares residual $||\mu^+||$ is defined as:

$$||\mu^+|| = ||\mathbf{u}_4^R - \mathbf{Y}_{42}^{AR}\mathbf{f}_2^{bl+}||. \tag{8.51}$$

It is plotted against the noise level $||\mathbf{e}_u||$ in figure 8.17. It can be seen that $||\mu^+||$ is greater than $||\mathbf{e}_u||$ at all frequencies. Especially at the orders of the compressor the least squares residual $||\mu^+||$ is large. As a stopping criterion for the iterations k, it was therefore chosen to include the least squares residual in the stopping criterion (as suggested in [15]):

$$\text{increase } k \text{ until:} \qquad ||\mu^\#|| \leq ||\mu^+|| + \eta||\mathbf{e}_u||, \tag{8.52}$$

where the regularized residual $||\mu^\#||$ is defined as in equation (8.30), and η has to be chosen by the user. In figure 8.18, the resulting filter factors for $\eta = 10$ are shown. This η was chosen, since it was observed that the least squares residual is roughly an order of magnitude higher than the noise floor at the non-order frequencies. Therefore, the regularized solution is given some 'slack' to double the least squares residual at the non-order frequencies. In figure 8.18, the resulting filter factors for the iterative Tikhonov method are shown. It can be observed, that the regularization is strong at the non-order frequencies, particularly at the frequencies where the measurement noise was large (multiples of the power grid frequency 50Hz). With increasing frequency, the filter factors for the lower singular values increase, since more degrees of freedom are needed to represent the compressor excitation. This
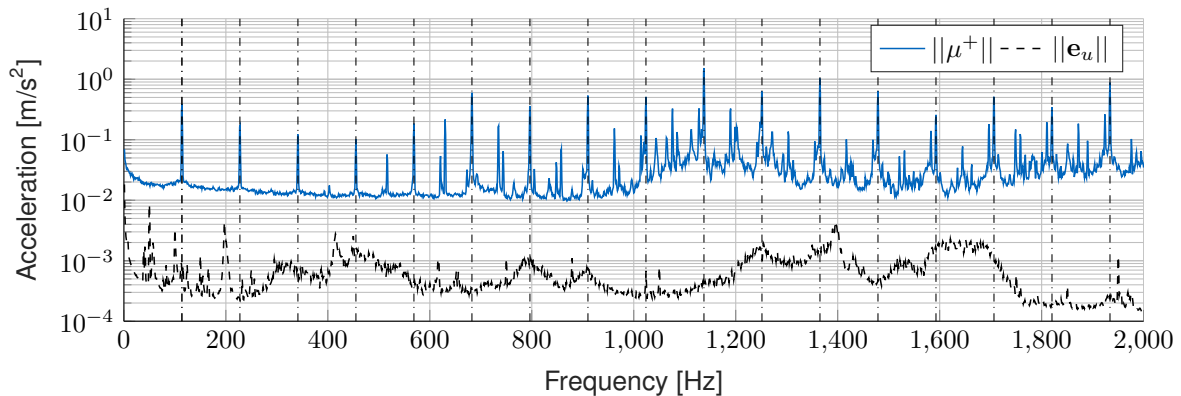
Figure 8.17: Least squares residual magnitude $||\mu^+||$ versus noise measurement magnitude $||\mathbf{e}_u||$. Dashed vertical lines indicate the compressor orders.

is to be expected, since for higher frequencies more modes are contributing to the overall motion. In figure 8.19, the results of the transfer validation can be seen. The prediction is improved especially in the lower frequency region. The sound files are not included, but the audible prediction improvement is similar to the SNR based filter in figure 8.3 and 8.4.

8.6 Conclusion

Regularization was found to be an essential tool for improving the blocked force estimation of the climate compressor. Note that in this chapter all results were shown only for one receiver channel, at one operating condition of the compressor. The channel was chosen since it highlighted the effects of the regularization best. It was the channel pointing in the global Y-direction of the sensor on the right arm (see the set of $\mathbf{u}_3^R$ in figure 6.2b). The largest operational vibration levels were observed in the channels pointing in the global Z-direction of the two sensors on the arms. The results in these channels are shown in figure 8.20. It can be seen that the deviations between blocked force predictions $\mathbf{u}_3^{B,TPA}$ and the reference measurement $\mathbf{u}_3^B$ are significantly smaller in the higher frequency region. The overall finding for the improvements in the lower frequency region remain the same. It can be concluded that regularization can take care of the needed DoF in the lower frequency region, since the vibration behavior there is dominated by only a few modes. In section 8.2 this was termed as a rank-deficient problem. At the start of this project, the author often thought it would be necessary to describe the compressor with a smaller set of DoF in the lower frequency region, and a larger set of DoF in the upper frequency region. Regularization turned out to be a handy tool to take care of this issue automatically, so the source can be modeled with the same (larger) set of DoF over the whole frequency range.

To the authors experience, the on-board validation is a valuable tool for finding general errors in the measurement setup or the code. But is not able to detect the issue of noise amplification if the blocked forces shall be transfered to a different design (see section 8.3). An applicable regularization method should require only knowledge of data obtained on a testrig (as is the case with the methods applied here). However, for the source of interest it should be verified at least once that the chosen regularization method yields satisfactory results, by performing a transfer validation. The compressor is a source component with a highly tonal excitation, and the SNR based filter suggested by Wernsen [193] yields stable results with minimal computing time (see section 8.5.3). Other than that, the iterative
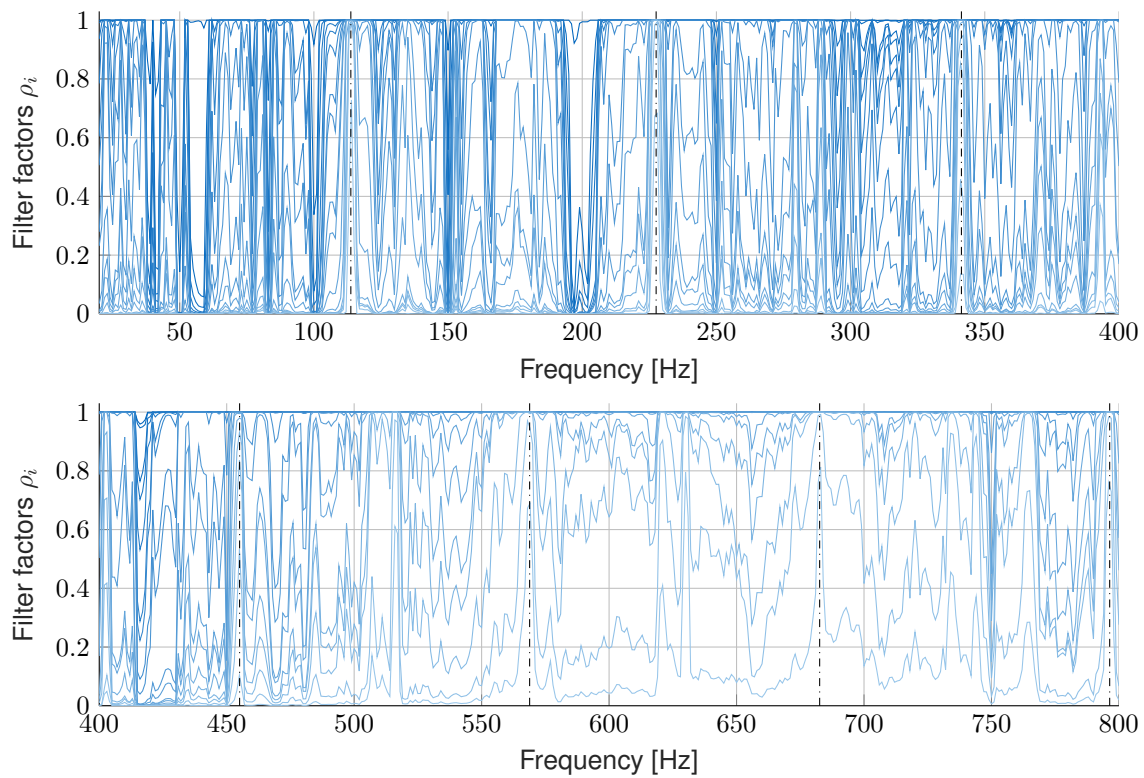
Figure 8.18: Filter factors ρ_i for individual singular values obtained by the iterative Tikhonov method. Vertical dashed lines indicate the order frequencies of the compressor.
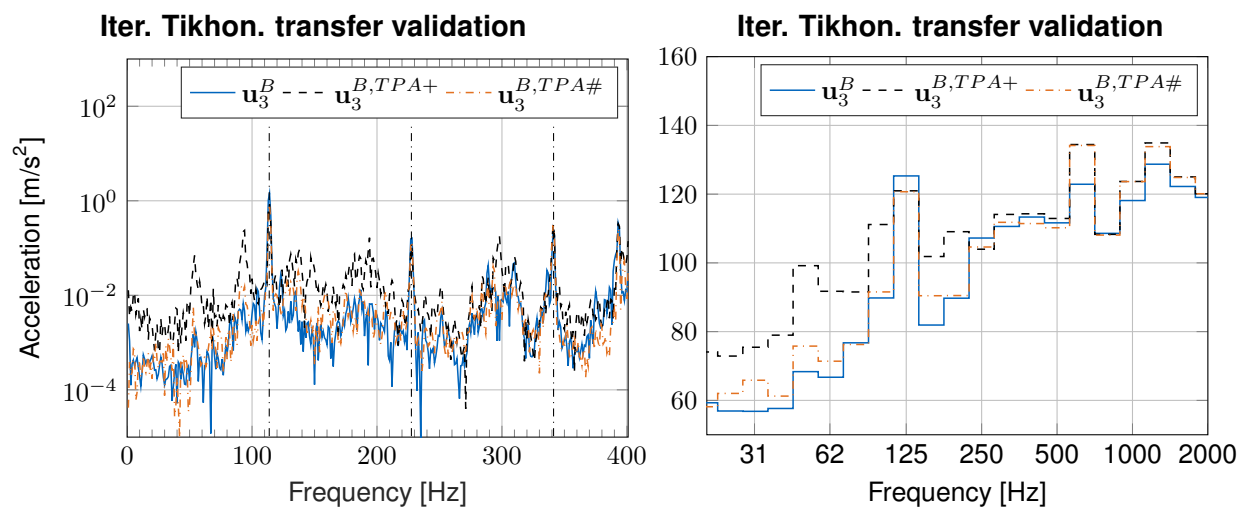
Figure 8.19: Blocked force predictions with validation measurements for the iterative Tikhonov method. *Left part*: Narrow band signals from 0-400Hz. *Right part*: Broad band signals from 0-2000Hz.
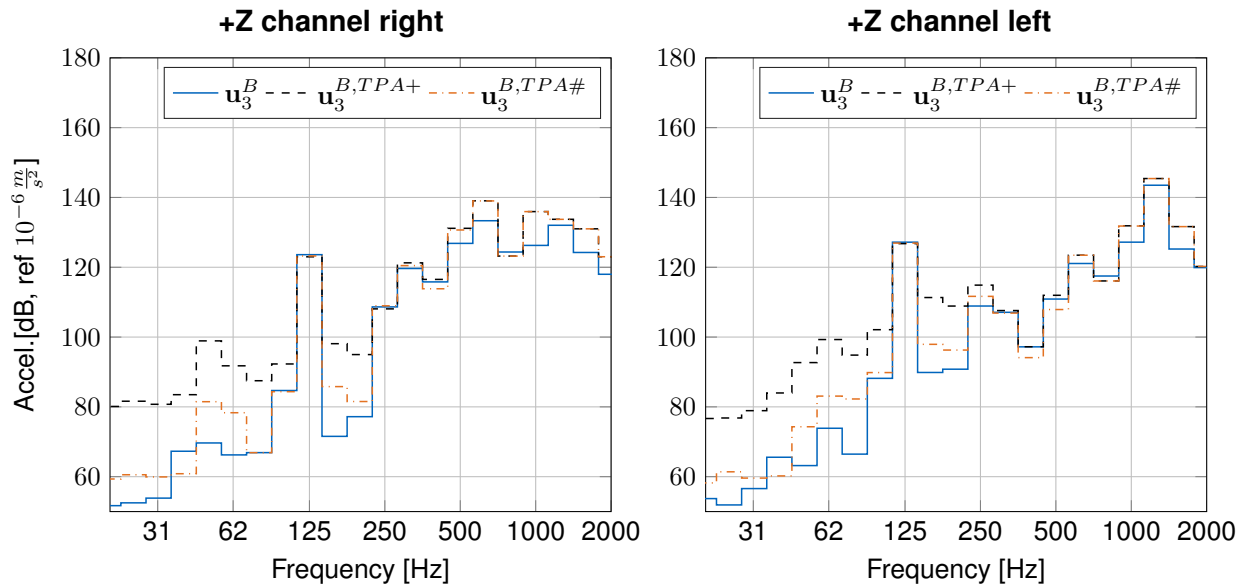
Figure 8.20: Blocked force predictions with validation measurements for the highly excited receiver channels. The regularized solution was computed with the SNR based Tikhonov regularization from section 8.5.3. *Left part*: sensor channel in globel +Z direction on right arm (see figure 6.2b). *Right part*: +Z channel of sensor channel on left arm (see figure 6.2b).

Tikhonov method (see section 8.5.7) was found to yield stable results, albeit taking longer to compute and converge. Which method works the best is however highly case specific and depends on the source type. For more broadband source excitation, the right regularization method might be different. The author would suggest a proper bench-marking of individual methods, if the blocked forces shall be computed for many specimens or variants of a given source component (e.g. as part of an end-of-line test or a bench-mark of different suppliers). This is in line with Hansen [64, chapter 7]:

"Our experience is that it may often be advantageous to monitor several strategies and base the choice of regularization parameter on the output of all these strategies."

Therefore, the focus of this chapter was pointed to the understanding of regularization methods and their effects particularly on blocked force TPA, rather than testing the countless other possibilities for implementation of a regularization strategy. All regularization methods can help suppressing the effect of unavoidable measurement noise. However, the author wants to stress that there is no way around taking proper measurements and all possible precaution when conducting the tests.

In this chapter, the fact that also the FRF matrix is subject to measurement errors was not discussed. This can be seen as a future field of study and the publications [71, 72, 141], which take the coherence of the FRF matrix into account for the regularization, can be seen as a good starting point. All FRF measurements had a good coherence in the shown frequency range and all error checks shown in section 2.6.2 and 3.4 have been validated.

The regularization can be interpreted as an added mechanical flexibility in all directions of the inverted matrix. The solved inverse problem is thus behaving less stiff. Regularization can also be used in FBS for solving the inverse problem determining the interface forces, equation (3.9). Thereby, the error propagation of measurement errors in the uncoupled FRF matrices $\mathbf{Y}^A$ and $\mathbf{Y}^B$ to variances in the coupled matrix $\mathbf{Y}^{AB}$ (the uncertainty propagation is described in [177]) can effectively be bounded, which was shown in Trainottis' master thesis

[176], but is beyond the scope of this thesis.

Part III

Airborne transmission paths and source modeling

Chapter 9

Vibro-acoustics

Contents:

> [...] if you demonstrate that you're willing to be wrong in pursuit of finding right - and freely admit if you are wrong - everybody else relaxes and feels free to put themselves out there in that same search.
>
> *Adam Stelzner,*
> *in "The right kind of crazy"*

The contents of this chapter were published in similar form in [59]. The text hereafter has been modified and adapted to the thesis.

Eventually, all structural vibrations are radiated from some structural surface and cause small fluctuations of air pressure that our ears can perceive, pleasant or unpleasant. Section 9.1 recaps the derivation of the Helmholtz equation which governs the sound pressure $p(t)$ as a primary variable in a given domain filled with air. The boundary conditions imposed on an acoustic field are explained in section 9.2, where the volume accelerations are identified as the Neumann boundary condition that is typically imposed to the sound pressure field at vibrating structural surfaces. The experimental measurement of airborne transfer functions with volume sources is briefly explained and exemplified in section 9.3. These experiences and findings were important for identifying the surface acceleration as the structural quantity which is the frequency un-biased driver of the sound pressure, at least in anechoic conditions (shown in section 9.4). This finding was an important reason for the decision to minimize surface acceleration instead of velocity in chapter 12. As velocity is the most commonly minimized quantity in the literature on acoustic optimization, the author puts the choice of accelerations up for questioning, but the following derivation, and the arguments in chapter 12 have been prepared as careful as possible. In section 9.5 the reciprocity principle for measuring transfer functions between structural and acoustic quantities is explained, since it was used for obtaining some of the transfer functions in the vehicle application described in chapter 11.
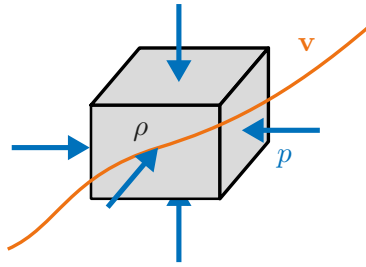
Figure 9.1: Fluid velocity $\mathbf{v}$, density ρ and pressure p on small volume (Eulerian point of view).

9.1 Helmholtz equation

The derivation will involve all quantities in the time domain. For a clearer distinction to the quantities in the frequency domain the explicit dependence on time t is stated.

The conservation of mass in a small control volume, see figure 9.1, that is fixed in space (Eulerian point of view) states that [131]:

$$\frac{\partial \rho(t)}{\partial t} + \nabla \cdot (\rho(t)\,\mathbf{v}(t)) = 0, \tag{9.1}$$

where $\rho(t)$ is the density of the fluid and $\mathbf{v}(t)$ is the velocity. The term $\frac{\partial \rho(t)}{\partial t}$ describes the change of density in the small control volume over time. For mass conservation, this has to be compensated by the in/out-flowing mass $\nabla \cdot (\rho(t)\,\mathbf{v}(t))$. The nabla operator $\nabla = [\frac{\partial}{\partial x}\ \frac{\partial}{\partial y}\ \frac{\partial}{\partial z}]^T$ describes the gradient in 3 dimensional space and $\cdot$ denotes the scalar product. Newtons second law, the conservation of momentum or 'force equals mass times acceleration', for the particles in the small volume (also from an Eulerian point of view) states:

$$\rho(t) \underbrace{\left(\frac{\partial \mathbf{v}(t)}{\partial t} + \left[\mathbf{v}(t)\,\nabla^T\right]\mathbf{v}(t) \right)}_{\text{particle acceleration}} = -\nabla p(t), \tag{9.2}$$

where $p(t)$ is the pressure in the fluid. The term $\frac{\partial \mathbf{v}(t)}{\partial t}$ describes the acceleration of particles in the small volume due to change of time. The term $\left[\mathbf{v}(t)\,\nabla^T\right]\mathbf{v}(t)$ describes the acceleration that the particles undergo due to changing their position in space ('convective acceleration'). The velocity gradient in space is the 3x3 matrix $\left[\mathbf{v}(t)\,\nabla^T\right]$, i.e. the three spatial components of the velocity vector $\mathbf{v}(t)$ derived with respect to the x, y, z-position. The particles flow with the velocity $\mathbf{v}(t)$ to the next position, and thus undergo a convective acceleration.

The external forces causing the particle acceleration are the pressure differences in space $-\nabla p(t)$. In acoustics, it is assumed that there are no other forces on the particles. E.g. the shear forces in air are assumed to be negligible. Further, it is assumed that the changes in pressure, density and velocity are only small pertubations $(\tilde{\star})$ around a mean value $(\star)_0$ that is constant in space and time.

$$p(t) = p_0 + \tilde{p}(t), \tag{9.3}$$

$$\rho(t) = \rho_0 + \tilde{\rho}(t), \tag{9.4}$$

$$\mathbf{v}(t) = \underbrace{\mathbf{v}_0}_{=\mathbf{0}} + \tilde{\mathbf{v}}(t), \tag{9.5}$$

where the mean value of velocity in air $\mathbf{v}_0$ is set to zero. With the assumption of small perturbations in equation (9.3) - (9.5), one can linearize the conservation of mass (9.1):

$$\frac{\partial \rho(t)}{\partial t} + \nabla \cdot (\rho(t)\,\mathbf{v}(t)) = \frac{\partial \rho(t)}{\partial t} + \nabla \rho(t) \cdot \mathbf{v}(t) + \rho(t)\,\nabla \cdot \mathbf{v}(t)$$

$$= \frac{\partial \tilde{\rho}(t)}{\partial t} + \nabla(\tilde{\rho}(t) + \rho_o) \cdot \tilde{\mathbf{v}}(t) + (\tilde{\rho}(t) + \rho_o)\nabla \cdot \tilde{\mathbf{v}}(t) \qquad (9.6)$$

$$\simeq \boxed{\frac{\partial \tilde{\rho}(t)}{\partial t} + \rho_0 \nabla \cdot \tilde{\mathbf{v}}(t) = 0}\,,$$

where the last line is the linearized version of the conservation of mass. The terms $\tilde{(\star)}$ are assumed to be small, and thus also their gradients $\nabla\tilde{(\star)}$ are small. A term of second order like $\nabla\tilde{\rho}(t) \cdot \tilde{\mathbf{v}}(t)$ drops out when linearizing around these small perturbations and only the first order terms remain[1]. If the linearization is then applied in the same manner to the conservation of momentum in equation (9.2), this yields:

$$\boxed{\rho_0 \frac{\partial \tilde{\mathbf{v}}(t)}{\partial t} = -\nabla \tilde{p}(t)}\,. \qquad (9.7)$$

A relation between the pressure $p(t)$ and the density of the fluid $\rho(t)$ is obtained for assuming that the state changes in the fluid volume happen as an adiabatic processes, i.e. without heat exchange to the surroundings. Consider a small number of particles (this corresponds to a Lagrangian point of view). As mentioned, their state changes happen without exchange of heat to the surrounding particles, but only due to mechanical work, e.g. the compression due to pressure fluctuations $\tilde{p}(t)$. The entropy in this small number of particles is then constant and the state changes in the fluid are reversible. This is a good assumption for changes in the fluid that happen quite fast, so there is not enough time to exchange heat. An adiabatic change from state $(\star)_1$ to state $(\star)_2$ in air, assumed to be an ideal gas, can be described by:

$$\frac{p_2}{p_1} = \left(\frac{V_1}{V_2}\right)^{\gamma}, \qquad (9.8)$$

where e.g. p_1 is the pressure in state 1 and V_2 is the volume in state 2. The heat capacity ratio is denoted as γ, where for air at room temperature $\gamma \approx 1.4$. The mass m of the fixed number of particles is constant, and thus the product of density ρ and volume V is constant.

$$\rho_1 V_1 = \rho_2 V_2 = const., \qquad (9.9)$$

which can be inserted in equation (9.8) to get the relation between pressure and density:

$$\frac{p_2}{p_1} = \left(\frac{\rho_2}{\rho_1}\right)^{\gamma}. \qquad (9.10)$$

With the small perturbations defined in equation (9.3) - (9.5) one can chose state 1 in equation (9.10) to be the state at rest (i.e. $p_1 = p_0$ and $\rho_1 = \rho_0$) and the second state is during some small non-zero perturbation (i.e. $p_2 = p_0 + \tilde{p}(t)$ and $\rho_2 = \rho_0 + \tilde{\rho}(t)$). Inserted in equation (9.10):

$$\frac{p_0 + \tilde{p}(t)}{(\rho_0 + \tilde{\rho}(t))^{\gamma}} = \frac{p_0}{\rho_0^{\gamma}} = const. \qquad (9.11)$$

This value has to stay constant for all time, since the mean values ρ_0 and p_0 are constant in time and space. This yields equivalently,

---

[1]This linearization is valid for up to about 130dB sound pressure level [41], which is a sound level that NVH engineers (hopefully) never encounter anyway.

$$p_0 + \tilde{p}(t) = \frac{p_0}{\rho_0^\gamma}(\rho_0 + \tilde{\rho}(t))^\gamma. \tag{9.12}$$

If the right hand side of the above equation is approximated with a Taylor expansion around the point $\tilde{\rho}(t) = 0$ one gets:

$$p_0 + \tilde{p}(t) = \frac{p_0}{\rho_0^\gamma}\left(\rho_0^\gamma + \gamma\rho_0^{\gamma-1}\tilde{\rho}(t) + \mathcal{O}(\tilde{\rho}(t)^2)\right). \tag{9.13}$$

since $\tilde{\rho}(t)$ describes small changes, the terms of higher order $\mathcal{O}(\tilde{\rho}(t)^2)$ vanish and one gets a relation between the small pressure and density fluctuations:

$$\boxed{\tilde{p}(t) = \gamma\frac{p_0}{\rho_0}\,\tilde{\rho}(t) = c_0^2\,\tilde{\rho}(t)}, \tag{9.14}$$

where c_0 turns out to be the speed of sound. For the Helmholtz equation, one wants to eliminate velocity $\mathbf{v}(t)$ and density $\rho(t)$ from the equations and express everything in terms of the primal variable: the pressure $p(t)$. For doing so, one can take the time derivative of the linearized conservation of mass (9.6):

$$\frac{\partial^2\tilde{\rho}(t)}{\partial t^2} + \rho_0\,\nabla \cdot \frac{\partial\tilde{\mathbf{v}}(t)}{\partial t} = 0, \tag{9.15}$$

and then replace $\frac{\partial\tilde{\mathbf{v}}(t)}{\partial t}$ in (9.15) with a pressure dependent term, so that the conservation of momentum equation (9.7) is automatically fulfilled. From equation (9.7) it follows that:

$$\frac{\partial\tilde{\mathbf{v}}(t)}{\partial t} = -\frac{1}{\rho_0}\nabla\tilde{p}(t). \tag{9.16}$$

which inserted in equation (9.15) yields:

$$\frac{\partial^2\tilde{\rho}(t)}{\partial t^2} - \underbrace{\nabla \cdot \nabla}_{=\Delta}\tilde{p}(t) = 0, \tag{9.17}$$

where Δ is the Laplace operator $\Delta = \left(\frac{\partial^2}{\partial x^2} + \frac{\partial^2}{\partial y^2} + \frac{\partial^2}{\partial z^2}\right)$. When additionally inserting the relation between density $\tilde{\rho}(t)$ and pressure $\tilde{p}(t)$ from equation (9.14) one gets the famous **Helmholtz equation**:

$$\boxed{\frac{\partial^2\tilde{p}(t)}{\partial t^2} = c_0^2\Delta\tilde{p}(t)}. \tag{9.18}$$

In summary, one could say that the Helmholtz equation is a result of the original conservation of mass (9.1) (a scalar equation), where the velocity has been replaced by a pressure dependent term that automatically fulfills the conservation of momentum, and the density has been replaced by a pressure dependent term as well (since air is assumed to be an ideal gas and the state changes happen adiabatic). All quantities are assumed to be only small pertubations around a state of equlibrium so that a linearization is applicable. The Helmholtz equation is governing the sound pressure distribution in the air, which is the input for the human hearing system.

9.2   Pressure boundary conditions

Like with any differential equation, it is essential to consider the boundary conditions that are imposed on the pressure field. A direct boundary condition on the primal variable, the sound
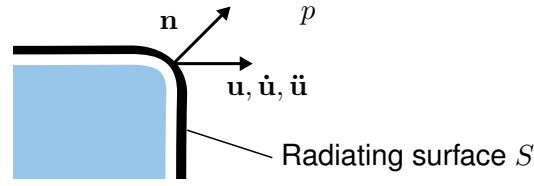
Figure 9.2: Radiating surface S with surface normal $\mathbf{n}$, surface vibration $\mathbf{u}$ and surrounding sound pressure field p.

pressure $p(t)$, is commonly called a Dirichlet boundary condition. It is e.g. often assumed at open ends of vibrating volumes. E.g. the classic academic example of an open ended tube, where the boundary condition at the open end is prescribed to equal the pressure of the surroundings.

Boundary conditions on the spatial gradient of the primal variable $\nabla \tilde{p}(t)$ are commonly called Neumann boundary conditions. They are often imposed at the surface of vibrating structures. On the radiating surface of the structure, it is assumed that the structure and air particles have the same displacement (and thus also velocity and acceleration) in the direction normal to the surface.[2] One can thus say that:

$$\frac{\partial \mathbf{u}(t)}{\partial t} \cdot \mathbf{n} = \dot{\mathbf{u}}(t) \cdot \mathbf{n} = \tilde{\mathbf{v}}(t) \cdot \mathbf{n}, \quad \text{on radiating surface } S, \tag{9.19}$$

where $\mathbf{u}(t)$ is the displacement of the structure, $\mathbf{n}$ is the normal vector on the radiating surface S and $\tilde{\mathbf{v}}(t)$ is still the small velocity perturbations in air, see figure 9.2. When inserting that into the linearized conservation of momentum equation (9.7), one finds:

$$\mathbf{n} \cdot \frac{\partial^2 \mathbf{u}(t)}{\partial t^2} = \mathbf{n} \cdot \ddot{\mathbf{u}}(t) = -\mathbf{n} \cdot \frac{1}{\rho_0} \nabla \tilde{p}(t), \quad \text{on radiating surface } S. \tag{9.20}$$

Thus, the accelerations $\ddot{\mathbf{u}}(t)$ on the vibrating structure are imposing a Neumann boundary condition on the sound pressure field. The input quantity of acoustic fields are thus often described as either volume-displacement, -velocity, or -acceleration which will be denoted as z, $\dot{z}$ and $\ddot{z}$ in the remainder of this thesis. It is the normal component of the structural vibration integrated over the radiating surface.

9.3 Measurement of airborne transfer functions

For measuring the dynamic transfer functions in air, one can use acoustic sources like the ones shown in figure 9.3a and figure 9.3b.

The acoustic sources used in this thesis are from the LMS Siemens Q-Source series. Their excitation is following an amplified signal generator input. The excitation strength is measured with a calibrated sensor in the source and recorded with the DAQ system.

In figure 9.3a, the small, low to mid frequency source, called Q-IND, is shown. It is close to the climate compressor in an anechoic chamber. According to the manufacturer specifications, it is capable of exciting the frequency range $50 - 1000$ Hz. For measuring an acoustic transfer function (ATF) in the anechoic chamber, the source was fed with a band noise signal from $50 - 1000$ Hz. The signal from the Q-IND source input channel is a volume displacement z. The transfer functions were estimated with an $H1$ estimator (see section 2.4) where

---

[2]In the tangential surface directions, it is assumed that structure and air do not necessarily undergo the same motion. This is due to the assumption of negligible viscosity in air.
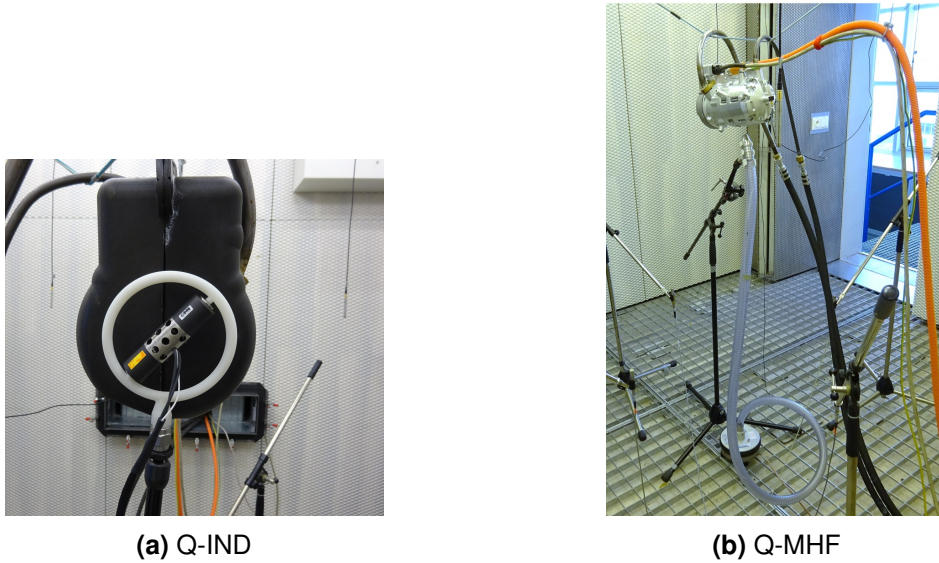
(a) Q-IND

(b) Q-MHF

Figure 9.3: Acoustic sources for airborne transfer function measurements. (a) Q-IND source behind the compressor wrapped in a sound-insulation capsule. (b) Q-MHF source with the long hose under the compressor.

the auto and cross power spectra of source and microphone signals were obtained from 500 timeblocks of $T = 1s$ length, with a 66% overlap and Hanning windows applied to the time-blocks. In figure 9.4, the FRF measured between the Q-IND source and one microphone is shown. It can be seen that the coherence γ^2 is good from $100 - 1000$Hz (also for the other microphones).

For the mid to high frequency range, a source called Q-MHF is used (see the tube shown in figure 9.3b). According to the manufacturer specifications, it is capable of exciting a frequency range from 200Hz to 10 kHz. It is also fed with a band noise signal in this frequency range and the same settings for the $H1$ estimation of the FRF are used. The input signal from the Q-MHF source is a volume acceleration $\ddot{z}$. In figure 9.5 the FRF measured between the Q-MHF source and the same microphone as before is shown. The Q-MHF source was placed at the same position as the Q-IND source for the FRF measurement in figure 9.4. It can be seen that the coherence γ^2 is good in the range of approx. 400Hz-10kHz (also for the other microphones).

For merging the two measured transfer functions, the volume displacement input z from the Q-IND source, was transformed to a volume accleration input $\ddot{z}$ in the frequency domain by:

$$\frac{p}{\ddot{z}} = \frac{1}{-\omega^2} \frac{p}{z} \tag{9.21}$$

The resulting 2 FRFs are shown in figure 9.6 and can subsequently be merged to only one FRF for the whole frequency range. For the measurements in this case, this was done by performing a linearly fading merge in the frequency range of $500 - 900$ Hz.

One can see, that the FRF between volume displacement z and sound pressure p in figure 9.4 has a slope of ω^2 in the frequency domain. The FRF between volume acceleration $\ddot{z}$ and sound pressure p in figure 9.6 is approximately a constant over frequency, which is expected since $\ddot{z}$ is the quantity imposing a direct Neumann boundary condition on the sound pressure field (see equation (9.20)). Also in [125, section 3.3] it is shown that for a monopole source in a free field:

"The sound pressure versus frequency characteristics $p \sim j\omega Q = bS$ are proportional to
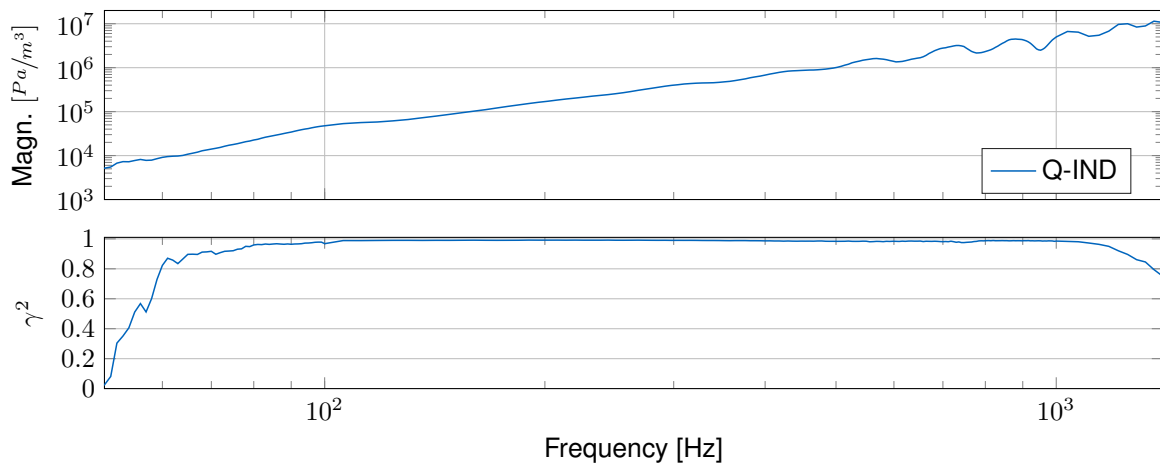
Figure 9.4: FRF measurement from small acoustic volume displacement source Q-IND in figure 9.3a. According to data sheet FRFs measurable in the frequency range 50 - 1000 Hz.

acceleration b."

were Q is the volume velocity ($Q = \int_S \mathbf{n} \cdot \dot{\mathbf{u}}_s dS$), S is the vibrating surface area and $\sim$ means "proportional to". The constant FRF can easily be understood by thinking about a Dirac impulse at the input point (constant amplitude for all frequencies in the frequency domain) which would create an impulsive pressure wave that travels with sonic speed to the surrounding microphones and yields a dirac impulse in sound pressure measured there. In a perfect anechoic chamber, all sound that could be reflected is absorbed by the walls. So the only signal in the microphone channel would be this initial Dirac impulse. The time delay that the wave needs to travel is what causes the linear phase increase with frequency that can be seen in figure 9.6. The slight 'waviness' of the magnitude in figure 9.6 is caused by non-perfect sound absorbtion of the anechoic chambers walls. Some sound was still reflected by the wall. If the reflected sound wave arrives with the same phase at the microphone as the primary sound from the source, it adds to the magnitude. If it arrives with an opposite phase of $180°$ it cancels out some of the direct sound from the source (dip in magnitude). The frequency distance of these "dips" and "ups" can be calculated from the distance between source, microphone and wall and fit the measurements well, which fits very well with the measurement (see [126]).

9.4 Frequency (un)biased relation of structural and acoustical quantities

One question that arose during the conduction of this research project was: What quantity on a radiating structure surface should be minimized, when the goal is to minimize the "annoyance" that the customer perceives? This included the question of what frequency dependent weighting should be applied to the identified structural quantity, in order to best capture the annoyance. This problem often arises in structural acoustic optimization, where one may not know the transfer function from a radiating surface to the microphones at positions of interest. In section 9.2, it was shown that the surface acceleration is the quantity that imposes a Neumann boundary condition on the sound pressure field. In section 9.3, one could observe that the FRF between a volume acceleration $\ddot{z}$ and the sound pressure p in an anechoic chamber (free-field conditions) is approximately constant over frequency
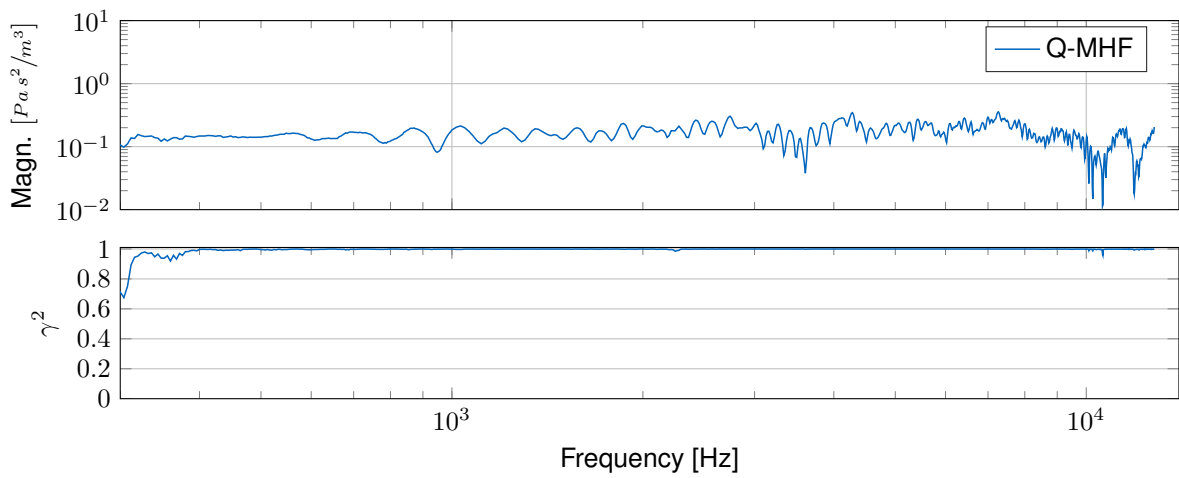
Figure 9.5: FRF measurement from acoustic volume acceleration source Q-MHF in figure 9.3b. According to the data sheet, with the 2m long tube FRFs are measurable in the frequency range 200 - 10000 Hz. Input was a band noise from 400 - 10000 Hz.
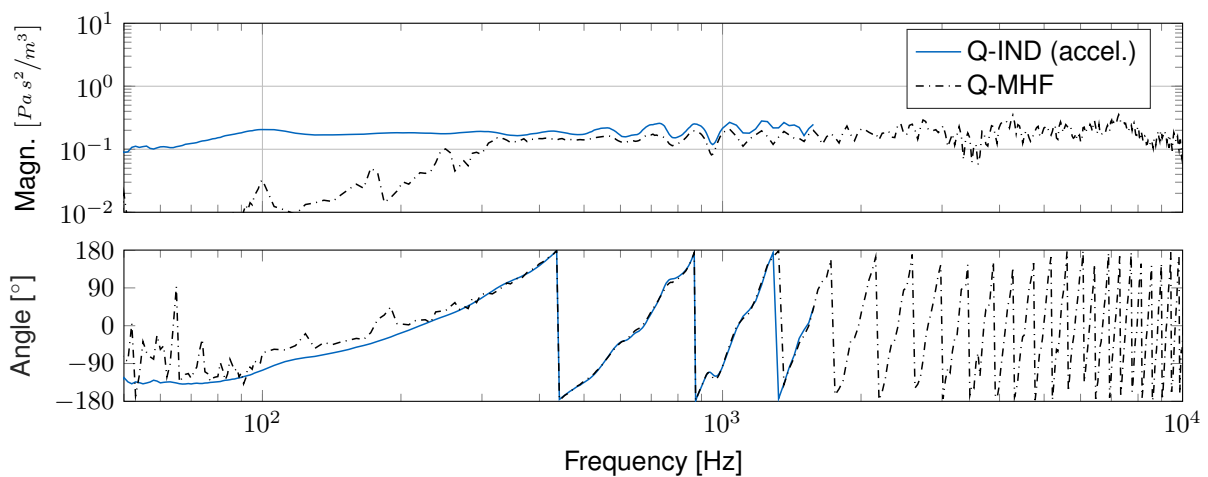
Figure 9.6: FRFs of both sources which are to be merged to get one FRF in the whole frequency spectrum 50 - 10000 Hz.
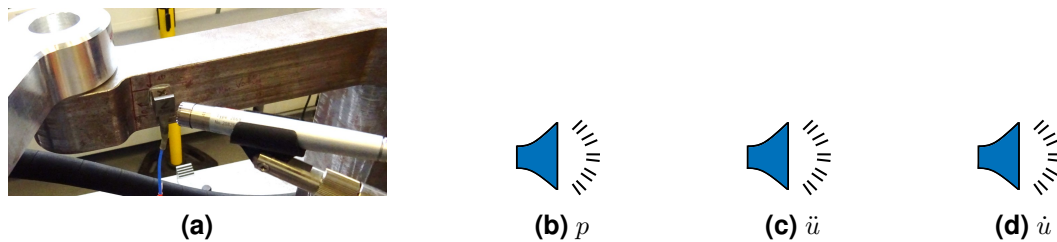
Figure 9.7: Hearing comparison of acceleration and velocity with sound pressure signal. Signals are for 60% of the compressors maximum rotational speed (approximately 5160 rpm). The auralization of the acceleration sensor signals are all for the x-channel of the sensor (see figure 9.7a). The conversion from acceleration to velocity was done in the frequency domain. (a) Figure of measurement setup, (b) Recorded microphone signal, (c) Acceleration measured in adjacent sensor, (d) Velocity measured in adjacent sensor.

(see figure 9.5). A hearing comparison of *i)* a sound pressure measurement, *ii)* an adjacent acceleration measurement, and *iii)* a velocity signal (computed from the acceleration signal), is given in figure 9.7. The measurements were recorded in the same setup as shown in figure 6.2. One can clearly hear that the lower frequency content is much more prominent in the velocity signal when compared to the sound pressure and acceleration.

The fact that the surface accelerations $\ddot{u}$ (resulting in volume accelerations when multiplied with the vibrating surface area) are the frequency unbiased input to the sound pressure field is by no means new (see e.g. [197] or the Siemens PLM forum post [138] on the topic). Therefore, in chapter 12 it was chosen to minimize the surface acceleration. The need for explaining this quantity for minimization in such detail arose from the fact that most of the literature on structural acoustic optimization minimizes velocities (as will be explained in chapter 12). However, the author is open for discussion on this choice, since it is uncommon.

9.5   Structural-acoustical transfer functions and reciprocity

Measuring so called structural-acoustical transfer functions means, a structural input (a force f_j at some point j) and an acoustical output (a sound pressure p_i at another point i). This can be done by hammer impacting the structure at point j, measuring the microphone response at i, and computing the FRF estimate. These transfer functions are of special interest in the realm of this thesis, since they allow to predict the sound at a microphone that originates from a structural vibration source attached to the car body (see e.g. the FRF in figure 3.1). However, often the physical space at the attachment points of the source is limited and performing shaker or impact tests there is cumbersome or impossible. The reciprocity of the transfer functions helps is this case. According to Wolde [196], reciprocity means that *"[...] the transmission of vibration from an arbitrary position i to an arbitrary position j has a simple relation to with the transmission from position j to position i"*. For purely structural FRFs, it holds that the transfer function Y_{ij} is equal to Y_{ji}, as can be seen from the modal superposition in equation (2.30). For structural-acoustical transfer functions, it means that one can also place an acoustic excitation z_i at the receiver position i, e.g. the drivers ear, and measure the structural response at the source position j, with e.g. accelerometers in the front compartment of the car. For structural-acoustical transfer functions it holds true that [41, 170, 196]:

$$\underbrace{\frac{p_i}{f_j}}_{\text{direct}} = \underbrace{-\frac{u_j}{z_i} = -\frac{\dot{u}_j}{\dot{z}_i} = -\frac{\ddot{u}_j}{\ddot{z}_i}}_{\text{reciprocal}},$$ (9.22)

where $u_j, \dot{u}_j, \ddot{u}_j$ is structural displacement, velocity and acceleration and $z_i, \dot{z}_i, \ddot{z}_i$ is air volume displacement, velocity and acceleration. For a derivation and experimental proof of the reciprocity principle see Wolde's PhD thesis [170], in which the topic of reciprocal transfer function measurements with applications to ship acoustics is treated. For systems with only a primal and dual field variable[3] [170, chapter 2] shows the reciprocity from the symmetry of the system matrices. The proof can be shown in general from linear network theory where it is assumed that the product of primal and dual variable at each point gives the power fed to the system. Note that the symmetry of the system matrices was also used for the derivation of the orthogonality of the eigenmodes in section 2.2, and is therefore also essential for showing the reciprocity with equation (2.30). This is however different from the proof given in [170, chapter 2]. Surprisingly, for a coupled structural-acoustical system, it is not as straightforward to prove that the coupled system matrices are symmetrical. In [41], the symmetry of the system matrices is shown by the derivation of the systems equations from potential fields $\mathcal{V}$ and the fact that:

$$\frac{\partial}{\partial x_j}\left(\frac{\partial \mathcal{V}}{\partial x_i}\right) = \frac{\partial}{\partial x_i}\left(\frac{\partial \mathcal{V}}{\partial x_j}\right).$$ (9.23)

However, the discussion in [196] and [41] shows that the applicability of reciprocity for structural-acoustical transfer functions includes a history of scientific debate. In [196], one finds an overview of reciprocity relations in common engineering systems (structural, fluid, electrical systems and coupled variants of these) which is taken from the appendix of Verheijs PhD thesis [184].

---

[3]This can be velocities and forces in **mechanics**, pressure and volume-velocity in **acoustics** or voltage and current in **electric** networks.

Chapter 10

Airborne transfer path analysis

Contents:

In your phase!

unknown Master student

The blocked forces $\mathbf{f}_2^{bl}$ can predict the sound and vibrations in the receiver B, which are introduced over the structural connection points with the source component A (see chapter 6). This contribution to the receiver noise will be called _structure borne_ sound in the rest of this thesis. The _airborne sound_ describes noise which is directly radiated from the housing of the source component, i.e. the compressor. In other words, the airborne contribution is what one would hear if the compressor was levitated in its place without any physical connection to the vehicle. Depending on the mounting conditions of the source, this can be a dominant transfer path. In [144], the compressor was rigidly connected to the front axle carrier, which resulted in a dominant structure borne contribution to the drivers' cabin sound. In the example shown in chapter 11, the compressor is isolated with two stages of soft rubber bushings from the front axle carrier, which lead to a relevant contribution of the airborne path to sound in the drivers' cabin. Therefore, the airborne path needs to be modeled for a complete modular sound and vibration engineering.

As with the structure borne TPA, the goal of this chapter is to circumvent modeling the exact source internal mechanisms which create the airborne excitation. A set of interface quantities shall be chosen, which describe the transmission of the airborne excitation equivalently, and can be transferred to a different design. This will be achieved with a set of equivalent monopoles describing the airborne compressor excitation.

10.1 Literature review and previous work

For airborne source description of a component, its emitted sound power can be utilized, see e.g. [121]. The method for evaluating the sound power is standardized in [17]. An evaluation of potential errors resulting from different ways to conduct and evaluate the sound power measurements can be found in [7]. In [92], the sound power was computed from direct velocity measurements on the radiating surface of an e-axle drive. The radiation efficiency was estimated from the recorded vibration shapes. Reichart [144] used the emitted sound power for airborne source description of the compressor. The sound power was mea-
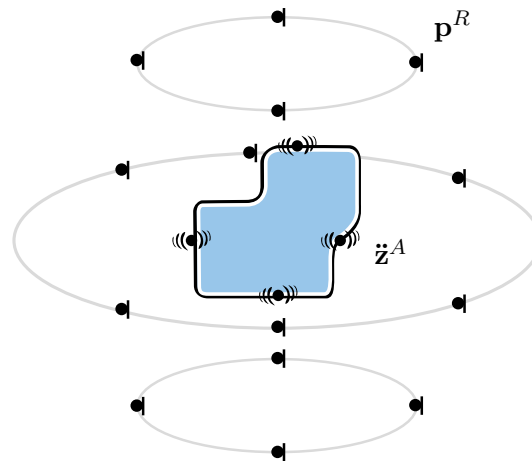
Figure 10.1: Schematic measurement setup for airborne source identification.

sured with a sound intensity probe, that was swept over an area enclosing the compressor. A dodecahedral loudspeaker was used as an acoustic excitation mechanism. Its emitted sound power was also measured while driven with white noise signal. Thereby, acoustic transfer functions between sound power and receiver microphones in the vehicle could be measured. Together with the measured sound power of the compressor, a prediction for the airborne noise was possible. However, the compressor was thereby effectively modeled as a monopole which turned out to be insufficient for higher frequent sound. Additionally, the missing phase information in the sound power made an auralization of the airborne transfer contributions difficult.

Based on these experiences, Müller [126] used an inverse method for identifying multiple equivalent monopoles as a proxy for the compressors airborne excitation, as previously described in [16, 124, 130, 181]. The airborne excitation of the compressor was modeled by six monopoles. The source strengths of the individual monopoles is described by volume accelerations contained in the vector $\ddot{\mathbf{z}}^A$, see figure 10.1. This approach is in principle very similar to the transfer path method used for the structure borne sound. This identification method will be explained in the following, and is applied to a vehicle development project in chapter 11. The inverse identification makes this method sensitive to measurement noise [27], hence a regularization strategy was applied. Berckmans [16] compared different regularization schemes for this inverse airborne source identification on the example of tire rolling noise. It was found, that an over-determination of at least a factor of two should be used, which was also recommended in [181]. In [106], it was shown that the airborne source description with equivalent monopoles is independent of the environment in which it was measured and is therefore transferable to other environments. Since in [106] no over determination was used, the beneficial effects of regularization where particularly large. The goal in this thesis was also to obtain an airborne source description of the compressor which can be obtained in a component testing environment, and can be transferred to different vehicle designs.

10.2   Airborne source identification & measurement setup

For identifying an equivalent airborne source description of the compressor, the airborne FRF matrix $\mathbf{Y}_{p\ddot{z}}^{AR}$ is measured. It describes the transfer from multiple volume acceleration points close to the compressor to surrounding microphones. As for the blocked force iden-

tification, A denotes the source component and R denotes the testrig environment. The compressor is then run in various operational conditions and the volume accelerations $\ddot{\mathbf{z}}^{bl}$, which would have equally caused the recorded sound pressures at a subset of indicator microphones $\mathbf{p}_4^R$, are computed via:

$$\ddot{\mathbf{z}}^{bl} = \left(\mathbf{Y}_{4\ddot{z}}^{AR}\right)^+ \mathbf{p}_4^R, \tag{10.1}$$

where $\mathbf{Y}_{4\ddot{z}}^{AR}$ is the part of the matrix describing the sound transfer to the indicator microphones. The volume accelerations $\ddot{\mathbf{z}}^{bl}$ can equivalently describe the airborne excitation of the source. This can be seen and derived from the same reasoning as the blocked forces (see section 6.2), which is not repeated here. The $\ddot{\mathbf{z}}^{bl}$ represent the volume accelerations needed for counteracting all volume accelerations radiated off the compressor surface[1]. The negative signs needed are omitted for brevity, as explained in section 6.2. The identified $\ddot{\mathbf{z}}^{bl}$ can therefore also be called *blocked volume accelerations*. They would in theory act like an active noise cancellation on the source and block/cancel all sound pressure at the surrounding microphones. This is based on the following assumptions:

1. As for the blocked forces, one assumption is that the internal source mechanisms (e.g. the imbalance, electromagnetic forces, etc.) are independent of the mounting condition. The compressor was intended for mounting with soft rubber isolators, see chapter 11, so this assumption was assumed valid.

2. Additionally, one is assuming that the whole "interface" of the compressor with the surrounding air is controllable by the chosen monopoles. This is much harder to achieve, since the interface in acoustic fields is a continuous surface. The representation with only a few monopoles is therefore subject to an inherent upper frequency limit.

3. If the compressor was mounted rigidly against a stiff receiver, the vibrations on the compressor housing would change. Therefore, one is assuming that the surface vibrations of the freely hung up compressor are the same as in the vehicle. In the specific case of this application, the compressor is mounted with very soft rubber bushings in the vehicle. Therefore, this assumption was considered to be valid (in the vehicle measurements this was validated by comparing the vibrations levels with the freely hung up compressor).

The measurement setup for identifying the blocked volume accelerations is shown in figure 10.2. The measurements were conducted in an anechoic room. In total, 14 microphones were placed on a spherical surface around the compressor (see also the schematic setup in figure 10.1). Two kinds of microphone sizes were used: 12 $1/2$" microphones (a mix of B&K TYPE 4955 and PCB 377B11), and 2 $1/4$" microphones (PCB 378C01). Unfortunately, the $1/4$" ICP microphones with only a quarter inch membrane diameter had a high base noise level (42 dB(A) base noise level is specified for the PCB 378C01, compared to 14dB(A) for the PCB 377B11). To the authors belief this is one of the reasons why a regularization had to be applied (see section 10.3). The transfer functions were measured with a low frequency and a mid to high frequency volume source, and the FRFs where merged in the overlapping frequency region, as explained in section 9.3. Thereby, a frequeny range from 50Hz - 10kHz could be measured. In total six input positions for the volume velocity source were measured. If one places an imaginary box around the compressor, then one volume acceleration monopole was placed in the middle of each box face. The compressor has a

---

[1]Remember from section 9.2, that in acoustic fields the volume acceleration corresponds to the force in structural dynamics, i.e. they are the dual variables. The primal variable in acoustics is the sound pressure, which is the displacement in structural dynamics.
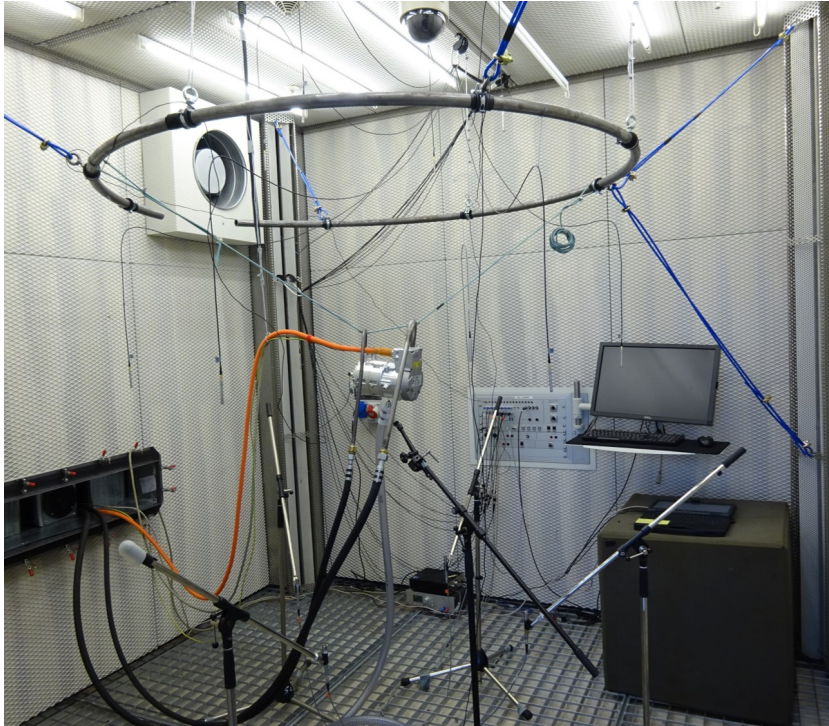
Figure 10.2: Measurement setup for airborne source identification of the compressor.

dimension of roughly $20 \times 15 \times 15 cm^3$. For the operational measurements, the compressor was connected to a high voltage power supply and load unit from IPEtronik. The hoses and cables were guided through an air ventilation duct to a neighboring room, so the side noise from the load unit was not audible in the anechoic chamber. A suite of operating conditions was recorded with the microphones:

- Constant operating speeds from 10% to 100% of the compressors maximum speed (8600rpm), with speed increments of 10%.

- Runups from 10% to 100% compressor speed in 60 and 120 seconds.

- Noise measurements with the compressor switched off.

These measurements were conducted once with an acoustic capsule (see figure 9.3a) and once without an acoustic capsule (see figure 9.3b) for the compressor. The performance of the acoustic capsule was tested in the vehicle in chapter 11.

10.3 On-board validation & regularization

For an initial check on the validity of the obtained results, one can perform an on-board validation, just like for the blocked forces (see section 6.3). In order to do this, one microphone in the anechoic chamber was left out of the inversion and could therefore be used as an on board validation signal $\mathbf{p}_3^R$. The signal recorded on this microphone can be predicted with the blocked volume accelerations. The accordance to the validation measurement $\mathbf{p}_3^R$ serves as an initial check on the quality of the identified $\ddot{\mathbf{z}}^{bl}$. The blocked volume accelerations used for the on-board validations were once computed with, and without regularization:
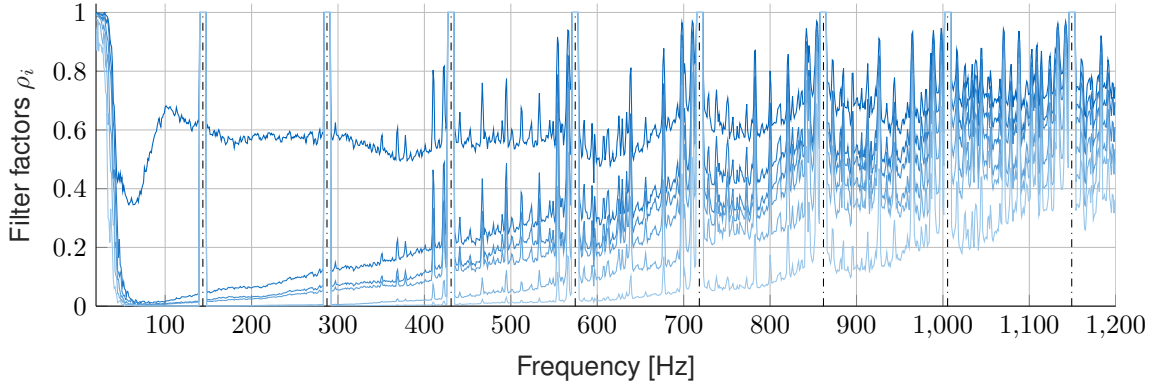
Figure 10.3: Filter factors ρ_i for individual singular values for the airborne inter-order filter at a operational speed of 8600rpm. Vertical dashed lines indicate the order frequencies of the compressor with the first order at around 143Hz

$$\ddot{\mathbf{z}}^{bl+} = \left(\mathbf{Y}_{4\ddot{z}}^{AR}\right)^{+} \mathbf{p}_4^R, \qquad\qquad \ddot{\mathbf{z}}^{bl\#} = \left(\mathbf{Y}_{4\ddot{z}}^{AR}\right)^{\#} \mathbf{p}_4^R, \qquad\qquad (10.2)$$

$$\mathbf{p}_3^{R,TPA+} = \mathbf{Y}_{3\ddot{z}}^{AR} \ \ddot{\mathbf{z}}^{bl+}, \qquad\qquad \mathbf{p}_3^{R,TPA\#} = \mathbf{Y}_{3\ddot{z}}^{AR} \ \ddot{\mathbf{z}}^{bl\#}. \qquad\qquad (10.3)$$

$$(10.4)$$

For the regularization, Wernsen's signal to noise ratio filter from section 8.5.3 was adapted. The algorithm follows the following steps:

1. Find the first order of the compressor from the recorded signal. We used the bary center method [116] for finding the "exact" compressor first order frequency, from the two frequency bins surrounding it. There are however numerous other methods for order detection, see the appendix of [99].

2. Apply a Tikhonov regularization with α being the inverse of the SNR at all frequencies (equation (8.33)), except for the frequencies close to a multiple of the first compressor order. Close means, that the frequencies within a range of $\pm$ 4 Hz of the compressor order were left unregularized.

This resulted in the filter behavior which can be seen from the filter factors in figure 10.3 (see the definition of filter factors in equation (8.25)). Note that the filter factors below 50Hz are not representative, since the volume source input spectrum ended there, and the FRFs are mostly noise (see figure 9.4). It can be observed from the filter factors that there is only one dominant singular value for lower frequencies, which indicates that the compressor could be modeled with just a monopole in this frequency region. For higher frequencies, the other five singular values become larger, and the compressor should therefore be modeled with all six (or even more) monopoles. The regularization is suppressing the sound which is not at a multiple of a compressor order. The on-board validation results can be seen and heard in figure 10.4. As for the structure borne sound, the regularization helps to suppress the effects of inverted measurement noise in the lower frequency region, whereas the results in the higher frequency region are mostly unchanged. When listening to the predictions in figure 10.4, one can hear this inverted measurement noise as ambient white noise in the results of the pseudo inverse $\mathbf{p}_3^{R,TPA+}$. As the airborne noise contribution was found to be mostly dominant for higher speeds of the compressor, the prediction results for 90% and 100% of the compressor speed are shown in figure 10.5.
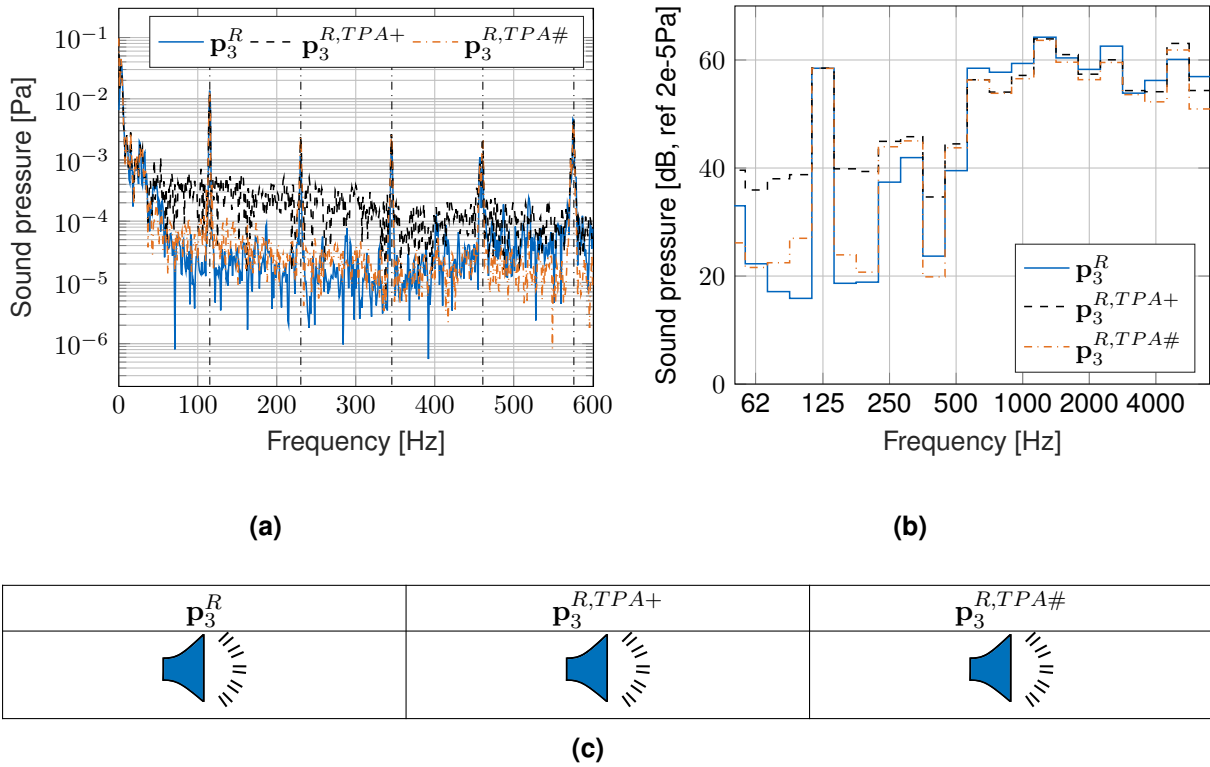
(a)

(b)

(c)

Figure 10.4: On Board validation for 80% of maximum compressor speed.
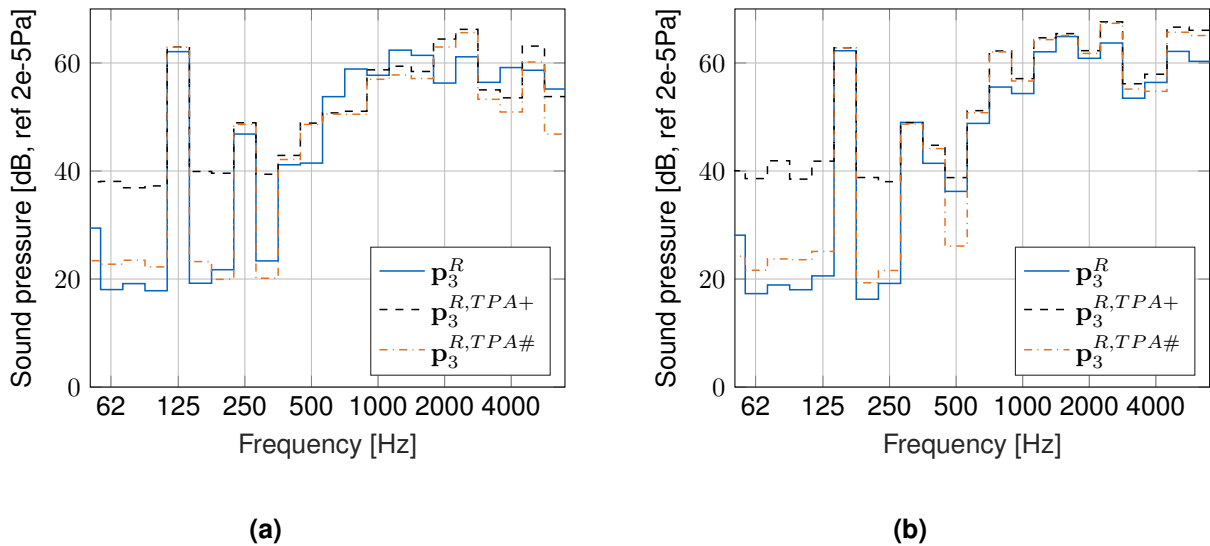

(a)

(b)

Figure 10.5: On Board validation for (a) 90% and (b) 100% of maximum compressor speed.

Figure 10.6: Modified room.

10.4 Transfer validation

In section 8.3 it was explained that an on-board validation can potentially give a too optimistic impression on the quality of the identified blocked forces. Therefore, also for the airborne source identification a transfer validation was performed. This was achieved by modifying the anechoic chamber with metal shelf boards placed on the walls, see figure 10.6. These plates increased the reflections in the room and thereby changed the acoustic transfer functions. In figure 10.7 the same FRF measured in either configuration of the room is compared. It can be seen that the "waviness" of the FRF is increased by adding the metal plates to the walls. This is expected, since the "waves" in the FRF magnitude are caused by reflections on the wall. The transfer validations were computed with the blocked volume accelerations obtained from the measurements in the anechoic chamber without the metal plates (section 10.3). The results can be seen and heard in figure 10.8. The results of the transfer validation showed roughly the same quality as the on-board validation.

10.5 Conclusion

In this chapter the airborne source modeling of the compressor by blocked volume accelerations $\ddot{\mathbf{z}}^{bl}$ was explained. The results proved to be promising for quantifying the airborne sound radiation of the compressor. This was shown by an on-board and a transfer validation. Due to a higher noise level on some microphones, a regularization which filters the non-order components of the compressor sound was applied. This resulted in clearer auralizations of the TPA predictions. The source description is limited in frequency, since the discretization with six monopoles is assumed to be insufficient for higher frequencies. From previous experience it was known that the compressor sound was only audible up to around 2kHz in the vehicle. The discretization with six monopoles was assumed to be valid in this frequency range (the compressor dimension is roughly $20 \times 15 \times 15 cm^3$ and the wavelength at 2kHz is ca. 16.5cm).

During the measurements, it was noted that towards higher frequencies, the influence of positioning errors on the volume source become more apparent. In figure 10.10, the same FRF with the orifice of the volume source moved $\pm$ 3cm is shown. When conducting the volume source measurements in the vehicle, it was found that positioning the volume source properly is often not possible due to space limitations, and the repositioning for measuring all six monopoles is labor intensive. In order to avoid this, in [126] an artificial compressor was developed, to speed up the measurements and reduce positioning errors. The artificial compressor is shown in figure 10.6. The first results showed an improved prediction quality,
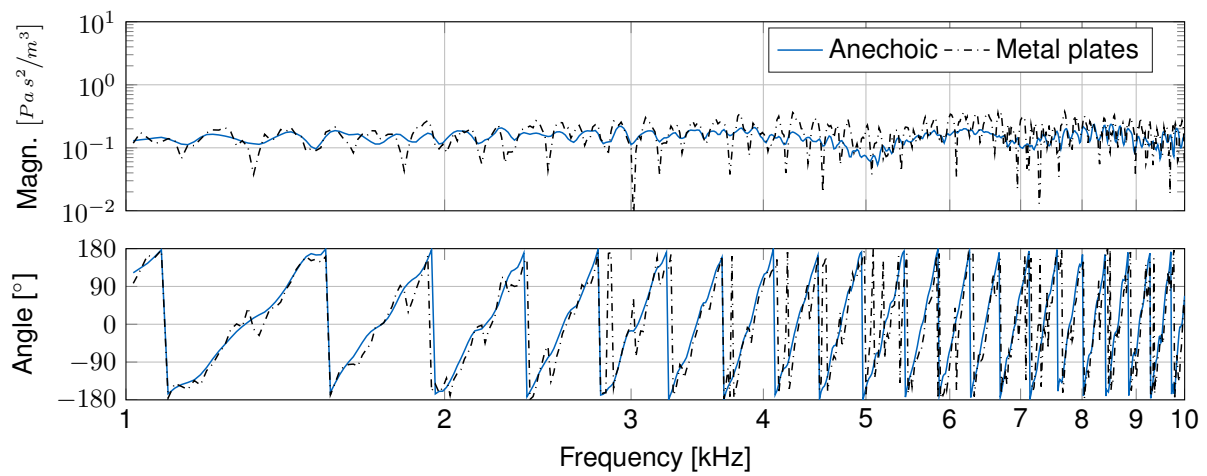
Figure 10.7: Comparison of anechoic room FRF with the same FRF in the room that was modified by metal plates on the wall.
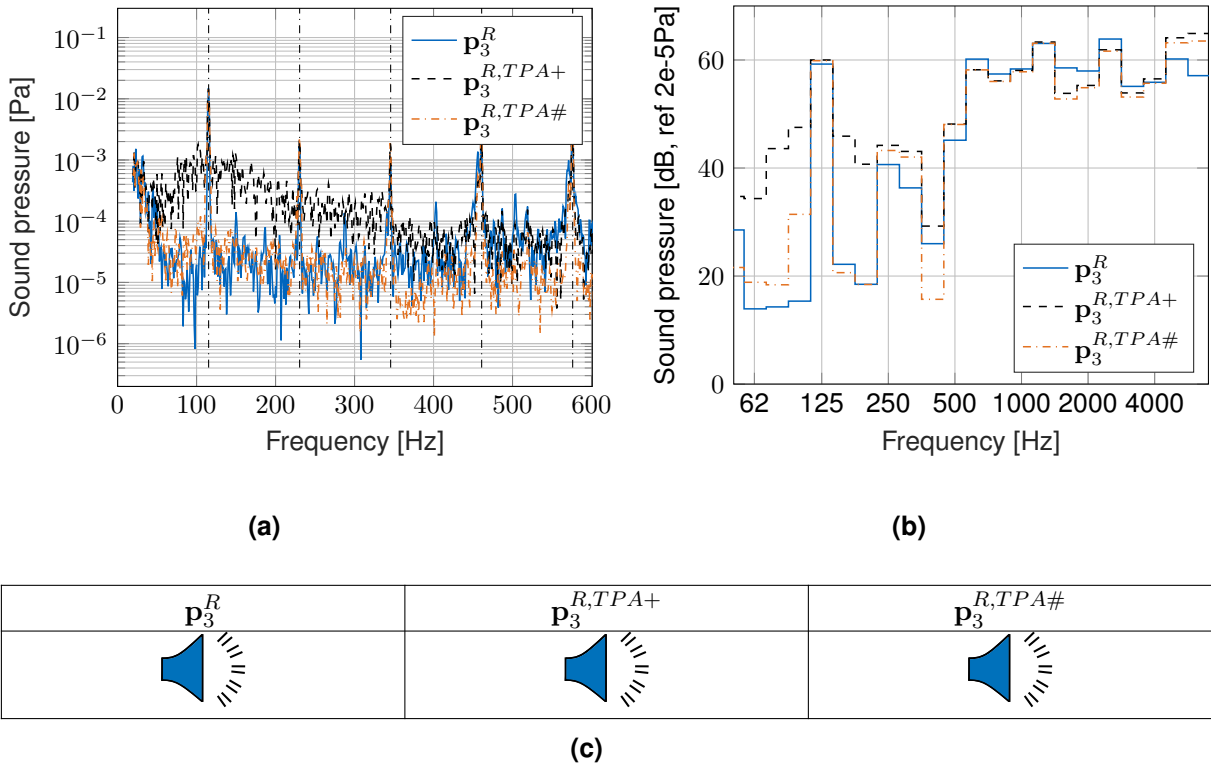
(a)

(b)

(c)

Figure 10.8: Transfer validation for 80 percent of maximum compressor speed.
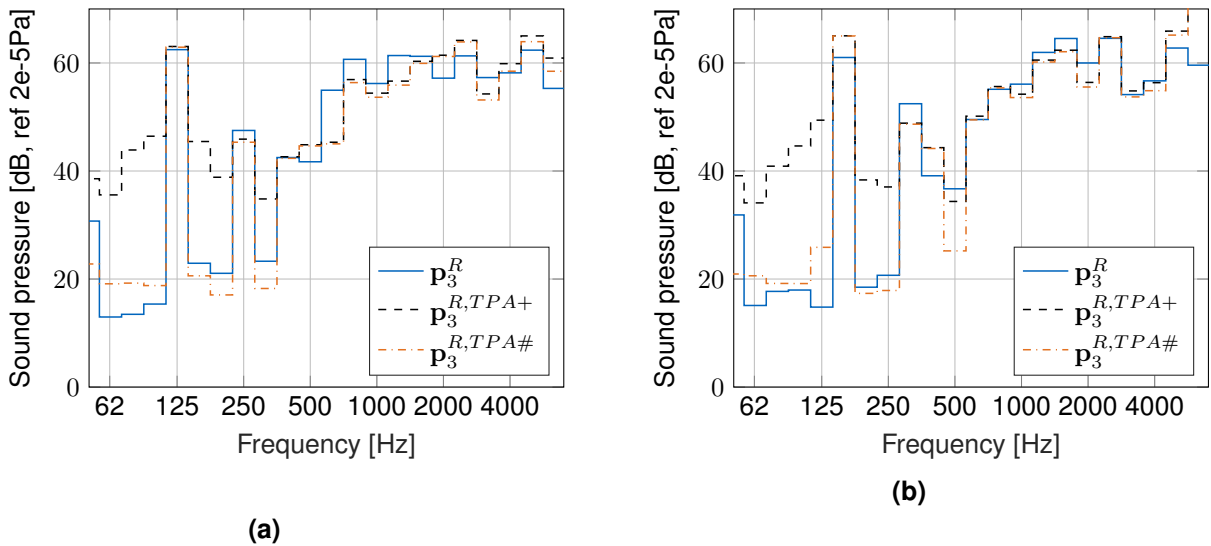

(a)

(b)

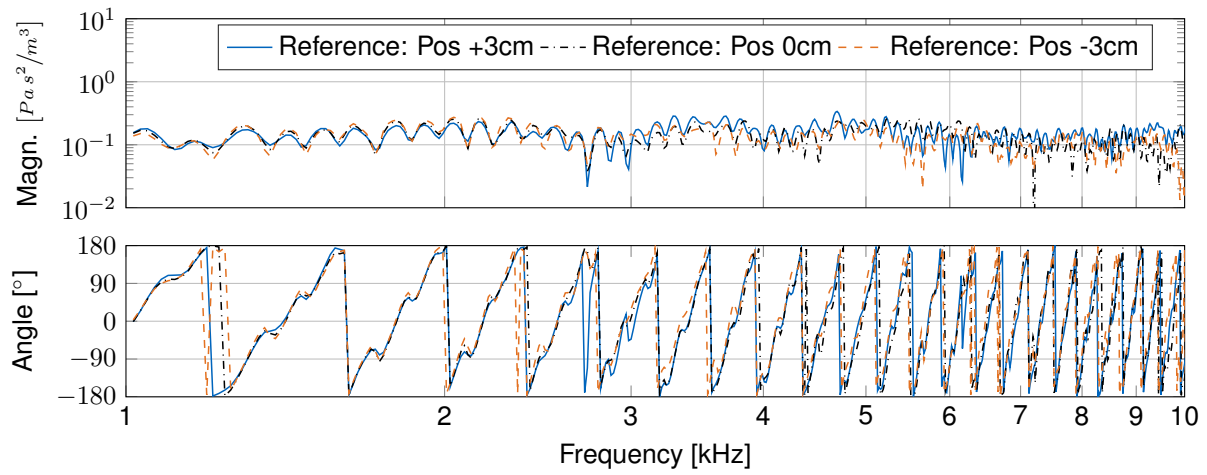**Figure 10.9:** Transfer validation for (a) 90 and (b) 100 percent of maximum compressor speed.

Figure 10.10: Positioning influence on the FRF measurements with the Q-MHF source.

but the artificial compressor will not be further treated in this thesis.

Part IV

Application to e-compressor NVH

Chapter 11

Automotive application example

Contents:

> Scientists study the world that exists, engineers create the world that never was.
>
> *Adam Stelzner,*
> *in "The right kind of crazy"*

In the preceding chapters, the required methods for building a modular virtual acoustic prototype have been explained in some detail. This included the virtual assembly of individual component models to obtain the full transmission path, and a vibration source description which is transferable from a source component testrig to a final receiver design. This was achieved by substructuring (see part I) and blocked forces (see part II). For the airborne path contributions, the measured airborne transfer paths[1] can be combined with blocked volume accelerations (see part III) to predict the sound pressure transmitted by a source over an acoustic path.

The interplay of these methods shall be exemplified on an industry relevant example in this section. The case shown here is a prototype of a long range battery electric vehicle (BEV). The focus was on studying the NVH performance of the electric climate compressor mounting concept. The goals of this study can be summarized as:

- Build up a modular model for the structure borne sound transfer path $\mathbf{Y}_{32}^{AB}$ with substructuring. Each substructure shall be described with the most appropriate method.

- Use a transferable source description for the structural excitation of the compressor, in the form of blocked forces $\mathbf{f}_2^{bl}$.

---

[1]Substructuring of airborne transmission paths is challenging due to the continuous interfaces between the individual "substructures". For promising advances on this topic see [53].
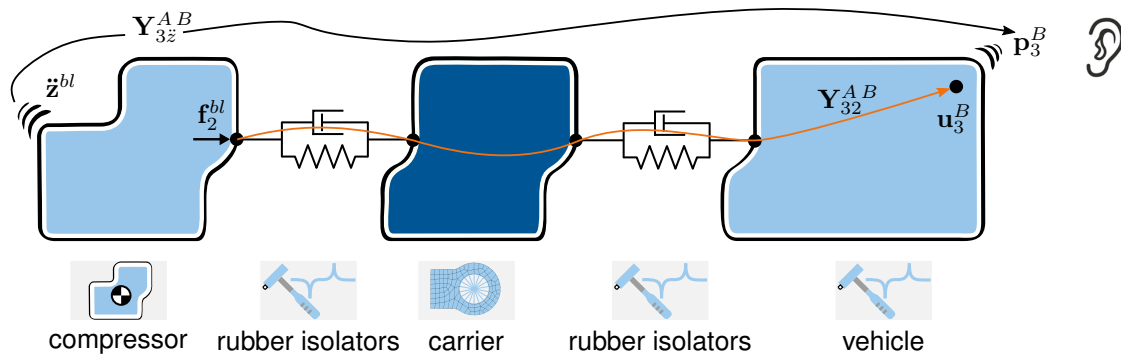
Figure 11.1: Schematic overview of the vehicle development example for e-compressor NVH. The small figures under the components indicate the modeling approach for each substructure. Rigid body model for compressor, experimental models for rubber isolators and vehicle, FEM model for carrier.

- Measure the airborne noise transfer functions $\mathbf{Y}_{3\ddot{z}}^{AB}$ in the vehicle prototype and predict the airborne path contribution with the blocked volume accelerations $\ddot{\mathbf{z}}^{bl}$ of the compressor.

- Validate the results with reference measurements in the vehicle prototype, and obtain a ranking of structure and air borne path contributions.

- Apply virtual design modifications to the structure borne path, by modifying components in the substructured model. Modify the airborne path contribution by applying blocked volume accelerations of a compressor *with* and *without* a sound insulation capsule[2] .

For confidentiality reasons the actual vehicle can not be shown, but the general setup of the isolation concept is shown in figure 11.1. The compressor is doubly isolated via two levels of rubber bushings from the car body. A component called "carrier" (see figure 11.1) serves, among other functions, as an intermediate isolation mass. The concept design was already given at the beginning of the campaign, so the goal was to validate the set of developed methods and to gain a deeper insight into the performance of the design (and discover potentials for design simplifications and cost savings).

11.1　Structure borne: substructuring of transmission path

From previous investigations, it was known that the compressor's structure borne contribution to cabin noise was well below 1000Hz. The frequency range of interest is an important aspect before performing any substrucuring and blocked force TPA project, since it defines the models that can be used and how the experiments shall be performed. In the following, all employed substructure models are explained before the substructured end result is validated with reference measurements on the prototype assembly in section 11.1.5.
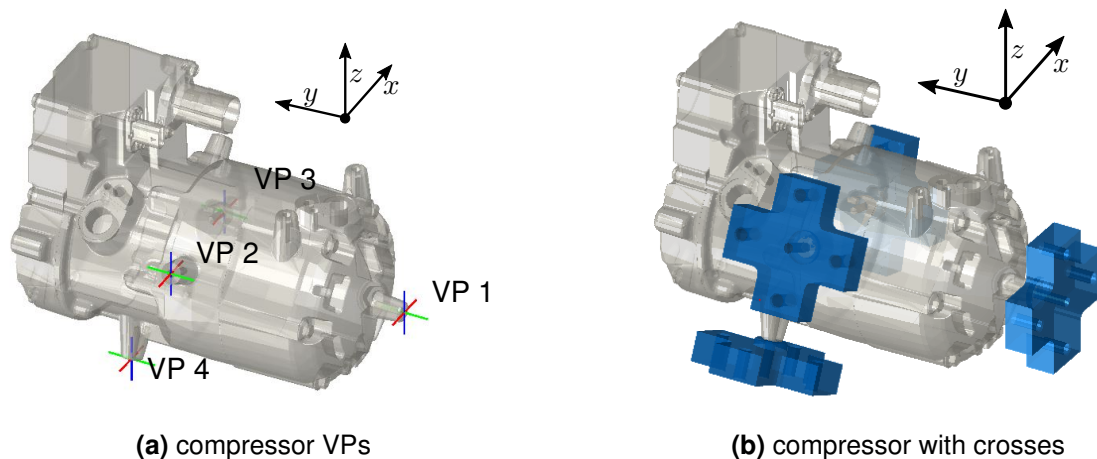
(a) compressor VPs

(b) compressor with crosses

Figure 11.2: Compressor model. (a) Depiction of the four connection points on the compressor indicated as VP1 to VP4. (b) Compressor with rigid crosses which were attached to apply enough sensors and impacts for obtaining the substructure model experimentally.

11.1.1 Rigid body compressor model

The compressor is isolated from the carrier at four points with rubber isolators, see figure 11.2a. Each of these connections shall be coupled via FBS to the rubber bushing models. The full degrees of freedom were taken into account, so each connection point was modeled as a full VP with six DoF, resulting in a 24×24 compressor FRF matrix $\mathbf{Y}^C$. Initially, it was unclear if an experimental, numerical or analytical model would best describe the compressor. Therefore, the intended compressor FRF was obtained experimentally first. Four crosses, rigid in the frequency range of interest[3], were attached at the four VPs of the compressor, see figure 11.2b. Thereby, enough sensors and impacts could be applied to each cross. Applying the virtual point transformation to the measured FRF, allowed to obtain the desired 24×24 FRF model of the compressor. The crosses could be modeled as rigid body components (see section 2.7). This allows decoupling them from the FRF measured on the compressor *with* the crosses (the same way as it is done for the rubber models in section 4.3.2). Upon inspection of the obtained FRFs, it was noted that at around 700Hz not the compressor had a first resonance, but the crosses had a tilting mode on the protruding connection points. This hindered obtaining a clean experimental compressor substructure model. The flexibility of the protruding connection points is part of the compressor, but the substructuring results obtained with this experimental model of the compressor were not as good as with with a rigid body model (not shown in this chapter).

It was therefore decided to treat the compressor as a rigid body. The experimentally obtained accelerances where just a constant over frequency up to 500Hz (see figure 11.3) and with the rigid body model assumed to be the same also above this frequency. Since the lower frequency region matched very well with an analytical rigid body model, it was chosen to model the compressor this way. The mass matrix of the compressor $\mathbf{M}^C$, in the center of gravity, can be built from its mass m^C (measured on a scale) and its rotational inertia tensor $\mathbf{\Theta}^C$ (taken from the CAD model):

---

[2]This is assuming that the surface vibrations of the compressor, which cause the blocked volume accelerations, are not altered by the modified structural suspension. In the simulated cases, the compressor was always mounted with very soft rubber bushings in the vehicle. Therefore, this assumption was considered to be valid.

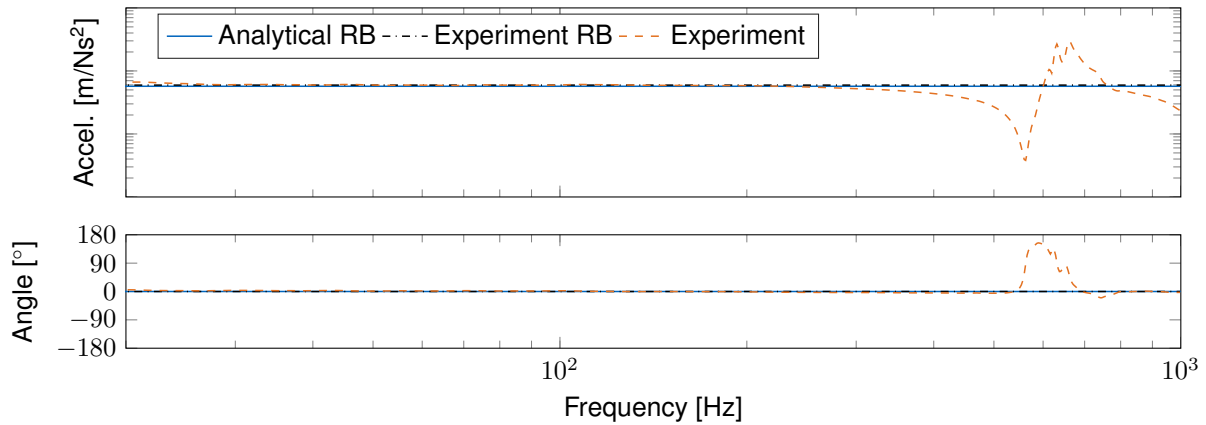[3]Validated by FEM, see also the discussion in section 2.7 on these helper crosses.

Figure 11.3: Rigid body model of compressor versus measured substructure model with the crosses shown in figure 11.2b. The shown FRF is a driving point FRF on VP1 for excitation and response in +X direction, see figure 11.2a.

$$\mathbf{M}^C = \begin{bmatrix} \mathbf{I}\, m^C & \\ & \mathbf{\Theta}^C \end{bmatrix}, \tag{11.1}$$

$$\tilde{\mathbf{Y}}^C = \left(\mathbf{M}^C\right)^{-1} \qquad\qquad \text{and:} \quad \tilde{\mathbf{Y}}^C \in \mathbb{R}^{6 \times 6}. \tag{11.2}$$

The mass matrix $\mathbf{M}^C$ is the same as in equation (2.59) without the off-diagonal terms, since the point of reference Q is equal to the center of gravity C, and therefore $\mathbf{r}_{QC} = \mathbf{0}$. The acceleration FRF of the rigid compressor $\tilde{\mathbf{Y}}^C$ is obtained by simply inverting the mass matrix. In order to obtain the desired 24×24 FRF matrix of the compressor, the 6×6 admittance in the in the center of gravity $\tilde{\mathbf{Y}}^C$, needs to be expanded to the desired coupling points. This is done by:

$$\mathbf{Y}^C = \mathbf{R}_u \tilde{\mathbf{Y}}^C \mathbf{R}_f^T \qquad \text{with:} \quad \mathbf{Y}^C \in \mathbb{R}^{24 \times 24}, \quad \text{and:} \quad \text{rank}(\mathbf{Y}^C) = 6. \tag{11.3}$$

This operation could be called an "inverse virtual point transformation", where one is starting with a lower set of DoF and projects them to multiple coupling points on the rigid body. The projection matrices $\mathbf{R}_u$ and $\mathbf{R}_f$ can be constructed in a similar way as in the VPT shown in section 3.3.2. In figure 11.3 this model is compared to the experimentally measured FRF on VP1 in +X direction. The tilting modes of the crosses appear at around 700Hz on each cross individually (see the few consecutive resonances in the "Experiment" FRF in figure 11.3). When the "Experimental" FRF matrix is averaged over the frequencies, in the frequency range from 50-250Hz, and this constant value is taken for all frequencies, this results in the curve called "Experiment RB" in figure 11.3. Note that this fits very well with the analytical compressor model stated in equation (11.2) and (11.3). Thus, for the further coupling, the analytical rigid body model of the compressor will be used.

11.1.2 Experimental rubber models

As already mentioned, the compressor is isolated with two stages of rubber isolators from the vehicle. The sets of rubber isolators will be called "level 1" and "level 2" isolators in the following. They decouple the compressor from the carrier (level 1) and the carrier from the vehicle (level 2). The rubber bushings in one level are all equal in geometrical dimension,
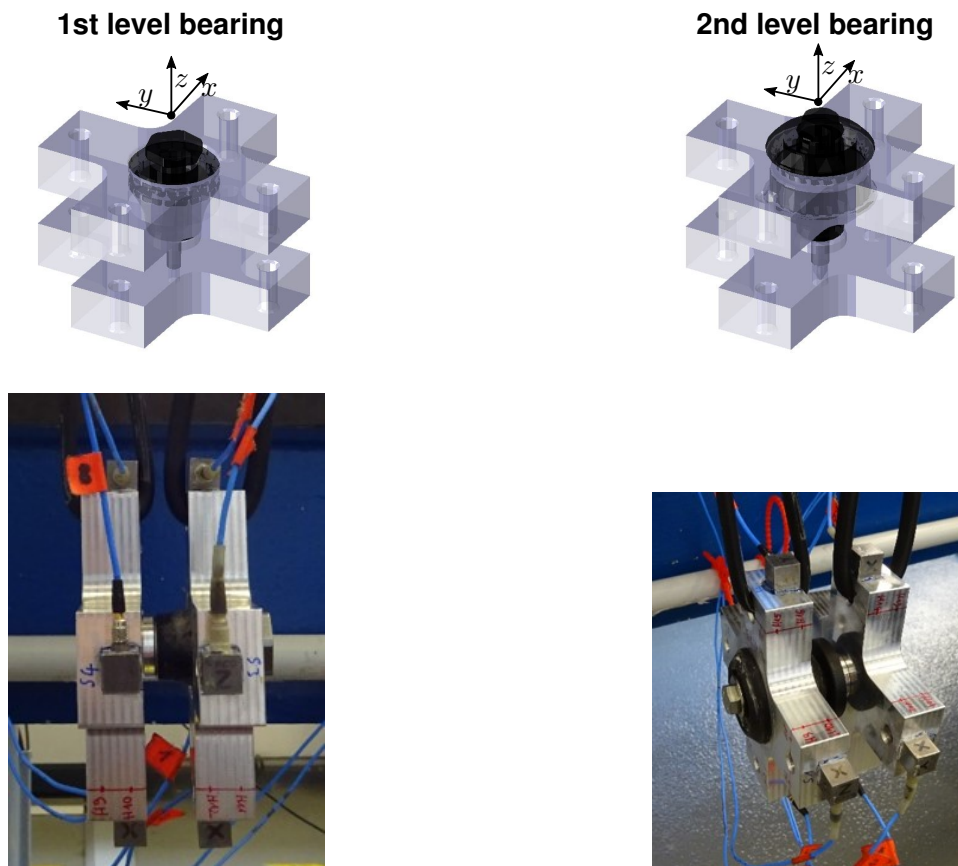
1st level bearing

2nd level bearing

Figure 11.4: CAD model of the rubber experiments and images of the measurement setup for both levels of rubber elements.

but two different materials / shore hardness (SH) are used in each level (due to heat stability and static load reasons). The substructure models of the rubber isolators were obtained as described in chapter 4. The setup with the cross fixtures for obtaining the experimental substructure models is shown in figure 11.4. The rubber elements are pressed into the upper cross, and then screwed to the lower cross, just like in the vehicle.

The crosses were analytically modeled as rigid bodies, including the added mass of the sensors (see section 2.7). Since it was known that the structure borne model shall be valid up to 1000Hz, the crosses were designed so that their first resonance frequency is well above 2000Hz. This was checked initially by FEM analysis, and thereafter by performing an FRF measurement on the freely hung up crosses. In figure 11.5, one FRF of each of the upper crosses is shown. It can be seen that their first resonances are both above 2500Hz. In figure 11.5, the consistency measure, as defined in section 3.4.3, is shown for the depicted input/output pair. As indicated as a rule of thumb in section 4.6, the crosses can be treated as a rigid body up to about half the frequency of the first resonance. This can be seen in the consistency of the crosses, which starts to drop after approximately 1250Hz.

The crosses were then decoupled from the measurements of rubber bearing with crosses via substructuring (equation (4.11)). This process resulted in a 12×12 FRF matrix for each rubber bushing, which is ready for coupling via FBS. The resulting dynamic stiffness in the radial and axial direction are shown in figure 11.6a and figure 11.6b respectively. It can be seen that their stiffness is approximately constant up to 100Hz, but starts to increase towards higher frequencies. In the radial stiffness of the level 1 natural rubber (NR) bushing, a clear dynamic stiffening at ca. 600Hz can be seen. The two different shore hardness (SH) for the level 2 bushings did not result in a significantly different dynamic stiffness.
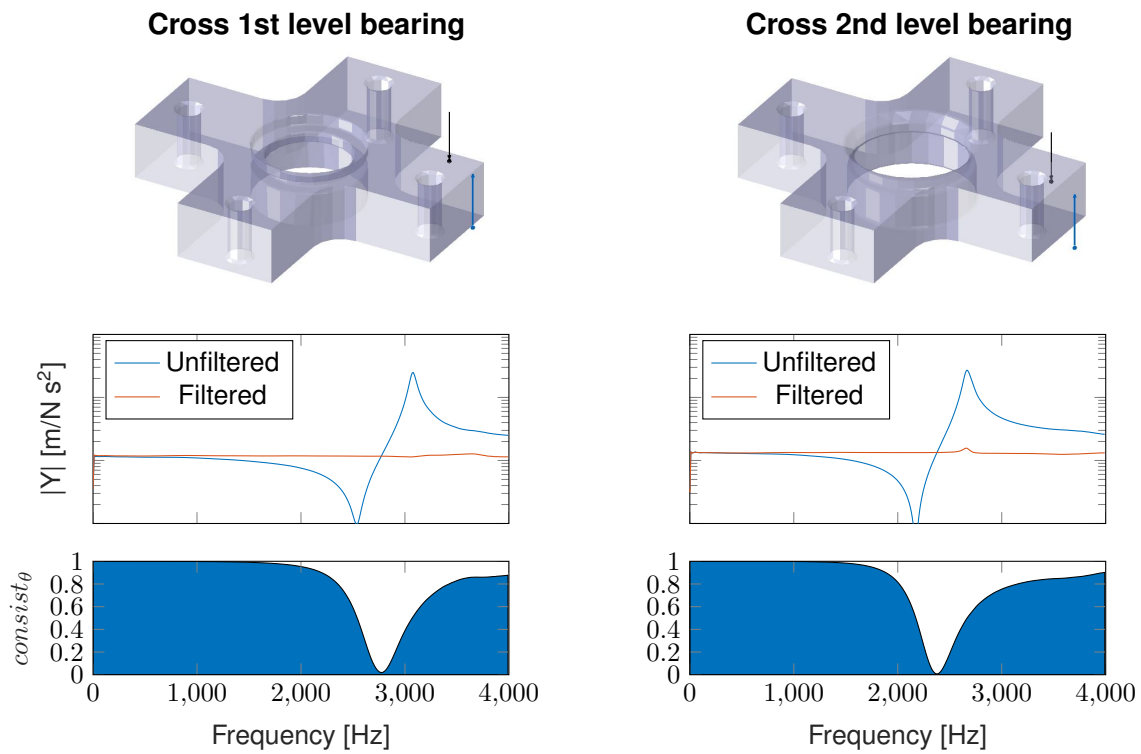
Cross 1st level bearing   **Cross 2nd level bearing**

Figure 11.5: FRFs measured on the freely hanging crosses (upper crosses for pressing in the rubber bushings). Hammer input is depicted as black arrow, Sensor output channel as blue arrow. Below the measured FRF and the VP filtered FRF is shown. The consistency is computed according to section 3.4.3 and shown below.
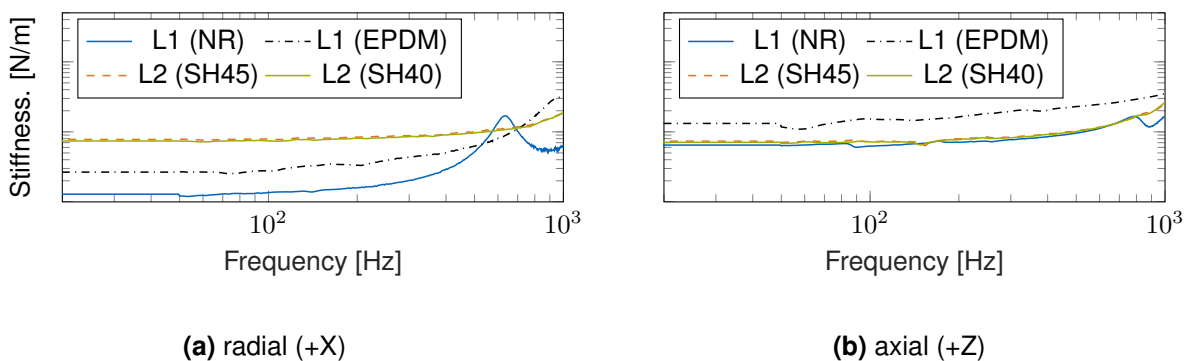

(a) radial (+X)   **(b)** axial (+Z)

Figure 11.6: Stiffness or rubber mounts, where L1 denotes the mounts for level 1 and L2 denotes the mounts for level 2. The mounts employed for level 1 differed in material, EPDM and natural rubber (NR). The mounts for level 2 also differed in material, shore hardness (SH) 40 and 45. Directions according to figure 11.4.

11.1.3 FEM carrier model

The carrier serves as an intermediate isolation stage, amongst other functions. Its "default" variant is from cast iron without any mechanical joints which could complicate the numerical modeling. Such structures can usually be modeled very accurately and without major effort by FEM. This comes with all advantages of good FEM models, e.g. the ease of investigating parameter changes to the design (as will be explored in section 11.6). The carrier was designed such that its first resonance is above the first compressor order at maximum operational speed. An initial FEM model, with standard material parameters from the ANSYS material library for cast iron, predicted a first resonance at 161Hz (already considering the added mass effect of the sensors, which can have a big effect on higher frequency modes, see figure 2.4). Once the first prototype was available, the first resonance was measured at 169Hz. The prototype was weighed on a scale, and the density of the FEM model was adjusted so the model mass matched the scale measurement (decrease of 3% from the material library value). An additional adjustment of the Youngs modulus (increase of 6% from the material library value), shifted the first FEM model resonance to the experimental reference[4]. In figure 11.7 this is shown as "FEM" for the model with the standard material parameters and "FEM updated" for the FEM model with the updated parameters. This is probably the easiest imaginable FEM model updating method, but served the purpose of this study well.

For using the model in substructuring, the coupling points where the rubber isolators shall be connected were equipped with RBE3 elements (see left part of figure 11.7)[5]. The carrier connected to four rubber isolators in level 1 with the compressor, and 3 isolators in level 2 for connection with the vehicle. The model therefore contained 7 RBE3 elements. The required 42×42 FRF matrix for FBS, was synthesized from the first 200 modes of the FEM model via equation (2.28). The frequency of the 200th mode was over 20kHz, so an additional compensation for higher order terms was not carried out. A modal damping of 0.1% was used, which fitted well with the experiment. As will be shown in section 11.6, one goal of this study was to apply virtual design changes to the structure borne transfer path. An easy change to the carrier is a simple material change, from cast iron to aluminum (which would result in a lower mass of the system). Therefore, one resulting FRF for changing the material of the carrier to aluminum is shown alongside in the right part of figure 11.7.

11.1.4 Experimental vehicle model

The last substructure for the full structure borne path, is the vehicle. This model needs to include the local dynamic FRFs on the coupling points with the level 2 rubber isolators. This meant 3 coupling points on the front axle carrier, shown in figure 11.8a. The noise transfer functions (NTFs) to microphones inside the vehicle were measured simultaneously, shown in figure 11.8b. For measuring the full 6 DoF at each connection point on the front axle carrier, rigid crosses where connected to these points which could be decoupled from the FRFs to obtain the FRF matrix without the added mass of the crosses. An automatic

---

[4]Note that the differences between the initial model and the first prototype could have also been due to geometrical deviations between CAD model and prototype. But adjusting the density and Youngs modulus was more practical.

[5]The ANSYS built-in RBE2 elements set all flexible motion in the remote point area to zero, and thus stiffen the connection area. RBE3 elements compute the rigid body motion in a least squares sense like the VPT, and do not constrain the connected nodes to only rigid motion. For all FE models in this thesis the RBE3 formulation was used. For the carrier this makes sense, since the metallic carrier was barely constraint by the attached rubber.
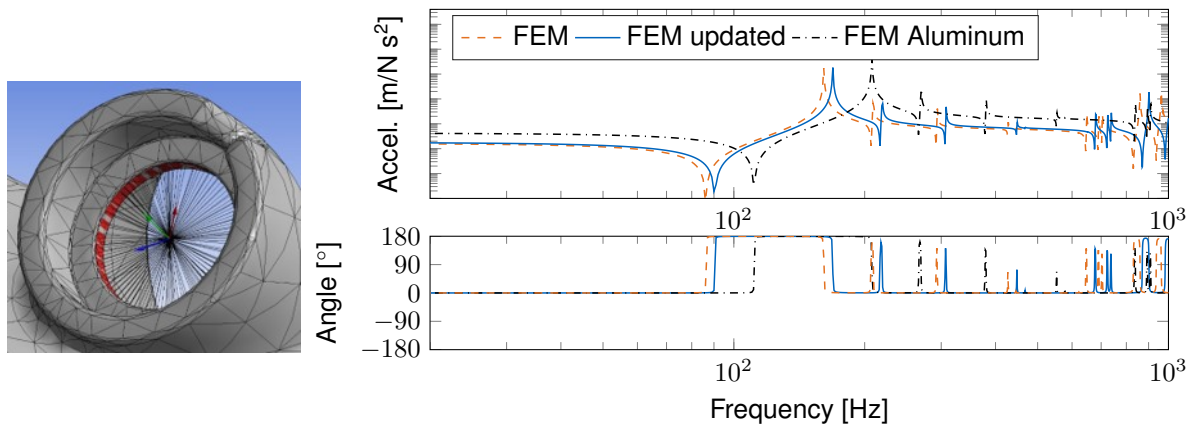
Figure 11.7: Left: Connection point of the carrier to the rubber models with 6 DoF RBE3 element. Right: Example driving point FRF of different carrier versions: initial cast iron model before material parameter update (FEM), material parameters updated with first prototype of carrier (FEM updated), and virtual change of material (FEM Aluminum).
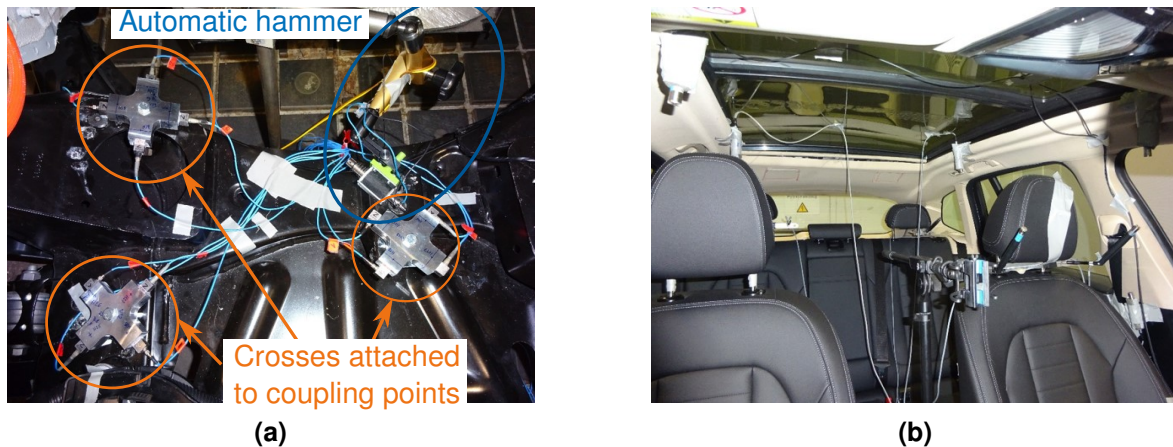

Figure 11.8: (a) Front axle carrier with crosses attached to each coupling point. The automatic hammer can be seen in the upper right part of the figure. (b) Multipe microphones in the driver's cabin which recorded the NTFs while impacting with the automatic hammer. The stand between driver and co-driver seat was to hold a 3D virtual reality microphone.
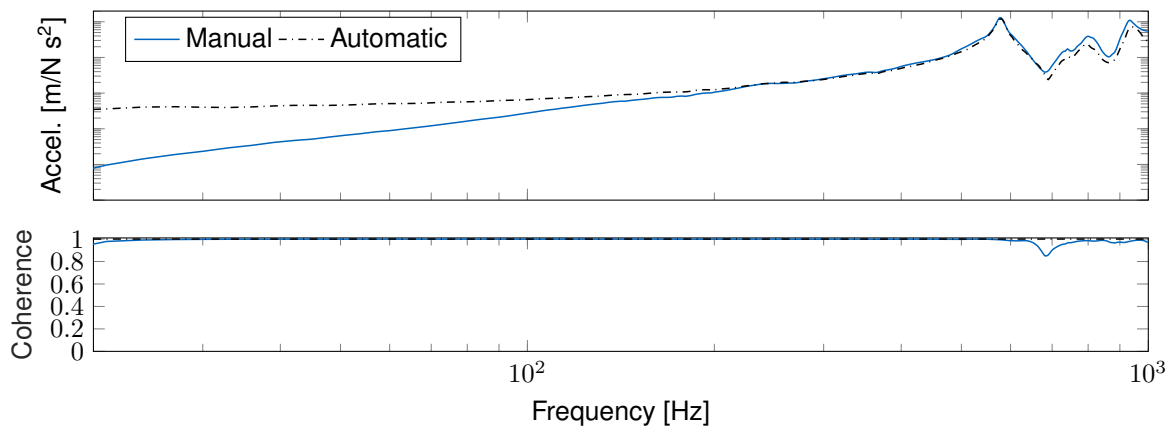
Figure 11.9: Driving point FRF on front axle carrier, once measured with the automatic and once with a manual hammer. The FRF shown is before decoupling the crosses.

hammer [100] was used for impacting on the crosses, which can be seen in figure 11.8a. One advantage of the automatic hammer is that after it has been positioned, the bonnet can be closed. Thereby, the transfer functions can be measured in a more realistic vehicle state. It was also easier to apply more repeatable impacts on the connection points, resulting in overall better coherences for the NTFs to to microphones inside the driver's cabin. On each cross, 9 impact positions with at least 5 averages were carried out, and four triaxial sensors were connected. After the VPT, this FRF model had the desired 6 DoF on each coupling point, making it ready for substructuring.

While inspecting the driving point FRFs measured with the automatic hammer, it was found that, though the coherence was very good, the measured FRFs in the lower frequency region did not make physical sense. Only the sensor channels on the cross that was directly impacted showed this unphysical behavior. For a structure without rigid body modes, as the vehicle is, an accelerance FRF should decrease quadratically towards lower frequencies (see section 2.6.2). This was not the case, see the "Automatic" FRF in figure 11.9. Rather the FRF seemed to be constant at lower frequencies, which would be typical for a freely suspended structure with rigid body modes. It was chosen to repeat the measurements with a manual impact hammer, also shown in figure 11.9 as "Manual". This FRF showed the expected behavior in the lower frequency region and was therefore considered more physical. An animation of the vibration shapes measured with the automatic hammer confirmed this finding. In the lower frequency region, the FRFs corresponding to the sensors on the cross that was directly impacted with the automatic hammer, made no physical sense[6]. It can also be seen that the FRFs measured with the automatic hammer matched well for higher frequencies (starting at ca. 200Hz) where the signal to noise ratio is better again. Therefore, the FRFs measured with the manual and automatic hammer were merged between 200 and 300Hz (linearly fading merge, with the manual hammer FRFs for the lower and the automatic hammer FRFs in the higher frequency region).

In figure 11.10, a NTF from the same impact position on the front axle carrier to a micro-

---

[6]The reason for this behavior of the automatic hammer FRFs is not yet clear. The author presumes that the hammer induces a small, impact like disturbance in the sensor signal close to the hammer (only in the sensors at the driving point). This impulse like signal could be of electromagnetic nature (the hammer is shot forward by an electrically powered coil). It could also be due to the acoustic pressure wave that is emitted when the hammer hits its stop position (this happens with an audible click). Further investigation is needed on this topic. It seems that this disturbance is very repeatable and not of a random nature, since the coherence is still very good.
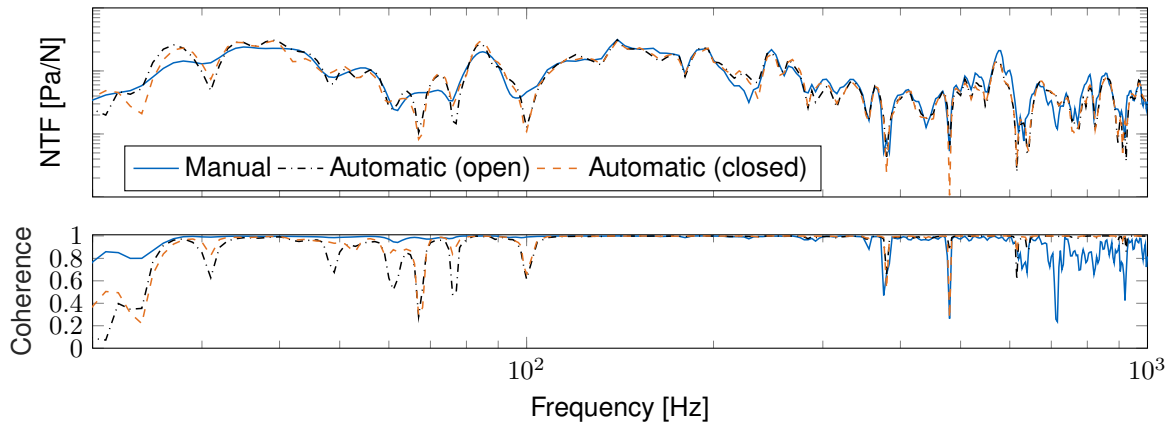
Figure 11.10: Vibro-acoustic FRF from front axle carrier to microphones in driver's cabin. Once measured with the "Manual" hammer (bonnet needed to be open for impacting) and twice with the automatic hammer (vehicle bonnet open and closed).
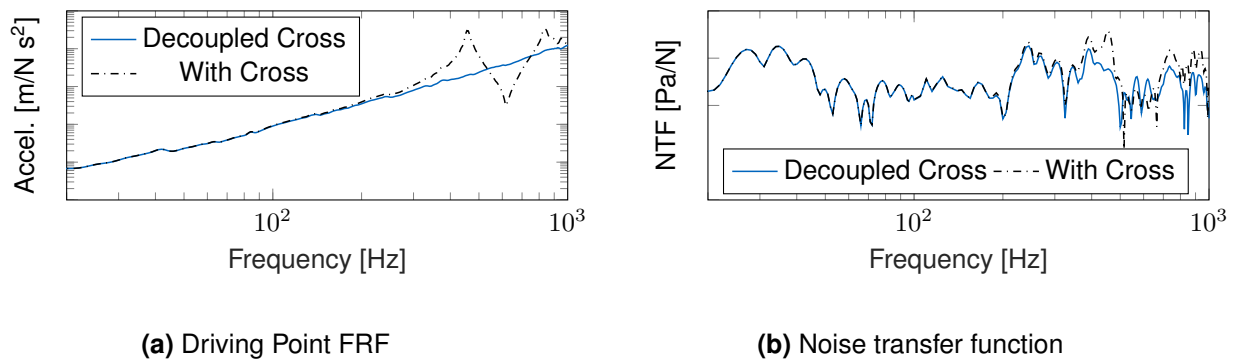

(a) Driving Point FRF

(b) Noise transfer function

Figure 11.11: Transfer Functions at the driving points before and after decoupling the crosses.

phone is shown, measured with the manual hammer and the automatic hammer (once with closed and open bonnet). During the manual hammer measurements, the bonnet naturally had to be open, since the test engineer needed to lean forward into the front compartment to perform the impacting. It can be seen that the NTFs for open versus closed bonnet are not significantly different. This indicates that the main transfer from front axle carrier vibrations to sound pressure in the driver's cabin are caused by structural vibrations that are transferred to surface vibrations in the cabin. The isolation of airborne sound or a stiffening of the structure by closing the bonnet, did not significantly alter the transfer behavior. It can also be seen that the NTFs measured with the automatic hammer generally achieved a better coherence for the NTFs in the higher frequency region.

Lastly, it was found that a decoupling of the crosses from the measured FRFs was indeed necessary. Initially, it was questioned if this is even needed, since the mass of the aluminum crosses is small compared to the mass of the front axle carrier. In figure 11.11a, one driving point FRF on the virtual point transformed FRF on the front axle carrier is shown. It can be seen that with the added mass of the cross, the FRF is showing some resonances, that are not visible after decoupling of the cross. In figure 11.11b, a NTF is shown before and after decoupling the rigid crosses. It can be observed that for higher frequencies (after ca. 300Hz) the added mass of the crosses also alters the noise transfer function into the cabin significantly.

To summarize the vehicle model for FBS:

- The FRFs of the vehicle were obtained by impacting on crosses at the front axle carrier connection points. The structural FRFs for FBS coupling, including the NTFs to microphones in the driver's cabin, were measured.

- The FRFs were measured with a manual and automatic hammer, which were merged from 200 - 300Hz, and transformed on the connection points via the virtual point transformation.

- The added mass effect of the rigid crosses was removed by decoupling them via FBS.

11.1.5   Substructuring result and validation

The previously described substructure models are compatible on their interfaces with 6 DoF on each connection point. They can be coupled by FBS, as explained in section 3.1, with the coupling formula in equation (3.19). The signed Boolean matrices $\mathbf{B}_u$ and $\mathbf{B}_f$, for enforcing compatibility and equilibrium respectively, have been constructed for each coupling stage. After coupling all components, the full systems FRF matrix $\mathbf{Y}^{AB}$ (see figure 11.1) was obtained. The full system FRF matrix comprised 14 VPs in total:

- 2×4 VPs on the compressor connection (before and after the bushing).

- 2×3 VPs on the connection of the carrier with the vehicle body (before and after the bushing).

The structural FRF matrix of the coupled system thus had a dimension of 84×84. Additionally, the full FRF matrix of the coupled system included a number of rows, which described the transfer to multiple microphones inside the driver's cabin. For validating the substructured FRF matrix of the full system, reference measurements on the assebled prototype were carried out. In the full assembly, not all points were accessible for attaching sensors and applying impacts. Therefore, only a few points were equipped with sensors and impacts were applied that would serve as a validation measurement. The validation impacts had to be carried out with a rubber tip, since the structural isolation over the bushings was so high, that otherwise it would have been impossible to insert enough energy into the system. For the H1 estimator, 5 impacts were averaged in each reference FRF measurement. Applying a shaker was not possible due to physical space restrictions.
The comparison between the substructured FRF and the validation measurement is shown in figure 11.12. In the upper part of figure 11.12, a force input on the compressor interface to an acceleration output on the carrier is shown. It can be seen that in the lower frequency region, the FRF is high in magnitude, as here the carrier and compressor show the typical resonances of two rigid bodies that are coupled via soft rubber isolators. The animated vibration shapes of the reference measurement and the substructured result showed a good visual agreement. In the lower frequency region, around 20Hz, it can be seen that the substructured model lacks a resonance that is seen in the reference measurement. The author believes that this resonance is due to the refrigerant hoses connected to the compressor, which have not been modeled. Initial results have shown that it is possible to model the passive dynamics of the refrigerant hoses in a similar manner to the rubber bushings, but this is not shown here. Towards higher frequencies, the compressor is isolated from the carrier and the FRF magnitude decreases, until the first resonances of the carrier at 169Hz and 210Hz. For frequencies higher than ca. 200Hz, the input spectrum of the rubber tip hammer is not enough to measure a clean FRF, as can be seen by the reference coherence in the lower part of the plot. Note that a nylon tip did not yield better coherences in this frequency region, the isolation over the rubber isolators was too much. Similar observations can be
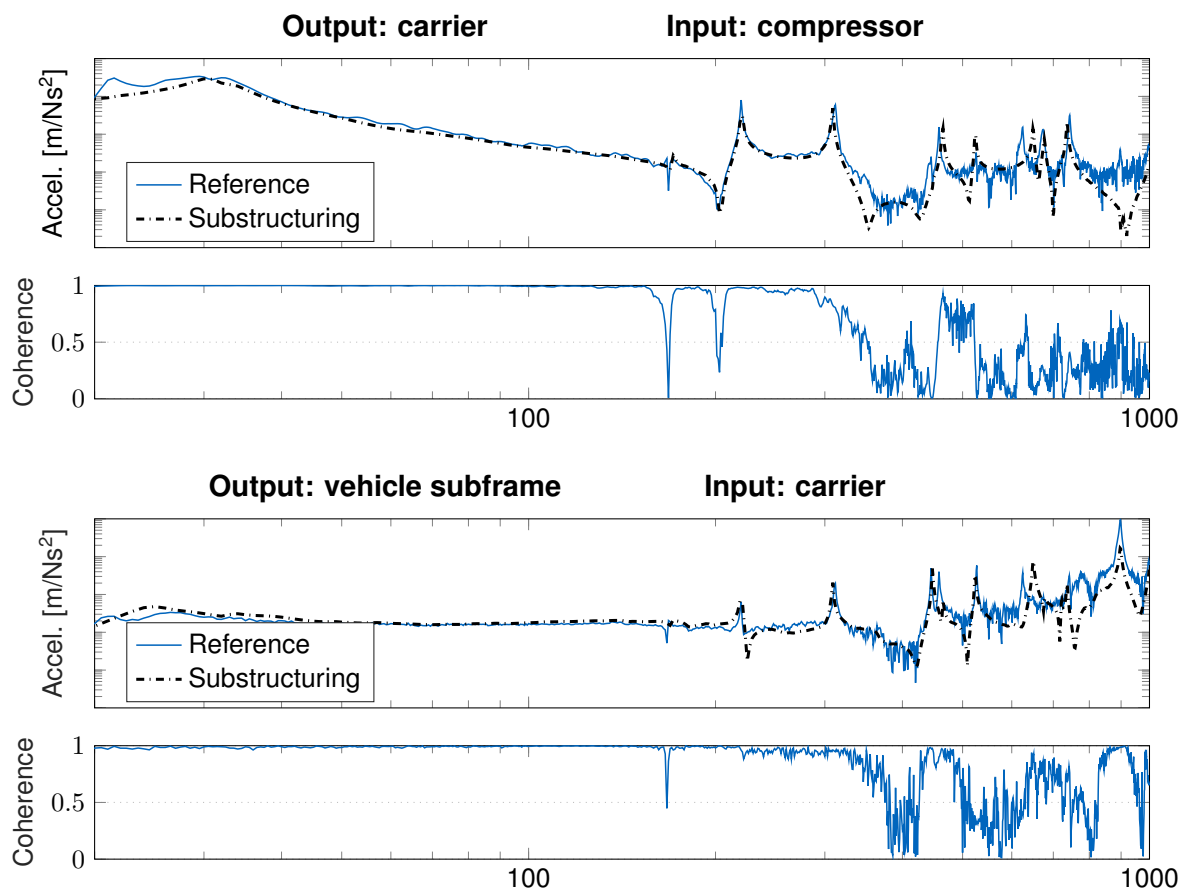
Figure 11.12: Substructuring Validation of structural FRFs with reference measurements
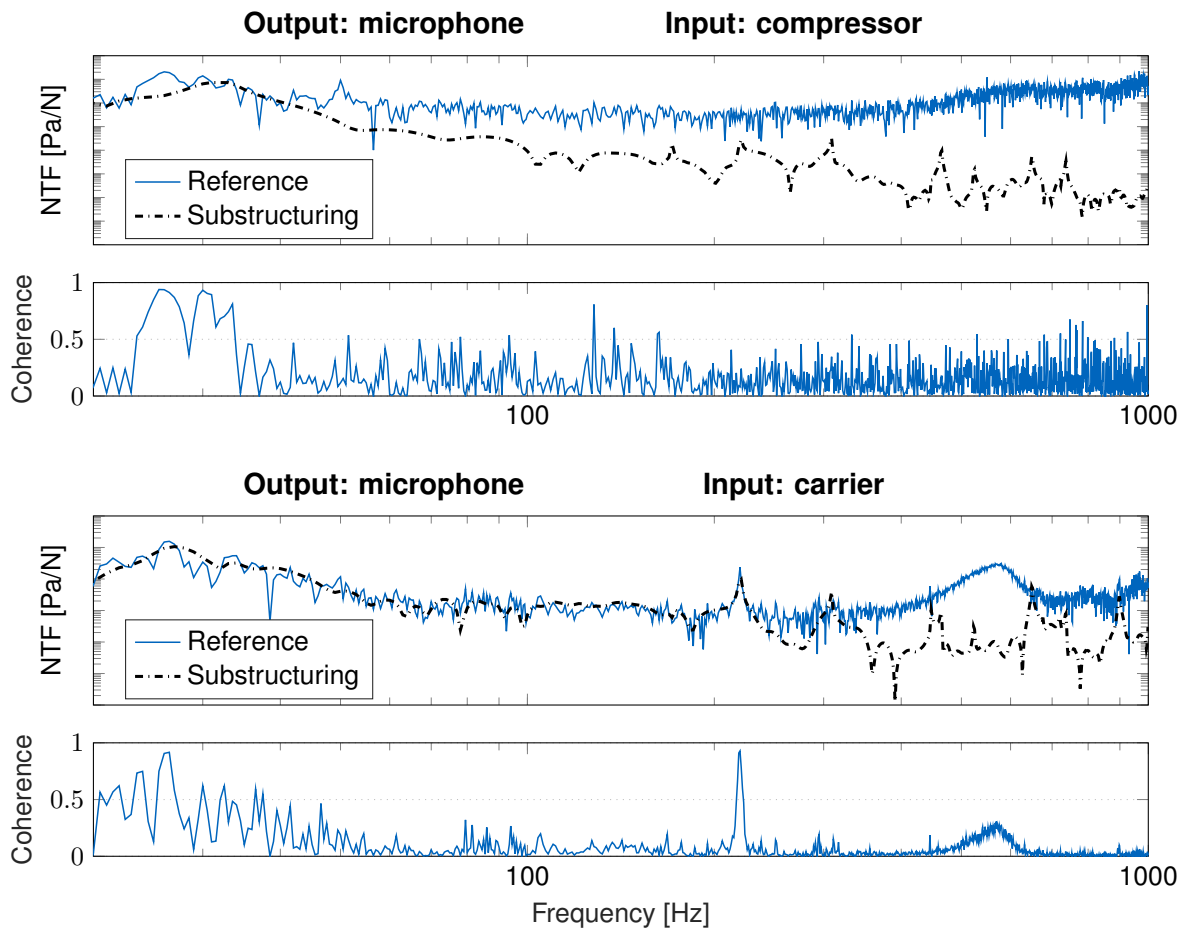
Figure 11.13: Substructuring Validation of noise transfer functions with reference measurements. Due to the low coherence and strong isolation of the rubber elements, no appropriately large input spectrum was achievable in the reference measurement

made for the FRF from an input on the carrier, to an output on the vehicle subframe, shown in the lower part of figure 11.12. Overall the FRFs in the reference measurements fitted the substructuring predictions very well, especially in the region with good coherence reference measurements. For higher frequencies, the substructured FRFs are believed to be more trustworthy than the reference measurement.

In figure 11.13, the vibro-acoustic NTFs from the reference measurement are compared to the substructuring results. In the upper part of figure 11.13 the NTF from an input on the compressor to an output on a microphone in the drivers cabin is shown. It can be seen that it is not possible to measure this NTF at all by experiment, since the input on the compressor is isolated over two levels of rubber bushings and the resulting sound pressure is too far below the noise floor of the microphones. Note that these NTFs from compressor to microphones are a critical requirement for performing the TPA predictions of the structure borne sound contribution later. The blocked forces will be applied to the compressor, and the resulting output on the microphones is predicted. Therefore, substructuring was in this case a critical enabler, without which the structure borne sound investigations would have been impossible.

In the lower part of figure 11.13, the NTF from an input on the carrier to the microphones is shown. Despite a still low SNR on the microphones, it can be seen that the H1 estimator ist still able to average out random measurement noise to some extend. The general trend of the predicted NTF fits the reference measurement well, and the increase in the NTF at

210Hz (which corresponds to the second resonance of the carrier) is predicted accurately. The advantages of substructuring can be summarized as follows:

- An FRF matrix of the whole system is obtained, with six DoF on each structural connection point. This would be unmeasureable due to space restrictions in the vehicle. It would also be challenging to simulate numerically due to the complexity of the system.

- By substructuring, FRFs that would be unmeasurable on the assembled system can still be obtained. On the full system, it is not possible to apply enough input energy on the compressor to measure the NTFs to microphones in the drivers cabin. Substructuring allows measuring or modeling each component individually, with a good signal to noise ratio, and obtaining the FRF of the assembled system by coupling them virtually.

- The substructured model is versatile, in the sense that it is easy to modify certain parameters on individual substructures, and study the effect on the transfer behavior of the full system.

- The FRF matrix of the full system can be predicted at an earlier stage in the development process (before an actual prototype of the full vehicle is available). The substructure models of the different components also allow for efficient collaboration between various departments or suppliers working of the individual subsystems.

11.2 Structure borne: source identification

The previous section determined the full transfer path from compressor to sound pressures in the driver's cabin. To predict the structure borne path contribution, the structural excitation of the compressor must now be obtained. This is done by blocked forces, which was in depth described in part II. Therefore, this section will not go into full detail of all the necessary steps. The blocked forces were obtained from freely suspending the compressor with rubber bands, and performing a set of operational runs, again in various conditions:

- Constant operating speeds from 10% to 100% of the compressors maximum speed (8600rpm), with speed increments of 10%.

- Runups from 10% to 100% compressor speed in 60 and 120 seconds.

- Noise measurements with the compressor switched off.

The compressor was hung up with the crosses shown in figure 11.2b, and the FRF matrix of compressor with the crosses $\mathbf{Y}_{42}^{AR}$ was obtained experimentally. The operational signals in the sensor channels $\mathbf{u}_4^R$ (sensors were applied to the crosses) were then used for inversely determining a set of 24 blocked forces contained in the vector $\mathbf{f}_2^{bl}$:

$$\mathbf{f}_2^{bl} = (\mathbf{Y}_{42}^{AR})^{\#} \mathbf{u}_4^R. \tag{11.4}$$

Wernsen's SNR filter was applied to the matrix inverse (see section 8.5.3). Leaving one sensor channel out of the inversion, and applying an on board validation (see section 6.3) yielded a fairly good prediction, which can be seen in figure 11.14 for two different operational conditions.
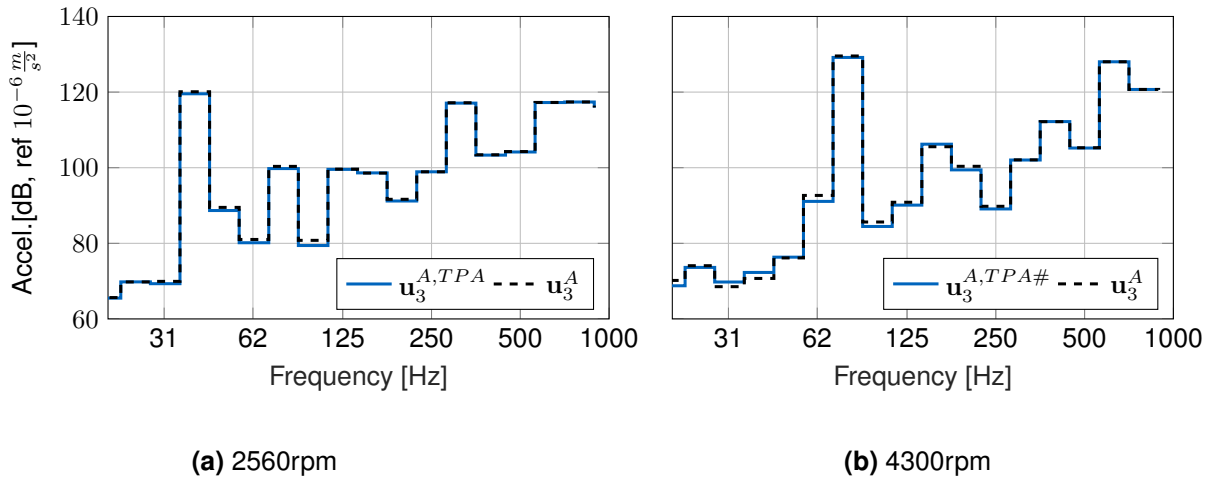
(a) 2560rpm **(b)** 4300rpm

Figure 11.14: On Board validation for the blocked forces, with $\mathbf{u}_3^{R,TPA}$ being the on-board prediction $(\mathbf{u}_3^{R,TPA} = \mathbf{Y}_{32}^{AR}\mathbf{f}_2^{bl})$ and $\mathbf{u}_3^{A}$ being the reference measurement recorded in this sensor channel.

11.3 Air borne: transmission path & validation

Next to the structure borne path, it was known that the airborne sound was a major contributor to the interior cabin noise. The measurement of airborne transfer functions (ATFs) and the computation of blocked volume accelerations $\ddot{\mathbf{z}}^{bl}$ as a component source description was explained in detail in part III. This section therefore only explains the specific conduction of measurements and computations for predicting the airborne path contribution in the vehicle.

11.3.1 Transfer function measurements

The ATFs from compressor to microphones inside the vehicle were obtained experimentally. For the lower frequency region from 50 - 1000Hz a Q-LMF volume source was used. This volume source is basically a big loud speaker which has the size of a human torso, and can be placed on the passenger seats. This was placed in the driver's cabin, as can be seen in figure 11.15a. Six microphones were attached at the monopole positions around the compressor (on which the blocked volume accelerations have been determined). The transfer functions in the lower frequency region were thus measured *reciprocally*. The ATFs in the mid to high frequency region (400 - 10kHz) were measured with the Q-MHF volume source (the source has already been shown in figure 9.3b). The orifice of the Q-MHF source hose was positioned next to the 6 monopole positions on the compressor. The ATFs to the microphones in the vehicle could thus be measured directly. An example of one airborne transfer function measured with both sources is shown in figure 11.16. The ATFs from both sources were merged between 500 - 900Hz (linearly fading merge on the complex values of the ATFs, with the Q-LMF for the lower and the Q-MHF measurements for the higher frequency region). All transfer function measurements were conducted with closed hood. This yielded the airborne FRF matrix $\mathbf{Y}_{3\ddot{z}}^{AB}$, see figure 11.1. AB indicates the full vehicle assembly, $\ddot{\mathbf{z}}$ indicates the volume accelerations as input and 3 denotes the receiver points, i.e. the microphones in the vehicle. The ATF matrix $\mathbf{Y}_{3\ddot{z}}^{AB}$ thus has 6 columns for applying the blocked volume accelerations describing the airborne compressor excitation.

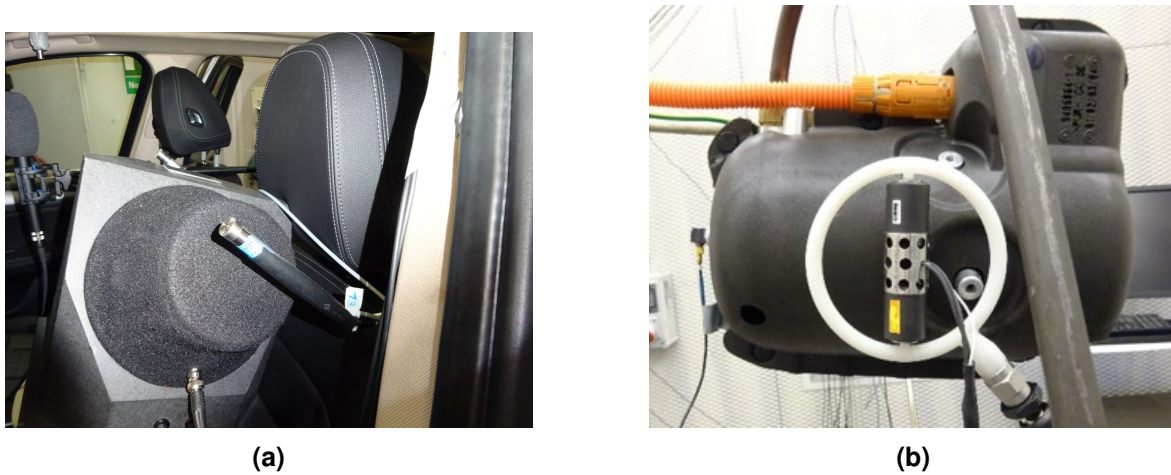**(a)**   **(b)**

Figure 11.15: (a) Q-LMF source for reciprocal measurement of ATFs in the vehicle, used for the frequency range from 50 - 1000Hz. (b) compressor with airborne sound capsule during the measurements of blocked volume accelerations in the anechoic chamber. Notice the single axis accelerometer attached at the front connection point of the compressor, which is needed for phase correct addition of airborne and structure borne sound contributions.
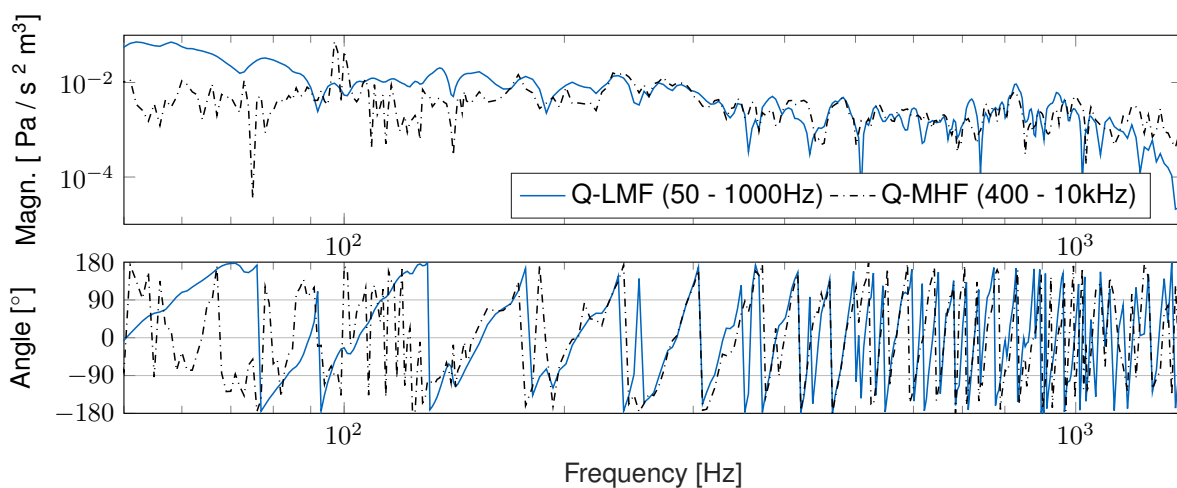
Figure 11.16: Reciprocal FRFs with low frequency source Q-LMF and mid to high frequency source Q-MHF. Measured without the compressor capsule

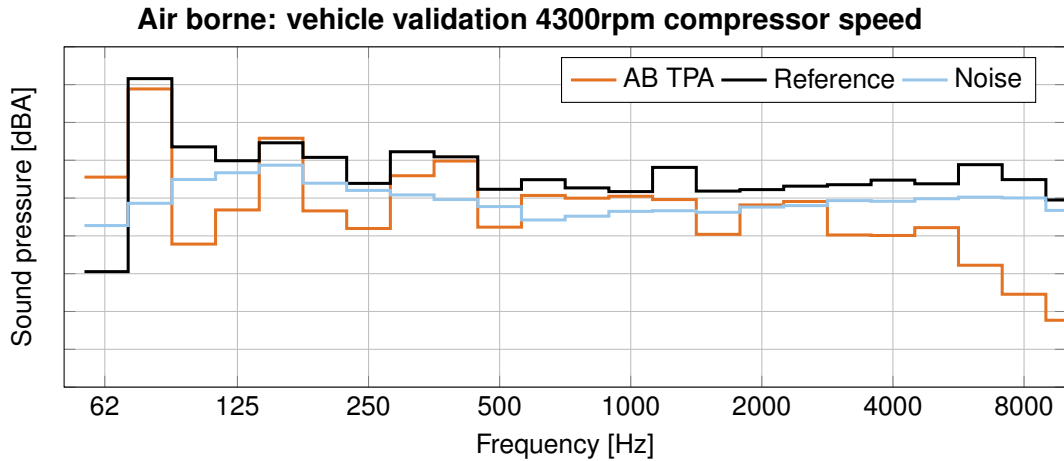**Air borne: vehicle validation 4300rpm compressor speed**

Figure 11.17: Validation of the airborne TPA contribution (AB TPA) with reference measurements in the vehicle (Reference) while the compressor was not touching the car. A noise measurement in the vehicle with the compressor switched off (Noise) is shown to indicate the noise floor in the vehicle. One y-axis increment denotes a 10dB difference.

11.3.2 Validation air borne TPA

For an initial validation of the airborne sound predictions with the blocked volume accelerations, the compressor was freely suspended in the vehicle front compartment so it wouldn't structurally touch the car at any point. The power supply cable and the refrigerant hoses were guided out of the car (without touching it) to an external load unit of IPEtronik, which allowed a controlled and repeatable operation of the compressor. The blocked volume accelerations were determined in the anechoic chamber (see the description in chapter 10). The sound pressures in the vehicle $\mathbf{p}_3^B$ were measured during operation of the compressor. Since the compressor was not touching the vehicle, it could be assumed that all sound in the driver's cabin should be a result of the direct airborne radiation from the compressor housing. The component TPA prediction of the airborne sound was done with the measured FRF matrix $\mathbf{Y}_{3\ddot{z}}^{AB}$ and the blocked volume accelerations $\ddot{\mathbf{z}}^{bl}$ that were determined in the anechoic chamber:

$$\mathbf{p}_3^{B,TPA} = \mathbf{Y}_{3\ddot{z}}^{AB}\,\ddot{\mathbf{z}}^{bl} \tag{11.5}$$

The validation for one operational condition is shown in figure 11.17. A good agreement between the reference measurements and the airborne sound predictions with the blocked volume accelerations could be achieved, especially for higher operational speeds of the compressor. For lower speeds of the compressor (ca. below 4000rpm) the sound pressure in the driver's cabin was barely above the noise level.

The blocked volume accelerations were determined in the anechoic chamber for a compressor with and without a sound insulation capsule (see the description in chapter 10). The compressor with sound insulation capsule can be seen in figure 11.15b) The performance of adding a sound insulation capsule can thus be determined, as will be shown in section 11.6.

11.4 Phase correct adding of structure - & air - borne contribution

In the previous sections, it was explained how the air and structure borne paths, from compressor to sound pressures in the driver's cabin can be obtained. Additionally, it was explained how the blocked forces $\mathbf{f}_2^{bl}$ and blocked volume accelerations $\ddot{\mathbf{z}}^{bl}$ can be used as an independent description of the sources structure and air-borne excitation. Hence, the path contributions for the airborne sound can be computed via equation (11.5), and the path contributions for the structure borne sound via:

$$\mathbf{p}_3^{B,TPA} = \mathbf{Y}_{32}^{AB}\mathbf{f}_2^{bl}. \tag{11.6}$$

Often it is desired to auralize both individual path contributions combined. This will be done with the non-cyclic convolution explained in section 7.6. The sound files will be provided in the next section.

However, if the combined predictions of the air and structure borne paths shall be auralized, additional care has to be taken. The computation of the blocked forces and blocked volume accelerations were done with operational data from different experiments. Not only is the operational speed of the compressor not perfectly the same during both experiments, also the phase of the compressor is shifted by an arbitrary amount during both operational measurements. The phase in which the compressor was in the operational measurement, basically depends on the millisecond in which the test engineer hit the "record" button. For adding the auralizations of both contributions in the time domain, both time signals have to be aligned in phase. Otherwise an unwanted amplification, or extinction due to non phase-correct adding could occur. Therefore, Müller [126] implemented an algorithm to allow this phase correct adding of air and structure borne contribution. For this, a reference channel on the compressor is needed, which was present in both operational measurements (for the determination of the blocked forces and the blocked volume accelerations). In this case, the phase in the +Z direction at the VP1 of the compressor was used (see figure 11.2a). This compressor vibration was recorded during the operational measurements for the blocked force evaluations and the blocked volume acceleration evaluations (see the accelerometer in figure 11.15b). The algorithm for aligning the phase of both measurements would basically:

- Determine the exact frequency of the first order $f^{1.Ord.}$ with the bary center method [116] based on the first frequency block of the each measurement.

- Change the length of the first time block, so that an exact integer number of operational cycles fits into the time block (preventing leakage and phase distortions).

- Compute the phase of the first order for the airborne operational measurements ϕ^A and the structure borne operational measurements ϕ^S.

- Crop the time signal of the structural operational measurements by Δt, so that both structure and air borne phases match in the first time block.

The small time Δt for cropping the structure borne measurements can be computed, by computing the phase difference between both measurements:

$$\Delta\phi = \phi^S - \phi^A. \tag{11.7}$$

The cropping time for the structure borne operational signal can then be computed via:

$$\Delta t = \frac{\Delta\phi}{2\pi\,f^{1.Ord.}} \tag{11.8}$$
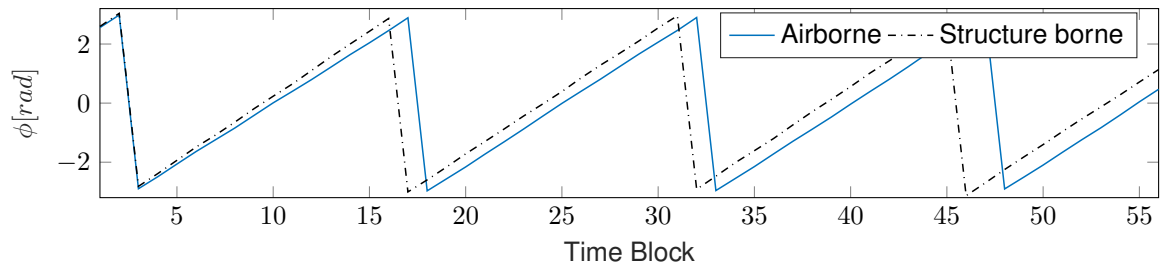
Figure 11.18: Aligned phase of the compressors first order on VP1 in +Z direction (see figure 11.2a and the accelerometer in figure 11.15b that was additionally recorded in the anechoic chamber). Phase is plotted over the individual time blocks during an operational run.

The resulting phase of the structure borne and airborne measurments over the time blocks is shown in figure 11.18. It can be seen that the phase matches over the first few time blocks, but starts to drift away over time. This is caused by slight differences in operational speed during both measurements. However, it allowed for a realistic auralization of the combined sound over the first time blocks.

> **Remark 11.1**: If the author was to perform the measurement campaign again, he would directly measure the airborne and structure borne excitation during the same operational measrurements. During the operational measurements in the anechoic chamber, additional accelerometers could be attached to the compressor. This way, the phase of both measurements would automatically be aligned with each other, rendering the operation discussed in this section superfluous. Since it turned out that the compressor can be realistically modeled as a rigid body, no impact measurements would have to be performed. Only the airborne FRFs and one set of operational measurements on the accelerometers and microphones would be needed, to obtain both, the airborne and structure borne excitation of the compressor.

11.5 Validation of air- and structure-borne paths

As compressor was mounted in the final suspension concept of the prototype vehicle (as shown in figure 11.1), the suite of operational measurements was carried out. Again the refrigerant and power-supply hoses were guided out of the vehicle, without touching it, to the IPEtronik load unit. The resulting sound pressures in the driver's cabin were a combination of the air and structure borne path contributions. The air and structure -borne contributions could be predicted via component TPA, see equation (11.5) and (11.6). In figure 11.19, the comparison of the predicted path contributions are shown with a validation measurement. The speed of the compressor was comparatively low with 2560rpm and the first compressor order being at 43Hz. The compressor noise in the drivers cabin ("Validation") is mainly dominated by a low frequency bass sound. It can be seen that the overall sound level is mainly caused by the structure borne path contribution ("SB TPA") at the first order. Confer also to the substructured NTF from the compressor to the microphones in figure 11.13. The mechanical isolation concept is not fully working at these low speeds of the compressor. Some resonances of the compressor and carrier oscillating as rigid bodies against each other, are excited by the first compressor order at 43Hz. Towards higher frequencies the struc-
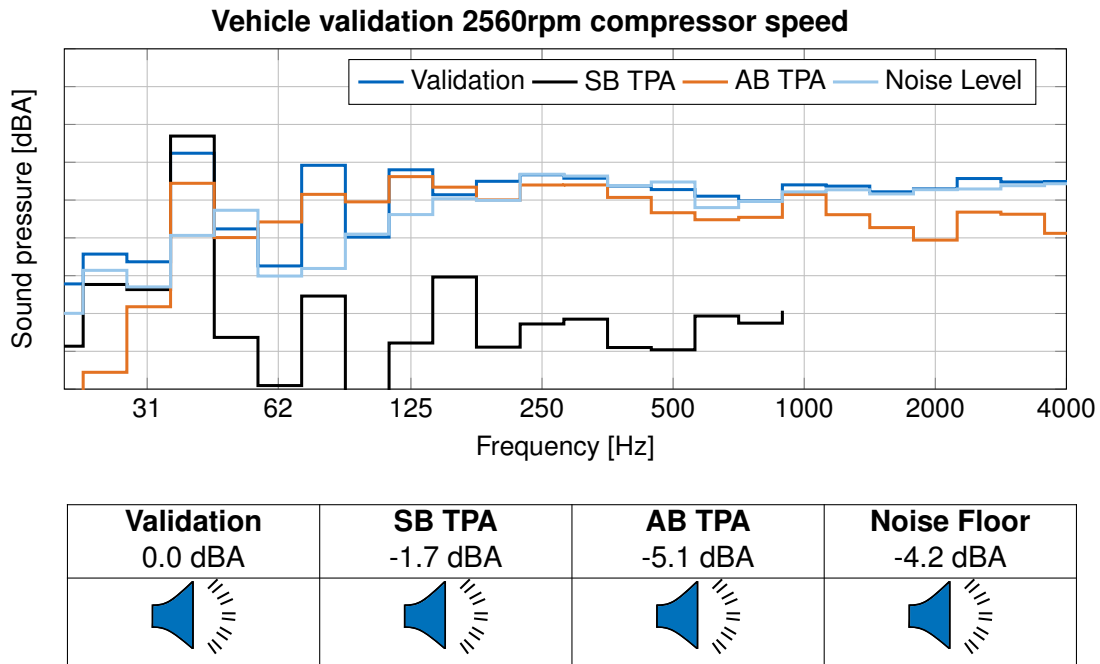
Vehicle validation 2560rpm compressor speed

Validation	**SB TPA**	**AB TPA**	**Noise Floor**
0.0 dBA	-1.7 dBA	-5.1 dBA	-4.2 dBA

Figure 11.19: 2560rpm: Third octave plot of sound pressure "Validation" in the drivers cabin and the airborne "AB TPA" and structure borne "SB TPA" prediction. Additionally, the "Noise Floor" on the microphone is shown (recorded with compressor switched off). One y-axis increment in the diagram corresponds to 10dBA. Overall sound pressure levels are given below the diagram, and sound files of the individual path contributions are provided. The overall sound pressure levels are referenced to the "Validation" measurement, which therefore has a sound level of 0.0dBA. Note that, as already mentioned in chapter 7, headphones usually have a "flatter" transfer function and playback the sound files in a more frequency unbiased manner.

ture borne contribution becomes significantly lower, as the isolation concept is fully working. Note that in all subsequent validation plots, a noise measurement on the microphone is additionally plotted. At this low operating speed of 2560rpm, the validation measurement on the microphone hits the noise floor at ca. 200Hz. The sound signal shown in all subsequent plots is always recorded/predicted at the left drivers ear.

In figure 11.20, the compressor at 4300rpm is shown, i.e. its first order was at 72Hz. It can be seen that the structure borne path contribution is already negligible compared to the reference measurement. At 72Hz also the first order of the compressor is well isolated from the receiver. As can be seen and heard in figure 11.20, the dominant path is the airborne transfer path. Also higher frequencies of the compressor can be heard inside the driver's cabin now. Overall, the sound insulation was still very good at this speed, and the compressor was only mildly audible.

In figure 11.21, the path contributions and validation measurement are shown for the maximum operating speed of the compressor at 8600rpm, meaning that the first order is at 143Hz. As expected the structure borne path contribution also negligible at this operating speed, as the compressor is structurally fully isolated by the two levels of rubber bushings. The resulting sound pressure is mainly caused by the airborne path. At this operating speed, the compressor was well audible in the driver's cabin. Note that for all validation measurements shown in this section, the compressor was not enclosed with an airborne sound insulation capsule.
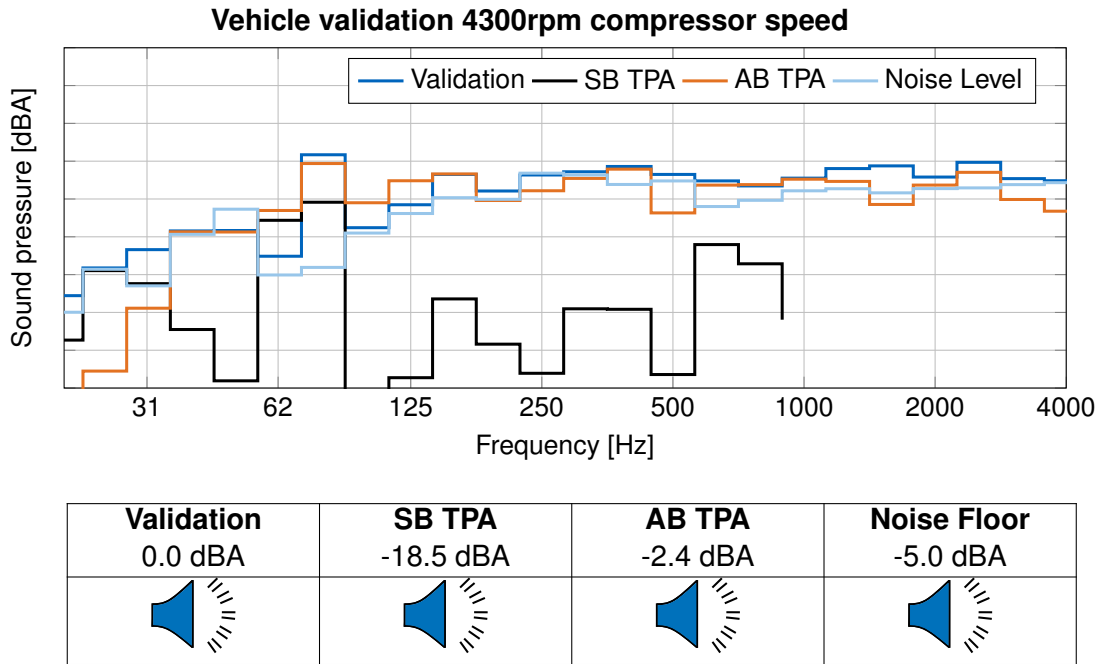
Vehicle validation 4300rpm compressor speed

Validation	**SB TPA**	**AB TPA**	**Noise Floor**
0.0 dBA	-18.5 dBA	-2.4 dBA	-5.0 dBA

Figure 11.20: 4300rpm: Same plot as in figure 11.19, confer to this caption.

Vehicle validation 8600rpm compressor speed

Validation	**SB TPA**	**AB TPA**	**Noise Floor**
0.0 dBA	-21.4 dBA	0.6 dBA	-10.2 dBA
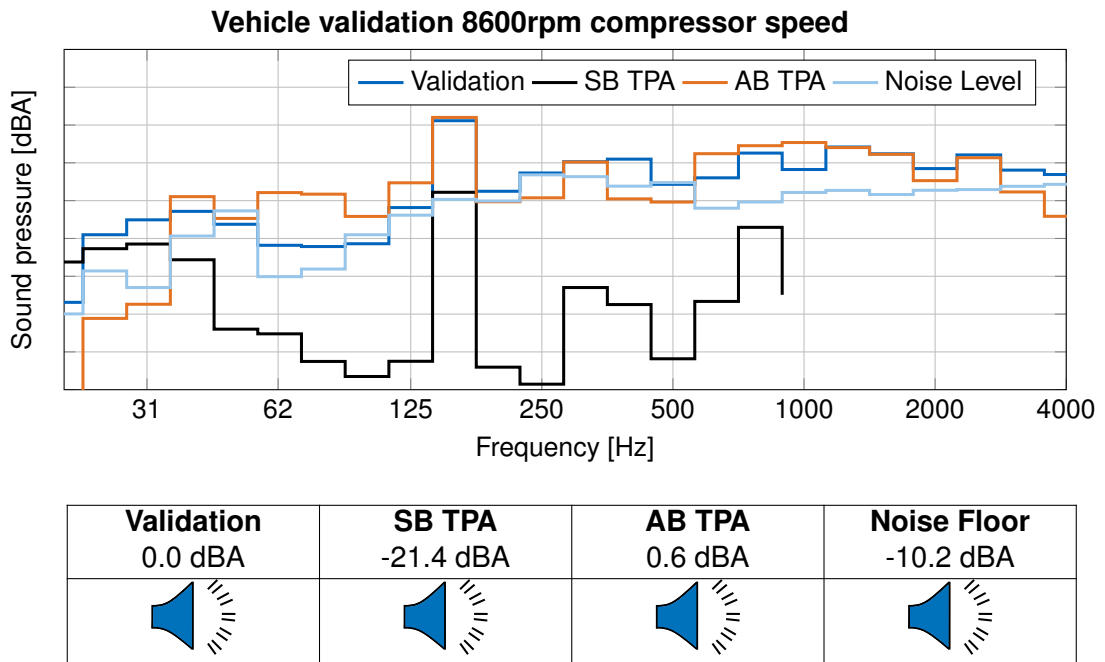
Figure 11.21: 8600rpm: Same plot as in figure 11.19, confer to this caption.
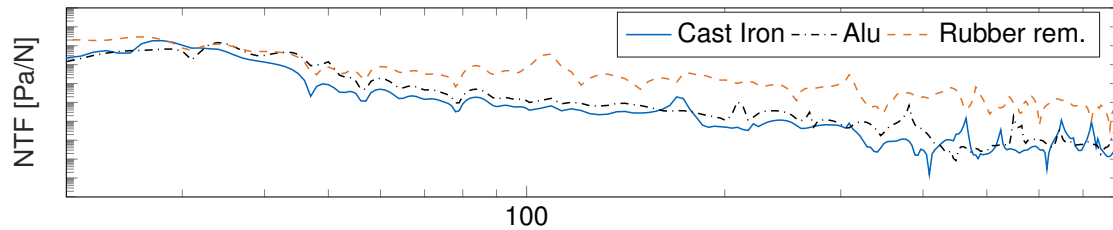
Figure 11.22: Virtual Design Modifications for the NTF from an input at the compressor and an output at a microphone in driver's cabin. "Cast Iron" being the default design, "Aluminium" representing the change of the carrier material to aluminum, and "Rubber rem." representing the removal of the second level of rubber isolators.

11.6   Virtual Design modifications

In the previous section, it was shown that the combination of substructuring, blocked forces and volume accelerations allows for a deeper insight in the individual path contributions. The flexibility coming with a substructured model allows for exploring the potential of design changes. It has been seen that the structure borne excitation was comparatively low, and only dominant for lower operational speeds of the compressor with the current design. Typical design goals are to make the assembly lighter or simplifying it, which would result in reduced cost and assembly time. In order to illustrate the possibilities of a modular substructured vehicle model, two virtual modifications of the structure borne path shall be investigated here:

- Changing the material of the carrier from cast iron to aluminum, which would make the whole design lighter.

- Removing the second level of rubber isolators completely, which would simplify the design and save costs.

Both of these design changes can be easily simulated, by exchanging the FEM substructure model of the carrier with one made of aluminum, or coupling the compressor-isolator-carrier subsystem directly to the vehicle without the second level of isolators. This results in a modified transfer FRF matrix $\mathbf{Y}_{32}^{AB}$ and the resulting sound pressures can be predicted by applying the blocked forces $\mathbf{f}_2^{bl}$ to them. Again, it is a great advantage that the blocked forces are a sole property of the compressor, independent of the final receiver (see chapter 6). The FRF for an input on the compressor and an output at the microphone inside the driver's cabin for the original and the modified designs is shown in figure 11.22. It can be seen that when the carrier material is changed to aluminium, the rigid body modes of compressor moving against the carrier are shifted to higher frequencies. This results in an isolation of the compressor that occurs at higher frequencies. For the removal of the second level of rubber bushings, the isolation of the compressor is less steep with increasing frequency, which is also expected from basic theory.

In figure 11.23, the predicted structure borne path contributions are shown for the lower compressor speed at 2500rpm. The reference signal is the recorded microphone signal that was band pass filtered from 20 to 1000Hz. It can be seen that with the material change to aluminium the contribution of the first order is increased by ca. 18dB. With the aluminium carrier, the compressor is exciting a rigid body mode, which in turn causes this significant increase in sound pressure level. Towards higher frequencies the structure borne sound contribution becomes negligible again, due to the two stage isolation. Removing the second level of rubber isolators also results in an increased contribution of the first order by ca.
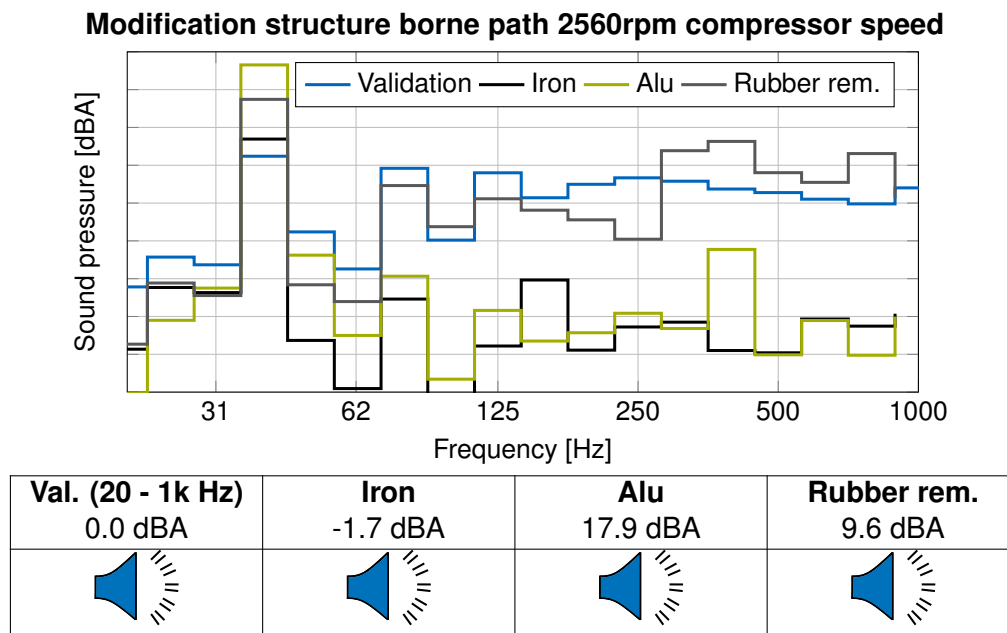
Modification structure borne path 2560rpm compressor speed

Figure 11.23: Virtual prediction of design modifications to the structure borne transfer path, with "Validation" being the reference measurement in the default design, "Iron" being the default design with iron carrier and two level isolation, "Alu" being the modified design with aluminum carrier, and "Rubber rem." being the iron carrier without second level of rubber bushings.

10dB. Additionally, the structure borne path would then also transfer higher frequencies into the drivers cabin, due the decreased isolation. Of course, simply removing the second level of rubber isolators or changing the material of the carrier would require further fine tuning of individual design parameters (e.g. the bushing stiffnesses could be decreased with the aluminum carrier, since the static load would be less due to the mass savings). However, the modifications presented here shall merely exemplify the potentials for studying new designs with substructuring.

As it was shown in the previous section, the airborne contribution of the compressor was a major contributor to the cabin noise for higher operational speeds. Therefore, the blocked volume accelerations were also determined for a compressor that was wrapped in a sound insulation capsule (see figure 11.15b). The compressor with sound insulation capsule was also tested in the vehicle as a validation measurement. The resulting validation measurements and airborne "AB TPA" predictions are shown in figure 11.24. Note that the validation measurements shown in figure 11.24 ("Val. cap." and "Val. no cap.") were both carried out with the compressor mounted in the vehicle, so the structure borne sound of the default design (cast iron carrier and two stages of isolation) is still present in these measurements. However, as was shown in figure 11.20, the structure borne contribution to the cabin noise can already be considered negligible at this operational speed. In figure 11.24, it can be seen that the airborne TPA predictions with the blocked volume accelerations are well able to predict the overall decrease in cabin noise by ca. 3dBA for the design with the sound insulation capsule.

11.7 Conclusion

In this chapter, the methods introduced in parts I - III of this thesis were applied to an industry relevant vehicle development project. It was shown that substructuring allows to virtually
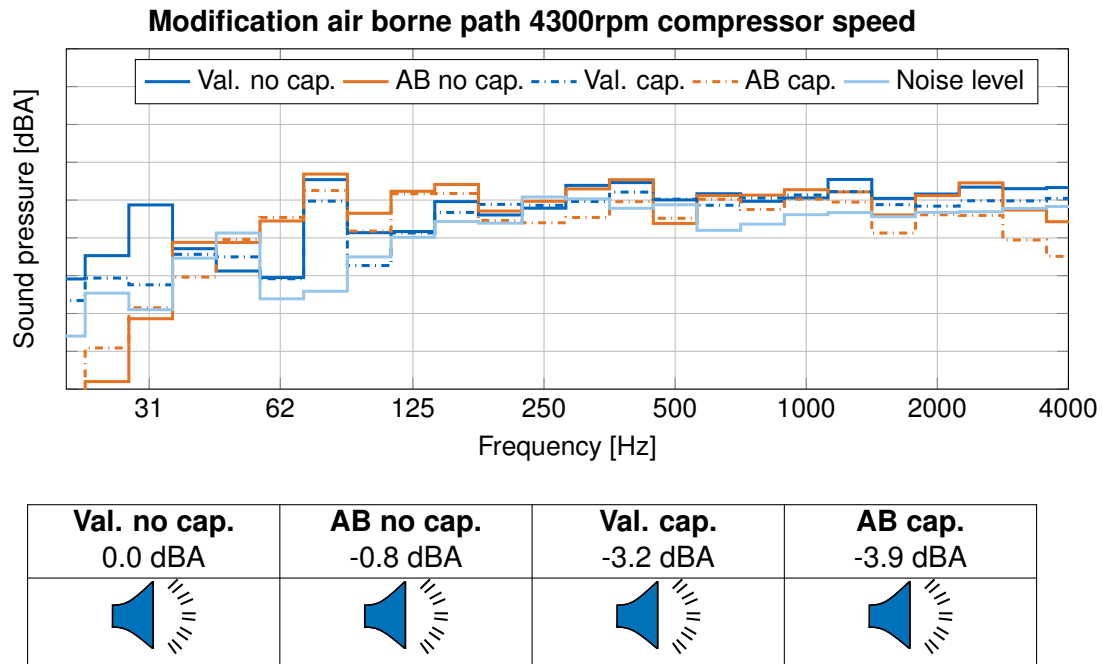
Modification air borne path 4300rpm compressor speed

Val. no cap.	**AB no cap.**	**Val. cap.**	**AB cap.**
0.0 dBA	-0.8 dBA	-3.2 dBA	-3.9 dBA

Figure 11.24: Comparison of design modifications to the air borne transfer path, with "Val. no cap." being the validation measurement of the compressor without capsule, "Val. cap." the reference measurement with capsule, "AB no cap." and "AB cap." the airborne predictions with the blocked volume accelerations.

couple different components, where each component can be modeled with the most appropriate method. Coupling a rigid body model of the compressor, experimental models of the rubber isolators and vehicle, and a numerical model of the carrier, resulted in clean and well validated predictions of the structural FRFs and NTFs into the driver's cabin (see figure 11.12 and figure 11.13). Additionally, it was possible to predict transfer functions that are non-measurable with standard measurement equipment, since the signal to noise ratio would have been to low. This was especially the case for the NTFs (see figure 11.13). The TPA predictions for the the sturcture and air borne path contributions provided a better insight in the important mechanisms creating the sound pressure in the drivers cabin. This approach naturally lends itself to virtual modifications and optimizations on the NVH concept. Some of these possibilities were outlined in section 11.6.

The potential for using this modular approach to sound and vibration engineering, will be further explored by setting up a parametric design optimization of the e-compressor isolation in the next chapter.

Chapter 12

Parametric design optimization on virtual acoustic prototypes

Contents:

> Schwingungstilger sind die Folge von nicht optimal durchgeführter Produktentwicklung.
> [transl. *Tuned-mass dampers are a consequence of sub-optimal product development.*]
>
> *Prof. Markus Zimmerman*
> *in "Reißwolf Ausgabe (02/18)"*

The contents of this chapter were published in similar form in [59]. The text hereafter has been modified and adapted to the thesis.

In the previous chapter, it was shown how the combination of substructuring and blocked forces allow for virtual design modifications to explore better designs. This combination lends itself naturally to parametric NVH design optimizations[1]. In the authors opinion, parametric NVH optimization is a major field of application for substructuring and blocked forces, that should be further used in the future. Thereby, NVH issues can be treated and optimized early in the development cycle, preventing potential late phase issues and redesigns.

Blocked forces are not dependent on one specific receiver structure, in contrast to interface forces of classical TPA (see chapter 6). Blocked forces can therefore be used as a source description in design optimization. For optimizing the assembly, different substructures are virtually coupled to each other, where each substructure is described by the most appropriate modeling approach. Frequency based substructuring (FBS) allows coupling analytical,

---

[1]This was a personal goal of the author since the beginning of his research project, since during his graduate studies he spend some courses and projects on design optimization algorithms. The author wants to thank Dawid Kobus [89] for his enthusiasm and the many late hours he spend preparing and updating the ANSYS models and implementing an efficient interface to Matlab.
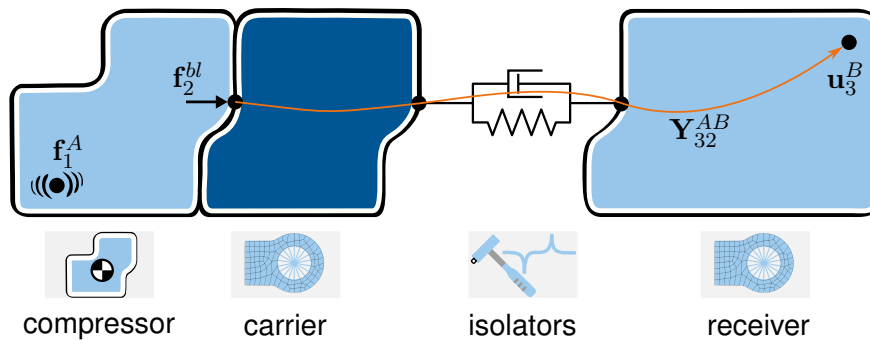
Figure 12.1: General optimization problem overview.

numerical or experimental models to each other (see chapter 3 for the theory and chapter 11 for an application). Numerical models are used for substructures which can be simulated with high accuracy. These can be parametrized for optimization. Experimental models are used for substructures that are hard to simulate accurately.

The application example presented here is again the electric climate compressor. The assembly was a testrig for principal investigations on an NVH isolation concept. It consists of: *a)* a FEM model of the receiver, *b)* experimental models of different rubber isolators, *c)* a parametrized FEM model for the carrier, and *d)* a rigid body model for the compressor (see figure 12.1). On the receiver the vibrations $\mathbf{u}_3^B$ are resulting from the compressor induced dynamic forces. These vibrations shall be minimized by optimally designing the carrier structure and suspending it with the right choice of rubber isolators. Applying the blocked forces to the coupled model, makes it possible to simulate the receiver vibration $\mathbf{u}_3^B$, which can be used for evaluating an objective function. The rubber isolator choice and the parametrized FEM model of the carrier, are iteratively optimized for minimal structure borne noise. Virtually coupling the substructures, and applying the compressors blocked forces to the assembly, makes it possible to simulate the loudness for different design parameters. The objective function is formulated such that it captures the success or failure of different designs. The design is then iteratively improved by a suitable algorithm. This approach seems favorable, as it also keeps the computational effort at a minimum by describing the complex substructures and the source excitation experimentally. This ultimately makes a numerical optimization applicable, where many evaluations of the objective function are required.

In section 12.1, a short review of relevant literature shall be given. Some basics on acoustic optimization will be explained in section 12.2. In section 12.3, the formulation of an objective function and the applicability of different optimization algorithms shall be discussed on a minimal example. In section 12.4 a genetic optimization algorithm is applied minimize the objective function for the compressor design (figure 12.1) . The simulated predictions for the optimal parameters are validated with measurements on the physically built design, including auralization of the results.

12.1   Review of relevant literature

The author could not find existing work that combines blocked force TPA, FBS and parametric design optimization for NVH. There are however numerous publications combining blocked forces and substructuring *or* performing a parametric NVH optimization.

Combining blocked forces and substructuring has in recent years been shown in the literature for some successful applications. The previous chapter in this thesis can be considered as one example. In [134] an analytical example of a similar approach is presented. For an experimental proof of concept there are [156] and [108], with promising results. In [156], the focus is more on a complete 6 DoF description of the interface with the VPT. In [109, chapter 7] and [110], examples are shown, whose complexity can be compared to what is encountered in industry. In [109] also the computation of confidence intervals for the predicted results is outlined.

Parametric NVH optimization for improving the acoustic behavior of structures has been the topic of many publications, e.g. [19, 37, 74, 102, 142]. Marburg has given an extensive review of work in the field [102]. In [19], an algorithm for minimizing the velocities on radiating surfaces due to forces acting in predefined positions is given. In [74], it is claimed that for minimizing the radiated sound power, one can also minimize the mechanical power that enters the passive system from the source (which is also found by [84, 179]). Thereby, the effort of solving the coupled structural and acoustical equations is spared. However, there are also other methods for getting estimates of radiated sound power from purely structural simulations [43]. In purely airborne acoustics, applications of topology optimization can be found [37]. There, the goal is to find the right distribution of material in absorbing layers to minimize the overall loudness in a given domain, resulting from a predefined source term. In all of these publications the definition of the dynamic forces causing the vibrations as well as the receiver systems stay somewhat academic. In [83], the acoustic optimization of a fibre reinforced plastic oil pan is investigated. As a source term, most often a unit force excitation over all frequencies in the range of interest or other simplified methods are utilized.

When using component TPA, real world dynamic force signatures of given sources can be described. Additionally, with FBS the receiver paths can include complex structures, since their transfer paths can be included from experimentally obtained models. The optimization algorithm can then focus on improving the part of the structure which can be described by numerical or analytical models with sufficient accuracy.

12.2 Acoustic design optimization

In this thesis, it was already explained how the noise transfer path of the source coupled to the receiver can be built up from single substructures in a modular fashion (part I), and how to model the excitation of a given noise source so that it is independent of the receiver structure (part II). The receiver can then be parameterized by certain design variables contained in the vector $\mathbf{x}$. The entries in $\mathbf{x}$ could be choosing from a discrete set of rubber bearings or the position of masses in a given design. The goal is to find the right choice for these parameters $\mathbf{x}^{opt}$, e.g. optimal position for the masses and optimal choice of rubber bearings, so that a defined objective function $\Phi(\mathbf{x})$ is minimized. The function $\Phi(\mathbf{x})$ might describe the minimization of vibrations at a specific location, or noise at the drivers ear. Alternatively, $\Phi(\mathbf{x})$ could be defined to minimize the assembly mass, where some constraints $g_i(\mathbf{x})$ require that defined levels of noise are not exceeded. In general, optimization problems are stated in the following manner:

$$
\begin{aligned}
\text{minimize} \quad & \Phi(\mathbf{x}), \\
\text{so that} \quad & g_i(\mathbf{x}) \leq 0 && \text{for } i = 1, \ldots, m; \\
\text{and} \quad & h_i(\mathbf{x}) = 0 && \text{for } i = 1, \ldots, l; \\
\text{and} \quad & \mathbf{x}_{lb} \leq \mathbf{x} \leq \mathbf{x}_{ub},
\end{aligned}
\tag{12.1}
$$

where $g_i(\mathbf{x})$ denotes each of the m inequality constraints, $h_i(\mathbf{x})$ each of the l equality constraints. The lower and upper boundaries for each entry in the design vector $\mathbf{x}$ are contained in the vectors $\mathbf{x}_{lb}$ and $\mathbf{x}_{ub}$ respectively. The constraint functions $g_i(\mathbf{x})$ and $h_i(\mathbf{x})$, the objective function $\Phi(\mathbf{x})$ as well as the design variables $\mathbf{x}$ are chosen by the engineer to best capture the possible solution space and the design goals of the specific application. The objective function used in this chapter is motivated in section 12.2.1. This is also put in context to other objective functions typically found in the literature on structural acoustic optimization. Once the problem has been stated, one needs to choose an appropriate optimization algorithm for finding a solution that minimizes the objective function and satisfies the constraints. In section 12.2.2, a brief overview of two main classes of optimization algorithms is given. The applicability of these algorithms to the problem at hand is checked by a minimal example in section 12.3.

12.2.1   Objective function for NVH optimization

A general task preceding each optimization is the formulation of a suitable objective function $\Phi(\mathbf{x})$. The envisioned goal of the optimization scheme is the reduction of noise perceived by passengers. The sound pressure in the vehicle is denoted as $\mathbf{p}_3^B$ in this thesis. The following quote from [187, chapter 1] sums up the goal of this optimization:

"[...] In acoustics, the sound pressure is typically the leading quantity of interest, mainly because the human ear is sensitive to sound pressure. Hence, calculations or measurements of sound pressure yield directly the input quantity of the human hearing system. [...]".

Ideally, the sound pressure spectrum in the driver's cabin would be simulated in each evaluation of a new design $\mathbf{x}$ (as it was done in chapter 11). The physical sound pressure $\mathbf{p}_3^B$, being the input to the human hearing system, should then be subjected to some form of 'transfer function' that accounts for the human perceived annoyance. There have been promising advances in the field of psycho-acoustics to study these dependencies [42]. A simpler construction of an objective function would subject the sound pressure $\mathbf{p}_3^B$ to e. g. an A-weighting [38] to account at least for the frequency-dependent human perception of sound. An objective function could thus be defined as:

$$\Phi(\mathbf{x}) = \int_{\omega_{min}}^{\omega_{max}} ||\mathbf{p}_3^B(\omega, \mathbf{x})\, R_A(\omega)||\, d\omega \qquad \text{with,} \tag{12.2}$$

$$\mathbf{p}_3^B(\omega, \mathbf{x}) = \mathbf{Y}_{32}^{AB}(\omega, \mathbf{x})\, \mathbf{f}_2^{bl}(\omega), \tag{12.3}$$

where $R_A(\omega)$ denotes the frequency dependent A-weighting filter. The filter's frequency dependence is the reason why ω is explicitly denoted for all quantities above. The transfer path from the source to the receiver $\mathbf{Y}_{32}^{AB}(\omega, \mathbf{x})$, and thus also the sound pressure $\mathbf{p}_3^B(\omega, \mathbf{x})$, depend on the design variables $\mathbf{x}$. Note that $\mathbf{p}_3^B(\omega, \mathbf{x})$ is a vector describing the sound pressure at multiple positions in the drivers cabin. Hence, a norm of the vector is used in equation (12.2) to end up with a scalar objective function $\Phi(\mathbf{x})$. Considering multiple sound pressures in $\mathbf{p}_3^B(\omega, \mathbf{x})$ is advisable, since otherwise the optimization might find a design that is only "quiet" at one specific position in the receiver [102, section 2.4]. E.g. by altering the design such, that many of the acoustic modes have a node at the microphone position.
Unfortunately, for the application example in this chapter, it was only possible to simulate $\mathbf{u}_3^B(\omega, \mathbf{x})$, i. e. displacements or its time derivatives on the receiver, since the noise transfer function to microphones inside the driver's cabin was unknown. Therefore, a short overview

of literature on NVH optimization based on purely structural vibrations shall be given. Subsequently the reasoning for the objective function chosen in this chapter is outlined.

Objective functions for structural acoustic optimization in literature

When consulting the existing literature on *structural* acoustic optimization, most authors try to minimize the level of the surface *velocities*, which will be denoted as $\mathbf{v}_3^B(\omega)$ in the following. In [19], various optimizations are performed, where the quantity to be minimized (or bounded in a constraint), is called the 'mean level of structure-borne sound' (MLS). Essentially, the MLS is related to the average squared value of all computed velocities normal to the vibrating surface, called v_{rms}^2 in [19]:

$$v_{rms}^2(\omega) = \frac{1}{m_i} \sum_{i=1}^{m_i} ||\dot{\mathbf{u}}_i(\omega) \cdot \mathbf{n}_i||^2,$$ (12.4)

where the surface velocity vectors $\dot{\mathbf{u}}_i(\omega)$ are a result of a prescribed harmonic force, and $\mathbf{n}_i$ denotes the surface normal vector at the respective point. The number of points for which the velocity is computed is denoted as m_i. This quantity is then integrated over the whole frequency range (without frequency dependent weighting) to yield the MLS in decibel[2]:

$$MLS = 10 \, log \left(\int_{\omega_{min}}^{\omega_{max}} v_{rms}^2(\omega) \, d\omega \right).$$ (12.5)

Also in [142] *"[...] the mean square velocity of the plate is used as an optimization criterion [...]"*. Jog [74] claims, that the mechanical power P_{mech} that enters a passive system from the source correlates to a high extent with the sound power P_{rad} radiated by the structure (which is also found by [84, 179]). The mechanical power entering the system would be:

$$P_{mech} = \frac{1}{2} Re \left(\int_{\omega_{min}}^{\omega_{max}} \boldsymbol{\lambda}(\omega)^* \, \dot{\mathbf{u}}_2^B(\omega) \, d\omega \right) = \frac{1}{2} Re \left(\int_{\omega_{min}}^{\omega_{max}} (\boldsymbol{\lambda}(\omega))^* \, \mathbf{Y}_{22}^B(\omega) \boldsymbol{\lambda}(\omega) \, d\omega \right),$$ (12.6)

where $\dot{\mathbf{u}}_2^B(\omega)$ is the velocity at the interface DoF between source and receiver. $\mathbf{Y}_{22}^B(\omega)$ is the driving point FRF matrix on the interface between source and receiver and $\boldsymbol{\lambda}$ are the interface forces acting on the receiver. The effective power is computed by taking only the real part $Re()$ of the quantity, and $(\star)^*$ denotes the complex conjugate of a vector. The mechanical power P_{mech} entering the system is either dissipated by damping in the structure or radiated to the surrounding air.
The radiated sound power of a structure can be computed by:

$$P_{rad} = \frac{1}{2} Re \left(\int_{\omega_{min}}^{\omega_{max}} \int_S p(\omega)^* \, \mathbf{n} \cdot \dot{\mathbf{u}}(\omega) \, dS \, d\omega \right),$$ (12.7)

where S is the radiating surface, $p(\omega)$ the sound pressure, $\mathbf{n} \cdot \dot{\mathbf{u}}(\omega)$ the scalar product of surface normal and velocity and dS is an infinitesimal part of the surface, see figure 12.2. As already mentioned, [74] shows that for a few numerical examples P_{mech} correlates to a high extent with P_{rad}. It is proposed that, for minimizing P_{rad}, one can also minimize P_{mech} with similar success. Thereby, one can save the additional computational effort of solving the coupled sound field equations, needed for computing $p(\omega)$ in equation (12.7). This is related to the general challenge of a purely structural acoustic optimization, namely that the sound pressure $p(\omega)$ is unknown. In Marburg's review on structural acoustic optimization [102], he

---

[2]This is a simplified version of the exact definition given in [19]. However, it differs only by constant terms, which would not influence the solution found by the optimization algorithm.
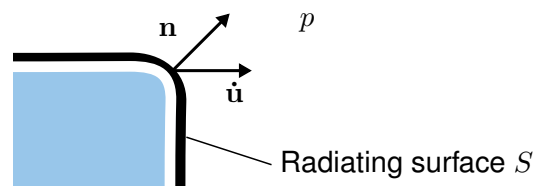
Figure 12.2: Radiating surface S with surface normal $\mathbf{n}$, surface velocity $\dot{\mathbf{u}}$ and sound pressure field p.

states that for the objective function:

"[...] Often, the average sound pressure at one or a few points in a frequency interval accounts for the objective function for interior problems, whereas the average sound power is mostly used for external problems. [...]"

For the case of an optimization purely based on structural quantities, Marburg [102] states that one is often minimizing the average squared particle velocity on the structural surface since this gives an estimate of the radiated sound power. So, implicitly, though often not stated in the literature, the choice of surface velocity as the minimized quantity relates to the fact that the radiated sound power P_{rad} shall be minimized. In [84], a more elaborate discussion and a comparison of quantities that relate purely structural quantities to the radiated sound power is given.

Objective function for present study

However, the goal for this optimization is not to minimize the sound power radiated by the structure, but rather to minimize the noise perceived by the passengers. The sound power may not be the right quantity to choose as an objective function for this purpose. As a practical example one could think about the electrical power needed by a subwoofer to create a certain human perceived loudness in the lower frequency region. Then compare that to the much lower electrical power needed by a high-pitch tweeter to create the same human perceived loudness or annoyance. For the objective function used here, the boundary conditions imposed by a vibrating structure to the pressure field in the surrounding air were taken into account. Since the sound pressure is implicitly the quantity of interest, it was tried to find the structural quantity that is most likely to be a frequency unbiased proxy for sound pressure. Following the reasoning in section 9.4, it was chosen to assume a constant magnitude transfer function for sound pressure over acceleration, as it would be the case in a free field (see e. g. the transfer functions in figure 9.5). Since ideally the A-weighted sound pressure like in equation (12.2) would be minimized, it was chosen to rather minimize the acceleration levels on the structure[3]. Therefore, the chosen objective function is:

$$\Phi(\mathbf{x}) = \int_0^{\omega_{max}} ||\ddot{\mathbf{u}}_3^B(\omega, \mathbf{x})\, R_A(\omega)||\, d\omega, \tag{12.8}$$

where $\mathbf{x}$ is the current design vector, and the sub- and superscripts on $\ddot{\mathbf{u}}_3^B$ refer to the same structure and points as before in $\mathbf{u}_3^B$ (see e.g. figure 12.1).

---

[3]Note that in a whole vehicle application, one could include the transfer function to microphones in the drivers cabin (as was done in chapter 11). This would render this discussion superfluous and avoid any assumptions.

12.2.2 Optimization algorithms

The important question after the definition of an objective function, is how to get from an initial design $\mathbf{x}_0$ to the optimal design $\mathbf{x}^{opt}$. Ideally, this should be done with the least possible amount of objective and constraint function evaluations, since these are typically computationally costly and time consuming. A well written book on numerical optimization algorithms is [128]. A review about optimization applied to structural acoustics can be found in [102]. Here, the basic ideas behind two main classes of optimization algorithms will be discussed. Then their applicability to the problem at hand is checked in section 12.3 with a minimal example.

Gradient based, 'local' optimization

The shape of the objective function $\Phi(\mathbf{x})$ over the entire design space ($\mathbf{x}_{lb} \leq \mathbf{x} \leq \mathbf{x}_{ub}$) is unknown and thus the best, or at least a better solution, $\mathbf{x}^{opt}$ must be found in an iterative manner. Algorithms from the so called class of 'local' optimization algorithms base their iteration strategy on one of the following methods (or a mix of both) [128]:

- **Line Search:** Starting from the current design $\mathbf{x}_i$, a search direction $\mathbf{p}_i$ is determined. One can e.g. compute or approximate the gradient of the objective function with respect to the design variables $\frac{\partial \Phi}{\partial \mathbf{x}}\big|_{\mathbf{x}_i} =: \nabla\Phi$. The direction of 'steepest descent' for the objective function could then be chosen as the search direction, i.e. $\mathbf{p}_i = -\nabla\Phi$. Other potentially more efficient choices for the search direction can be computed with Newton, Quasi-Newton or Conjugate Gradient methods [128]. Often the search direction has to be amended so that the new designs in the direction $\mathbf{p}_i$ do not violate any of the constraints. The problem of the optimization then reduces to finding the scalar step length α:

$$\text{minimize: } \Phi(\mathbf{x}_i + \alpha\mathbf{p}_i). \tag{12.9}$$

  This can e. g. be done by just testing a few discrete values for α and then choosing the α which produces the highest decrease in the objective function value without violating any constraint.

- **Trust region:** Here the objective function is approximated in the vicinity around the current design point $\mathbf{x}_i$ by e.g. a quadratic model of the objective function:

$$\Phi(\mathbf{x}_i + \mathbf{p}_i) \approx \Phi(\mathbf{x}_i) + \nabla\Phi\mathbf{p}_i + \tfrac{1}{2}\mathbf{p}_i^T\mathbf{B}_i\mathbf{p}_i, \qquad \text{with } ||\mathbf{p}_i|| \leq \Delta_i \tag{12.10}$$

  In this context the 'trust region' is defined by the radius Δ_i around the current design point, where the approximation is assumed to be valid. The Hessian matrix (second derivatives) $\nabla^2\Phi$ is approximated with $\mathbf{B}_i$ that is usually obtained from the previous evaluations of the gradient $\nabla\Phi$ with the Broyden-Fletcher–Goldfarb-Shanno (BFGS) formula [128]. This way the excessive effort of directly computing or approximating the Hessian is avoided, while still being able to achieve a fast convergence of the algorithm. There are of course many different methods for approximating the objective function in the trust region.

For example, the Sequential Quadratic Programming (SQP) algorithm computes the search direction from a local quadratic approximation of the objective function and then determines the step size from a line search. The applicability of SQP is checked in the minimal optimization example in section 12.3.
The algorithm iterations are terminated once the algorithm can't find any significant design improvements or has exceeded the maximum number of iterations. Most algorithms for

constrained optimizations base their convergence criterion on the fulfillment of the Karush-Kuhn-Tucker (KKT) conditions, which are mathematically necessary for a local optimum:

$$\nabla \Phi(\mathbf{x}^{opt}) = \sum_{i=1}^{m} \mu_i \nabla g_i(\mathbf{x}^{opt}) + \sum_{j=1}^{\ell} \lambda_j \nabla h_j(\mathbf{x}^{opt}), \tag{12.11}$$

$$g_i(\mathbf{x}^{opt}) \leq 0, \qquad\qquad\qquad \text{for } i = 1, \ldots, m \tag{12.12}$$

$$h_j(\mathbf{x}^{opt}) = 0, \qquad\qquad\qquad \text{for } j = 1, \ldots, \ell \tag{12.13}$$

$$\mu_i \leq 0, \qquad\qquad\qquad \text{for } i = 1, \ldots, m \tag{12.14}$$

$$\mu_i\, g_i(\mathbf{x}^{opt}) = 0, \qquad\qquad\qquad \text{for } i = 1, \ldots, m. \tag{12.15}$$

The first condition of equation (12.11) requires that, at a local optimum $\mathbf{x}^{opt}$, the gradient of the objective function $\nabla \Phi$ can be represented as a linear combination of the equality constraint gradients ∇h_i and the inequality constraint gradients ∇g_i of the 'active' inequality constraints. Loosely formulated, an 'active' inequality constraint is one whose value is zero at the optimum ($g_i(\mathbf{x}^{opt}) = 0$) and that is actually preventing the objective function from being further decreased. The values μ_i and λ_i are the so called Lagrange multipliers necessary for fulfilling the linear combination stated in equation (12.11). In practice, equation (12.11) means that at a local optimum there is no more direction in which the objective function value could be decreased, without violating the constraints, as all directions perpendicular to the gradient $\nabla \Phi$ would keep the objective function value constant. Equations (12.12) and (12.13) just require that the constraints are not violated. Equation (12.14) is taking care of the fact that the gradient of an 'active' inequality constraint ∇g_i (i.e. the direction in which the value of $g_i(\mathbf{x})$ would increase and thus violate the constraint) must be pointing in a direction in which the objective function would decrease. Otherwise the inequality $g_i(\mathbf{x})$ would not be active, since the value of the objective function could be decreased in a direction that is not violating the constraint ($g_i(\mathbf{x})$ would be decreased in that direction). The last equation (12.15) is often called the 'complementary slackness'. It is the decisive factor for determining if the inequality constraint is active, i.e. $g_i = 0$ and thus $\mu_i \neq 0$ so the gradient must be considered in (12.11), or inactive, i.e. $g_i < 0$ and thus $\mu_i = 0$ so the gradient of the inequality constraint is not considered for the linear combination in (12.11). A good explanation and visualization of these concepts can be found in a video lecture of the MIT open course ware [8].

The KKT conditions are necessary conditions for a local optimum of the optimization function, i.e. there is no direction in the vicinity of the found solution $\mathbf{x}^{opt}$ which could improve the objective function any further without violating the constraints. Thus, the found $\mathbf{x}^{opt}$ is at least a local optimum. Gradient-based optimization schemes are very efficiently converging to such local optima. However, there might still be better designs, which cannot be found with a gradient-based approach. The applicability of these algorithms thus depends very much on the shape of the specific objective function. If many local optima exist and the engineer is unable to identify a starting point $\mathbf{x}_0$ that is close to a global optimum, heuristic optimization schemes might yield better results.

Heuristic, 'global' optimization

As mentioned above, gradient based algorithms find a 'local' solution to the optimization problem, assuring that there is no better feasible solution in the proximity of the found optimum. This is however not necessarily the global solution, i.e. the point in the design space with the overall lowest objective function value. In practice it is often already enough to find a design that is better than the initial one. Depending on the case however, significant performance gains of the design might be possible by searching for the overall lowest objective value. As mentioned, this depends very much on the shape of the objective function over

the design space, which will be checked for the problem at hand in section 12.3. If the objective function has a lot of local minima, then chances are that a gradient based optimization scheme will get trapped in a local optimum.

There are many classes of global optimization schemes, which won't be explained in detail here. An overview can be found in [175]. One class of global optimization which will be used in this chapter are genetic algorithms (GA), which try to mimic evolution in nature. They create a large set of initial designs $\mathbf{x}_{1i}$ which can e.g. be random and uniformly distributed over the whole design space. This initial set is called the initial population. The $(\star)_1$ denotes the first generation and $(\star)_i$ is the index for each individual, i.e. each single design vector, in the population. They then calculate the objective function value $\Phi(\mathbf{x}_{1i})$ and the constraint function values for each of the design vectors in the initial population, to determine a fitness value for each individual design. Then, some members of the population are transferred to the 'mating pool', typically the ones with the best fitness value (e.g. lowest objective function value without violating constraints). The members of the next generation are created by recombining the design vector entries from designs in the mating pool. Thereafter, some statistical variation is performed on the values in the design entries (called mutation). The algorithm eventually converges when no more designs can be created that are better then the ones from previous generations.

A practical advantage of this optimization scheme is that it is easy to include integer design variables (e.g. only a discrete choice of different rubber bearings), since they don't need any continuous derivatives of the objective function for finding a search direction. However, they usually need more objective function evaluations and generally converge slower than gradient based optimization schemes.

12.3 Choice of compressor operating conditions & optimization algorithm

In most structural acoustic optimizations the design variables alter the mass and stiffness distribution of the structure. The optimization tries to find their right distributions to minimize the vibration at the receiver points. The minimal example presented here aims at answering the following 2 questions for the optimization of e-compressor NVH:

- What are the right operational conditions of the compressor, for which the blocked forces are computed, and subsequently used to evaluate the resulting vibrations on the receiver? Discrete load conditions will be compared to a continuous runup of the compressor.

- What is the right optimization algorithm for converging to a solution that is not too far from the global optimum? A gradient based SQP algorithm will be compared to a global genetic algorithm.

The minimal example here is intended to answer these questions, and provide a clearer insight than the full example which will be shown in section 12.4. Especially since for the minimal example it is possible to plot the objective function shape over the whole design space, since the objective function evaluations are computationally not that demanding.

Minimal example

The example is the truss frame shown in figure 12.3a (taken from [47, section 5.3.4]). The design vector is composed of two variables $\mathbf{x} = [x_1 \ x_2]$. The first design variable x_1 is
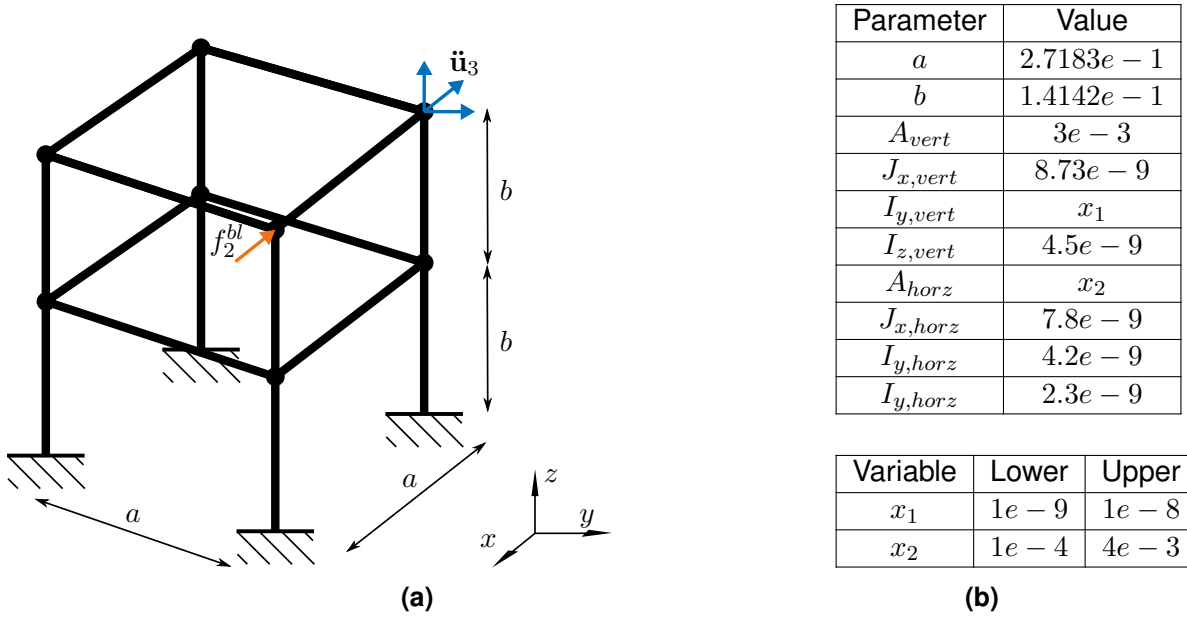
Parameter	Value
a	$2.7183e-1$
b	$1.4142e-1$
A_{vert}	$3e-3$
$J_{x,vert}$	$8.73e-9$
$I_{y,vert}$	x_1
$I_{z,vert}$	$4.5e-9$
A_{horz}	x_2
$J_{x,horz}$	$7.8e-9$
$I_{y,horz}$	$4.2e-9$
$I_{y,horz}$	$2.3e-9$

Variable	Lower	Upper
x_1	$1e-9$	$1e-8$
x_2	$1e-4$	$4e-3$

(a)   **(b)**

Figure 12.3: Minimal Example from [47] the examination of the objective function shape and testing different optimization algorithms. a) Overview of the truss frame example with point of application for the blocked force f_2^{bl} and evaluation of response $\mathbf{u}_3^B$. b) Tables with values of variables and upper and lower bounds for optimization variables. All values in SI units.

the bending stiffness around the global $y-axis$ of all vertical beams, see figure 12.3. The second design variable x_2 is the cross-sectional area of all horizontal beams, which directly scales with their mass. The FEM model of the structure in figure 12.3 is setup in ANSYS Mechanical APDL. The beam sections between each intersect are discretized with 30 beam elements of type *beam 189* [6]. For the material typical values for structural steel are chosen, i.e. a Youngs modlus of $210GPa$, a density of $7800\frac{kg}{m^2}$ and a Poisson ratio of 0.3. The beam element cross-sections are chosen as 'arbitrary' so the parameters like cross sectional area and bending stiffness can be varied independently from each other. As an excitation, a single force entry f_2^{bl} from the 6 forces and moments in the equivalent forces $\mathbf{f}_2^{bl}$ of the compressor (see section 6.3) has been used. It is the translational force in z-direction, see figure 6.2b. This excitation is applied at one point of the structure, see figure 12.3a, and the resulting acceleration $\ddot{\mathbf{u}}_3$ is computed at another point of the structure. The frequency response function $\mathbf{Y}_{32}$ that relates the force input to the accelerations is obtained by computing the first 500 modes of the structure and subsequently synthesizing the FRFs with these modes (frequency range $0-500Hz$, $1Hz$ spectral resolution, see section 2.3.2). A modal damping ratio of 0.1% is assumed. Also the spectrum of the blocked forces has been cropped to $0-500Hz$, to speed up the calculations. For the objective function, first the A-weighted signal power of the acceleration $P_3(\mathbf{x},b)$ is computed by integrating over frequency:

$$P_3(\mathbf{x},b) = \int_0^{\omega_{max}} || \underbrace{\mathbf{Y}_{32}(\mathbf{x},\omega)\, f_2^{bl}(\omega,b)}_{\ddot{\mathbf{u}}_3(\mathbf{x},\omega,b)} \, R_A(\omega)||^2 \, d\omega, \qquad \text{with } b=1,...,N_b; \qquad (12.16)$$

where $f_2^{bl}(\omega,b)$ denotes the blocked force computed for the time block b from the operational runs of the compressor (see section 6.4). N_b is the total number of time blocks. The root mean square over all blocks b is then computed:

$$P_{3,rms}(\mathbf{x}) = \sqrt{\frac{1}{N_b} \sum_{b=1}^{N_b} [P_3(\mathbf{x}, b)]^2}. \tag{12.17}$$

This way the highest responses $P_3(\mathbf{x}, b)$ from operational conditions in certain time blocks b, are penalized more in the optimization. The final objective function is then defined as the level of $P_{3,rms}(\mathbf{x})$ given in decibels:

$$\Phi(\mathbf{x}) = 10 \, log_{10} \left(\frac{P_3(\mathbf{x})}{a_0^2} \right), \qquad \text{with } a_0 = 10^{-6} \left[\frac{m}{s^2} \right], \tag{12.18}$$

where a_0 is the typical reference value used for computing acceleration levels in decibel.

Operational compressor conditions for evaluation of objective function

For the example, it is possible to visualize the shape of the objective function over the two design variables (bending stiffness x_1 and mass x_2). Originally, it was intended to use 10 discrete operating conditions of the compressor for computing the blocked forces. The operational speeds were $10\%, 20\%, ..., 100\%$ of the compressor's maximum speed. 10 time blocks were taken from each measurement of the 10 operating conditions. So in total $N_b = 100$ time blocks were used in each evaluation of the objective function. The resulting objective function shape is shown in figure 12.4a. It can be seen that the objective function exhibits large elevations that are on straight lines in the x_1-x_2 plane. This effect can be explained by the input spectrum of the excitation force $f_2^{bl}(\omega, b)$ and the design variables. Each blocked force $f_2^{bl}(\omega, b)$ was obtained for an integer multiple of the speed 10%. Thus, the compressors order frequencies, at which the blocked forces are particularly high, are exciting always the same frequencies, with no excitation at the frequencies between. In figure 12.5, the blocked force in z direction which was computed for compressor speeds that are multiples of each other are shown to illustrate this matter. If an eigenfrequency of the truss frame structure coincides with one of these strongly excited frequencies, the objective function value will increase dramatically. These increases are on straight lines in the x_1-x_2 plane in figure 12.4a, since x_1 is the bending stiffness of the vertical beams and x_2 is the mass of the horizontal beams. A straight line in the x_1-x_2 plane describes a constant ratio of stiffness and mass, which means that some modes stay at a fixed frequency.

This objective function behavior is unwanted, since in practice the NVH engineer would want to design a structure that isolates the force input for all possible compressor operating conditions. The time blocks for computing the forces can also be taken from a runup measurement of the compressor. For the objective function shown in figure 12.4b, the vibration signal for computing the blocked forces was recorded during a runup from 10% to 100% speed in 60 seconds. Time blocks of 1 second length each, with an overlap of half a second have been used, so that $N_b = 120$. This way, the blocked forces are better representing the compressor excitation in the whole operating range. It can be seen from the comparison in figure 12.4 that the objective function is somewhat smoothed by this definition, which might also help the applicability of gradient based algorithms. The objective function used for the rest of the chapter is computed from the overlapping time blocks taken from this runup measurement.

Choice of optimization algorithm

As discussed in section 12.2.2, optimization algorithms can generally be classified into 'local' or 'global' algorithms. On the minimal example sequential quadratic programming (SQP) and a genetic algorithm (GA) shall be tested as representatives of both classes. In figure 12.6,
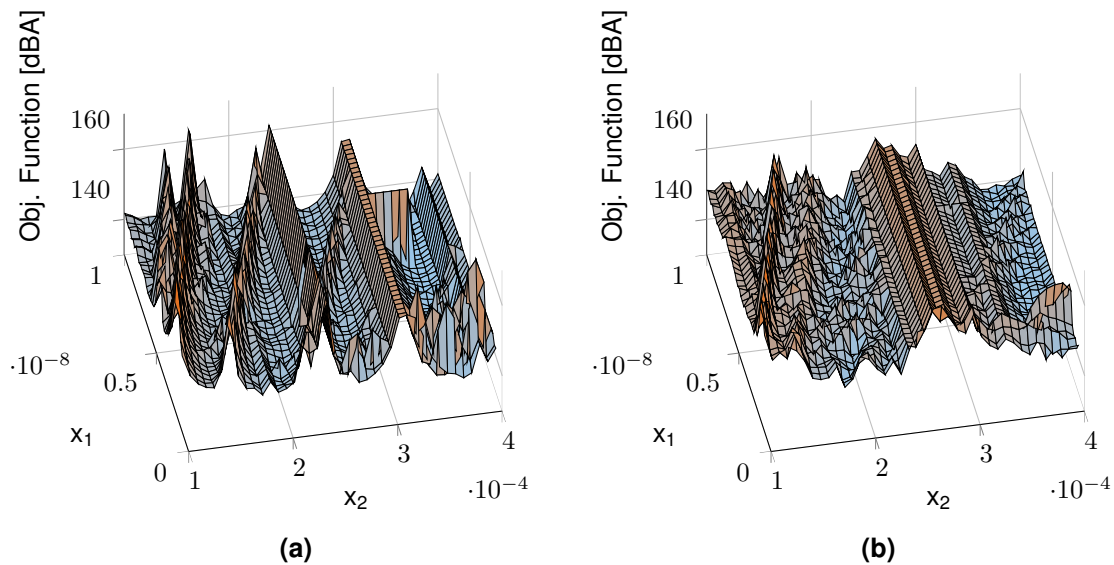
Figure 12.4: Visualization of objective function shape for different choices of compressor operational conditions used for computing the blocked force f_2^{bl}. (a) blocked forces from discrete compressor speeds. (b) blocked forces from overlapping timeblocks taken from a compressor runup.
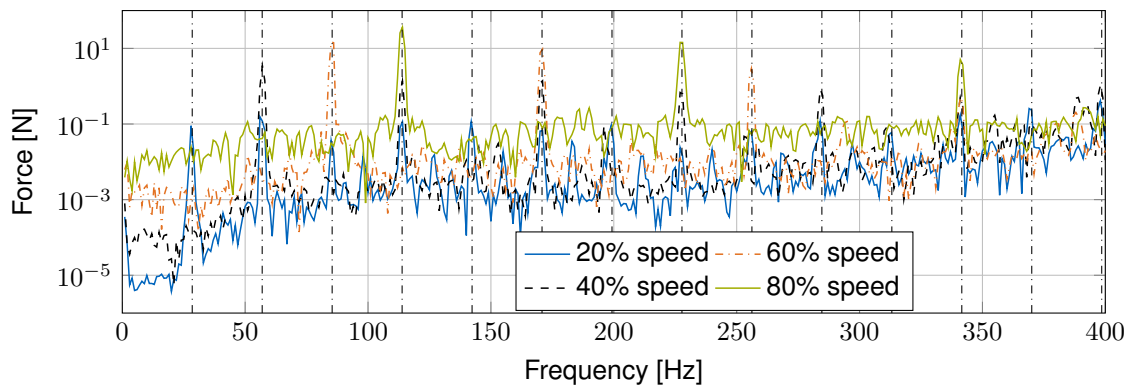

Figure 12.5: Excitation spectrum for discrete frequencies given in percent of maximum compressor speed. Vertical lines indicate multiples of the first compressor order at 20% speed. The plotted spectrum belongs to the z-direction of the translational forces at the front connection of the compressor.
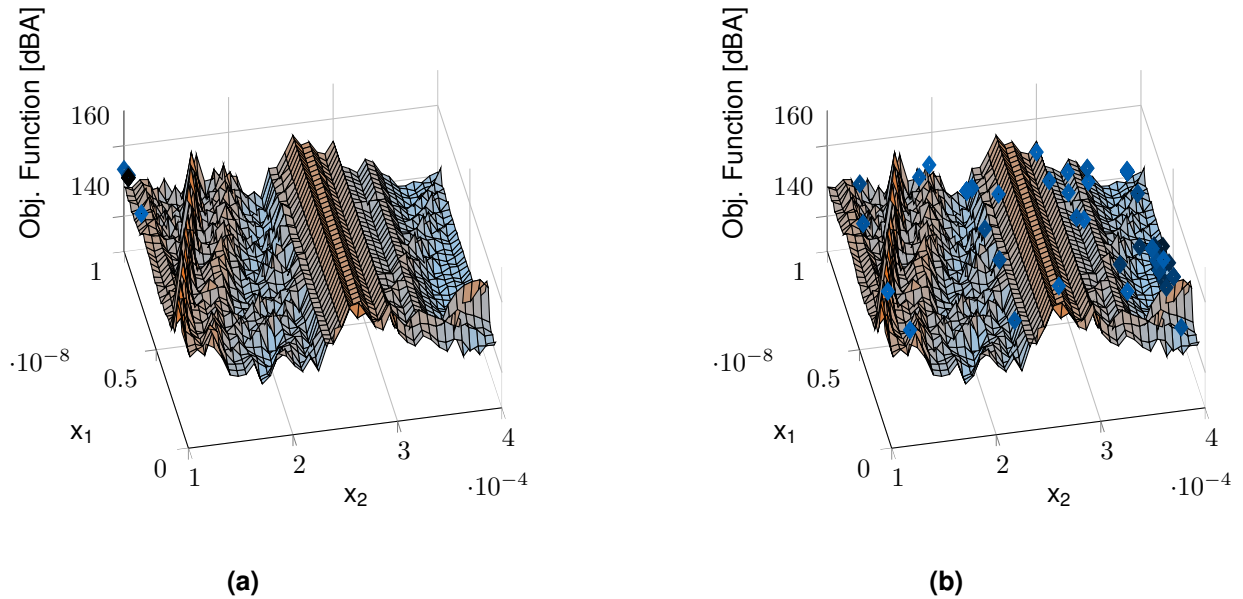
Figure 12.6: Performance comparison for different optimization algorithms. All design points evaluated by the algorithms are shown as diamonds in the plot. The color of the diamonds slowly changes from blue for the first evaluated design, to black for the last evaluated design point. All points are artificially lifted by $5dBA$ in the plot, so it is easier to see them. a) sequential quadratic programming (SQP). b) Genetic Algorithm (GA).

their performance for finding an optimum are compared. The SQP algorithm stops prematurely after evaluating only 9 points in the design space at an objective function value of $\Phi(\mathbf{x}_{opt}) = 145.7$ [dBA]. The GA algorithm evaluates 1600 design points (though convergence was reached after ca. 400 evaluations) with an objective function value of $\Phi(\mathbf{x}_{opt}) = 137.9$ [dBA]. It seems that the non-convex shape of the objective function makes it necessary to use 'global' optimization algorithms for the application case. In figure 12.7, the starting design of SQP and the found optima of SQP and GA are compared over the whole runup. The objective function was computed for each time block b separately. So one can plot its evolution over the runup for the comparison in figure 12.7. One can observe that the RMS over the time blocks in equation (12.17) is penalizing time blocks with a particularly high response. The solution found by the SQP algorithm has mostly reduced the large peak of the initial design at around 42 seconds. The solution of the GA is generally lower and is more effectively preventing outliers of high cost function values over the compressor runup. Under figure 12.7, hearing comparisons of the different designs response to the runup forces are provided (SQP starting point, SQP optimum and GA optimum). The sound files are a playback of one 'channel' or rather FE node direction of the acceleration $\ddot{\mathbf{u}}_3$ in the response point, namely the x-direction in figure 12.3a. One can hear the slowly increasing speed of the compressor, with some constant frequency tones in the background, which are related to the resonances of the system which are always slightly excited by the compressor forces. If an order frequency of the compressor matches with a resonance frequency of the structure, a large increase in loudness is audible.

12.4 Application to e-compressor NVH optimization

After examining the optimization algorithms performance on the defined objective function, the method shall be applied to the actual example where the goal is to find a better support

Figure 12.7: Comparison of the objective function value over the compressor runup. Objective function values were computed according to equations (12.16) - (12.18) for each timeblock seperately, i.e. with $N_b = 1$. Hearing comparisons are for the signal in the x-channel of the response point in figure 12.3a. (a)-(c): 0-20sec, 20-40sec and 40-60sec of the SQP starting point design. (d)-(f): 0-20sec, 20-40sec and 40-60sec of the SQP optimum design. (g)-(i): 0-20sec, 20-40sec and 40-60sec of the GA optimum design.

for the climate compressor. The modular assembly of different subcomponents is explained in section 12.4.1. This assembly via FBS will be executed in each optimization run. A validation of the so obtained assembled FRF matrix with a reference measurement is given. Thereafter, the design variables and the objective function for the optimization are defined in section 12.4.2. The program and data flow that executes during each run of the optimization is also briefly explained. Three designs of interest are then compared with reference measurements to assess the quality and reliability of the optimization results in section 12.4.3.

12.4.1 Dynamic model

The assembly which shall be optimized is shown in figure 12.8. The compressor is mounted under a carrier plate, which also holds a large mass on top of it. This plate is isolated with rubber bearings in all four corners against a final receiver which has the shape of four support arms. In this section, the models of the different subcomponents are explained. A schematic depiction of the compressor suspension was already shown in figure 12.1, where the small symbols underneath the structures indicate the modeling approach used for each subcomponent. The compressor is modeled as rigid body, indicated by the symbol underneath in figure 12.1. The carrier plate is modeled as a FEM Model, whereas the rubber bearing model is obtained from experimental tests to save the effort material modeling. The receiver legs are modeled with the FEM.
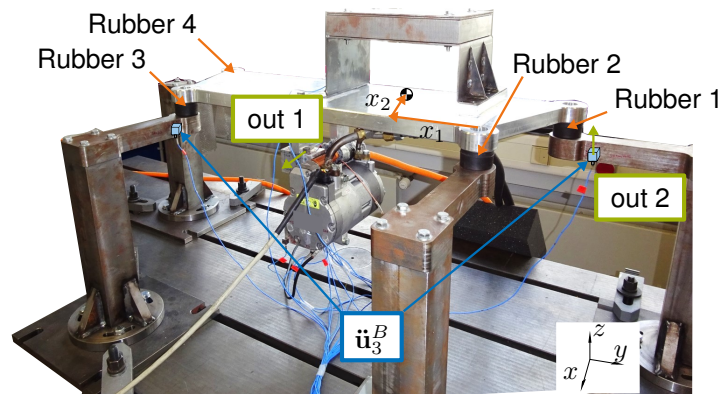
Figure 12.8: Physical testrig with mass and rubber bearings. Outputs for validation FRF measurements are indicated as 'out 1' and 'out 2'. The six sensor channels used in the objective function are indicated as $\ddot{\mathbf{u}}_3^B$.

Compressor: dynamic model and excitation

The compressor is modeled as rigid body, as already explained in section 11.1.1. The mass and rotational inertia are taken from its CAD model. The excitations that the compressor applies to the whole assembly are described by means of 6 blocked forces, like it was described in section 6.3.

Model of carrier plate and mass

The compressor is connected to a carrier plate that is also carrying a mass with a flexible metal sheet support. The model of compressor, carrier plate and mass is directly setup in ANSYS Workbench, as can be seen in figure 12.9a. The compressor's rigid body properties are concentrated in its center of gravity, which is shown as a grey point in figure 12.9a. It is rigidly coupled to the three bolt holes which the compressor is actually connected to. The bolt holes for connecting the compressor sit in two lengthy adapters. Each of these adapters are screwed with two bolts into the carrier plate. The contact area between the adapters and the plate is modeled as a rigid surface contact in ANSYS (multi point constraint (MPC) contact). Also the contact areas between the mass and the plate are modeled as rigid contact.

The degrees of freedom where the FRFs shall be synthesized are the 6 DoF of the rigid compressor, which are needed for applying the blocked forces, and the 4 connection points of the plate with 6 DoF each. The resulting FRF is thus a frequency dependent 30×30 matrix. The four connection points are modeled with 'remote points' using the RBE3 formulation to the neighboring nodes [6]. See figure 12.9b for a depiction of one of these 6 DoF remote points. ANSYS Workbench is then used to compute the first 100 modes of this model. The eigenfrequencies vary with the position of the mass (which will be part of the design variables). Typically the first flexible eigenfrequency is around $75 Hz$ and the 100th frequency around $6500 Hz$. The computed modes are then used to synthesize the 30×30 FRF matrix in the frequency range $0 - 2000 Hz$ with a frequency resolution of $1 Hz$.

Rubber bearing models

The carrier plate is isolated from the receiver in either of the four corners with a rubber bearing. The dynamic models of the rubber bearings are obtained with the experimental identification method explained in chapter 4, which yields a 12×12 frequency dependent FRF matrix for each rubber element. The choice of rubber bearings for this example was
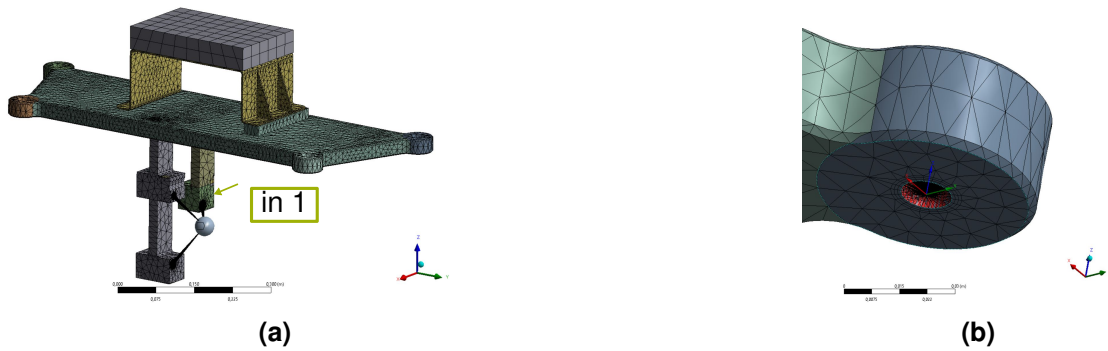
Figure 12.9: Overview of FEM modeling. (a) FEM Model of Carrier plate with mass and compressor. Hammer input point for validation measurements is indicated as 'in 1' (b) Remote point in one coupling point for 6 DoF model used in the FBS coupling of each connection.
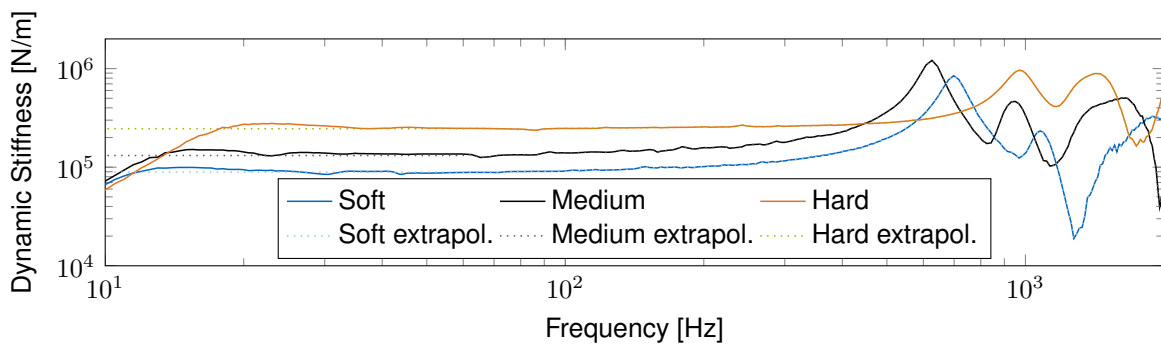

Figure 12.10: Comparison of axial transfer stiffness of all rubber bearings.

limited to three discrete rubber elements. In the following they will simply be called 'soft', 'medium', and 'hard' rubber bearings. Their static axial stiffness (the vertical direction in figure 4.1c) was specified by the manufacturer with $94 \cdot 10^3 \left[\frac{N}{m}\right]$, $155 \cdot 10^3 \left[\frac{N}{m}\right]$ and $255 \cdot 10^3 \left[\frac{N}{m}\right]$ respectively. The dynamic stiffness of the three rubber bearings in the axial direction which were identified with this method are shown in figure 12.10. It can be seen that in the lower frequency region the rubber bearings have a dynamic stiffness which is similar to the static stiffness specified by the manufacturer. In the very low frequency region (below approximately $30 Hz$), their stiffnesses are dropping, which is unphysical and merely a problem of low frequency rigid body resonances of the whole assembly (two crosses with rubber bearing in between) in the rubber bands which they were hung up with (see figure 4.1a). These rigid body resonances were all well below 10Hz. From reference measurements with a hydraulic testing machine (see figure 4.4), it was known that the dynamic stiffness of the rubber bearings is constant over frequency for this low frequency region. A remedy to this issue is introduced by extrapolating a constant stiffness value, computed as the average stiffness in the range $60 - 80 Hz$, down to the lower frequencies. The effect in the axial direction is shown as dotted lines in figure 12.10, but the procedure is applied to all entries of the 12×12 dynamic stiffness matrix. This matrix can then be converted back to an accelerance matrix which is suited for FBS with the other components. It can be seen in figure 12.10 that for the higher frequencies it is desirable to have these accurate frequency dependent models of the bearings, since there are large stiffness increases and decreases with frequency. These are mostly a result of (anti-) resonances in the rubber itself. This effect is well known [1, 54], the earliest publication on the topic we found being of Harris in 1952 [66].
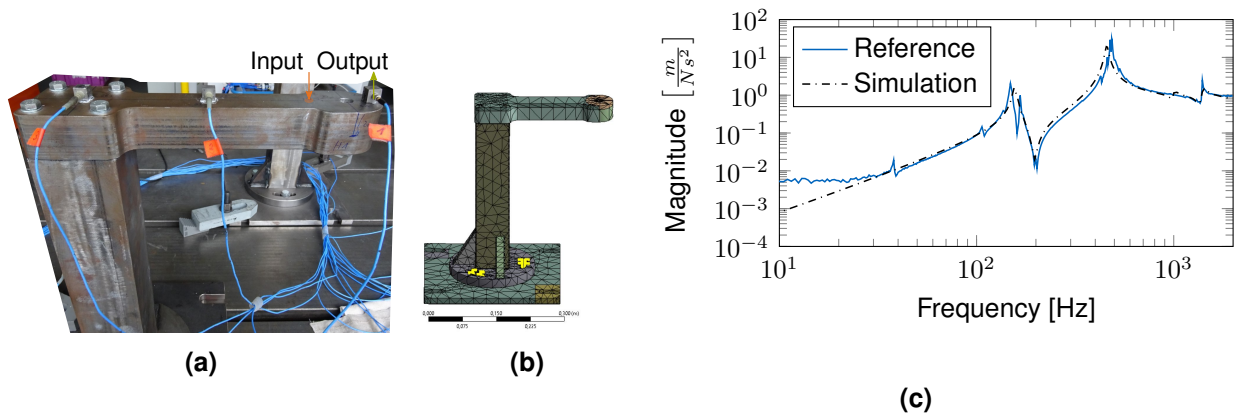
Figure 12.11: Depiction and validation of FEM model of the support arms, (a) reference FRF measurement on one arm, (b) FEM model of the arm, (c) Comparison of measured and simulated FRF for the force input and acceleration output shown in figure 12.11a.

Model of carrier arms

The last substructure of the final assembly are the carrier arms. These are the receivers on which the vibrations caused by the compressor shall be minimized. They are also modeled with the FEM, as can be seen in figure 12.11b. A single, decoupled arm equiped with sensors for model updating is shown in figure 12.11a, where also the position of a hammer impact and an output of one acceleration sensor is indicated. For the FRF of this input and output a comparison between measurement and the FEM FRF synthesis is shown in figure 12.11c. The arms are clamped with brackets to the testbed, as can be seen in figure 12.11a. For obtaining the right eigenfrequencies, it was not sufficient to model the contact with the testbed as a rigid support, but as a flexible support with a certain foundation stiffness. As can be seen in figure 12.11c, the mode frequencies are similar in the FEM model and the validation measurement. The modes at approx. $180Hz$ and $450Hz$ are both variants of forward rocking modes of the arm, which are properly excited by the impact location shown in figure 12.11a. However, it seems like there are multiple modes around these frequencies. An evaluation of the operational deflection shapes of the reference measurements show that the excitation on the arm, shown in figure 12.11a, is also transfered via the testbed to the other arms (there was one sensor still on another arm, which made this observation possible). It is assumed that the modes of all arms are approximately but not exactly at the same frequencies. Due to a cross coupling over the not perfectly rigid testbed and the arms slightly shifted frequencies, it seems like there are multiple smaller peaks overlayed with the main peak of the FEM model. The FEM model however did not model this cross coupling between the arms. If it was possible to perform the measurements again, the author would probably take an experimental model of the arms directly, which would then include this cross coupling effect. However, the model is considered accurate enough for obtaining meaningfull predictions. The mode at around $40Hz$ which can be seen in the reference in figure 12.11c, is in a direction which should not be excited by the hammer impact, but due to slight imperfections in the experiment it shows up in the reference measurement.

Validation of FBS assembly model

The FRF matrices of all subcomponents are coupled via FBS to each other. Some of the possible design choices (the design variables are explained in the next section) were not only virtually simulated with the FBS approach, but also assembled physically on the testrig for validation measurements. Part of the validation measurements was a hammer impact

FRF measurement, where the assembly was impacted in the global x-direction on the front connection of the compressor, which can be seen in figure 12.9a as 'in 1'. The FRFs to two output channels of sensors, indicated as 'out 1' and 'out 2' in figure 12.8, are compared for the design also shown in figure 12.8. These FRFs are shown in figure 12.12a and figure 12.12b respectively. Note, that in the simulated FBS Model all DoF are in the form of virtual point degrees of freedom. Hence, a direct comparison with a measured reference FRF of a hammer input and sensor channel output is not possible. For the comparisons shown in figure 12.12, the FRF from the FBS assembly was transformed back to hammer impacts and sensor outputs with an inverse virtual point transformation:

$$\mathbf{Y}_{uf} = \mathbf{R}_u \mathbf{Y}_{qm} \mathbf{R}_f^T, \tag{12.19}$$

where $\mathbf{Y}_{qm}$ represents the FBS result in terms of virtual point DoF. $\mathbf{R}_u$ is the IDM matrix containing the geometric information about the relation between virtual point motions and the resulting sensor motion at specific positions (see section 3.3). Similarly $\mathbf{R}_f$ is the IDM matrix containing the information about the virtual point forces and moments that are caused by a specific hammer impact.

Figure 12.12 shows a comparison for using the plain decoupling models of the rubber bearings (continuous lines in figure 12.10) and the rubber bearing models with the extrapolated stiffnesses in the lower frequency region (dotted lines in figure 12.10) in the FBS model. It can be seen in figure 12.12a that the extrapolated rubber models perform significantly better for predicting the lower frequency modes. The mode shapes of these resonances show the whole compressor, carrier plate and mass moving like a rigid unit on the flexible support of the rubber bearings. The first resonance in figure 12.12a is found at 10.5 Hz in the experimental validation and 9 Hz in the FBS model with the extrapolated rubber stiffness. The second resonance is at 19 Hz in the experimental validation and 18 Hz in the FBS model with the extrapolated rubber stiffness. One could argue that these modes are not important from an acoustic point of view, since they are below the audible range that starts at approximately 20 Hz. Nevertheless, it is valuable to be able to predict these resonances for other issues (e.g. rattling or fatigue of compoments), so the extrapolated rubber models were used for all predictions.

In figure 12.12a, it can be seen that the magnitude of the FRF is overall predicted with reasonable accuracy by the FBS modeling, despite the challenge of modelling all connections between individual parts (multiple screw connections and surface contacts. The mass on top of the plate was actually glued on with dental cement). The comparison in figure 12.12b for the output channel shows a more challenging modeling task. First of all, the coherence of the measurement validation, shown underneath the magnitude plot, is not as good as for the output on the compressor carrier. This is due to a poorer signal to noise ratio, since the input energy is isolated with the rubber bearings from the receiver. From experience the noise floor for experimental FRF measurements with the equipment used is around a magnitude between 10^{-2} and $10^{-3} \left[\frac{m}{Ns^2} \right]$, as can be seen in the coherence in figure 12.12b as well. In these regions the FBS model is believed to be even more accurate than the reference model (see e.g. the lower frequency region in figure 12.12b where it is known that the accelerance of a system without rigid body modes has to approach zero for lower frequencies). The same can be seen at the antiresonance at around 200 Hz that is shown by the FBS model but cannot be measured by the measurement equipment due to the noise floor. The mode around 160 Hz which is showing as two separate peaks in the experimental validation, but as only one peak in the FBS model, is related to the cross coupling of the arms over the testbed, as was explained in section 12.4.1. However, the FBS model seems to have problems predicting the FRF in the higher frequency region above 1000 Hz. In the experimental validation there are large peaks showing, which are not predicted by the FBS
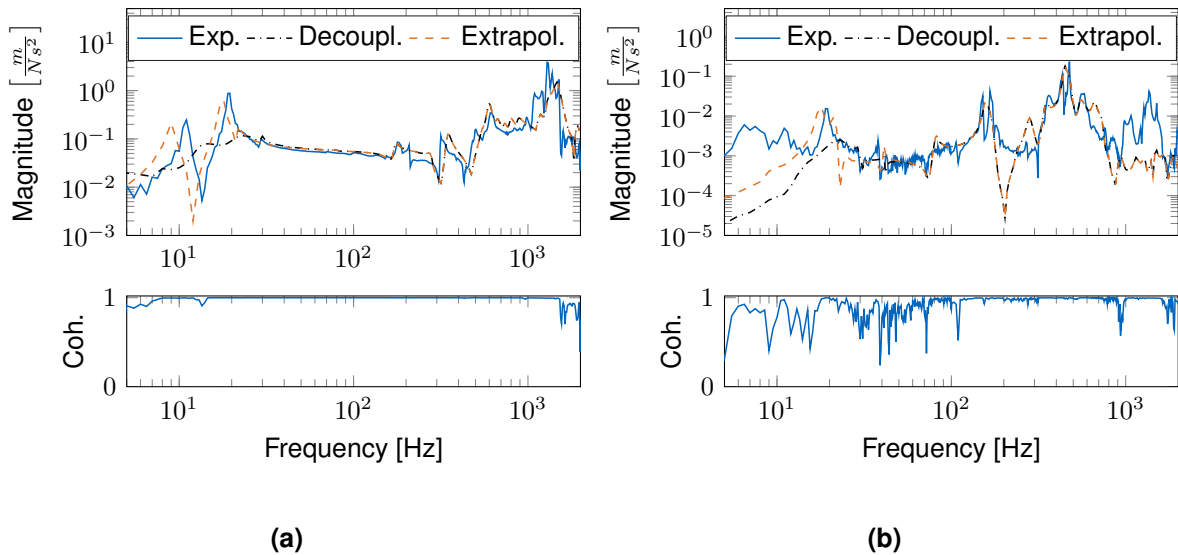
Figure 12.12: Validation: dynamic substructuring models with normal decoupling rubber models ('Decoupl.') and extrapolation ('Extrapol.'), see figure 12.10 for the lower frequencies, versus Reference FRF measurement ('Exp.'). Input as can be seen in figure 12.9a as 'in 1'. (a) Output channel indicated as 'out 1' in figure 12.8. (b) Output channel indicated as 'out 2' in figure 12.8.

model. It is believed that this issue is related to the FEM model of the arms. As already mentioned in section 12.4.1, this subcomponent model is where the author would either put additional modeling effort in, or use an experimental model, if time had permitted to do so.

12.4.2 Optimization problem setup

After explaining the assembly of the system model with FBS, this section proceeds to the actual optimization problem. The design vector $\mathbf{x}$ is composed of six entries $x_1, ..., x_6$, which describe the following parameters:

- x_1: y axis distance of the mass on the plate from the edge point as shown in figure 12.8 in $[mm]$.

- x_2: x axis distance of the mass on the plate from the edge point as shown in figure 12.8 in $[mm]$.

- x_3: Discrete choice of rubber bearing indicated as Rubber 1 in figure 12.8.

- x_4: Discrete choice of rubber bearing indicated as Rubber 2 in figure 12.8.

- x_5: Discrete choice of rubber bearing indicated as Rubber 3 in figure 12.8.

- x_6: Discrete choice of rubber bearing indicated as Rubber 4 in figure 12.8.

The position of the mass on top of the plate is constrained by upper and lower bounds to the feasible space. The choice of rubber bearings for each connection point is limited to four discrete choices:

Design vector $\mathbf{x}$	Objective Fcn. Prediction [dBA]	Objective Fcn. Validation [dBA]
$\mathbf{x} = [54, 157, 4, 4, 4, 4]$	139.8	135.9
$\mathbf{x} = [67, 23, 3, 3, 3, 3]$	114.2	114.1
$\mathbf{x} = [57, 154, 1, 3, 1, 3]$	108.8	111.5

Table 12.1: Comparison of predicted and validated objective function value of different designs.

1. : Soft rubber bearing,

2. : Medium rubber bearing,

3. : Hard rubber bearing,

4. : No rubber bearing, i.e. a rigid coupling.

The objective function is defined similarly to the definition in the minimal example in section 12.3. The receiver acceleration signals $\ddot{\mathbf{u}}_3^B$ which shall be minimized are measured by the two sensors shown in figure 12.8. The predicted vibrations are subjected to an A-weighting and integrated over frequency to sum power levels:

$$P_3(\mathbf{x}, b) = \frac{1}{2} \int_0^{\omega_{max}} || \underbrace{\mathbf{Y}_{32}(\mathbf{x}, \omega) \, \mathbf{f}_2^{bl}(\omega, b)}_{\ddot{u}_3(\mathbf{x}, \omega, b)} \, R_A(\omega)||^2 \, d\omega, \qquad \text{with } b = 1, ..., N_b \quad (12.20)$$

This definition is only different by a factor of $\frac{1}{2}$ from equation (12.16), since we are taking into account two acceleration sensors now. The definition of the final objective function $\Phi(\mathbf{x})$ from $P_3(\mathbf{x}, b)$ in equation (12.20) is then equivalent to equation (12.17) and (12.18).
In each evaluation of the objective function, the program is calling ANSYS for recomputing the FRFs of the compressor, plate, mass assembly with the updated position of the mass. The model is then assembled with the right rubber bearings in each connection point in Matlab. The blocked forces from a 60 second runup are applied to the assembled FRF matrix and the objective function is evaluated. The workflow during one optimization function evaluation is schematically shown in figure 12.13, where Matlab successively fills out ANSYS input file templates with the current design variables, saves them, and executes ANSYS on these input files in batch mode. ANSYS saves the FRFs in separate FRF files which can be read in by Matlab. Note, that initially it was tried to read the full mass and stiffness matrix from ANSYS in each optimization run, via writing them into files in the 'Harwell Boeing Format'. However, this is an ASCII format and the read-in process was way to slow to be suitable for an optimization. Reading in the synthesized FRFs which are only containing the virtual points of interest (as explained in section 12.4.1) was almost two orders of magnitude faster and the amount of data needed is significantly reduced. The optimization algortihm used is a GA, for the reasons explained in section 12.3.

12.4.3 Results and validation measurements

Of course it is not meaningful to investigate all 1600 results evaluated by the optimization algorithm, but rather pick out three interesting designs and actually test them in a physical assembly for comparison. The three designs together with their predicted objective function value and the measured reference is shown in table 12.1.
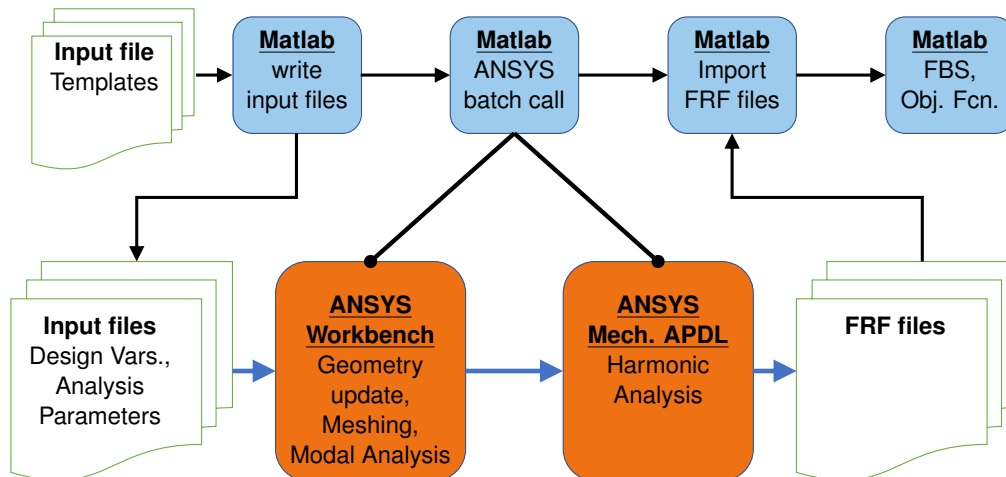
Figure 12.13: Schematic Coupling between ANSYS and Matlab.

The first design is with no rubber bearings ('4' in the entries of the design vector $\mathbf{x}$ for the rubber bearing choice), i.e. a rigid coupling in each connection of the plate with the arms. This design was actually not evaluated by the algorithm (since its objective function value is too high), but it is merely tested for validation purposes. The second design in table 12.1 has the hard rubber bearings in all corners (3 in the last design vector entries). This design is the one acutally shown in figure 12.8. Reference FRF measurements for this design were also already shown in figure 12.12. The third design is the optimal design found by the optimization. Peculiarly enough, it still used the hard rubber bearings for Rubber 2 and Rubber 4 shown in figure 12.8. For Rubber 1 and 3 the soft rubber bearings were choosen. This makes sense when considering the position of the reference sensors that measure $\ddot{\mathbf{u}}_3^B$ for evaluating of the objective function. The arms on which the vibration shall be minimized are choosen to get the soft rubber bearings for minimal force transmission. The arms on which the vibration levels do not enter the objective function are choosen to get he hard rubber bearings then. This is another indicator for how important it is to define the objective function properly. However, it is not a handicap for the method development shown in this chapter.

The position of the mass is more centered over the connection point of the compressor support. This position can be seen in figure 12.9a. From basic NVH development this solution is also easily understood, as it is increasing the 'input impedance' of the source. The compressor under the plate has to work against a heavy mass which keeps the overall vibration levels lower. So the results of the optimization are not surprising, but easy to make sense of.

Figure 12.14 shows a validation FRF measurement on the optimal design (third row in table 12.1), for the two outputs shown in figure 12.8 as before. The same arguments as for the other design in section 12.4.1 could be made. A critical factor is again the higher frequency region for an output on the receiver arms, as can be seen in figure 12.14b.

The evolution of the objective function over time for both designs is shown in figure 12.15. They are also compared to the validation measurement with the rigid coupling, to see the large difference between introducing rubber bearings and rigid coupling. It can be seen that the objective function value of the optimal design stays below 110 dBA for most of the compressor runup (figure 12.15b). Conversely, the non optimal design, with the hard rubber

(a)   **(b)**
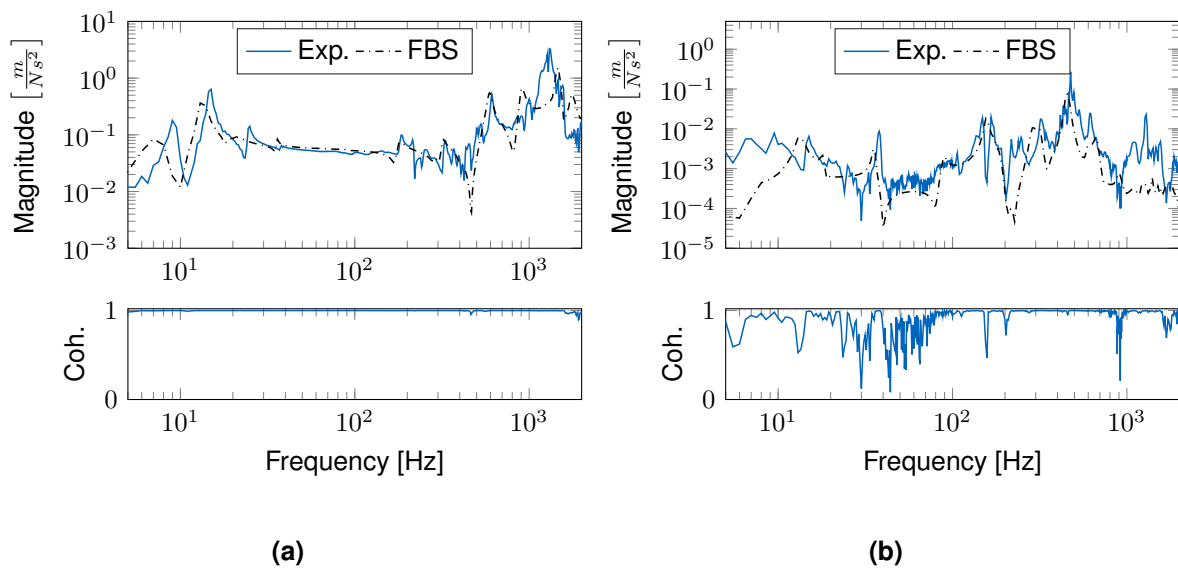
Figure 12.14: Validation: dynamic substructuring model for the third and best performing design in table 12.1. Input as can be seen in figure 12.9a as 'in 1'. (a) Output channel indicated as 'out 1' in figure 12.8. (b) Output channel indicated as 'out 2' in figure 12.8.

(a)   **(b)**

Figure 12.15: Validation of objective function over the complete runup. (a) Design $\mathbf{x} = [67, 23, 3, 3, 3, 3]$ (b) optimal Design $\mathbf{x} = [57, 154, 1, 3, 1, 3]$

Figure 12.16: Comparison of objective function for channel 'out 2' for the validation measurement of the rigid coupling, the FBS & TPA prediction and validation for the optimized Design $\mathbf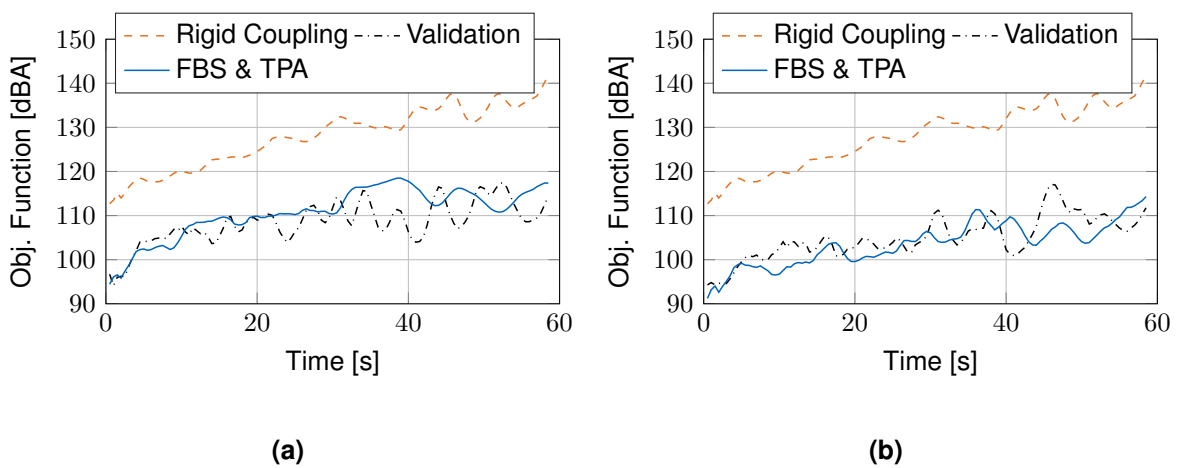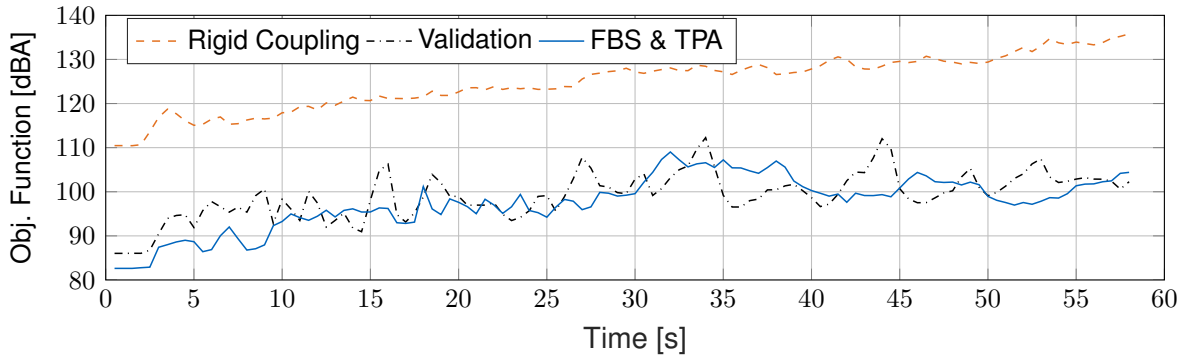{x} = [57, 154, 1, 3, 1, 3]$. Auralization in the table for the rigid coupling, the validation measurement on the optimized design and the FBS & TPA prediction of the optimized design.

bearings in each support, starts to yield an objective function value over 110 dBA after approximately 30 seconds of the runup and then stays above that value for large parts of the following runup (figure 12.15a).

As can be seen in figure 12.15, there are still some deviations between the prediction of the objective function value and the validation measurement. These can be due to multiple reasons. E.g. the compressor is not applying the same excitation forces during each runup. The pressures in the refrigerant fluid on the high and low pressure port (compression and suction port) are not perfectly stable during successive runups, though they are controlled by the load unit that the compressor is connected to. Additionally, the evaluation of the blocked forces was conducted on a different day than the validation measurements, and the refrigerant cycle was disconnected and refilled between the seperate measurements. So slightly different amounts of refrigerant and oil might have been in the system during force identification and validation measurements. Also the FRF prediction in the higher frequency region could be improved, if additional modeling effort is put in e.g. the substructure model of the receiver arms.

Figure 12.16 shows the objective function over time in only the channel 'out 2' as indicated in figure 12.8. The rigid connection validation as well as prediction and validation for the optimal design (third row of table 12.1) is shown in figure 12.16. Taking only one channel facilitates a hearing comparison on the time signal. In the lower part of figure 12.16 hearing examples of this channel are provided. It can be heard that the rigid coupling is, as expected, louder than the design with rubber bearings in the connection. The overall loudness impression seems comparable for the DS prediction and the validation measurement for the opimal design. However, the validation exhibits some larger elevations of the objective function around 27, 34 and 42 seconds which are not heard in the prediction created from FBS & TPA. These elevations of the objective function are caused by a higher pitch noise

around 440Hz and some even higher content at 1.3kHz and are not properly predicted by the simulation. These inaccuracies in the model are related to the lack of accuracy in the FRF prediction for the higher frequency region (see figure 12.14b), which would have to be remedied for further accuracy.

12.5   Conclusion

It was shown that the combination of FBS and blocked forces allows for NVH optimization of complex industrial problems. The vibration on a receiver can be simulated and optimized for minimum NVH. It was found that formulations of objective functions found in literature on structural acoustic optimization typically minimize surface velocities. The choice to minimize accelerations in the objective function was motivated subsequently. However, in a vehicle application, the final receiver would include the noise transfer functions to the sound inside the cabin. The vibration isolation mechanism would then directly be optimized for minimal sound pressure in the cabin, which makes the optimization more effective and render the question about minimizing velocities or accelerations superfluous.

A minimal example was used to derive guidelines on the e-compressor operating conditions, which shall be included in the the objective function evaluation. The operating conditions of the compressor should better be a runup measurement, to cover the whole excitation spectrum properly. The applicability of different optimization algorithms to the problem was tested on the minimal example. It was found that, due to the non-convex nature of the objective function, 'global' optimization algorithms are more likely to find a suitable optimum than 'local' gradient based algorithms. Therefore, it was chosen to use a genetic algorithm (GA) rather than the tested sequential quadratic programming (SQP). The GA could find a solution which was $-7.8dBA$ lower than the one found by SQP. The method was then applied to an e-compressor NVH supsension, where the optimal choice of rubber bearings and position of a mass had to be found. Validation measurements on physically built designs showed good agreement with the predictions from FBS & TPA. Hearing examples confirmed this impression. The presented combination of methods was found capable of comparing the success of different isolation concepts. The overall sound levels can be reasonably predicted (accuracy of about ±4 dBA considering the whole compressor runup). Keeping in mind that, for this virtual iterative testing and improving of isolation concepts, no actual prototype of the system (e.g. a whole car) is needed, the method has proven to be valuable in the early development stage of NVH design engineering.

Hardware
For all measurements a Mueller BBM MKII data acquisition system, PCB Model TLD356A32 acceleration sensors, and a PCB Model 086C03 impact hammer was used. For the example shown in section 12.4, each evaluation of the objective function took around 3 minutes on a regular laptop (i7 core, 16GB RAM, SSD drive). The optimization algorithm was stopped after 1600 evaluations, which took a little longer than 3 days of computing.

Part V

Conclusions and Outlook

Chapter 13

Conclusions and Outlook

Contents:

One could summarize the goal stated in the introduction, by shortening the project task to:

Simulate how "loud" the driver will perceive the electric climate compressor, for different vehicle isolation concepts, at an early-stage in development.

At an early-stage, the design can still be freely explored, which often results in better performance and less material consumption. In contrast, finding a noise problem late in the development phase, when the full-vehicle prototypes are already available, frequently causes the formation of task-force teams which need to tackle the problem quickly. The late-phase solution is often the addition of costly counter masses or dynamic vibration absorbers.

Looking back at the vehicle development example shown in chapter 11, one can say that the composition of individual methods described in the thesis are a viable approach to solve the vision for early-phase NVH engineering. The results and insights on the applied methods will be summarized in the following. An outlook on the practical industry application and further research directions are given at the end of this chapter.

13.1   Substructuring results

The structure-borne transfer path of the compressor noise was built up from individual component models. Provided the modeling assumptions are right, it doesn't matter if a component is represented by a rigid body, a finite element or an experimental model. The inclusion of rigid body models in the transfer path was found to be a valuable addition to the substructuring 'toolbox'. As a rule of thumb, it was found that up to half of the components' first resonance frequency, it can be modeled as rigid mass.

The experimental models for the rubber bushings, introduced in chapter 4, have been successfully tested for correctness by analytic developments and an academic experiment. Additionally, they have shown their validity in more complex application examples in chapters 11 and 12.

Theoretically, one would need to include the gyroscopic terms in the substructured model, due to the revolving parts in the compressor. In chapter 5 a method for analytically coupling the gyroscopic terms to an assembly was developed. It could be shown that the effects are significant, but only in a lower frequency range and therefore not relevant for the acoustic prototyping that was the aim of this thesis.

The examples in chapters 11 and 12 have shown that the hybrid assembly models, consisting of experimental and analytical/numerical models, are valid representations of the full system. Additionally, it was found that the assembled models can predict noise transfer functions that would not be measurable, even if the full prototype was available for testing. On the full system, typical measurement equipment applied too little input energy for measuring the transfer functions from compressor to drivers ear, especially at higher frequencies. In contrast, the substructuring result consists of component models that where measured individually, with a good signal to noise ratio. Thereby, physically valid transfer functions can be predicted at higher frequencies than previously measurable with standard equipment (see e.g. the results in figure 11.12).

13.2   Listening to virtual prototypes

Modeling the transfer path of a system is one thing, but for simulating its response in operation, one needs to model the excitation mechanisms of the noise source. This was done by means of blocked forces for the structure-borne excitation, and blocked volume accelerations for the air-borne excitation.

For listening to the NVH simulation results, it is necessary to convert the TPA results from the frequency domain back to the time domain. Different approaches for doing so are explained and compared in chapter 7. It was found that all methods based on a block-wise calculation in the frequency domain produced artifacts in the resulting sound files, clearly audible as "clicks". The artifacts can be removed by converting the matrix operations in the frequency domain to a finite impulse response filter, which is convoluted with the test bench signal.

Additionally, the matrix inverse required for determining the blocked forces and blocked volume accelerations of the compressor, tend to amplify random measurement noise in the recorded signals. In chapter 8, it was shown how this noise amplification is particularly prominent in the "stiff" directions of the system, i.e. the ones with the smallest singular values. Different regularization methods were compared, to deal with this problem. For the climate compressor, it was found that regularization methods yield the best results if they automatically increase the regularization at frequencies with a low signal level, but apply only a small regularization at frequencies with a high signal level (e.g. at the order frequencies of the compressor). This resulted in an audible reduction of spurious back ground noise in the sound predictions.

13.3   Early phase NVH optimization

The combination of an equivalent source description (e.g. blocked forces) with a substructured model of the transfer path not only allows for a prediction of sound in one specific setup, but in many different potential setups. This was shown in chapter 11 for an example of a complex vehicle development project, by virtually modifying the structural isolation of the compressor. Additionally, the blocked volume accelerations for different sound insulation capsules were applied to the air-borne transfer path.

In chapter 12, the idea was taken one step further, by using a parameterized model of the substructured transfer path. An optimization algorithm was used to find the "optimal" set of parameters to minimize the noise at given receiver points. The reference results, created on a physical realization of some simulated designs, confirmed that the method is well able to discover a better design and that the simulation can predict the overall cost function value

with ± 4dBA accuracy over the compressor run-up.

13.4 From research to application

What is the fundamental reason for doing research? Well, for some it is the search for something new, for understanding the existing world and answering the questions that are important, but complex. This is a wonderful endeavor, and reading the vitas of great historic scientists is often engaging. Think of Galileo next to his telescope, slowly coming to the conclusion that he could predict the motion of heavenly bodies with the Copernican theory [70]. This is probably as exciting (and dangerous) as fundamental research has ever been. Research in engineering is a rather "applied" science. The fundamental physical relations are accepted, for applying them to the solution of technically relevant questions. This frequently includes the question of:

"How do we solve the equations of physics on a complex domain?"

See for example the development of variational methods in mechanics [91]. The origin of these methods lies within the field of engineering: Galerkin applying variational methods to the static stress solution of a bridge, and later Rayleigh and Ritz applying it to the solution of vibration problems. In some sense, the methods described in this thesis are also answering the question stated above, but with a different approach. The fundamental idea is still to divide the system and then find the solution to smaller subsystems. However, if a subsystem can't be computed, it will be measured. This "experimental modeling" is an interesting direction of engineering research, since it allows to include fairly complex substructures in the full assembly. For NVH, this seems to be a promising approach.

At the time of writing this section, the author has already been out of university for 10 months. The time spent in industry beckoned the belief that experimental models are a useful addition to the engineering "toolbox". New methods should be available to the public in a most accessible way, to further advance technology as a whole. The currently fastest way to achieve this is software. Despite searching for new solutions, a good engineering scientist will make his results available in software, so others can build with and on top of it.

13.5 Further research topics

There are still many fields of research to advance and improve the current state of NVH modeling, of which the author wants to give a few suggestions:

- *Amplitude and temperature dependency in rubber models:* These non-linear effects in rubber mounts are well known, but currently not implemented in the substructuring models. The linearized rubber model is a fair start, but the possible simulation accuracy gains by including non-linear effects should be studied further. The heat dependency could be considered by including the Youngs Modulus' relation to material temperature. The amplitude dependence would require an iterative solution of the final noise prediction (often done by the harmonic balance method). In principle, both should be possible to achieve.

- *Optimization with sophisticated cost function:* Expressing the goal of pleasant acoustics in a deterministic cost function is hard. The addition of psycho-acoustic quantities

to the cost function might improve the optimization results. One could also think about using a neural net, which has "learned" how a good car sounds, as a cost function.

- *Joint identification:* The dynamic effects that take place in the coupling area between two substructures seems to be an important phenomenon. Practical methods for including these effects in substructued models are eagerly awaited.

- *Regularization:* The suppression of amplified measurement noise by regularization methods, yielded well audible improvements in the prediction quality for the compressor case. The optimal regularization method for a different noise source will most likely be different. The compressor has a very tonal excitation spectrum, which made signal-to-noise ratio based regularization methods quite successful. For noise sources with more broad-band, or impulse like spectra (like road noise or steering gear rattling), the optimal regularization strategy will most likely be a different one.

- *Coupling of stiff structures:* The same noise amplification as in the determination of the blocked forces (see chapter 8), seems to take place in the substructure assembly, when computing the coupling forces. The coupling of two stiff components with a modal behavior still frequently poses a challenge to the methods. Investigating the potential for regularization methods also in the field of substructuring seems a valuable direction of further research [176].

- *Uncertainty Quantification:* A model is a model, not the reality. Using the tools of uncertainty quantification can give the required insights in the simulation robustness. It could also predict the spread of production vehicles, by including the manufacturing tolerances in the simulation. Fortunately, this field is already seeing some current research attention [105, 177].

- *Artificial air-borne sound sources:* Standard components like the electric climate compressor will be in all vehicle variants. The creation of artificial air-borne sound sources [126] can speed up the measurements of air-borne transfer paths and the inverse source identification. These can be a box with multiple loudspeakers, which achieve the same, if not better, accuracy as the equivalent monopole approach discussed in chapter 10.

- *Source component target setting:* This is an industrially important question, but a very relevant and somewhat difficult one. Usually, one tries to define a noise target at the drivers ear and cascade it down to targets for the individual components in the transfer path and the noise source itself. This is inherently challenging, since the noise at the drivers ear obviously depends on the combination of all components and the source excitation. Source targets based on the blocked forces are probably not the right approach. How shall we define upper limits for individual forces, when a noise source contains e.g. 4 connection points to the vehicle, so that the blocked force vector contains 12 forces and 12 moments in total? Additionally, the noise amplification in the matrix inverse might further distort the targets on individual blocked forces (see chapter 8). The use of free-velocities could at least prevent the noise amplification. Using scalar quantities like energies or directly the sound levels predicted in predecessor vehicles might be a successful alternative.

Thanks for reading!

Part VI

Appendix

Assumptions underlying inverse substructuring

This section aims at clarifying when the assumption underlying inverse substructuring is valid or an approximation. The assumption is that the main and off-diagonal block matrices are equal, apart from a negative sign (see equation (4.7)). This assumption is however not generally true, even if the isolator elements mass would be negligible. Consider the simple case shown in figure A.1. Two DoF on either side are connected by two springs k_1 and k_2 with one spring k_3 introducing a cross coupling between the DoF.

The resulting equation and isolator stiffness matrix $\mathbf{Z}$ would then write as:

$$\mathbf{Zu} = \mathbf{f}, \quad \text{with} \quad \mathbf{Z} = \left[\begin{array}{cc:cc} k_1 & 0 & -k_1 & 0 \\ 0 & k_2 + k_3 & -k_3 & -k_2 \\ \hdashline -k_1 & -k_3 & k_1 + k_3 & 0 \\ 0 & -k_2 & 0 & k_2 \end{array} \right] \tag{A.1}$$

It can be seen that even for this simple case $\mathbf{Z}_{11} \neq -\mathbf{Z}_{12}$. The reason for this is the cross-coupling spring k_3. If k_3 was removed, the assumption underlying inverse substructuring would be valid again. For that reason, we have assumed for the ISD method a DOF to DOF model as depicted in figure 4.3.

Reconstructing the stiffness matrix with graph theory

The stiffness matrix of the system shown in figure A.1 could however still be recovered from only knowing the off-diagonal matrix $\mathbf{Z}_{12}$. The matrices of linear systems with simple nodes (i.e. DoFs in our case) and edges (i.e. springs in our case) can be constructed from graph theory (see e.g. [165, section 2]). For directed graphs, the so-called incidence matrix $\mathbf{A}$ describes the connectivity of the nodes. In this case, it computes the elongation of the single springs from the DoF values. In the example in figure A.1, it would be:
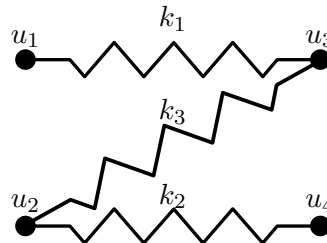

Figure A.1: Simple connection element with three springs connecting two DoF on either side of the connection element.

$$\mathbf{A} = \begin{bmatrix} -1 & 0 & 1 & 0 \\ 0 & -1 & 1 & 0 \\ 0 & -1 & 0 & 1 \end{bmatrix} \tag{A.2}$$

The product of the incidence matrix and the displacements in the single DoF, $\mathbf{Au}$ gives the elongation in all springs. These elongations can be multiplied with the single stiffness of each spring contained in the constitutive matrix $\mathbf{C}$ to yield the reaction forces within the spring, i.e. $\mathbf{CAu}$. In this case $\mathbf{C}$ would be:

$$\mathbf{C} = \begin{bmatrix} k_1 & 0 & 0 \\ 0 & k_2 & 0 \\ 0 & 0 & k_3 \end{bmatrix}. \tag{A.3}$$

These internal forces in the springs then need to be distributed with the right sign to either connection on the DoFs to yield the applied forces $\mathbf{f}$. The matrix doing this is $\mathbf{A}^T$, so:

$$\underbrace{\mathbf{A}^T\mathbf{C}\mathbf{A}}_{=\mathbf{Z}}\mathbf{u} = \mathbf{f}. \tag{A.4}$$

This symmetric pattern appears often in nature and engineering (see [165, section 2]). The important point for this thesis is that one could find the DoF pairs on either side of the interface which are connected by springs, from identifying the non-zero elements in the submatrix $\mathbf{Z}_{12}$. The incidence matrix $\mathbf{A}$ can be reconstructed from knowing which elements are non-zero then. The constitutive matrix can then be constructed from the values of the non-zero entries found in $\mathbf{Z}_{12}$. Thereby, the full stiffness matrix of the system could still be reconstructed from only knowing the off-diagonal sub-matrix $\mathbf{Z}_{12}$, even though $\mathbf{Z}_{11} \neq -\mathbf{Z}_{12}$. This approach could be used for arbitrarily complex cross couplings also for more DoF on either side of the interface. For using this with real measurements, one would have to devise a threshold for deciding what a non-zero element is.

However, this approach would still not be able to identify the system if the following two assumptions would not be fulfilled:

- The connection element itself has no mass.

- The DoF on the same side have no couplings to each other. E.g. if there was a spring coupling DoFs u_1 and u_2 in figure A.1, this could not be seen from merely knowing the submatrix $\mathbf{Z}_{12}$.

Considering these theoretical limitations, we decided that we would not also try this graph theory approach on the data presented in this thesis, even though it could help putting the cross coupling terms in the right positions for the main diagonal submatrices.

Stiffness matrix of a three-dimensional beam element

A relevant theoretical example for a coupling element is that of a three dimensional beam, see figure A.2. The isolator elements used in this thesis could be seen as an, admittedly thick, beam. The stiffness matrix for a three dimensional Euler-Bernoulli beam element, with standard Hermitian polynomials as shape functions, is (see e.g. [29, chapter 14.2] or [47, chapter 5.3]):
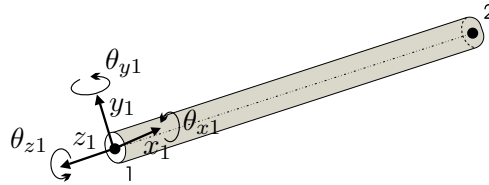
Figure A.2: Standard 3D beam element (taken from [47])

$$\mathbf{K}_{eL} = \begin{bmatrix} \frac{12EI}{\ell^3} & & & & & & & & & & & \\ 0 & \frac{12EI}{\ell^3} & & & & & & & & & \\ 0 & 0 & \frac{EA}{\ell} & & & \text{Sym.} & & & & & \\ 0 & \frac{6EI}{\ell^2} & 0 & \frac{4EI}{\ell} & & & & & & & \\ \frac{-6EI}{\ell^2} & 0 & 0 & 0 & \frac{4EI}{\ell} & & & & & & \\ 0 & 0 & 0 & 0 & 0 & \frac{GJ_x}{\ell} & & & & & \\ \frac{-12EI}{\ell^3} & 0 & 0 & 0 & \frac{6EI}{\ell^2} & 0 & \frac{12EI}{\ell^3} & & & & \\ 0 & \frac{-12EI}{\ell^3} & 0 & \frac{-6EI}{\ell^2} & 0 & 0 & 0 & \frac{12EI}{\ell^3} & & & \\ 0 & 0 & \frac{-EA}{\ell} & 0 & 0 & 0 & 0 & 0 & \frac{EA}{\ell} & & \\ 0 & \frac{6EI}{\ell^2} & 0 & \frac{2EI}{\ell} & 0 & 0 & 0 & \frac{-6EI}{\ell^2} & 0 & \frac{4EI}{\ell} & \\ \frac{-6EI}{\ell^2} & 0 & 0 & 0 & \frac{2EI}{\ell} & 0 & \frac{6EI}{\ell^2} & 0 & 0 & 0 & \frac{4EI}{\ell} \\ 0 & 0 & 0 & 0 & 0 & \frac{-GJ_x}{\ell} & 0 & 0 & 0 & 0 & 0 & \frac{GJ_x}{\ell} \end{bmatrix}$$

where we have adopted the coordinate system to the definitions used throughout the rubber chapter, and assumed that the beam has the same cross-section inertia for the bending around the y and the z axis, like the rubber elements presented here. Remember the 12 DoF definition of this presentation of rubber models, i.e. $\mathbf{q}_1 = [x_1 \ y_1 \ z_1 \ \theta_{x1} \ \theta_{y1} \ \theta_{z1}]$ and $\mathbf{q}_2$ accordingly (refer to the coordinate system in figure 3.9). One can see that for a beam element, neither the inverse substructuring assumption is fulfilled, i.e. $\mathbf{Z}_{11} \neq \mathbf{Z}_{21}$, nor could one identify the whole stiffness matrix with graph theory, due the cross couplings between the DoFs on the same interface side. The only approach that would (at least theoretically) be correct, is to identify the beam properties from the off-diagonal matrix $\mathbf{Z}_{12}$, and then place these in the right positions on the main diagonals. This could then be done for a few regular shapes of isolator elements, like cylinders or cubic blocks, similar to Verheijs approach [184].

Bibliography

[1]   A J Beijers, C. and Boer, A. de. "Numerical modelling of rubber vibration isolators". In: *Tenth International Conference on Sound and Vibration*. Stockholm, 2003.

[2]   Allemang, R. and Brown, D. "A complete review of the complex mode indicator function (CMIF) with applications". In: *Proceedings of International Conference on Noise and Vibration Engineering (ISMA2006)* (2006), pp. 3209–3246.

[3]   Allen, J. B. and Rabiner, L. R. "A Unified Approach to Short-Time Fourier Analysis and Synthesis". In: *Proceedings of the IEEE* 65.11 (1977), pp. 1565–1596. ISSN: 0018-9219.

[4]   Allen, M. S. and Mayes, R. L. "Comparison of FRF and modal methods for combining experimental and analytical substructures". In: *25th International Modal Analysis Conference (IMAC XXV)* (2007), p. 19. ISSN: 21915644.

[5]   Allen, M. S., Rixen, D., Seijs, M. van der, Tiso, P., Abrahamsson, T., and Mayes, R. L. *Substructuring in Engineering Dynamics - Emerging Numerical and Experimental Techniques*. 1st ed. Springer International Publishing, 2019. ISBN: 978-3-030-25531-2. DOI: 10.1007/978-3-030-25532-9.

[6]   Ansys Inc. *Ansys Mechanical APDL Help*. 2018.

[7]   Arendt, I. and Berger, A. "Systematische Fehler bei der Anwendung verschiedener Verfahren zur Ermittlung des Schallleistungspegels". In: *DAGA*. 2015.

[8]   Auroux, D. *Lecture 13, Lagrange Multipliers, course Multivariable Calculus MIT 18.02*. 2007. URL: https://www.youtube.com/watch?v=15HVevXRsBA.

[9]   Avitabile, P. "The Modal Space Articles". In: *Experimental Techniques, Society for Experimental Mechanics* appeared over multiple issues (2014), p. 225. URL: https://www.uml.edu/Research/SDASL/Education/Modal-Space.aspx%20https://www.uml.edu/research/sdasl/education/modal-space.aspx.

[10] Avitabile, P. *Modal Testing: A Practitioner's Guide*. 1st ed. Wiley, 2017. ISBN: 978-1119222897.

[11] Banwell, G., Hopper, H., Moorhouse, A., Elliott, A., and Meggitt, J. "Methods for auralising sounds with tonal components". In: *22nd International Congress on Sound and Vibration, ICSV 2015* July (2015), pp. 12–16.

[12] Bathelt, H., Scheinhardt, M., Sell, H., Sottek, R., Guidati, S., and Helfer, M. "Messung und Analyse". In: *Sound-Engineering im Automobilbereich*. Ed. by Genuit, K. Berlin, Heidelberg: Springer, 2010, pp. 339–425. ISBN: 978-3-642-01414-7. DOI: 10.1007/978-3-642-01415-4_8.

[13] Bendat, Julius S and Piersol, A. G. *Engineering applications of correlation and spectral analysis*. 2nd. New York: Wiley-Interscience, 1980.

[14] Benner, F. "Auralisierung von Transfer Pfad Analyse Resultaten für harmonische Quellen (transl. "Auralization of Transfer Path Analysis results for Harmonic Sources")". Semester thesis. Technical University of Munich, 2018.

[15] Benner, F. "Vergleich von Regularisierungsmethoden zur Bestimmung von Blocked Forces (transl. "Comparison of Regularization methods for Blocked Force computation")". M.Sc. Thesis. Technical University Munich, 2019.

[16] Berckmans, D., Kindt, P., Sas, P., and Desmet, W. "Evaluation of substitution monopole models for tire noise sound synthesis". In: *Mechanical Systems and Signal Processing* 24.1 (2010), pp. 240–255. ISSN: 0888-3270.

[17] *Bestimmmung der Schallleistungspegel von Geräuschquellen aus Schallintensitätsmessungen Teil 2: Messung mit kontinuierlichen Abtastung.* Norm. Berlin: Deutsches Institut für Normung e.V., Aug. 1996.

[18] Bobrovnitski, Y. I. "A Theorem on the Representation of the Field of Forced Vibrations of a Composite Elastic System". In: *Acoustical Physics* 47.5 (2001), pp. 507–510.

[19] Bös, J. "Numerical optimization of the thickness distribution of three-dimensional structures with respect to their structural acoustic properties". In: *Structural and Multidisciplinary Optimization* 32.1 (2006), pp. 12–30. ISSN: 1615147X. DOI: 10.1007/s00158-005-0560-y.

[20] Brandl, F., Biermayer, W., and Brandl, S. "Herausforderung Transfer Pfad Analyse (transl. "Challenge Transfer Path Analysis")". In: *ATZ / MTZ Tagung* (2008).

[21] Brandt, A. *Noise and Vibration Analysis: Signal Analysis and Experimental Procedures.* 1st ed. Wiley, 2011. ISBN: 9780470746448.

[22] Bregar, T., Holeček, N., Čepon, G., Rixen, D. J., and Boltežar, M. "Including directly measured rotations in the virtual point transformation". In: *Mechanical Systems and Signal Processing* (2019), p. 106440.

[23] Bucher, I. and Ewins, D. J. "Modal analysis and testing of rotating structures". In: *Philosophical Transactions of the Royal Society of London A: Mathematical, Physical and Engineering Sciences* 359.1778 (2001), pp. 61–96. ISSN: 1364-503X. DOI: 10.1098/rsta.2000.0714.

[24] Carne, T. G. and Dohrmann, C. R. "Improving Experimental Frequency Response Function Matrices for Admittance Modeling". In: *IMAC-XXIV: International Modal Analysis Conference.* St. Louis: Society for Experimental Mechanics, 2006.

[25] Chen, K.-Y. "Gyroscopic Effect in Dynamic Substructuring". M.Sc. thesis. Technical University of Munich, 2018.

[26] Choi, H. G., Thite, A. N., and Thompson, D. J. "Comparison of methods for parameter selection in Tikhonov regularization with application to inverse force determination". In: *Journal of Sound and Vibration* 304.3-5 (2007), pp. 894–917. ISSN: 0022460X. DOI: 10.1016/j.jsv.2007.03.040.

[27] Comesaña, D. F., Holland, K., Wind, J., and De Bree, H.-E. "Comparison of inverse methods and particle velocity based techniques for transfer path analysis". In: *Acoustics.* 2012.

[28] Courant, R. "Variational methods for the solution of problems of equilibrium and vibrations". In: *Bull. Amer. Math. Soc* 49.1 (1943), pp. 1–23.

[29] Craig Jr., R. R. and Kurdila, A. J. *Fundamentals of Structural Dynamics.* 2nd ed. John Wiley & Sons, 2006. ISBN: 978-0-471-43044-5.

[30] Crowley, J. R. and Klosterman, A. "Direct structural modification using frequency response functions". In: *IMAC II - International Modal Analysis Conference.* 1984.

[31] De Klerk, D., Rixen, D. J., and Voormeeren, S. N. "General framework for dynamic substructuring: History, review, and classification of techniques". In: *AIAA Journal* 46.5 (2008), pp. 1169–1181. ISSN: 00011452. DOI: 10.2514/1.33274.

[32] Dickens, J. D. and Norwood, C. J. "Universal Method to measure dynamic Performance of Vibration Isolators under Static Load". In: *Journal of Sound and Vibration* 244.4 (July 2001), pp. 685–696. ISSN: 0022460X. DOI: 10.1006/jsvi.2000.3516.

[33] Dobson, B. J. and Rider, E. "A review of the indirect calculation of excitation forces from measured structural response data". In: *Proceedings of the Institution of Mechanical Engineers, Part C: Journal of Mechanical Engineering Science 1989-1996 (vols 203-210)* 204.23 (1990), pp. 69–75. DOI: 10.1243/PIME_PROC_1990_204_080_02.

[34] Drozg, A., Čepon, G., and Boltežar, M. "Full-degrees-of-freedom frequency based substructuring". In: *Mechanical Systems and Signal Processing* 98 (2018), pp. 570–579. ISSN: 10961216. DOI: 10.1016/j.ymssp.2017.04.051.

[35] Du, Y., Burdisso, R., Nikolaidis, E., and Tiwari, D. "Effects of isolators internal resonances on force transmissibility and radiated noise". In: *Journal of Sound and Vibration* 268.4 (Dec. 2003), pp. 751–778. ISSN: 0022460X. DOI: 10.1016/S0022-460X(03)00036-1.

[36] Duarte, M. L. M. and Ewins, D. J. "Some Insights into the Importance of Rotational Degrees-of-freedom and Residual Terms in Coupled Structure Analysis". In: *Proceedings of the 13th International Modal Analysis Conference*. Society for Experimental Mechanics, 1995, pp. 164–170.

[37] Duehring, M. B., Jensen, J. S., and Sigmund, O. "Acoustic design by topology optimization". In: *Journal of Sound and Vibration* 317 (2008), pp. 557–575. DOI: 10.1016/j.jsv.2008.03.042.

[38] *Electroacoustics - Sound level meters - Part 1: Specifications*. 2013.

[39] Elliott, A. S., Moorhouse, A. T., Huntley, T., and Tate, S. "In-situ source path contribution analysis of structure borne road noise". In: *Journal of Sound and Vibration* 332.24 (2013), pp. 6276–6295. ISSN: 0022460X. DOI: 10.1016/j.jsv.2013.05.031.

[40] Ewins, D. J. *Modal testing: theory and practice*. Vol. 15. Research studies press Letchworth, 1984.

[41] Fahy, F. J. "Some applications of the reciprocity principle in experimental vibroacoustics". In: *Acoustical Physics* 49.2 (2003), pp. 217–229. ISSN: 1562-6865. DOI: 10.1134/1.1560385. URL: https://doi.org/10.1134/1.1560385.

[42] Fastl, H. and Zwicker, E. *Psychoacoustics, Facts and Models*. 3rd ed. Springer-Verlag Berlin Heidelberg, 2007. ISBN: 978-3-540-68888-4. DOI: 10.1007/978-3-540-68888-4.

[43] Fritze, D., Marburg, S., and Hardtke, H.-J. "Estimation of Radiated Sound Power : A Case Study on Common Approximation Methods". In: *Acta Acustica united with Acustica* 95 (2009), pp. 833–842. DOI: 10.3813/AAA.918214.

[44] Ganguly, V. and Schmitz, T. L. "Phase correction for frequency response function measurements". In: *Precision Engineering* 38 (2014), pp. 409–413. ISSN: 0141-6359. DOI: 10.1016/j.precisioneng.2013.12.007.

[45] Gazi, O. *Understanding Digital Signal Processing*. Vol. 13. Singapore: Springer Singapore, 2018. ISBN: 978-981-10-4961-3. DOI: 10.1007/978-981-10-4962-0.

[46] Genuit, K. and Sottek, R. "Das menschliche Gehör und Grundlagen der Psychoakustik". In: *Sound-Engineering im Automobilbereich*. Ed. by Genuit, K. Berlin, Heidelberg: Springer, 2010, pp. 39–88. ISBN: 978-3-642-01414-7. DOI: 10.1007/978-3-642-01415-4_2.

[47] Geradin, M. and Rixen, D. J. *Mechanical Vibrations: Theory and Application to Structural Dynamics*. 3rd ed. Wiley, 2015. ISBN: 9781118900208.

[48] Gialamas, P. T., Tsahalis, D., Bregant, L., Otte, D., and Auweraer, H. van der. "Substructuring by Means of FRFs: Some Investigations on the Significance of Rotational DOFs". In: *IMAC-XIV*. Orlando, Florida, 1996.

[49] Gibbs, B. M. and Petersson, B. A. T. "Measurement and characterization of sources of structure-borne sound." In: *Inter-Noise, Liverpool*. 1996, pp. 1307–1312.

[50] Giron-Sierra, J. M. *Digital Signal Processing with Matlab Examples, Volume 2: Decomposition, Recovery, Data-Based Actions*. Signals and Communication Technology. Singapore and s.l.: Springer Singapore, 2017. ISBN: 978-981-10-2536-5. DOI: 10.1007/978-981-10-2537-2.

[51] Golub, G. H. and Van Loan, C. F. *Matrix Computations*. 4th editio. John Hopkins University Press, 2012.

[52] Gong, D., Duan, Y., Wang, K., and Zhou, J. "Modelling rubber dynamic stiffness for numerical predictions of the effects of temperature and speed on the vibration of a railway vehicle car body". In: *Journal of Sound and Vibration* 449 (June 2019), pp. 121–139. ISSN: 0022460X. DOI: 10.1016/j.jsv.2019.02.037.

[53] Grialou, M. "Vibro-acoustics Substructuring: Combining simulations and experimental identification of subdomains for low frequency vehicle acoustics". PhD thesis. Université de Lyon, 2018. URL: https://tel.archives-ouvertes.fr/tel-02187316/document.

[54] Haeussler, M., Klaassen, S. W., and Rixen, D. J. "Experimental twelve degree of freedom rubber isolator models for use in substructuring assemblies". In: *Journal of Sound and Vibration* 474 (2020). ISSN: 10958568. DOI: 10.1016/j.jsv.2020.115253.

[55] Haeussler, M., Reichart, R., Bartl, A., and Rixen, D. J. "Post correcting for gyroscopic effects via dynamic substructuring". In: *International Conference on Sound and Vibration* (2017).

[56] Haeussler, M., Sendlbeck, S., and Rixen, D. J. "Automated Correction of Sensor Orientation in Experimental Dynamic Substructuring". In: *Dynamics of Coupled Structures, Volume 4*. Ed. by Linderholt, A., Allen, M. S., Mayes, R. L., and Rixen, D. Springer International Publishing, 2018, pp. 65–70. ISBN: 978-3-319-74654-8.

[57] Haeussler, M., Klaassen, S. W. B., and Rixen, D. J. "Comparison of substructuring techniques for experimental identification of rubber isolators dynamic properties". In: *Proceedings of ISMA 2018 - International Conference on Noise and Vibration Engineering and USD 2018 - International Conference on Uncertainty in Structural Dynamics*. 2018. ISBN: 9789073802995.

[58] Haeussler, M., Kobus, D., and Rixen, D. J. "Combining Blocked Force Transfer Path Analysis And Dynamic Substructuring For Acoustic Design Optimization". In: *Proceedings of ICEDyn 2019-International Conference on Structural Engineering Dynamics,* Viana do Castelo, Portugal, 2019.

[59] Haeussler, M., Kobus, D. C., and Rixen, D. J. "Parametric design optimization of e-compressor NVH using blocked forces and substructuring". In: *Mechanical Systems and Signal Processing (submitted)* (2020).

[60] Haeussler, M. and Rixen, D. J. "Optimal transformation of frequency response functions on interface deformation modes". In: *Dynamics of Coupled Structures, Volume 4. Conference Proceedings of the Society for Experimental Mechanics Series*. Ed. by Allen, M., Mayes, R., and Rixen, D. J. Springer, Cham, 2017, pp. 225–237.

[61] Hanna, P. and Desainte-Catherine, M. *Adapting the overlap-add method to the synthesis of noise*. Ed. by Proceedings of the Digital Audio Effects Conference. Hamburg.

[62] Hansen, P. "The L-Curve and Its Use in the Numerical Treatment of Inverse Problems". In: *Computational Inverse Problems in Electrocardiology*. Vol. 4. 2001, pp. 119–142.

[63] Hansen, P. C. "Analysis of Discrete Ill-Posed Problems by Means of the L-Curve". In: *SIAM Review* 34.4 (1992), pp. 561–580. DOI: 10.1137/1034115.

[64] Hansen, P. C. *Rank-Deficient and Discrete Ill-Posed Problems*. 1st ed. Society for Industrial and Applied Matematrics (SIAM), 1998. ISBN: 978-0-89871-403-6. DOI: 10.1137/1.9780898719697.

[65] Harris, J. A. "Dynamic Testing under Nonsinusoidal Conditions and the Consequences of Nonlinearity for Service Performance". In: *Rubber Chemistry and Technology* 60.5 (Nov. 1987), pp. 870–887. ISSN: 0035-9475. DOI: 10.5254/1.3536161.

[66] Harrison, M., Sykes, A. O., Martin, M., Harrison, M., Sykes, A. O., and Martin, M. "Wave Effects in Isolation Mounts". In: *The Journal of the Acoustical Society of America* 24.62 (1952). DOI: 10.1121/1.1906850.

[67] Helderweirt, S., Van der Auweraer, H., Mas, P., Bregant, L., and Casagrande, D. "Application of accelerometer-based rotational degree of freedom measurements for engine subframe modelling". In: *Proceedings of the International Modal Analysis Conference - IMAC*. 2001.

[68] Hillary, B. "Indirect measurement of vibration excitation forces." PhD Thesis. Imperial College London (University of London), 1983. URL: http://hdl.handle.net/10044/1/8450.

[69] Hinsch, P. "Einige Untersuchungen zum Messen dynamischer Moduln von Elastomeren (transl. "Investigations on measuring the dynamic modulus of Elastomers")". In: *Kautschuk + Gummi Kunststoffe* 42.9 (1989), pp. 752–756.

[70] History, H. *Galileo Galilei: A Life From Beginning to End*. Biographies of Physicists. Independently Published, 2017. ISBN: 9781520994703. URL: https://books.google.de/books?id=OFpCswEACAAJ.

[71] Janssens, M. H. and Verheij, J. W. "A Pseudo-forces methodology to be used in characterization of structure-borne sound sources". In: *Applied Acoustics* 61.3 (2000), pp. 285–308. ISSN: 0003682X. DOI: 10.1016/S0003-682X(00)00035-9.

[72] Janssens, M. H., Verheij, J. W., and Thompson, D. J. "The use of an equivalent forces method for the experimental quantification of structural sound transmission in ships". In: *Journal of Sound and Vibration* 226.2 (1999), pp. 305–328. ISSN: 0022460X. DOI: 10.1006/jsvi.1999.2303.

[73] Jetmundsen, B., Bielawa, R. L., and Flannelly, W. G. "Generalized Frequency Domain Substructure Synthesis". In: *Journal of the American Helicopter Society* 33.1 (Oct. 1988), pp. 55–64.

[74] Jog, C. "Reducing Radiated Sound Power by Minimizing the Dynamic Compliance". In: *IUTAM Symposium on Designing for Quietness*. Vol. 102. Dordrecht: Springer, 2002, pp. 215–236. DOI: 10.1007/978-94-017-0095-5_13.

[75] Kammeyer, K.-D. and Kroschel, K. *Digitale Signalverarbeitung*. Wiesbaden: Vieweg Teubner Verlag, 2002. ISBN: 978-3-519-46122-7. DOI: 10.1007/978-3-663-09805-8.

[76] Kari, L., Eriksson, P., and Stenberg, B. "Dynamic stiffness of natural rubber cylinders in the audible frequency range using wave guides". In: *KGK-Kautschuk und Gummi Kunststoffe* 54.3 (2001), pp. 106–113. ISSN: 09483276.

[77] Karlsson, S. E. "Identification of external structural loads from measured harmonic responses". In: *Journal of Sound and Vibration* 196.1 (1996), pp. 59–74. ISSN: 0022460X. DOI: 10.1006/jsvi.1996.0467.

[78] Keersmaekers, L., Mertens, L., Penne, R., Guillaume, P., and Steenackers, G. "Decoupling of mechanical systems based on in-situ frequency response functions: The link-preserving, decoupling method". In: *Mechanical Systems and Signal Processing* 58 (2015), pp. 340–354. ISSN: 10961216. DOI: 10.1016/j.ymssp.2014.11.016.

[79] Kim, J., Yoon, J.-C., and Kang, B.-S. "Finite element analysis and modeling of structure with bolted joints". In: *Applied Mathematical Modelling* 31.5 (2007), pp. 895–911. DOI: 10.1016/j.apm.2006.03.020.

[80] Kim, S. and Singh, R. "Multi-Dimensional Characterization of Vibration Isolators over a wide range of Frequencies". In: *Journal of Sound and Vibration* 245.5 (Aug. 2001), pp. 877–913. ISSN: 0022460X. DOI: 10.1006/jsvi.2001.3617.

[81] Kim, Y. and Nelson, P. A. "Optimal regularisation for acoustic source reconstruction by inverse methods". In: *Journal of Sound and Vibration* 275.3-5 (2004), pp. 463–487. ISSN: 0022460X. DOI: 10.1016/j.jsv.2003.06.031.

[82] Klaassen, S. W. B., Seijs, M. V. van der, and Klerk, D. de. "System equivalent model mixing". In: *Mechanical Systems and Signal Processing* 105 (2018), pp. 90–112. ISSN: 0888-3270. DOI: https://doi.org/10.1016/j.ymssp.2017.12.003.

[83] Klaerner, M. and Wuehrl, M. "Efficient Vibro-Acoustic Optimisation of a Thermoplastic Composite Oil Pan". In: *SAE Technical Paper* (2018), pp. 1–10. DOI: 10.4271/2018-01-1480.Abstract.

[84] Klaerner, M., Wuehrl, M., Kroll, L., and Marburg, S. "FEA-based methods for optimising structure-borne sound radiation". In: *Mechanical Systems and Signal Processing* 89 (2017), pp. 37–47. ISSN: 0888-3270. DOI: 10.1016/j.ymssp.2016.07.019.

[85] Klerk, D. de. "Dynamic Response Characterization of Complex Systems through Operational Identification and Dynamic Substructuring". PhD thesis. TU Delft, 2009. ISBN: 978-90-90240-95-4.

[86] Klerk, D. de, Rixen, D. J., Voormeeren, S. N., and Pasteuning, F. "Solving the RDoF Problem in Experimental Dynamic Substructuring". In: *Proceedings of the 26th International Modal Analysis Conference - IMAC*. 2008. ISBN: 9781605600666.

[87] Klerk, D. D., Rixen, D., and Jong, J. D. "The frequency based substructuring (FBS) method reformulated according to the dual domain decomposition method". In: *International Modal Analysis Conference (IMAC), Proceedings of the Society for Experimental Mechanics Series*. 2006. ISBN: 0912053941.

[88] Koblar, D. and Boltežar, M. "Evaluation of the Frequency-Dependent Young's Modulus and Damping Factor of Rubber from Experiment and their Implementation in a Finite-Element Analysis". In: *Experimental Techniques* (Nov. 2013). ISSN: 07328818. DOI: 10.1111/ext.12066. URL: http://doi.wiley.com/10.1111/ext.12066.

[89] Kobus, D. C. "Acoustic Structural Optimization using New Developments in Frequency Based Substructuring and Transfer Path Analysis". M. Sc. thesis. Technical University of Munich, 2018.

[90] Lanczos, C. "An iteration method for the solution of the eigenvalue problem of linear differential and integral operators". In: *Journal of research of the National Bureau of Standards* (1950).

[91] Lanczos, C. *The Variational Principles of Mechanics*. 4th revise. Dover Publications, 1986, p. 464. ISBN: 978-0486650678.

[92] Lennström, D., Johnsson, R., Nykänen, A., and Ågren, A. *Determination of Radiated Sound Power from an Electric Rear Axle Drive In-Situ and its Contribution to Interior Noise*. Nov. 2013. DOI: https://doi.org/10.4271/2013-01-9120. URL: https://doi.org/10.4271/2013-01-9120.

[93] Lennström, D., Olsson, M., Wullens, F., and Nykänen, A. "Validation of the blocked force method for various boundary conditions for automotive source characterization". In: *Applied Acoustics* 102 (Jan. 2016), pp. 108–119. ISSN: 0003682X. DOI: 10.1016/j.apacoust.2015.08.019.

[94] Liao, X., Li, S., Liao, L., and Meng, H. "Virtual decoupling method: a novel method to obtain the FRFs of subsystems". In: *Archive of Applied Mechanics* 87.9 (2017), pp. 1453–1463. ISSN: 14320681. DOI: 10.1007/s00419-017-1264-7.

[95] Lienkamp, M. and Homm, F. "The state of electromobility 2018: It's the customers turn". In: (2018). URL: https://www.researchgate.net/publication/326377089%7B%5C_%7DThe%7B%5C_%7DState%7B%5C_%7Dof%7B%5C_%7DElectromobility%7B%5C_%7D2018.

[96] Liljerehn, A. and Abrahamsson, T. "Dynamic sub-structuring with passive state-space components". In: *26th International Conference on Noise and Vibration Engineering, ISMA 2014*. 2014, pp. 3879–3890.

[97] Lin, T. R., Farag, N. H., and Pan, J. "Evaluation of frequency dependent rubber mount stiffness and damping by impact test". In: *Applied Acoustics* 66.7 (July 2005), pp. 829–844. ISSN: 0003682X. DOI: 10.1016/j.apacoust.2004.10.004. URL: https://www.sciencedirect.com/science/article/pii/S0003682X04001835.

[98] Liu, W. and Ewins, D. "The Importance Assessment of RDOF in FRF Coupling Analysis". In: (2001).

[99] Lyons, R. G. *Understanding Digital Signal Processing*. 3rd ed. Boston: Prentice Hall, 2011. ISBN: 013702741-9.

[100] Maierhofer, J., El Mahmoudi, A., and Rixen, D. J. "Development onf a low cost automatic hammer for applications in sustructuring". In: *International Modal Analysis Conference (IMAC), Proceedings of the Society for Experimental Mechanics Series*. Orlando, Florida, 2019. DOI: 10.13140/RG.2.2.21408.43527.

[101] Malvar, H. S. *Signal processing with lapped transforms*. The Artech House telecommunications library. Boston: Artech House, 1992. ISBN: 0890064679.

[102] Marburg, S. "Developments in structural-acoustic optimization for passive noise control". In: *Archives of Computational Methods in Engineering* 9.4 (2002), pp. 291–370. ISSN: 1134-3060. DOI: 10.1007/BF03041465.

[103] Mayes, R. L. and Stasiunas, E. C. "Lightly damped experimental substructures for combining with analytical substructures". In: *25th international modal analysis conference (IMAC XXV), Orlando, FL*. 2007.

[104] McConnell, K. G. and Varoto, P. S. *Vibration testing: theory and practice*. 2nd Editio. John Wiley & Sons, 2008.

[105] Meggitt, J. W. R., Moorhouse, A. T., Wienen, K., and Sturm, M. "A Framework for the Propagation of Uncertainty in Transfer Path Analysis". In: *Journal of Sound and Vibration 2020* 483.115425 (2020).

[106] Meggitt, J. W., Elliott, A. S., Moorhouse, A. T., Banwell, G., Hopper, H., and Lamb, J. "Broadband characterisation of in-duct acoustic sources using an equivalent source approach". In: *Journal of Sound and Vibration* 442.November (2019), pp. 800–816. ISSN: 10958568. DOI: 10.1016/j.jsv.2018.10.041.

[107] Meggitt, J. W., Elliott, A. S., Moorhouse, A. T., and Lai, H. K. "In situ determination of dynamic stiffness for resilient elements". In: *Proceedings of the Institution of Mechanical Engineers, Part C: Journal of Mechanical Engineering Science* 230.6 (2015), pp. 986–993. ISSN: 20412983. DOI: 10.1177/0954406215618986.

[108] Meggitt, J., Elliott, A., and Moorhouse, A. "Virtual assemblies and their use in the prediction of vibro-acoustic responses". In: *Proceedings of the Institute of Acoustics*. September. 2016. ISBN: 9781510830219.

[109] Meggitt, J. "On In-situ Methodologies for the Characterisation and Simulation of Vibro-Acoustic Assemblies". PhD thesis. University of Salford, 2017. DOI: 10.13140/RG.2.2.32585.80483.

[110] Meggitt, J., Elliott, A., Moorhouse, A., Clot, A., and Langley, R. "Development of a Hybrid FE-SEA-eXperimental Model - Experimental Sub-system Characterisation". In: *NOVEM 2018: Noise and vibration emerging methods*. Ibiza, 2018.

[111] Meggitt, J. and Moorhouse, A. "The in-situ decoupling of resiliently coupled sub-structures". In: *ICSV - International Congress on Sound and Vibration, London* (2017). Ed. by Gibbs, B.

[112] Meggitt, J. and Moorhouse, A. "In-situ sub-structure decoupling of resiliently coupled assemblies". In: *Mechanical Systems and Signal Processing* 117 (2018), pp. 723–737. DOI: 10.1016/j.ymssp.2018.07.045.

[113] Meggitt, J., Moorhouse, A., and Elliott, A. "On the Problem of Describing the Coupling Interface Between Sub-structures: An Experimental Test for 'Completeness'". In: 2018, pp. 171–182. ISBN: 978-3-319-74653-1. DOI: 10.1007/978-3-319-74654-8_14.

[114] Meyer, M. *Signalverarbeitung*. Wiesbaden: Springer Fachmedien Wiesbaden, 2017. ISBN: 978-3-658-18320-2. DOI: 10.1007/978-3-658-18321-9.

[115] Miller, K. "Least Squares Methods for Ill-Posed Problems with a Prescribed Bound". In: *SIAM Journal on Mathematical Analysis* 1.1 (1970), pp. 52–74. DOI: 10.1137/0501006.

[116] Ming, X. and Kang, D. "Corrections for frequency, amplitude and phase in a fast fourier transform of a harmonic signal". In: *Mechanical Systems and Signal Processing* 10.2 (1996), pp. 211–220. ISSN: 08883270. DOI: 10.1006/mssp.1996.0015.

[117] Moeller, S. *VW ID3: Geleakte Insider Infos zu Preisen, Konfigurator, Bestellstart, Reichweite, Wärmepumpenschock*. 2020. URL: https://www.youtube.com/watch?v=vc1ARV0s-Rw%7B%5C&%7Dt=100s.

[118] Moler, C., Diepold, K., Florian, H., and Broy, M. *Cleve Moler - Panel Discussion TUM Speaker Series*. 2015. URL: https://www.youtube.com/watch?v=ekcLT8QgB60 (visited on 06/22/2019).

[119] MOORHOUSE, A. T. "On the characteristic power of structure-borne sound sources". In: *Journal of Sound and Vibration* 248.3 (2001), pp. 441–459. ISSN: 0022-460X. DOI: https://doi.org/10.1006/jsvi.2001.3797.

[120] Moorhouse, A. T., Elliott, A. S., and Evans, T. A. "In situ measurement of the blocked force of structure-borne sound sources". In: *Journal of Sound and Vibration* 325.4-5 (Sept. 2009), pp. 679–685. ISSN: 0022460X. DOI: 10.1016/j.jsv.2009.04.035.

[121] Moorhouse, A. T. and Seiffert, G. "Characterisation of an airborne sound source for use in a virtual acoustic prototype". In: *Journal of Sound and Vibration* 296.1-2 (2006), pp. 334–352. ISSN: 10958568. DOI: 10.1016/j.jsv.2006.03.017.

[122] Moorhouse, A. "Virtual acoustic prototypes: Listening to machines that don't exist". In: *Acoustics Australia* 33.3 (2005), pp. 97–105. ISSN: 08146039.

[123] Moorhouse, A., Elliot, A. S., and Heo, Y. "Intrinsic characterisation of structure-borne sound sources and isolators from in-situ measurements." In: *Proceedings of Meetings on Acoustics* 19 (2013), pp. 1–9. ISSN: 1939800X. DOI: 10.1121/1.4799691.

[124] Moorhouse, A. T., Meggitt, J. W. R., Elliott, A. S., Moorhouse, A. T., Banwell, G., Hopper, H., and Lamb, J. "In-situ Characterisation of Ducted Sources of Airborne Sound". In: *Inter-Noise 2016*. September. 2016, pp. 5931–5942.

[125] Möser, M. *Engineering Acoustics*. Ed. by Ellis, R. and Zimmermann, S. 2nd ed. Berlin, Heidelberg: Springer, 2009. ISBN: 978-3-642-44371-8. DOI: 10.1007/978-3-540-92723-5.

[126] Müller, T. "Luftschall-Transferpfadanalyse am Beispiel eines elektrischen Kältemittelverdichters (transl. "Airborne Transfer Path Analysis on the example of an electric refrigerant compressor")". M.Sc. thesis. Technical University of Munich, 2019.

[127] Nashif, A. D., Jones, D. I. G., and Henderson, J. P. *Vibration damping*. John Wiley & Sons, 1985. ISBN: 0-471-86772-1.

[128] Nocedal, J., Wright, and J., S. *Numerical Optimization*. second. New York, NY: Springer, 2006.

[129] O'Callahan, J., Avitabile, P., and Riemer, R. "System equivalent reduction expansion process (SEREP)". In: *Proceedings of the 7th international modal analysis conference*. Vol. 1. Union College Schnectady, NY. 1989, pp. 29–37.

[130] Ochmann, M. "Die Multipolstrahlersynthese - ein effektives Verfahren zur Berechnung der Schallabstrahlung von schwingenden Strukturen beliebiger Oberflächengestalt". In: *Acta Acustica united with Acustica* 72 (1990), pp. 233–246.

[131] Ohayon, R. and Soize, C. "Chapter X - Linear Acoustic Equations". In: *Structural Acoustics and Vibration: Mechanical models, variational formulations and discretization*. Ed. by Ohayon, R. and Soize, C. London: Academic Press, 1998, pp. 169–187. ISBN: 978-0-12-524945-4. DOI: https://doi.org/10.1016/B978-012524945-4/50010-4.

[132] Otto, N., Amman, S., Eaton, C., and Lake, S. "Guidelines for Jury Evaluations of Automotive Sounds". In: *SAE Technical Paper*. SAE Technical Paper Series. SAE International400 Commonwealth Drive, Warrendale, PA, United States, 1999. DOI: 10.4271/1999-01-1822.

[133] Pasma, E., Seijs, M. der, Klaassen, S., and Kooij, M. van der. "Frequency Based Substructuring with the Virtual Point Transformation, Flexible Interface Modes and a Transmission Simulator". In: *International Modal Analysis Conference (IMAC) XXXVI*. Ed. by Linderholt, A., Allen, M. S., Mayes, R. L., and Rixen, D. J. Orlando, Florida: Springer, Cham, 2018, pp 205–213. DOI: https://doi.org/10.1007/978-3-319-74654-8_18.

[134] Pavić, G. and Elliott, A. S. "Structure-Borne Sound Characterization of Coupled Structures — Part II : Feasibility". In: *Journal of Vibration and Acoustics* 132.4 (2010). DOI: 10.1115/1.4000981.

[135]   Pavić, G. and Elliott, A. S. "Structure-Borne Sound Characterization of Coupled Structures—Part I: Simple Demonstrator Model". In: *Journal of Vibration and Acoustics* 132.4 (2010), p. 041008. ISSN: 07393717. DOI: 10.1115/1.4000980.

[136]   Pfeiffer, F. *Einführung in die Dynamik*. 2nd. Stuttgart: Teubner Studienbücher, 1992, p. 236. ISBN: 3519123673.

[137]   Pfeiffer, F. *Mechanical system dynamics*. Vol. 2. Springer Science & Business Media, 2008, p. 545. ISBN: 9783540794356. DOI: 10.1007/978-3-540-79436-3.

[138]   PJS. *What is the acoustic quantity called Q?* 2016. URL: https://community.plm. automation.siemens.com/t5/Testing-Knowledge-Base/What-is-the-acoustic-quantity-called-Q/ta-p/354776 (visited on 03/27/2019).

[139]   Plunt, J. "Finding and Fixing Vehicle NVH Problems with Transfer Path Analysis". In: *Sound And Vibration* November (2005), pp. 12–16. ISSN: 15410161.

[140]   Popp, A. "Mortar methods for computational contact mechanics and general interface problems". PhD thesis. Technical University of Munich, 2012.

[141]   Powell, R. E. and Seering, W. "Multichannel Structural Inverse Filtering". In: *Journal of Vibration Acoustics Stress and Reliability in Design* 106.1 (1984), p. 22. DOI: 10.1115/1.3269147.

[142]   Ratle, A. and Berry, A. "Use of genetic algorithms for the vibroacoustic optimization of a plate carrying point-masses". In: *The Journal of the Acoustical Society of America* 104.6 (1998), pp. 3385–3397. DOI: 10.1121/1.423922.

[143]   Rayleigh, J. *The Theory of Sound*. second edi. Dover, 1896.

[144]   Reichart, R. "Airborne and structure-borne transfer path analysis for virtual acoustic prototyping". M.Sc. Thesis. Technical University of Munich, 2017.

[145]   Richter, M. *Inverse Probleme; Grundlagen, Theorie und Anwendungsbeispiele*. 1st ed. Springer Spektrum, 2015. ISBN: 978-3-662-45810-5. DOI: 10.1007/978-3-662-45811-2.

[146]   Ritz, W. "Über eine neue Methode zur Lösung gewisser variations Probleme der mathematishen Physik". In: *Journal für die Reine und Angewandte Mathematik* 135 (1909), pp. 1–61.

[147]   Rixen, D. J. "How measurement inaccuracies induce spurious peaks in frequency based substructuring". In: *IMAC XXVI - International Modal Analysis Conference*. 2008. ISBN: 0-912053-98-4.

[148]   Rixen, D. J. "A dual Craig-Bampton method for dynamic substructuring". In: *Journal of Computational and Applied Mathematics* 168.1-2 (2004), pp. 383–391. ISSN: 03770427. DOI: 10.1016/j.cam.2003.12.014.

[149]   Rixen, D. J., Boogaard, A., Van Der Seijs, M. V., Van Schothorst, G., and Van Der Poel, T. "Vibration source description in substructuring: A theoretical depiction". In: *Mechanical Systems and Signal Processing* 60 (Aug. 2015), pp. 498–511. ISSN: 10961216. DOI: 10.1016/j.ymssp.2015.01.024.

[150]   Rixen, D. J. and Van Der Valk, P. L. C. "An impulse based substructuring approach for impact analysis and load case simulations". In: *Journal of Sound and Vibration* 332.26 (2013), pp. 7174–7190. ISSN: 0022460X. DOI: 10.1016/j.jsv.2013.08.004. URL: http://dx.doi.org/10.1016/j.jsv.2013.08.004.

[151] Roncen, T., Sinou, J.-J., and Lambelin, J.-P. "Experiments and nonlinear simulations of a rubber isolator subjected to harmonic and random vibrations". In: *Journal of Sound and Vibration* 451 (July 2019), pp. 71–83. ISSN: 0022460X. DOI: 10.1016/j.jsv.2019.03.017. URL: https://linkinghub.elsevier.com/retrieve/pii/S0022460X19301774.

[152] Sanchez, J. and Benaroya, H. "Review of force reconstruction techniques". In: *Journal of Sound and Vibration* 333.14 (2014), pp. 2999–3018. ISSN: 10958568. DOI: 10.1016/j.jsv.2014.02.025. URL: http://dx.doi.org/10.1016/j.jsv.2014.02.025.

[153] Schneider, M. *Einführung in die Physiologie des Menschen*. Berlin Heidelberg: Springer, 2013.

[154] Schwarz, H. *Gesammelte Mathematische Abhandlungen*. 2nd ed. Berlin: Springer Verlag, First published in Vierteljahrsschrift der Naturforschenden Gesellschaft in Zürich, volume 15, 1870, pp. 272–286., 1890, pp. 133–143.

[155] Seijs, M. V. van der, Klerk, D. de, Rixen, D. J., and Rahimi, S. "Validation of Current State Frequency Based Substructuring Technology for the Characterisation of Steering Gear–Vehicle Interaction". In: ed. by Mayes, R., Rixen, D., and Allen, M. Topics in Experimental Dynamic Substructuring, Volume 2: Proceedings of the 31st IMAC, A Conference on Structural Dynamics, 2013. New York, NY: Springer New York, 2014. Chap. 20, pp. 253–266. ISBN: 978-1-4614-6539-3. DOI: 10.1007/978-1-4614-6540-9.

[156] Seijs, M. V. van der, Pasma, E. A., Bosch, D. D. van den, and Wernsen, M. W. F. "A Benchmark Structure for Validation of Experimental Substructuring, Transfer Path Analysis and Source Characterisation Techniques". In: *Allen M., Mayes R., Rixen D. (eds) Dynamics of Coupled Structures, Conference Proceedings of the Society for Experimental Mechanics Series*. 4 (2017), pp. 295–305. DOI: 10.1007/978-3-319-54930-9_26.

[157] Seijs, M. V. van der. "Experimental Dynamic Substructuring, Analysis and Design Strategies for Vehicle Development". PhD Thesis. Delft University of Technology, 2016.

[158] Seijs, M. V. van der, Bosch, D. D. van den, Rixen, D. J., and Klerk, D. de. "An improved methodology for the virtual point transformation of measured frequency response functions in dynamic substructuring". In: *4th ECCOMAS Thematic Conference on Computational Methods in Structural Dynamics and Earthquake Engineering* 2013.June (2013), pp. 4334–4347. DOI: 10.13140/RG.2.1.2715.3126.

[159] Seijs, M. V. van der, De Klerk, D., and Rixen, D. J. "General framework for transfer path analysis: History, theory and classification of techniques". In: *Mechanical Systems and Signal Processing* 68-69 (2016), pp. 217–244. ISSN: 10961216. DOI: 10.1016/j.ymssp.2015.08.004.

[160] Seijs, M. V. van der, Pasma, E., Klerk, D. de, and Rixen, D. "A robust Transfer Path Analysis method for steering gear vibrations on a test bench". In: *Proceedings of the international conference on noise and vibration engineering (ISMA)*. 2014, pp. 4027–4040. ISBN: 978-907380291-9. DOI: 10.13140/RG.2.1.4297.8647.

[161] Sendlbeck, S. "Optimierungsstrategien zur Positions- und Richtungskorrektur von Messpunkten (transl. "Optimization strategies for position and orientation correction on measurement points")". Semester Thesis. Technical University of Munich, 2017.

[162] Series, B. 3. *BMW 3 Series celebrates 40 years!* URL: http://www.classicblog.cz/en/bmw-3-series-celebrates-40-years/ (visited on 05/24/2020).

[163] Shabana, A. A. *Dynamics of multibody systems*. Cambridge: Cambridge University Press, 2013. ISBN: 9781107337213. DOI: 10.1017/CBO9781107337213. URL: http://ebooks.cambridge.org/ref/id/CBO9781107337213.

[164] Sjövall, P. and Abrahamsson, T. "Component system identification and state-space model synthesis". In: *Mechanical Systems and Signal Processing* 21.7 (2007), pp. 2697–2714. ISSN: 08883270. DOI: 10.1016/j.ymssp.2007.03.002.

[165] Strang, G. *Computational Science and Engineering*. First Edit. Wellesley-Cambridge Press, 2007. ISBN: 9780961408817.

[166] Strang, G. *Power Series/Euler's Great Formula*. 2010. URL: https://www.youtube.com/watch?v=N4ceWhmXxcs (visited on 06/23/2019).

[167] Strang, G. *Introduction to Linear Algebra*. Wellesley - Cambridge Press, 2016, p. 574. ISBN: 978-09802327-7-6.

[168] Sturm, M., Yankonis, M., Bosch, R., Marchand, C., Sherman, S., Hirscher, J., Priebe, M., Parikh, P., and Moorhouse, A. "Robust NVH Development of Steering Systems Using In-Situ Blocked Forces from Measurements with Low-Noise Driver Simulators". In: *Noise-Con* June (2017).

[169] Sturm, M. "Identification and quantification of transient structure-borne sound sources within electrical steering systems". PhD thesis. University of Salford Manchester, 2013.

[170] Ten Wolde, T. "Reciprocity experiments on the transmission of sound in ships". doctoral Thesis. Technical University Delft, 1973. URL: http://resolver.tudelft.nl/uuid:91058a22-1e2a-4ac2-8a9c-5c349289c134.

[171] Thévenin, L. "On a new theorem of dynamic electricity". In: *Comptes Rendus,* 97.4 (1883), pp. 159–161. URL: https://www.scopus.com/record/display.uri?eid=2-s2.0-0000305762%7B%5C&%7Dorigin=inward.

[172] Thite, A. N. and Thompson, D. J. "The quantification of structure-borne transmission paths by inverse methods. Part 1: Improved singular value rejection methods". In: *Journal of Sound and Vibration* 264.2 (2003), pp. 411–431. ISSN: 0022460X. DOI: 10.1016/S0022-460X(02)01202-6.

[173] Thite, A. N. and Thompson, D. J. "The quantification of structure-borne transmission paths by inverse methods. Part 2: Use of regularization techniques". In: *Journal of Sound and Vibration* 264.2 (2003), pp. 433–451. DOI: 10.1016/S0022-460X(02)01203-8.

[174] Thite, A. N. and Thompson, D. J. "Selection of response measurement locations to improve inverse force determination". In: *Applied Acoustics* 67.8 (2006), pp. 797–818. ISSN: 0003682X. DOI: 10.1016/j.apacoust.2006.01.001.

[175] Törn, A. and Žilinskas, A. *Global optimization*. Vol. 350. Berlin, Heidelberg: Springer, 1989. ISBN: 978-3-540-46103-6. DOI: https://doi.org/10.1007/3-540-50871-6.

[176] Trainotti, F. "Frequency Based Substructuring: Uncertainty Quantification and Regularization of Error Propagation". M.Sc. Thesis. Technical University of Munich, 2018.

[177] Trainotti, F., Haeussler, M., and Rixen, D. J. "A practical handling of measurement uncertainties in frequency based substructuring". In: *Mechanical Systems and Signal Processing* 144 (Oct. 2020), p. 106846. ISSN: 08883270. DOI: 10.1016/j.ymssp.2020.106846. URL: https://linkinghub.elsevier.com/retrieve/pii/S0888327020302326.

[178] Ullmann, R., Sicklinger, S., and Müller, G. "Validation experiment for structural power Phase-Correct Power Measurement". In: *Conference ISMA-USD*. Ed. by Desmet, W. and Pluymers, B. Leuven, 2018.

[179] Ullmann, R., Sicklinger, S., and Müller, G. "Validation of a uniaxial structure-borne sound benchmark with emphasis on power and phase accuracy". In: *Journal of Sound and Vibration* 459 (Oct. 2019), p. 114786. ISSN: 0022-460X. DOI: 10.1016/ J.JSV.2019.05.049. URL: https://www.sciencedirect.com/science/article/abs/pii/ S0022460X19303189.

[180] Valk, P. L. C. van der and Rixen, D. J. "An Impulse Based Substructuring method for coupling impulse response functions and finite element models". In: *Computer Methods in Applied Mechanics and Engineering* 275 (June 2014), pp. 113–137. ISSN: 00457825. DOI: 10.1016/j.cma.2014.03.003.

[181] Van Der Auweraer, H., Bianciardi, F., Van De Ponseele, P., and Janssens, K. "Transfer Path Analysis Innovations for Airborne Noise Problems with Focus on Pass-By-Noise". In: *SAE Technical Papers* 2014-Novem.November (2014). ISSN: 01487191. DOI: 10.4271/2014-36-0801.

[182] Van Der Giet, M., Blum, J., Dietrich, P., Pelzer, S., Muller-Trapet, M., Pollow, M., Vorländer, M., and Hameyer, K. "Auralization of electrical machines in variable operating conditions". In: *2011 IEEE International Electric Machines and Drives Conference, IEMDC 2011*. 2011, pp. 1462–1467. ISBN: 9781457700613. DOI: 10.1109/IEMDC. 2011.5994824.

[183] Vecchio, A. and Auweraer, H. der. "Transfer Path Analysis in the Critical Path of Vehicle Refinement: The Role of Fast, Hybrid and Operational Path Analysis". In: *SAE 2007 - Noise and vibraiton conference*. 2007. DOI: 10.4271/2007-01-2352..

[184] Verheij, J. W. "Multi-path sound transfer from resiliently mounted shipboard machinery - Experimental methods for analyzing and improving noise control". PhD thesis. Technical College Delft (now Technical University Delft), 1982. DOI: 10.13140/RG.2. 2.29505.35683.

[185] Vleck, E. B. V. "The Influence of Fourier's Series upon the Development of Mathematics". In: *Science* 39.995 (1914), pp. 113–124. ISSN: 00368075, 10959203. URL: http://www.jstor.org/stable/1640940.

[186] Voormeeren, S. N. and Rixen, D. J. "A family of substructure decoupling techniques based on a dual assembly approach". In: *Mechanical Systems and Signal Processing* 27.1 (2012), pp. 379–396. ISSN: 08883270. DOI: 10.1016/j.ymssp.2011.07.028.

[187] Vorländer, M. *Auralization: Fundamentals of Acoustics, Modelling, Simulation, Algorithms and Acoustic Virtual Reality*. RWTHedition. Berlin, Heidelberg: Springer-Verlag, 2008. ISBN: 9783540488293. DOI: 10.1007/978-3-540-48830-9.

[188] Wang, J., Sun, G.-h., Lu, L.-X., and Wang, Q.-L. "General Formulation of Inverse Substructuring Method for Multicoordinate Coupled System". In: *Advances in Mechanical Engineering* 2014 (2014), p. 475128. ISSN: 1687-8140. DOI: 10.1155/2014/475128. URL: https://doi.org/10.1155/2014/475128.

[189] Wang, Z., Peng, Z., Liu, C., and Shi, X. "Virtual decoupling of mechanical systems considering the mass effect of resilient links: Theoretical and numerical studies". In: *Mechanical Systems and Signal Processing* 123 (May 2019), pp. 443–454. ISSN: 08883270. DOI: 10.1016/j.ymssp.2019.01.028.

[190] Weinzierl, S. *Handbuch der Audiotechnik*. Berlin, Heidelberg: Springer, 2008. ISBN: 978-3-540-34300-4. DOI: 10.1007/978-3-540-34301-1.

[191] Welch, P. D. "The Use of Fast Fourier Transform for the Estimation of Power Spectra: A Method Based on Time Averaging Over Short, Modified Periodograms". In: *IEEE-Transactions on Audio and Electroacoustics* 2 (1967), pp. 70–73.

[192] Wernsen, M. W., Seijs, M. V. van der, and Klerk, D. de. "An indicator sensor criterion for in-situ characterisation of source vibrations". In: *Conference Proceedings of the Society for Experimental Mechanics Series* 5B (2017), pp. 55–69. ISSN: 21915652. DOI: 10.1007/978-3-319-54987-3_7.

[193] Wernsen, M. W. "Observability and transferability of in-situ blocked force characterisation". Master thesis. Technical University Delft, 2017. URL: http://resolver.tudelft.nl/uuid:8163a56c-5bb3-4aaa-983d-ffedf3ee9c4b.

[194] Wienen, K. and Moorhouse, A. "Robust NVH Engineering Using Experimental Methods - Source Characterization Techniques for Component Transfer Path Analysis and Virtual Acoustic Prototyping". In: 2019, pp. 1–13. DOI: 10.4271/2019-01-1542. Abstract.

[195] Williams, A., Chipman, C., and Avitabile, P. "Modal and frequency based substructuring using rotational DOF considerations". In: *Proceedings of the 26th International Modal Analysis Conference, Orlando, Florida*. 2008.

[196] Wolde, T. ten. "Reciprocity Measurements in Acoustical and Mechano-Acoustical Systems. Review of Theory and Applications". In: *Acta Acustica united with Acustica* 96 (2010), pp. 1–13. DOI: 10.3813/AAA.918250.

[197] Yintao, W., Feng, X., Fuqiang, Z., and Xiang, D. "Simulation of Rolling Noise Based on the Mixed Lagrangian–Eulerian Method". In: *Tire Science and Technology* 44 (2016), pp. 36–50. DOI: 10.2346/tire.16.440103.

[198] Zabel, D. F. "Structure-borne sound transmission within electric power steering systems". PhD thesis. University of Salford, Sept. 2018.

[199] Zabel, D., Sturm, M., Moorhouse, A., and Alber, T. H. *Internal Transfer Path Analysis based on In-Situ Blocked Forces and Transimissibility Functions*. July 2017.

[200] Zeller, P. *Handbuch Fahrzeugakustik - Grundlagen, Auslegung, Berechnung, Versuch*. 3rd ed. Springer, Vieweg Teubner, 2012. ISBN: 9783834814432. DOI: 10.1007/978-3-8348-8657-6.

[201] Zhen, J., Lim, T. C., and Lu, G. "Determination of system vibratory response characteristics applying a spectral-based inverse sub-structuring approach. Part I: analytical formulation". In: *International journal of vehicle noise and vibration* (2004). ISSN: 1479148X.

[202] Zienkiewicz, O. C. *The finite element method in engineering science*. 2nd ed. London: McGraw Hill, 1971.